
Optical spectroscopy of exoplanets and hosts stars

A thesis
submitted for the degree of
Doctor of Philosophy

in

The Department of Physics,
Pondicherry University,
Puducherry - 605 014, India



by

Athira Unni
Indian Institute of Astrophysics,
Bangalore - 560 034, India



December 2022

Optical spectroscopy of exoplanets and hosts stars

Athira Unni

Indian Institute of Astrophysics



Indian Institute of Astrophysics
Bangalore - 560 034, India

Title of the thesis : **Optical spectroscopy of exoplanets and hosts stars**

Name of the author : **Athira Unni**

Address : Indian Institute of Astrophysics
II Block, Koramangala
Bangalore - 560 034, India

Email : athira.u@iiap.res.in

Name of the supervisor : **Prof. Sivarani Thirupathi**

Address : Indian Institute of Astrophysics
II Block, Koramangala
Bangalore - 560 034, India

Email : sivarani@iiap.res.in

Declaration of Authorship

I hereby declare that the matter contained in this thesis is the result of the investigations carried out by me at the Indian Institute of Astrophysics, Bangalore, under the supervision of Prof. Sivarani Thirupathi. This work has not been submitted for the award of any other degree, diploma, associateship, fellowship, etc., of any other university or institute.

Signed:

Date: 31-12-2022

Certificate

This is to certify that the thesis titled '**Optical spectroscopy of exoplanets and hosts stars**' submitted to Pondicherry University by Ms. Athira Unni for the award of the degree of Doctor of Philosophy is based on the results of the investigations carried out by him under my supervision and guidance, at the Indian Institute of Astrophysics. This thesis has not been submitted for the award of any other degree, diploma, associateship, fellowship, etc., of any other university or institute.

Signed:

Date: 31-12-2022

List of Publications

1. **Athira Unni**, Thirupathi Sivarani, Gordon Yip, Apurva Oza, Bharat Chandra ..., "*Feasibility of Low-Resolution Transmission Spectroscopy Using 2m Himalayan Chandra Telescope*". (in preparation)
2. **Athira Unni**, Thirupathi Sivarani, Apurva Oza, H. Jens Hoeijmakers, Julia V. Seidel, Carl Schmidt, Katherine d kler,.. "*High-Resolution transmission spectroscopy of WASP-49b using KECK/HIRES*" (in preparation)
3. **Athira Unni**, Thirupathi Sivarani, Anisha Sen, Rajguru,.. "*Contribution of disk-inhomogeneity in the observed exoplanet transmission Spectra*" (in preparation)
4. **Athira Unni**, Mayank Narang, Thirupathi Sivarani, Manoj Puravankara, Ravinder K Banyal, Arun Surya, SP Rajaguru, C Swastik, "*Carbon Abundance of Stars in the LAMOST-Kepler Field*"
5. S. Sriram, Amit Kumar, Arun Surya, T. Sivarani, Sunetra Giridhar, S. Kathiravan, M. N.Anand, Damien Jones, Deon Grobler, Robert Jakobsson, Anantha Chanumolu, **Athira Unni**, Angchuk Dorje, Tsewang Dorje, Tsewang Gyalsen, Proc. SPIE 10702, Groundbased and Airborne Instrumentation for Astronomy VII, 107026K (6 July 2018), "*Hanle Echelle Spectrograph: Design and Performance*"
6. K Aravind, Shashikiran Ganesh, Kumar Venkataramani, Devendra Sahu, Dorje Angchuk, Thirupathi Sivarani, **Athira Unni**, Monthly Notices of the Royal Astronomical Society, Volume 502, Issue 3, April 2021, Pages 3491–3499, "*Activity of the First interstellar Comet 2I/Borisov Around Perihelion: Results from Indian Observatories*"
7. A Susmitha, D K Ojha, T Sivarani, J P Ninan, A Bandyopadhyay, Arun Surya, **Athira Unni**, Monthly Notices of the Royal Astronomical Society, Volume 506, Issue 2, September 2021, Pages 1962–1977, "*Optical and NIR Spectroscopy of Cool CEMP Stars to Probe the Nucleosynthesis in Low-Mass AGB Binary System*"

8. Susmitha, A., Sivarani, T., Ojha, D.K., Joe p. Ninan, A. Bandyopadhyay, A.Surya, **U.Athira**, J Astrophys Astron 41, 50 (2020), "*Oxygen Abundances of Carbon-Enhanced Stellar Population in the Halo*"
9. C. Swastik, Ravinder K. Banyal, Mayank Narang, P. Manoj, T. Sivarani, S. P. Rajaguru, **Athira Unni**, and Bihan Banerjee, "*Galactic Chemical Evolution of Exoplanet Hosting Stars: Are High-mass Planetary Systems Young?*"
10. Paul A. Dalba, Stephen R. Kane, Diana Dragomir, Steven Villanueva Jr., Karen A. Collins, Thomas Lee Jacobs, Daryll M. LaCourse, Robert Gagliano, Martti H. Kristiansen, Mark Omohundro, Hans M. Schwengeler,....., Jana Steuer, Thirupathi Sivarani, **Athira Unni**, Nora L. Eisner, Tara Fetherolf,...., *The TESS-Keck Survey. VIII. Confirmation of a Transiting Giant Planet on an Eccentric 261 Day Orbit with the Automated Planet Finder Telescope*

Oral Presentations

1. Presented a talk titled “**Exoplanet host stars using Hanle Echelle Spectrograph**” in *Young Astronomers’ Meet, 24-28 September 2018*, PRL, Ahmedabad, India.
2. Oral presentation on the topic “**Exoplanet host stars using Hanle Echelle Spectrograph**” in the *Astronomical Society of India meeting 2018* held at Christ University, Bengaluru, Karnataka, India, during 18-22 February 2019.
3. Presented a talk titled “**Exploring the feasibility of low-resolution transit spectroscopy using 2m telescope**” in *Young Astronomers’ Meet, 23-27 September 2019*, Kodaikanal Solar Observatory (IIA), Tamilnadu, India.
4. Presented an invited talk on “**Feasibility of low-resolution transmission spectroscopy using Himalayan Chandra Telescope**” in the monthly meeting, 2nd April 2020, ISRO, India, Online.

Poster Presentations

1. Presented poster on “**Carbon abundance of stars in the LAMOST-Kepler field**” in *39th Meeting of the Astronomical Society of India, 25-29 March 2022*, IIT Roorkee & ARIES Nainital, India.

Acknowledgements

I learned something new every day I was here. I am grateful to the Director, the Dean, and the Board of Graduate Studies (BGS) for allowing me to work at this institute and providing all the resources necessary for my research. Sincere thanks to my Doctoral committee members, Prof. Ravinder Banyal and Dr. KVP. Latha, for all the support and suggestions.

I am grateful to the librarian for assisting me in locating the required books and journals. I appreciate the assistance with computer and internet-related concerns that Ashok, Fayaz, Anish, and other employees of the "Data Center" provided. My sincere gratitude to Mr. Sankaranarayan, the administrative officer, the personnel officer, the accounts officer, and the rest of the administrative team for their prompt assistance with administrative duties. With the help of every employee, all official tasks were completed without incident. I appreciate the care the Bhaskara cooks, supervisors, and other employees gave me while I was here. Bhaskara has always seemed like home to me. It was very beneficial during the COVID pandemic.

Observations and going to CREST Campus were always memorable. I would like to express my sincere thanks to the observing assistants, Pramod, Kiran, Sujith, and Anaswer, for their support and dedication.

My guide, Prof. Sivarani, is to be thanked for all the guidance, support, love, and care. She taught me a lot that I have used in my personal and professional life. Thank you for understanding me and accepting me for who I am. She was there for me all the time.

I thank all the teachers who have helped me throughout the years. Sincere appreciation and respect to Dr. Shyama and Prof. Mayya, sir. You both believed in

me and gave me the courage to take greater action.

I am lucky and grateful to have met Dr. Avrajit, my senior, who stood as a pillar of strength for these five years. He taught me the basics of spectroscopic observations and data reductions. He taught me to appreciate myself, read, travel, and be content with who I am. I will always treasure the lovely times we shared.

Thanks to Dr. Susmitha, Dr. Arun Surya, Devika, Pallavi, and Manjunath, for all the help. I had a wonderful team here to support me.

Thank you so much, Dr. Apurva Oza. It was a long journey with him at work, filled with highs and lows. Thank you for being so understanding, providing me with the time and space to learn, showing me how beautiful a person can be, and opening the door of high-resolution transmission spectroscopy.

Sincere thanks to Dr. Avinash, Dr. Raghu, Phanindra, Bharat, Sonith, Dr. Bibhuti, and Dr. Arun Surya for helping me to debug the errors in some of the python codes I have used. Also, thanks to Prof. Manoj Purvankara, Prof. Ravinder Banyal, Dr. Mayank, Swastik, Pallavi, Anisha Sen, Julia Seidel, Jens Hoeijmakers, Carl Schmidt, and Gordon Yip for all the support in the work.

I sincerely appreciate the help and company of my fellow batchmates Partha, Dr. Bibhuti, Soumya, Satabdwa, Sharmila, and Manika. Over the years, I have learned a lot from them.

Aside from my work life, the company of some lovely people is my greatest accomplishment here. Partha, Bibhuti, and Avrajit were always there as a brother to support and guide me. I am thankful to Bharat, Sonith, Dhanush, and Manjunath for all the support, love, and care in my ups and downs. Also, for never giving up on my complaints and mood swings. I thank you for being there for me always,

Dr. Bhoomika. Devika, thank you for believing in me and always supporting me. Many thanks to Dr. Rubi for her kindness and concern. Since day one at IIA, she has been there as a big sister. Thanks to Dr. Nancy and Dr. Chandrasekhar for all the love and support. My sincere thanks to Sharmila and Satabdwa for all the love and care. Many thanks to Shubhangi and Rupesh for their love and company.

The sport was a major part of my life here. Thanks to Dr. Chayan, Dr. Bhoomika, Dr. Deepak, and Dr. Nagaraju for supporting and encouraging me to participate in all the games.

Thanks to Anirban, Deepthi, Fazlu, Sioree, and Indrani. They always treated me as their batchmate. Thanks to Pallavi, Ankit, Dr. Binu Kumar, Shubham, Suman, Vishnu Madhu, Dr. Ramya, Ameya, Parvathi, Akhil, and Khushbu for their support, love, and company. Thanks to the beautiful seniors like Prasanta, Piyali, Kshama, Amit, Rakesh Mazmudar, Debjit, Brajesh sir, Manoj, and Priya for making life more cherishable.

Thanks to my friends Nimal, Vijesh, and Baheeja, who always stood with me in my ups and downs. Finally, the best thing that has happened so far is my sisters; I never felt alone because they were always there for me. I am grateful to my parents for their unconditional love, support, and sacrifice.

Everything I have accomplished thus far and who I am today is solely the result of the people I have encountered at various points in my life. Thank you, everyone, from the bottom of my heart.

-Athira

Data usage

Data from several ground-based facilities were primarily employed in the study. I sincerely thank the individual instrument teams for making the data available in the public domain, and I acknowledge their use in my work.

For the first work in the thesis, we used low-resolution spectroscopic survey data from the LAMOST archive along with Gaia DR2 data, *NASA Exoplanet Archive* and Kepler Input Catalogue (KIC) details. I sincerely thank each of the communities mentioned above for granting access to the data.

A part of the thesis work is completely focusing on the data acquired from the Himalayan Faint Object Spectrograph (HFOSC) and Hanle Echelle Spectrograph (HESP) mounted on the 2m Himalayan Chandra Telescope (HCT) maintained by the Indian Institute of Astrophysics, Bangalore. I sincerely thank the Indian Astronomical Observatory community for scheduling observation nights and helping me with observations.

Two thesis chapters used high-resolution spectroscopic observations from the KECK/HIRES (High REsolution Echelle Spectrograph) telescope. Sincere thanks to the KECK community for providing observing time and for providing access to the data.

The final chapter completely depends on three years of the Sun as a star, a unique observation done by HARPSN spectrograph. I thank HARPS team for releasing the data in the public domain. I want to express my sincere thanks to SDO/HMI communities for providing access to the data.

Dedicated to

*my parents for their love and sacrifices to impart the best possible
quality of education to me*

*my sisters & the people I met at different stages of life who helped
me to grow as a person*

Abstract

The thesis work '**Spectroscopic Characterization of Exoplanets and Host Stars,**' tries a tiny step towards understanding the connection between the exoplanet and the host star. We study the observational perspective of exoplanets and host stars using optical spectroscopy. Our analysis of host star carbon abundances as a function of planet occurrence rate in the LAMOST-Kepler field shows giant planets are preferentially found around iron-rich and carbon-rich host stars. However, the sub-solar $[C/Fe]$ value of giant planet host stars indicates that carbon may not be as important as iron or that the overall metallicity is crucial rather than a single element like carbon or iron for planet formation. Differential abundance analysis of planet hosts in visual binary twin systems shows that planet-induced pollution in the host star chemical abundance is less than 0.01 dex. It is well within the typical error in abundance estimates, which indicates that occurrence rate calculations are not influenced by planet pollution in the host star photosphere. The accuracy of differential abundances needs to be better than 0.01dex to infer any trend in the abundances due to planet formation.

The low-resolution transmission spectroscopy from the 2 m Himalayan Chandra Telescope using long-slit multi-object observations successfully detected several atmospheric features in the atmosphere of three exoplanets HAT-P-1 b, KELT-18 b, and WASP-127 b. The advantage of having a bluer part of the spectra, we were able to detect CaI (4227 Å) in the atmosphere of HAT-P-1 b and Rayleigh scattering slope in the atmosphere of WASP-127 b. We observed flat, featureless transmission spectra of KELT-18 b for the first time at low resolution. Simultaneous observation of reference stars helped to avoid the systematic errors introduced during the observations. We perform transmission spectroscopy with Keck-HIRES for the first time. We achieved a wavelength calibration accuracy of 60 m/s for HIRES, using a wavelength recalibration method. We detect residual sodium signals at a blue-shifted stellar rest frame location.

Occulted and unocculted stellar inhomogeneity can change the observed transit signal or can add extra noise to the observed data. Here we studied three years of disk-integrated solar spectra from HARPS to quantify the inhomogeneity using the spectral indices. From the preliminary analysis, we found that the faculae fraction than the spot fraction influences the line indices. Ca II H & K linearly correlated with faculae fraction, and all the Balmer lines are sensitive to faculae fraction but have a complex trend compared to CaII H & K lines.

Contents

-1

Abstract	i
List of Figures	ix
List of Tables	xvii
Abbreviations	xix

1 Introduction	1
1.1 History of exoplanet searches	1
1.1.1 Exoplanet Populations	3
1.1.2 Planet formation and host star abundances	10
1.2 The scope of the thesis	15
1.3 Plan of the thesis	15
2 Observations and Data Analysis	17
2.1 LAMOST Survey	18
2.2 High-resolution spectroscopy	20
2.2.1 Keck-HIRES	20
2.2.2 Hanle Echelle Spectrograph (HESP)	21
2.2.3 HARPS-North spectrograph & Solar spectra	23
2.3 Hanle faint object spectrograph	23
2.4 SDO Data	24
2.5 Spectroscopic Data Reduction	25
2.6 Stellar chemical abundances	28
2.6.1 Stellar parameters	29
2.6.2 Atomic and molecular data	32
2.6.3 Stellar model atmospheres	32
2.6.4 Equivalent width measurement and abundance calculation	33
2.6.5 Estimating stellar parameters	33
2.6.6 Abundance estimation	35

2.7	Methodology: Exoplanet atmospheric characterization with spectroscopy	38
2.7.1	High-resolution transit spectroscopy with Keck/HIRES	39
3	Carbon abundance of stars in the LAMOST-Kepler field	43
3.1	Introduction	44
3.2	Data acquisition and target selection	46
3.2.1	Estimation of carbon abundances	48
3.2.2	Scaling the derived carbon abundances	50
3.2.3	Searching for systematic trends	52
3.3	Results	56
3.3.1	Elemental abundance of the host stars as a function of planet population	56
3.3.2	Occurrence rate of planets and the host star abundance	57
3.3.3	Galactic space velocity dispersion	60
3.4	Discussion	64
3.5	Conclusion	67
4	Differential Abundance Analysis of Planet Host Visual Binary Systems	75
4.1	Introduction	76
4.2	Observation and Data reduction	78
4.3	Determining stellar parameters	80
4.4	Deriving the abundances of all the elements	83
4.5	Discussion	84
5	Transit Spectrophotometry of Hot Jupiters Using 2m Himalayan Chandra Telescope	105
5.1	Introduction	106
5.2	Observations and analysis	107
5.3	Data reduction	110
5.3.1	Constructing light curve	111
5.3.2	Constructing low-resolution transmission spectra	113
5.4	Result and Discussion	115
5.5	Conclusion	118
6	High-Resolution Transmission Spectroscopy of WASP-49 b Using KECK/HIRES	123
6.1	Introduction	124
6.2	Observation	126
6.3	HIRES data reduction	126
6.3.1	Accurate Wavelength Calibration	128
6.3.2	Distortion correction	129

6.3.3	Telluric correction	131
6.3.4	Final transmission spectra	133
6.4	Discussion	137
6.5	Conclusion	139
7	Characterizing The Solar Disk inhomogeneity From Disk-Integrated Spectra	141
7.1	Introduction	142
7.2	Observation & Data Analysis	143
7.2.1	Estimating spot and faculae fraction	144
7.3	Line index measurement	146
7.4	Results and Conclusion	147
8	Conclusion	153

List of Figures

1.1	Exoplanet detected each year from the first detection using different methods. Image credit: NASA Exoplanet Archive	2
1.2	Different exoplanet population as a function of the orbital period (Image credit: NASA)	3
1.3	Exoplanets detected as a function of orbital period and planet mass m_p (left) and orbital period and planet radius R_p (right)(Gaudi et al. 2021)	4
1.4	Demonstrating transit method of exoplanet detection. t_1, t_2, t_3 , and t_4 represent just before ingress, ingress, egress, and just after the egress. The transit event is happening between t_1 and t_4 . Image credit : Britastro	5
1.5	The image illustrates the blue and red shift in the observed host star spectra as a planet orbiting around the host star.	6
1.6	Figure represents the major possible process happening in the exoplanet atmosphere (Madhusudhan 2019). Possible species can be detected in each layer and in which region of the electromagnetic spectrum.	7
1.7	Figure represents the transit light curve at various wavelength for HD209458b, based on the HST data from Knutson et al. (2007) and the figure taken from Winn (2010) . The transit depth and shape clearly vary across wavelengths.	7
1.8	Illustration of Primary transit of a planet with radius R_p and atmospheric height 'H' around a star of stellar radius R_s	9
1.9	Prominent features in the transmission spectra of a typical exoplanet at different wavelength region (Credits: Matteo Brogi- Evry Schatzman School 2019, Aussois, France)	9
1.10	Figure displays the diversity of exoplanets as compared to the Solar system planets, the image taken from Raymond et al. (2020)	11
1.11	Figure shows an image of a protoplanetary disk HL TAU observed with ALMA. The ring-like shape of the disk is due to the planetary size objects clearing material, causing a gap in the disk (ALMA Partnership et al. 2015)	13

2.1	Figure from Yan <i>et al.</i> (2022) shows LAMOST telescope optical layout. A combination of spherical primary and an active spherical correcting mirror provides a wide field of view of 5 deg).	18
2.2	Typical wavelength calibrated spectra from LAMOST archive.	19
2.3	LK field of observation, Common field of observation colored in blue Ren <i>et al.</i> (2016)	19
2.4	Figure shows the light path of the High-REsolution Spectrograph (HIRES) at Keck.	21
2.5	The light path of the Hanle Echelle fiber-fed Spectrograph at HCT.	21
2.6	HARPS spectrograph with the vacuum enclosure at the 3.5m, Nazionale Galileo Telescope (TNG) at La Palma.	22
2.7	Schematic of the HFOSC instrument	24
2.8	2D stellar image and sky from a high-resolution echelle spectrograph from Keck/HIRES (CCD1).	25
2.9	2D stellar image and sky from a low-resolution long slit observation of two stars from HCT/HFOSC.	25
2.10	The top panel is a typical bias frame from Keck/HIRES (CCD1, one of the mosaics). The bottom panel is a bias frame for HFOSC CCD.	26
2.11	Typical flat frame from HIRES spectrograph CCD1. The exposure time is in the order of seconds.	27
2.12	Typical flat frame from HCT/HFOSC. The exposure time is in the order of seconds.	27
2.13	Typical ThAr frame from HIRES CCD1. The typical exposure time is in the order of seconds.	28
2.14	Typical FeAr frame HCT/HFOSC. The typical exposure time is in the order of seconds.	28
2.15	Typical wavelength calibrated high-resolution spectra cover different orders from Keck/HIRES.	28
2.16	Typical wavelength calibrated low-resolution spectra from HCT/HFOSC grism 7.	29
2.17	The diagram shows the main steps included in the calculation of stellar abundance by combining observation and modeling.	29
2.18	Synthetic spectra around $H\alpha$ region with different T_{eff} . All the other parameters are fixed.	31
2.19	Synthetic spectra around one of the Mg triplet regions with different $\log g$ values. All the other parameters are fixed.	31
2.20	Area under the absorption line and the area of the rectangle are the same. Equivalent width is the width (b) of the rectangle. Image credit: Cosmos	34
2.21	Number of atoms present as a function of the equivalent width of the absorption line from <i>Aller, Atoms, Stars and Nebulae, Revised edition, Harvard University Press, Cambridge, MT, 1971.</i>	36

2.22	Best fit model (solid black line) for the abundance of both Fe I (blue) and Fe II (red) lines independent of lower excitation potential. for HD 202772 B using Keck/HIRES observations.	37
2.23	Best-fit model (solid black line) for the abundance of both Fe I (blue) and Fe II (red) lines independent of reduced equivalent width for HD 202772 B using Keck/HIRES observations.	37
2.24	Step-by-step data analysis procedure of the low-resolution transmission spectroscopy.	38
2.25	Possible telluric lines present in the Earth's atmosphere, in the optical part of the spectra (Smette <i>et al.</i> 2015).	40
2.26	Pictorial representation of expected velocity shift in the absorption line during transit.	41
3.1	The entire sample from the LAMOST-KEPLER field is shown as a density plot. And the selected samples within the restricted stellar parameters for the current study are shown as an inset. The black and red dots indicate the field and the planet host stars, respectively.	47
3.2	Distribution of SNR, T_{eff} and $\log g$ of the final sample ($4800 \leq T_{eff} \leq 6500$ K and $\log g > 4.0$). The small planet host with planet radius $R_p \leq 4R_{\oplus}$, giant planet ($R_p > 4R_{\oplus}$) host stars, and field stars are in green, red and blue respectively.	48
3.3	Observed spectra of Sun (blue) and the synthetic spectra (red). The top panel shows the best fit with input parameters from LAMOST. The bottom-left panel shows an enlarged view of the CH G-band region. Bottom right panel shows the χ^2 variation with $[C/H]$ for obtaining the best fit $[C/H]$ value for the Sun with $T_{eff} = 5774$ K and SNR= 76.	50
3.4	Observed spectra (blue) and synthetic spectra (red). The top panel shows the best fit for a star of $T_{eff} = 4800$ K and SNR= 75.07. The bottom-left panel shows the best fit for a star with $T_{eff} = 6496$ K and SNR= 44.10	51
3.5	Comparison of the derived T_{eff} values from CKS and the LAMOST. The black line is the 1:1 line.	52
3.6	Comparison of the derived $[Fe/H]$ values from CKS and the LAMOST pipeline. A linear fit is established between the CKS and the LAMOST $[Fe/H]$ values. The best fit coefficients are $[Fe/H]_{new} = [Fe/H]_{lamost} * 0.791 + 0.005$. The blue dashed line is the 1:1 line, and the black dashed line is the best-fit line.	53
3.7	Comparison of the derived $[C/H]$ values from CKS and the LAMOST as a function of T_{eff} . The black dashed line is the 1:1 line, and the blue dashed line is the best-fit line.	53
3.8	Comparison of $\delta[C/H] = [C/H]_{CKS} - [C/H]_{LAMOST}$ as a function of T_{eff} . A linear fit is established, and the best fit coefficients are $\delta[C/H] = -0.762 * \log(T_{eff}(lamost)) + 6.820$	54

3.9	Variation in $[C/H]$ as a function of T_{eff} (a), $\log g$ (b) and $[Fe/H]$ (c) after CKS correction. Giant planet host stars (red), Small planet host stars (black), field stars (grey), and Sun (yellow). Variation in $[C/H]$ error (shifted for the visual purpose at different x values plotted in blue. In Figure 3.9 (c), the black dashed line shows the 1:1 correlation. (d) shows $[C/Fe]$ as a function of $[Fe/H]$	55
3.10	Distribution of carbon among small planet($R_p \leq 4R_{\oplus}$) host, giant planet($R_p > 4R_{\oplus}$) host stars and field stars. A dashed vertical line represents the mean value of each distribution.	58
3.11	(a) Occurrence rate of exoplanets as a function of the planetary radius and the host star metallicity. (b) The total occurrence rate of the sample without subdividing it into different metallicity bins. (c) The normalized occurrence rate of the exoplanets as a function of the planetary radius and the host star metallicity. The error bars in these plots are the Poissonian errors based on the number of planets in each bin.	61
3.12	(a) Occurrence rate of exoplanets as a function of the planetary radius and the host star $[C/H]$. (b) The normalized occurrence rate of the exoplanets as a function of the planetary radius and the host star $[C/H]$	62
3.13	(a) Occurrence rate of exoplanets as a function of the planetary radius and the host star $[C/Fe]$. (b) The normalized occurrence rate of exoplanets as a function of the planetary radius and the host star $[C/Fe]$	63
3.14	The total velocity dispersion and the velocity dispersion of the individual components (σ_U , σ_V , and σ_W) as a function of $[Fe/H]$. We have used a running average with a bin size of 1000 and a step size of 200. The error bar on the velocity dispersion is computed following Binney et al. (2000) . On the right-hand y-axis are the corresponding ages computed using Equation 3.4. The same axis and error bar, as well as the binning scheme, are followed for all subsequent figures.	65
3.15	The total velocity dispersion and the velocity dispersion of the individual components (σ_U , σ_V and σ_W) as a function of $[C/H]$	66
3.16	The total velocity dispersion and the velocity dispersion of the individual components (σ_U , σ_V and σ_W) as a function of $[C/Fe]$	67
4.1	HD 80606/HD 80607 visual binary system from <i>Aladin</i> . Two circles illustrate two pinholes of HESP to observe stars and sky simultaneously.	79
4.2	Overplotted different regions of the spectra of both the planet host star (HD80606) in black and companion star (HD80607) in red.	80

4.3	The top panel indicates the zero-slope model for abundance versus lower excitation potential for the companion star using the absolute method. The bottom panel represents the stellar parameters of the planet host star using differential equilibrium (Fe I lines in blue and Fe II lines in red dots) for HD 80606/HD80607.	82
4.4	The top panel depicts the zero-slope model for abundance versus reduced equivalent width for the companion star using the absolute method. The bottom panel shows the stellar parameters of the planet host star using differential equilibrium (Fe I lines in blue and Fe II lines in red dots) for HD80606/HD80607.	82
4.5	Differential abundance as a function of atomic number for HD 80606/HD 80607. The mean abundance and the error of volatile elements C, O, and S are presented in grey, and the mean abundance and the error of refractory elements are presented in blue.	84
4.6	The absorption lines of Co, Ca, S, and Zn of HD 80606 (solid black line) overplotted with HD 80607 (solid red line). The blue line is the residual spectra.	85
4.7	The absorption lines of C, Sc, Si, Fe, and Mg of HD 80606 (solid black line) overplotted with HD 80607 (solid red line). The blue line is the residual spectra.	86
4.8	Condensation temperature as a function of differential abundance for HD 80606/HD 80607.	87
4.9	AO image from KECK/NIRC2 of the binary system. A companion is separated by 1.3" (Wang <i>et al.</i> 2019). The entrance slit width of Keck/HIRES is 0.7".	87
4.10	CCD1 raw image and extracted spectra from KECK/HIRES pipeline (MAKEE).	88
4.11	Normalized spectra of planet host star (HD 202772 A) and the binary companion star (HD 202772 B) in the wavelength range of 4500 Å- 4580 Å.	89
4.12	Figure indicates different regions of the spectra of both the planet host star HD202772 A (red) and HD202772 B (black).	89
4.13	The top panel represents the best fit zero slope model for abundance as a function of lower excitation equilibrium for the companion star using the absolute method. The bottom panel shows the stellar parameters of the planet host star using differential equilibrium (Fe I lines in blue and Fe II lines in red dots) for HD202772A/B.	90
4.14	The top panel illustrates the best fit zero slope model for abundance as a function of reduced equivalent width for the companion star using the absolute method. The bottom panel shows the stellar parameters of the planet host star using differential equilibrium (Fe I lines in blue and Fe II lines in red dots) for HD 202772 A/B.	91
4.15	Condensation temperature as a function of differential abundance for HD 202772 A/B.	91

5.1	The figure depicts the schematic diagram explaining the steps included in the data analysis for low-resolution transmission spectroscopy.	111
5.2	The figure shows the object and reference stars (connected with a red line in the figure) selected for the observation. Images from left to right are HAT-P-1, WASP-127, and KELT-18. (Image credit: <i>Aladin</i>)	111
5.3	CCD images of HAT-P-1, WASP-127, and KELT-18, along with the reference star from left to right observed using HCT/HFOSC single exposure.	112
5.4	Single exposure, wavelength calibrated spectra of HAT-P-1 (Grism 7), WASP-127 (Grism 7), and KELT-18 (Grism 8) from left to right. The solid black line is the object star, and the solid red line is the reference star.	112
5.5	Observed white lightcurve of HAT-P-1b, WASP-127 b, and KELT-18 b from left to right with the best fit model.	113
5.6	The figure indicates the schematic diagram explaining the steps included in the lightcurve analysis.	114
5.7	Observed white lightcurve (scattered point) of WASP-127 with the best fit model (solid line).	114
5.8	Residual plot from the Figure 5.7	114
5.9	Lightcurve in a wavelength bin of WASP-127 after common mode correction.	115
5.10	Lightcurve before (red) and after (blue) applying Kalman filter . . .	115
5.11	Grism 7 lightcurves in each wavelength bin (scattered point) and the best-fit transit models (solid line) stacked from top to bottom for WASP-127b and applied a constant scaling factor of 0.01 for visibility.	116
5.12	Grism 8 lightcurves in each wavelength bin (scattered point) and the best-fit transit models (solid line) stacked from top to bottom for KELT-18b and applied a constant scaling factor of 0.01 for visibility.	117
5.13	Grism 7 lightcurves in each wavelength bin (scattered point) and the best-fit transit models (solid line) stacked from top to bottom for HAT-P-1b and applied a constant scaling factor of 0.01 for visibility.	118
5.14	Observed transmission spectra of WASP-127 b (blue) and the best fit model (grey) computed using <i>Exo-Transmit</i> with $1\times$ solar models TiO/VO, Na/K, and $T_{equ} = 1400$ K. We separately calculated the Rayleigh scattering slope (yellow) from Lecavelier Des Etangs <i>et al.</i> (2008)	119
5.15	Observed transmission spectra of KELT-18 b (blue) with the best fit model (teal) using <i>Exo-Transmit</i> with $0.1\times$ solar models without TiO/VO and with Na/K and $T_{equ} = 1400$ K. Binned model spectra represents in grey.	120

5.16	Observed transmission spectra of HAT-P-1 b (blue) with the best fit model using <i>Exo-Transmit</i> with $1.0\times$ solar models without TiO/VO and with Na/K and $T_{equ} = 1500$ K (teal) and binned model in solid black line.	121
6.1	Various analysis steps are shown in the flow chart	128
6.2	Radial velocity shift in each exposure with respect to the first exposure as a function of time is shown for three echelle orders. The first order is in black, the last order is in red, and the order containing the sodium doublet around 589 nm is in blue. There is a shift of 0.8 km/s from the first to the last exposure.	129
6.3	A residual RV shift vector map across different echelle orders is shown here. The possible residual shift in each exposure is calculated by measuring the centroid of a set of lines in each exposure (Figure 6.4). The calculated the shift in each line (length of the red arrow) with respect to the corresponding line in the first exposure (black dot). The Center wavelength of each order is considered to be zero. And y-axis represents the order number in CCD2.	130
6.4	Observed spectra (in black) and selected clean lines for calculating distortion correction and gaussian fits to the lines are shown in red. Zoomed version of a gaussian fit is shown in the subplot.	131
6.5	Distortion (Figure 6.4) correction to the wavelength solution is applied order by order using the first exposure, based on more than ten narrow stellar lines in each order. An example of order five is shown in the top panel. A cubic spline fit to the distortion gives a residual of less than 50 m/s (shown in the lower panel).	132
6.6	Final residual in wavelength calibration after distortion correction for all the exposures is shown for the case of order-1.	132
6.7	Telluric corrected spectrum in the synthetic lab frame (red), the telluric model spectrum (green) from <i>Molecfit</i> and the spectra before telluric correction (black) close to Sodium region.	133
6.8	Master out-of-transit spectra combining all the out-of-transit spectra.	134
6.9	The figure indicates the transit spectra created by subtracting the master out-of-transit spectra. The first to the last exposures are stacked from bottom to top. The wavelengths are in the stellar rest frame, and we scale the residuals by a factor of 2.3 for visibility. The stellar rest frame location of Na D1 and D2 lines is a red dashed line. The red dots across exposures denote the expected wavelength location of the residual signal due to planet transit. One can also note that there is no residual signal in the location of the stellar Fe I (5892.9 Å) line between the Na-D lines represented by a dashed blue line.	135

- 6.10 Stacked residual spectra (scaled for visibility purpose) along with the masked region of 0.15 Å bandpass (grey vertical bar), the central wavelength of the sodium D2 and D1 line in the SRF (dashed red vertical line), and expected planetary signal position (red dot). . . . 135
- 6.11 The residual spectra are shifting back to the planetary rest frame (PRF) and combined to obtain the final transit spectra. There is no detectable Sodium in the PRF. That is the residual what we observed without masking is pure stellar contamination. 136
- 6.12 Left plot shows the region chosen for masking (the region between the vertical red dashed line), and the right plot shows the transmission spectra obtained after masking. 136
- 6.13 Left side plot shows the region near the sodium doublet used for lightcurve analysis. The right side plot shows the lightcurve obtained. 137
- 6.14 Left plot shows the region chosen for lightcurve calculation (the region between the vertical red dashed line), and the right plot shows the lightcurve obtained. 138
- 6.15 Left plot shows a stacked residual plot around the K region, and the right plot shows the final transmission spectra. 138
- 6.16 Left side plot shows the region around K line used for lightcurve analysis. The right side plot shows the lightcurve obtained. 138
- 7.1 This illustration shows how the transmission spectra changes in the presents of stellar inhomogeneity ([Rackham *et al.* 2018](#)). 143
- 7.2 Upper panels indicate the SDO/HMI radial magnetogram and SDO/HMI flattened continuum intensity, observed on 1st January 2015; Lower panels: show two threshold images on the same date. The left one displays faculae and sunspots separately in different colors, and in the right panel, we have further divided faculae into plage and network fields. 145
- 7.3 Left and right continuum (cyan) and the line core regions (red) selected for calculating line index for Ca II H & K (left) and H δ (right). 147
- 7.4 Left and right continuum (cyan) and the line core regions (red) selected for calculating line index for H β (left) and Na D2 & D1 (right) 148
- 7.5 Left and right continuum (cyan) and the line core regions (red) selected for calculating line index for H α. 148
- 7.6 The image indicates the Sunspot fraction as a function of the normalized line indices of Ca II H & K, Hα, Hβ, Hδ, and the Sodium doublet for the years 2015 and 2018. 149
- 7.7 The Figure represents the normalized line indices of Ca II H & K, Hα, Hβ, Hδ, and the Sodium doublet as a function of faculae fraction for the years 2015 and 2018. 150

List of Tables

3.1	Each column represents the different category of stars, mean [Fe/H], mean [C/H], and mean [C/Fe] values from the histogram distribution.	57
3.2	Sample data of LAMOST-Kepler field stars. Each column represents RA, DEC, effective temperature of the star, logg, [Fe/H], and the [C/H]	70
3.3	Sample data of LAMOST-Kepler field stars. Each column represents RA, DEC, effective temperature of the star, logg, [Fe/H], and the [C/H]	71
3.4	Sample data of LAMOST-Kepler field stars. Each column represents RA, DEC, effective temperature of the star, logg, [Fe/H], and the [C/H] (continue)	72
3.5	Sample data of LAMOST-Kepler field stars. Each column represents RA, DEC, effective temperature of the star, logg, [Fe/H], and the [C/H] (continue)	73
4.1	Estimated stellar parameters for HD 80606/HD 80607	83
4.2	Differential abundance of HD80606/ HD80607.	93
4.3	Estimated stellar parameters fo HD 202772A/B	94
4.4	Differential abundance of HD202772 A/B	95
4.5	The complete linelist used for the analysis HD 202772A/B. The Wavelength, element, and equivalent width of both stars are represented in each column.	96
4.6	The complete linelist used for the analysis (HD 202772A/B) (continue)	97
4.7	The complete linelist used for the analysis (HD 202772A/B) (continue)	98
4.8	The complete linelist used for the analysis (HD 202772A/B) (continue)	99
4.9	The complete linelist used for the analysis (HD 202772A/B) (continue)	100
4.10	The complete linelist used for the analysis (HD 202772A/B) (continue)	101
4.11	The complete linelist used for the analysis (HD 80606/HD80607). The Wavelength (\AA), element, and equivalent width ($m\text{\AA}$) of both stars are represented in each column.	102
4.12	The complete linelist used for the analysis (HD 80606/HD80607) (continue)	103

5.1	Observational details: Name of the object, Date of Observation, Signal to Noise Ratio, Exposure time, Parallax angle, and airmass at the beginning and end of the observation are listed.	109
5.2	Stellar parameters: Name of the object, Visual magnitude, Effective temperature, the logarithm of gravity, and metallicity and separation between the object star and the reference star are given below.	110
5.3	Comparison of observed transit depth from the white lightcurve and from literature.	113
6.1	Observation details of WASP-49. Ingress, mid-transit and egress are underlined	127
7.1	The reference wavelength region selected left and right of the absorption line and the wavelength region centered around the absorption line used for the line index measurement.	147

Abbreviations

AU	A stronomical U nit
CARMENES	C alar A lto high- R esolution search for M -dwarfs with E xoearths with N ear-infrared and optical É chelle S pectrographs
CKS	C alifornia- K epler S urvey
CoRoT	C onvection, R otation and planetary T ransits
ESPRESSO	E chelle S pectrograph for R ocky E xoplanet- and S table S pectroscopic O bservations
EXPRESS	E Xtreme P REcision S pectrograph
GAIA	G lobal A strometric I nterferometer for A strophysics
GCE	G alactic C hemical E volution
HARPS	H igh A ccuracy R adial velocity P lanet S earcher
HATNet	H ungarian-made A utomated T elescope N etwork
HCT	H imalayan C handra T elescope
HD	H enry D raper
HESP	H anle E chelle S pectrograph
HFOSC	H imalayan F aint O bject S pectrograph
HIRES	H Igh R esolution E chelle S pectrograph
HMI	H elioseismic and M agnetic I mager
HST	H ubble S pace T elescope
IAO	I ndian A stronomical O bservatory
IRAF	I mage R eduction and A nalysis F acility
KELT	K ilodegree E xremely L ittle T elescope

LAMOST	L arge A rea M ulti O bject S pectroscopic T elescope
NASA	N ational A eronautics and S pace A dministration
NIST	N ational I nstitute of S tandards and T echnology
SDO	S olar D ynamics O bservatory
SNR	S ignal to N oise R atio
TESS	T ransiting E xoplanet S urvey S atellite
VALD	V ienna A tomc L ine D atabase
WASP	W ide A ngle S earch for P lanets

Chapter 1

Introduction

"My goal is simple. It is a complete understanding of the universe, why it is as it is and why it exists at all."

- Stephen Hawking.

1.1 History of exoplanet searches

Astronomy is one of the oldest science that started with the early humans who were curious and vigilant about the celestial phenomenon. The Solar system planets have been known since prehistoric times from cave drawings. These planets also became part of calendars that are used to date. The origin of name "planet" comes from the Greek word that means wandering star, meaning that the position of the planets in the sky changes with respect to the background stars. The modern definition of a planet represents a satellite to a star. The idea of alien civilization

existed probably even before the idea of planets around other stars. William Stephen Jacob made the first claim of exoplanet detection in 1855 the director of the Madras observatory, where the Indian Institute of Astrophysics (IIA) traces its origin. IIA is also my Alma mater. He studied binary stars, made an extensive catalog, and also proposed that the orbital anomaly of 70 Ophiuchus was due to a planetary-mass object, which turned out to be erroneous. Aleksander Wolszczan and Dale Frail successfully detected an exoplanet around the pulsar named PSR B1257+12. They used the time delay of the pulse arrival to discover two planets of 3-4 M_{\oplus} mass.

Serious exploration of exoplanet studies began with the first discovery of an exoplanet around a Sun-like star 51 Pegasi in 1995 [Mayor and Queloz \(1995\)](#), who received the Nobel Prize for physics in 2019. The planet is around 51 Peg and was a Jupiter-like planet, orbiting close to the host star (0.05 AU), which was surprising. This new category of planets is called 'Hot Jupiters.' The heroic efforts from dedicated radial velocity and transit searches and space missions like the [Kepler \(Borucki et al. 2010\)](#) and [CoRoT \(Barge et al. 2008\)](#) have led us to the modern era of exoplanet studies with more than 5200 exoplanets (Figure 1.1) known to date, making exoplanets one of the most exciting areas of astrophysics.

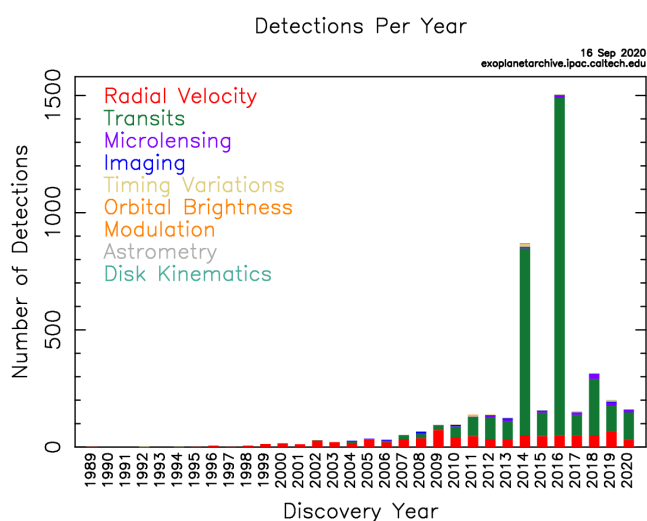


FIGURE 1.1: Exoplanet detected each year from the first detection using different methods. Image credit: [NASA Exoplanet Archive](#)

1.1.1 Exoplanet Populations

Hertzsprung Russell diagram gives a reasonable representation of a star and its evolutionary status (though there are degeneracies due to chemical composition, mass-loss, etc.). In the case of planets, their current location on the mass-radius plot can be reached through several pathways. It is also closely linked to the property of the host star and proto-planetary disk environment. It can be seen from Figure 1.2 that exoplanets of similar masses have a wide range of surface compositions. Based on the radius exoplanets are divided into Jupiters ($8R_{\oplus} \leq$

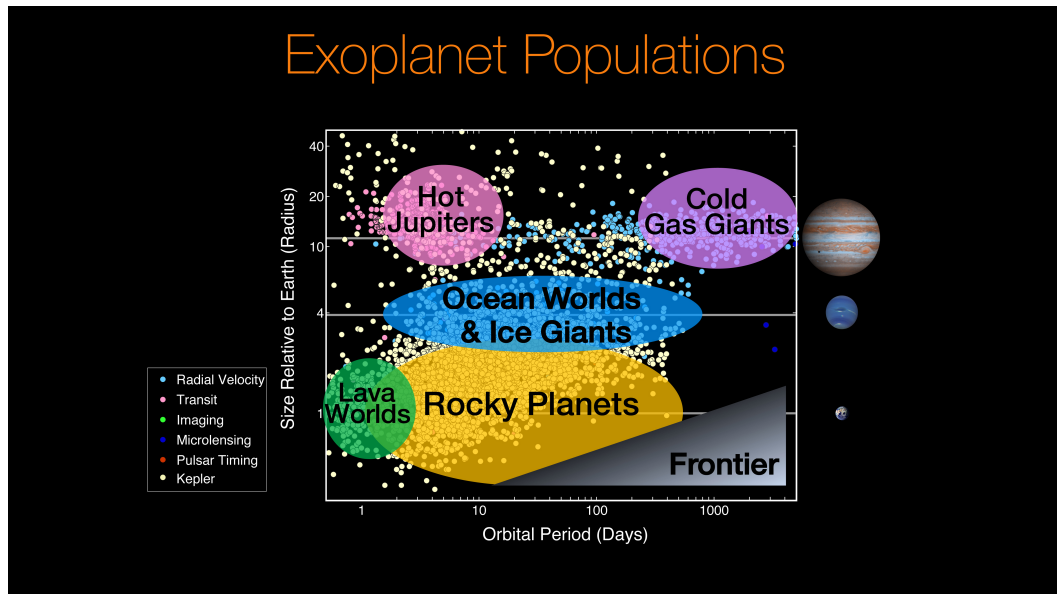


FIGURE 1.2: Different exoplanet population as a function of the orbital period (Image credit: NASA)

$R_p \leq 20R_{\oplus}$), sub-Saturns ($4R_{\oplus} \leq R_p \leq 8R_{\oplus}$), Neptunes ($2R_{\oplus} \leq R_p \leq 4R_{\oplus}$), and Super-Earths ($1R_{\oplus} \leq R_p \leq 2R_{\oplus}$). All these planets are further classified into hot (1-10 days), warm (10-100 days), and cold (orbital period more than 100 days) based on the orbital period of the planet. Also, planets with an orbital period of $P \leq$ one day and radii of $0.5-2R_{\oplus}$, known as ultrashort-period planets (USPs), represent an extreme planet population. The most common exoplanets have a radius between $1 - 4R_{\oplus}$, and our Solar system does not have such a planet. A paucity of planets found between the radius of super-Earths and sub-Neptunes,

known as the *Fulton gap* [Fulton et al. \(2017a\)](#). A possible reason for the Fulton gap is the atmospheric loss due to photoevaporation. Radius and mass will provide the bulk composition of exoplanets; combining this with the atmospheres and ages of the host stars will help understand the evolutionary pathways. Unfortunately, masses are only limited to systems with bright host stars, and estimating the accurate ages of field stars is a big challenge. Figure 1.3, called the *mass-period*

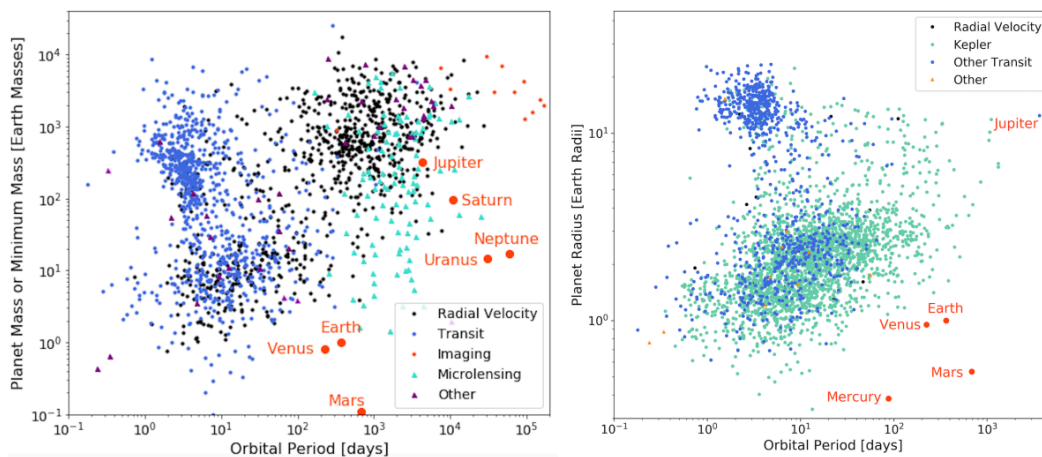


FIGURE 1.3: Exoplanets detected as a function of orbital period and planet mass m_p (left) and orbital period and planet radius R_p (right) ([Gaudi et al. 2021](#))

diagram, provides a visual comparison of the mass and orbital period of Solar system planets and the exoplanets detected so far. The main exoplanet detection techniques are transit photometry, radial velocity (RV), microlensing, astrometry, and directing imaging. The exciting aspect is that each technique has sensitivities covering a unique parameter space of exoplanets that maximizes the discovery space.

1.1.1.1 Transit method

A transit can occur for an exoplanet system whose orbital plane is along the line of sight of an observer. During transit, the flux coming from the star will drop by an amount equal to the area covered by the planet in the visible hemisphere of the

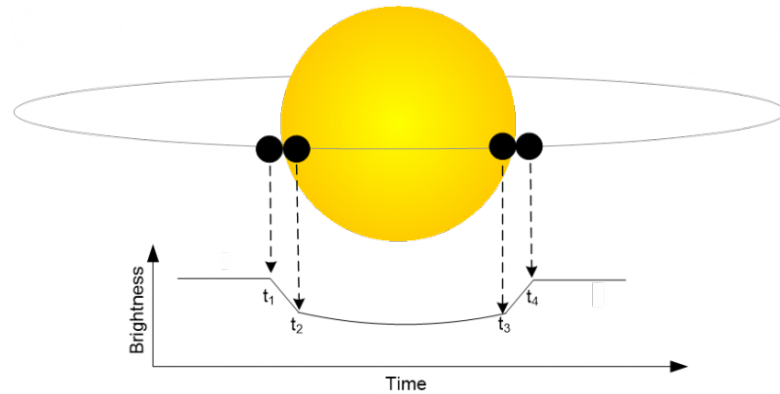


FIGURE 1.4: Demonstrating transit method of exoplanet detection. t_1 , t_2 , t_3 , and t_4 represent just before ingress, ingress, egress, and just after the egress. The transit event is happening between t_1 and t_4 . Image credit : [Britastro](#)

star $((R_p/R_*)^2)$. Transit photometry directly gives the planet's size if we know the host star radius. For a Jupiter size planet around a Sun-like star at Jupiter's orbital distance, the flux drop is 10^{-6} , which is very small. The ground-based and space-based missions like Kepler, CoRoT, WASP, TESS, and HATNet surveys have detected thousands of exoplanets using this transit method. The probability of detecting a transit signal is R_*/a where 'a', the semi-major axis and ' R_* ', the stellar radius. For a system with a small R_p/R_* and a planet with a large 'a' will be difficult to detect using this transit method. A basic sketch of transit geometry is shown in figure 1.4.

1.1.1.2 Radial Velocity (RV) Technique

In a star and planet system, the planet and the star move around the center of mass (COM), which will cause the movement of the planet in a large orbit, and the host star moves little around the COM. Since the planet is too faint and the host star is several orders brighter, it is possible to detect the star's small wobbling motion around the system's COM using the doppler shift in the spectral lines from the host star. This method can be used for exoplanet detection and to derive the planet's mass. Figure 1.5 illustrates the RV method. Besides

detecting planets, the RV method plays a vital role in deriving the planet's minimum mass. RV measurements during transit can be used for deriving the inclination of the orbit. The amplitude of the RV curve directly indicates the mass of the planet. For a Jupiter-analog, the doppler shift is around 13m/s, and for an Earth-analog, it is 9 cm/s. Highly stable spectrographs like HARPS, ESPRESSO, CARMENES, NEID, EXPRES, and MAROON-X have the required instrument stability to detect Earth-like planets. However, characterizing the stellar jitter is a major stumbling block that does not allow the taking advantage of the stable instruments. There are consented efforts to characterize stellar inhomogeneities and stellar jitter, e.g., (Cegla 2019).

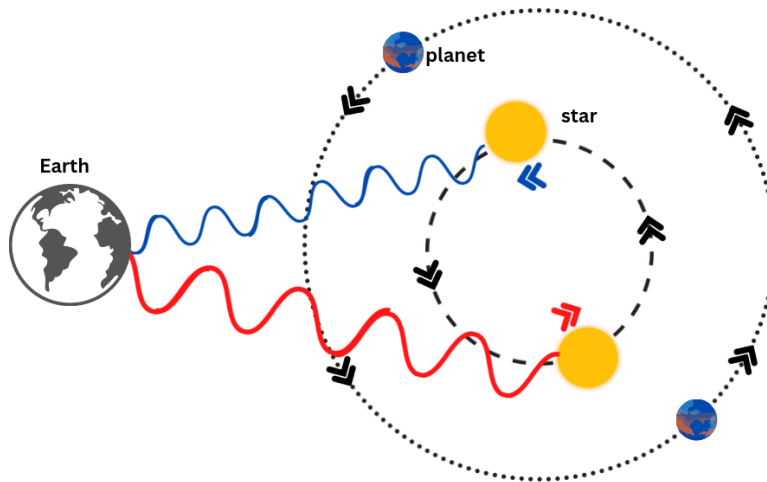


FIGURE 1.5: The image illustrates the blue and red shift in the observed host star spectra as a planet orbiting around the host star.

1.1.1.3 Transmission Spectroscopy

Transit spectroscopy is very similar to the transit method of planet detection but performed at several narrow bandpasses. This is achieved by taking a series of low-resolution spectra during transit.

In an exoplanet atmosphere, different atomic and molecular species form at a range of heights depending on the physical conditions, as shown in Figure 1.6. Hence,

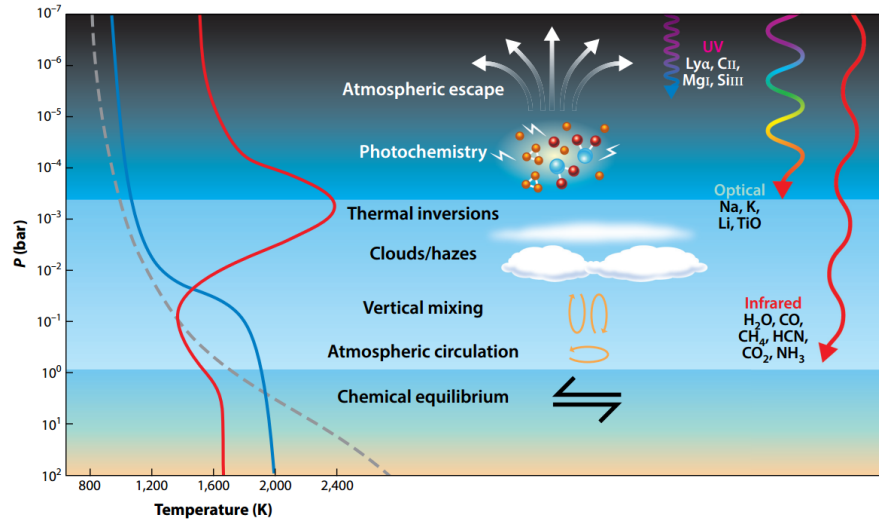


FIGURE 1.6: Figure represents the major possible process happening in the exoplanet atmosphere (Madhusudhan 2019). Possible species can be detected in each layer and in which region of the electromagnetic spectrum.

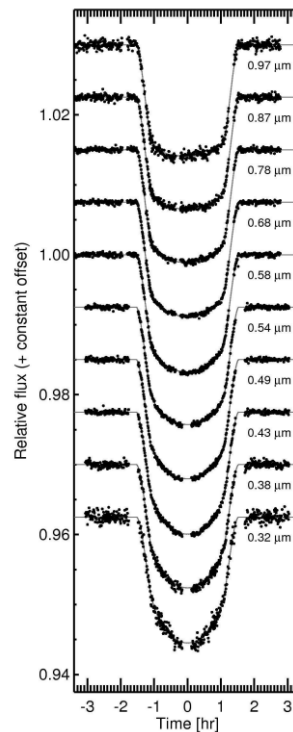


FIGURE 1.7: Figure represents the transit light curve at various wavelength for HD209458b, based on the HST data from Knutson *et al.* (2007) and the figure taken from Wimm (2010). The transit depth and shape clearly vary across wavelengths.

the planet's radius is expected to be different at different wavelengths depending on the presence of the atoms and molecules and their abundance (Figure 1.7). If the scale height is 'H'(Change in height in the exoplanet atmosphere over which the pressure drops by a factor of e), then according to the ideal gas law(assuming hydrostatic equilibrium), we can write,

$$H = \frac{K_b T_{eq}}{\mu g}$$

where K_b is Boltzman constant, T_{eq} is the equilibrium temperature of the planet, μ is the mean molecular mass of the total atmospheric composition, and g is surface gravity. And the amplitude of the spectral feature is

$$\delta = \frac{(R_p + nH)^2}{R_s^2} - \frac{R_p^2}{R_s^2}$$

$$\approx \frac{2R_p nH}{R_s^2}$$

here n represents the multiples of scale heights crossed at wavelengths with high opacity.

Early transit spectroscopy was from space facilities, using the *Wide Field Camera* (WFC3) and *Space Telescope Imaging Spectrograph* (STIS) on board HST and IRAC (*Infrared Array Camera*) on board Spitzer. These instruments jointly cover spectroscopy from UV to near IR. In the case of low-resolution spectroscopy, the transit depth at different wavelengths is given as inputs to a retrieval code that tries to match the output spectra generated using several thousands of combinations of planet parameters and abundances. Wide wavelength coverage of transmission spectra is crucial for removing degeneracies in fitting the planet parameters to the transmission spectra. It is possible to resolve individual atomic and molecular lines in transmission spectra at high spectral resolution and also deduce the velocity

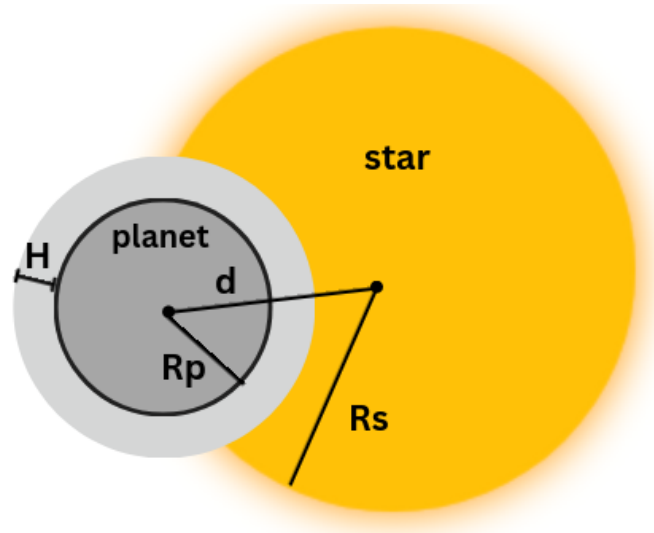


FIGURE 1.8: Illustration of Primary transit of a planet with radius R_p and atmospheric height 'H' around a star of stellar radius R_s .

drift of the absorption feature in the transmission spectra as the planet transits the stellar disk.

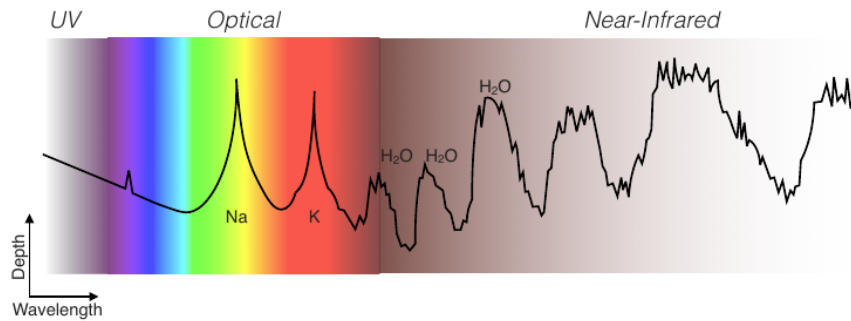


FIGURE 1.9: Prominent features in the transmission spectra of a typical exoplanet at different wavelength region (Credits: Matteo Brogi- Evry Schatzman School 2019, Aussois, France)

The first successful low-resolution transmission spectroscopy was performed for a hot Jupiter HD209458b, using HST-STIS (Charbonneau *et al.* 2002b), and detected the sodium resonance doublet at 5890 Å. Since then, Na and K have been the most commonly detected features in the optical transmission spectra Sing *et al.* (2011) Nikolov *et al.* (2014) Seidel *et al.* (2020c). Figure 1.9 demonstrates typical transmission spectra covering the optical and near-IR regions of the electromagnetic spectrum. Apart from the prominent features Na, K, and H₂O, one can see

the steep slope in the bluer region of the spectra. A $1/\lambda^4$ dependency of Rayleigh scattering causes the slope in the transmission spectra; also, high-altitude clouds can block the detection of possible spectral features. High-resolution transit spectroscopic observations started around 2010 (Snellen *et al.* 2010) are mostly done using a 10 m class telescope from the ground because the observations demand better SNR within a short exposure time (Wyttenbach *et al.* 2015a, 2017b; Seidel *et al.* 2020c; Wyttenbach *et al.* 2015b). Along with Spitzer observation, WFC3/HST observation, H₂O, NH₃, CO, CH₄, CO₂, HCN, TiO/VO (Sánchez-López *et al.* (2019) Moses *et al.* (2013)) are the commonly detected molecules in the IR part of the transmission spectra. Atmospheric escape and mass loss are observable in the UV region, mainly detecting the Ly α signature Owen (2019) and ionized metals in the escaping atmosphere.

A secondary eclipse (planet goes behind the star) observation generally gives the thermal emission and the reflected spectra from the planet. In contrast, the planet moves behind the host star with respect to the observer's line of sight. The thermal part of the spectra is more visible in the IR region, and reflected spectra are more visible in the optical part of the spectra. These observations help to understand the day-side of the exoplanet.

1.1.2 Planet formation and host star abundances

The solar system planets influenced the early planet formation models; however, we now know that the solar system has little resemblance with the rest of the exoplanet populations. To state a few differences, a solar system planet does not host a super-Earth, the most common planetary system. Also, there are no planets found within the orbital distance of Mercury. In contrast, most exoplanets are found within an orbital distance of Mercury (e.g., Figure 1.11).

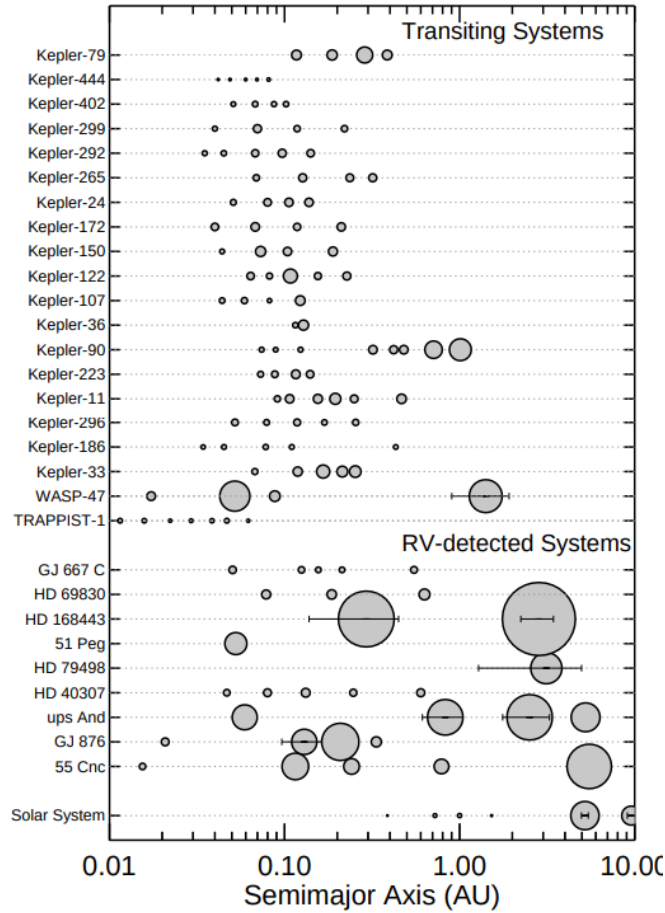


FIGURE 1.10: Figure displays the diversity of exoplanets as compared to the Solar system planets, the image taken from [Raymond *et al.* \(2020\)](#)

The two main models of planet formation are the core accretion model, where solid ice and dust stick together to form a 1 – 100 Km-sized planetesimal core. These kilometer-sized planetesimals stick together to form a massive core of ($M_{core} \leq 10M_{\oplus}$). Then the core will accrete gas from the protoplanetary disk before the disk dissipates. Furthermore, this will continue until the core mass becomes comparable with the mass of the gaseous envelope. Different stages in a core accretion model are growing a micron size core to mm-size pebbles and then growing the pebbles to planetesimals of a meter to kilometer size and finally, a rapid accretion leading to planets size objects ([Pollack *et al.* 1996b](#)). Though radial drift due to the interaction with sub-Keplerian gas and bouncing of dust mass makes growth

beyond pebble size difficult (e.g., (Birnstiel *et al.* 2016)).

In the disk instability scenario, the protostellar disk that is dense and cold will undergo gravitational instability, and the collapsed disk fragments clump together to form the planetary core. This formation is a rapid (10^3 years) process, and strong metallicity dependency is not expected (Boss 1997). Disk instability is found helpful in explaining the formation time scale of 1 Ky–1 Myr (Mandell 2011) and planets with mass $M_p \geq 4M_J$ in wide orbits. Although the core accretion model can explain 90% of the planet’s population, giant planets in wider orbits will have issues. Hence, both models play a role in planet formation under various conditions.

The current exoplanet numbers indicate a frequency of at least one planet around every star, indicating planet formation could be an integral part of star formation. The high-resolution ALMA (Atacama Large Millimeter Array) images have shown protoplanetary disks with gaps that are possibly carved by planet mass objects around the star (ALMA Partnership *et al.* 2015). Considering the diversity of the exoplanets, the standard solar model of planet formation needs revision, as it does not include planet migration and expected that planets would retain the chemical signature of the current location in the proto-planetary disk. The exoplanet and proto-planetary disk demographics, along with host star and exoplanet abundances together, will enable astronomers to understand the formations of planets in general and the history of our solar system.

1.1.2.1 Planet formation and host star abundances

Our capacity to precisely derive the physical parameters of exoplanets is also closely related to the precise host star parameters. The bulk properties of the exoplanets, such as radius and mass, are measured relative to the host stars using

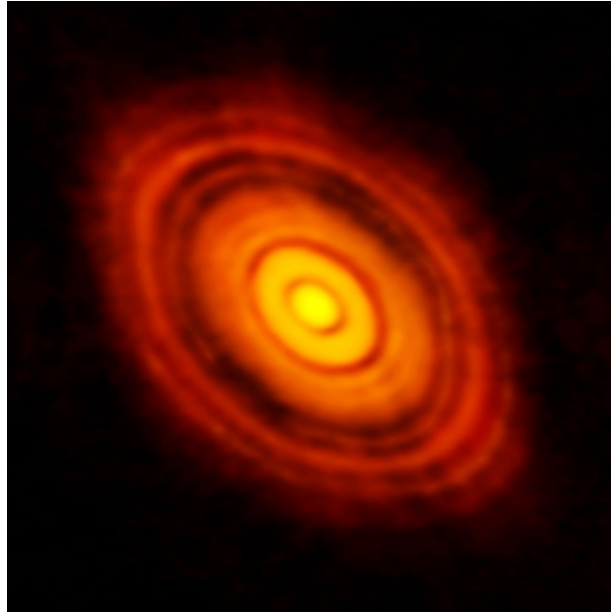


FIGURE 1.11: Figure shows an image of a protoplanetary disk HL TAU observed with ALMA. The ring-like shape of the disk is due to the planetary size objects clearing material, causing a gap in the disk ([ALMA Partnership *et al.* 2015](#))

transit and radial velocity methods; hence precise stellar radius and mass are critical. Thanks to Gaia, Kepler, and CoRoT, we can derive stellar luminosity, radius, and masses more accurately than ever. Extensive spectroscopic surveys and the kinematic information of stars from Gaia will provide a better estimate of the ages and birthplaces of the stars in the Galaxy; hence it allows an understanding of the exoplanets in the Galactic context.

Even with the first few exoplanet discoveries, the stellar metallicity and planet occurrence rate were noticed ([Gonzalez 1997b](#)), indicating favorable conditions of planet formation ([Fischer and Valenti 2005a](#)). Among the short-period planets in the Kepler sample, there was a lack of metal-poor stars ([Beaugé and Nesvorný 2013](#)). Stellar activity and UV radiation affect habitability and possibly cause the radius gap ([Fulton *et al.* 2017b](#)) in the exoplanet population. Radial distribution of chemical inventories in a protoplanetary disk, along with host star chemical abundances and atmospheric and bulk composition of exoplanets, will be able to paint a realistic picture of exoplanet formation and evolution based on large sample

size. Accurate stellar ages will help with the timescale of exoplanet formation and evolution milestones. The exoplanet studies have brought renewed interest in stellar physics.

1.2 The scope of the thesis

In the thesis, we cover some aspects of host star properties and exoplanet properties using optical spectroscopy. Host star chemical composition, exoplanet transmission spectroscopy, and the impact of stellar activity on the observations of transmission spectroscopy are presented in different chapters. First, two chapters cover the introduction, methodology, and observing facilities. From the third chapter onwards, original results are presented. The last chapter presents a conclusion and future outlook.

1.3 Plan of the thesis

- **Introduction** : This chapter covers the status of the exoplanet field in terms of exoplanet detection, demographics, atmospheres, planet formation, and host stars. (refer to Chapter 1).
- **Observations and Data Analysis** : This chapter presents observations, facilities and instruments used in this project, data reduction, analysis, modeling, and software used as part of the thesis (refer to Chapter 2).
- **Carbon abundance of stars in the LAMOST-Kepler field** : The third chapter presents the carbon abundance of main-sequence dwarf stars in the LAMOST-Kepler field. We perform planet occurrence rate and its relation to host star carbon abundances (refer Chapter 3).
- **Differential Abundance Analysis of Planet Host Visual Binary Systems** : Here we performed an accurate line-by-line differential abundance analysis of two visual binary systems in which one of the stars hosts a planet. Assuming the binary stars inherit the same initial composition, any difference may reveal the influence of planet formation. (refer Chapter 4).

-
- **Transit Spectrophotometry of Hot Jupiters Using 2m Himalayan Chandra Telescope** : We present successful transmission spectrophotometry of three hot Jupiters with a 2m telescope, confirm previous results, and present new results for KELT-18b (refer to Chapter 5).
 - **High-Resolution Transmission Spectroscopy of WASP-49 b Using KECK/HIRES** : High dispersion spectroscopy of highly irradiated hot Jupiter WASP-49b using KECK/HIRES is presented for the first time (refer to Chapter 6).
 - **Characterizing The Solar Disk inhomogeneity From Disk-Integrated Spectra** : We present possible spectral line diagnoses that correlate with spots and faculae using HARPS-N solar spectra and SDO data to be helpful in atmospheric exoplanet retrieval. (refer to Chapter 7).
 - **Conclusion** : All of the thesis's findings and results are compiled in the final chapter. (refer to Chapter 8).

Chapter 2

Observations and Data Analysis

Abstract

We have use low and high-resolution spectroscopic observational data to characterize the exoplanet and the host stars. The results in the various chapters are based on observational data in the optical wavelengths. Most of these observations were carried out with the 2m Himalayan Chandra Telescope (HCT) at Hanle, Ladakh, India. In addition, Dr. Katherine de Kler kindly carried out high-resolution transmission spectroscopic observations with Keck-HIRES for WASP-49b. We have also extensively use archive data, thanks to LAMOST, Kepler, HARPS-N, Gaia-DR2, and the Keck Observatory Archive (KOA). The observational data covers a wavelength coverage of 3500 Å to 10000 Å, and the spectral resolution varies from $R= 150$ to 80000. The following sections explain the observational facilities and data analysis used in the thesis work.

2.1 LAMOST Survey

The Large Sky Area Multi-Object Fibre Spectroscopic Telescope (LAMOST), also known as the Guoshoujing Telescope, is a 4-meter class telescope that provides a wide field of view (Figure 2.1) located at Xinglong station of the Beijing Astronomical Observatory, China. The telescope uses 4000 optical fibers and 16 spectrographs to provide spectral resolution of $R=1800$ (LRS) that covers a wavelength region 370-900 nm [Cui *et al.* \(2012\)](#), [Zhao *et al.* \(2012a\)](#), [Zhao *et al.* \(2012b\)](#). The ten years of survey data that started in 2011 has more than 16 million spectra of stars covering a magnitude range of 9.0 -17.5 and stellar parameters for about 7.5 million stars.

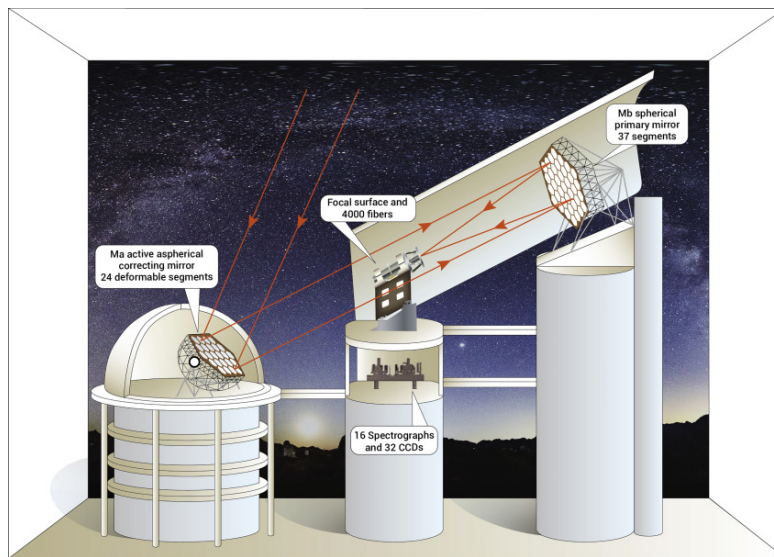


FIGURE 2.1: Figure from [Yan *et al.* \(2022\)](#) shows LAMOST telescope optical layout. A combination of spherical primary and an active spherical correcting mirror provides a wide field of view of 5 deg).

The LRS data is obtained through two primary surveys, the LAMOST Galactic Understanding and Exploration (LEGUE) survey and the LAMOST Extra-Galactic Survey (LEGAS). There are also special surveys like the spectroscopy of the Galactic anti-center and the LAMOST Kepler project (LK-project). The reduced spectra from the public data release 8 are available at [LAMOST DR8 release](#) and also through the [ESA Sky](#) interface. A typical LAMOST spectrum

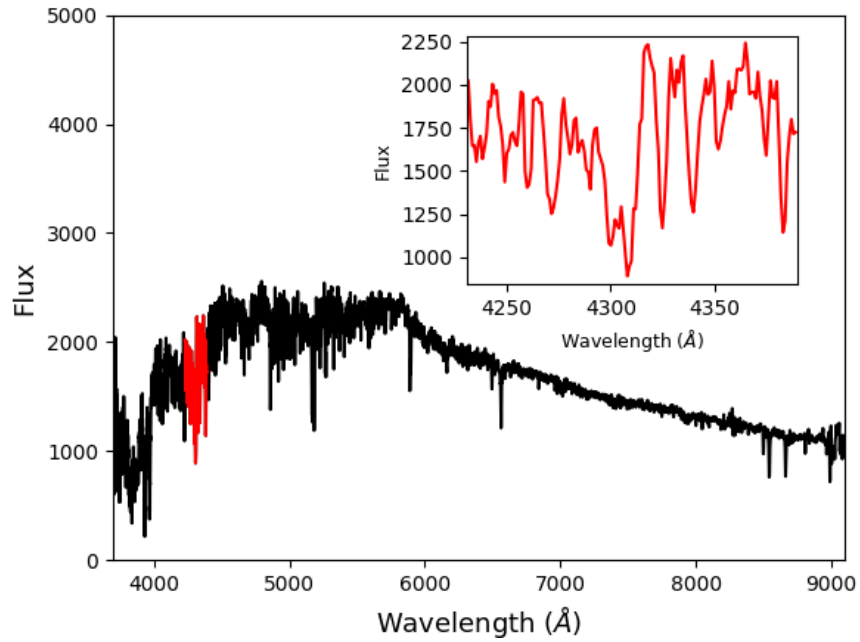
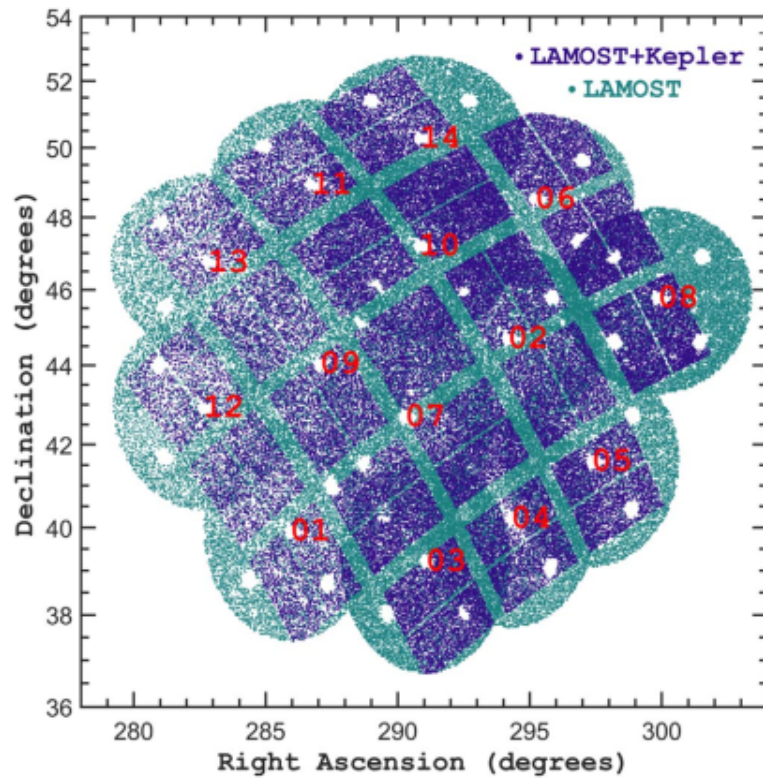


FIGURE 2.2: Typical wavelength calibrated spectra from LAMOST archive.

FIGURE 2.3: LK field of observation, Common field of observation colored in blue [Ren et al. \(2016\)](#)

is shown in Figure 2.2. We have used the low-resolution spectra from the LK project for the study discussed in chapter 3. The LK-project [Ren *et al.* \(2016\)](#) has 1,52,000 targets. LAMOST observed this field from 2012 to 2014 by dividing the entire Kepler field into 14 sub-fields (Figure 2.3).

2.2 High-resolution spectroscopy

We have used high-resolution spectroscopy for the detailed host star chemical abundance and the high dispersion transmission spectroscopy of exoplanets. We have used the High Resolution Spectrograph (HIRES) mounted on the 10m Keck-I telescope situated at the summit of Mauna Kea, Hawaii, 4145 m above sea level, and the Hanle Echelle SPectrograph (HESP), in Hanle installed at the 2m Himalayan Chandra Telescope (HCT). For the spectral diagnosis of surface inhomogeneities on the Solar surface, such as sunspots and faculae, we have used the HARPS spectrograph with the solar feed.

2.2.1 Keck-HIRES

HIRES is an echelle spectrograph that uses grating as a cross disperser also. Two instrument configuration HIRES-b, HIRES-r, uses different cross disperser and collimator that is optimized for blue and red wavelengths. The entire optical band from 300-1000 nm is accessible through the two instrument configurations and using three CCD mosaics (blue, green, and red). Different slits allow spectral resolutions between $R=25000 - 85000$ [Vogt *et al.* \(1994b\)](#). Figure 2.4 indicates the optical path of the spectrograph. HIRES uses large optical components available to maximize the throughput with minimum optical reflections.

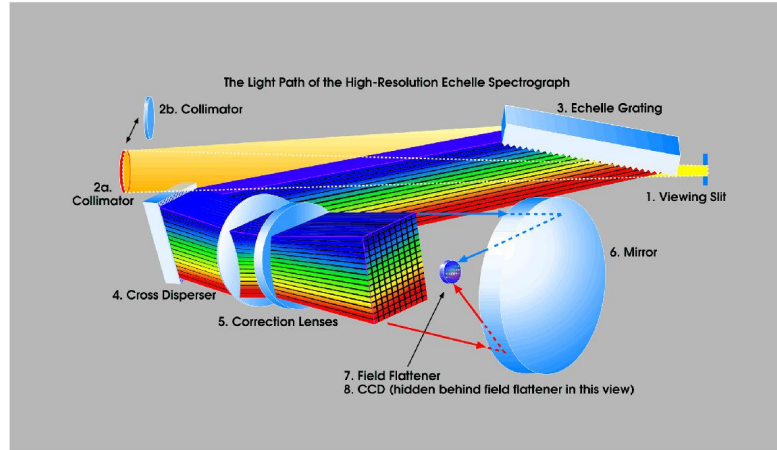


FIGURE 2.4: Figure shows the light path of the HIGH-REsolution Spectrograph (HIRES) at Keck.

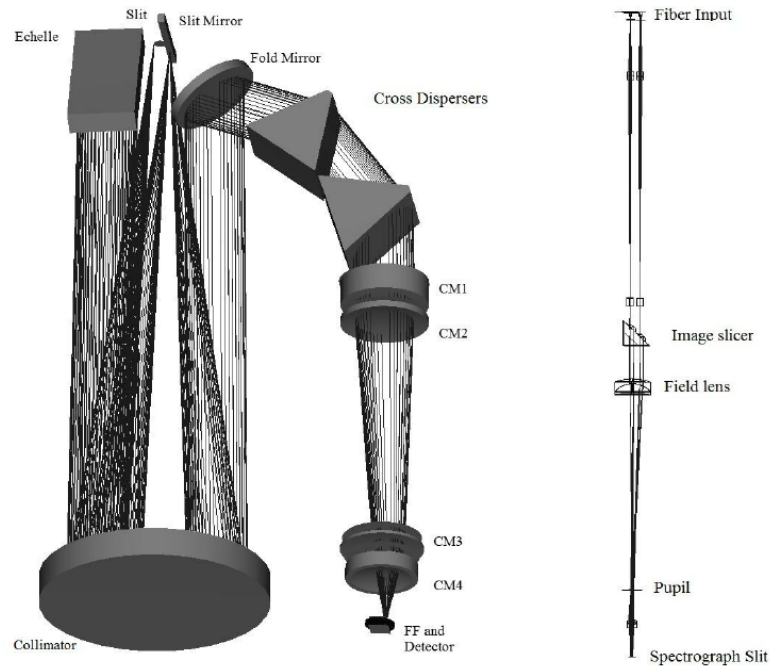


FIGURE 2.5: The light path of the Hanle Echelle fiber-fed Spectrograph at HCT.

2.2.2 Hanle Echelle Spectrograph (HESP)

The HESP spectrograph is installed at the Himalayan Chandra Telescope (HCT), located at the Indian Astronomical Observatory (IAO) at Hanle, India, 4500 m above sea level. HCT is a 2m telescope with three science instruments, Hanle

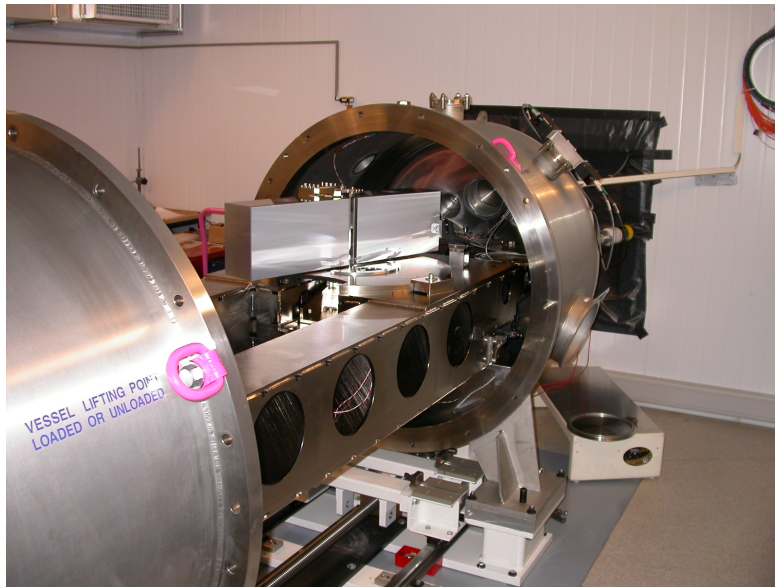


FIGURE 2.6: HARPS spectrograph with the vacuum enclosure at the 3.5m, Nazionale Galileo Telescope (TNG) at La Palma.

Echelle Spectrograph (HESP), Himalayan Faint Object Spectrograph (HFOSC), which is a low-resolution spectrograph and an imager in optical, and a NIR imager/spectrograph, the TIRSPEC (Tata institute of fundamental research InfraRed SPECTrograph). HESP is a dual fiber-fed echelle spectrograph with a cross disperser. The spectrograph is mounted on a thermally controlled optical table. The instrument has a low-resolution mode of $R = 30000$ and a high-resolution mode $R = 60000$ covering the optical wavelength range from 350-1000 nm in a single instrument setup. Light from the Cassegrain unit on the telescope passes through the atmospheric dispersion corrector (ADC). The two pinholes allow the photons from the star and the nearby background. Then the photons are fed into the optical fiber system and the slicer in the case of high-resolution. Out of the two fibers, one is used to focus the target, and the other is used for simultaneous observation of the nearby sky background or calibration lamp, depending on the science (Sriram *et al.* 2018). Figure 2.5 illustrates the optical layout of the instrument optics. HESP uses the popular white pupil spectrograph design and a triple pass monolithic collimator.

2.2.3 HARPS-North spectrograph & Solar spectra

In the thesis work in chapter 6, we have used the data from the HARPS-North spectrograph. The data is on the disk-integrated spectra of the Sun using the Solar feed that is available from HARPS-North. HARPS-N has routinely observed the Sun since July 2015 at a cadence of 5 minutes during a clear day. We analyzed the three years (2015-2018) data of the Sun from the archive of HARPS-N spectrograph. The data covers the optical band from 3800\AA - 6900\AA and observes the Sun as a point source. A low-cost Solar telescope consists of a 200 mm achromatic lens fed the light to an integrating sphere to scramble the resolved disk information of the Sun and fed to the spectrograph using a fiber of $300\mu\text{m}$ core size. The guiding camera connected to the telescope will keep track of the Sun ([Dumusque *et al.* 2015](#)). Unlike HIRES and HESP, HARPS is an ultra-stable spectrograph. The entire spectrograph is housed inside a vacuum vessel with precision temperature and pressure control. A radial velocity stability of 1m/s is routinely obtained with HARPS-N.

2.3 Hanle faint object spectrograph

We used the Hanle faint object spectrograph (HFOSC) for transit spectroscopy, which is discussed in chapter 4. HFOSC is an imaging spectrograph that allows imaging and low-resolution spectroscopy. The instrument is mounted at the straight port of the Cassegrain unit on the 2m HCT. The instrument allows a range of slit width ($0.7''$ - $15''$) and slit lengths ($10''$ - $660''$) and has a suit of grisms that will provide a resolution of $R=200$ - 4500 . There is a range of filters provided for imaging and order overlap cutoff. There are three filter wheels; one houses the slits and apertures at the telescope focus. The imager filters and grisms are located between the collimator and the spectrograph camera in the parallel beam

path. We have used grism 8 (5800-8350 Å) with a resolution of 2190 and grism 7 (3800-6840 Å) with a resolution of 1330 with the longest slit available. Figure 2.7 shows the schematic diagram of the instrument with an aperture wheel, filter wheel, grism wheel, collimator, camera, and detector.

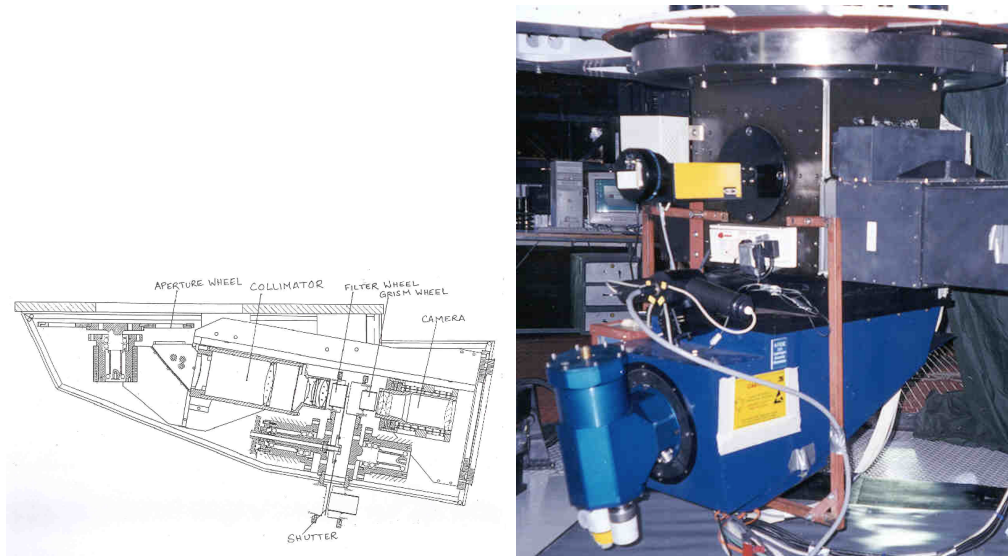


FIGURE 2.7: Schematic of the HFOSC instrument

2.4 SDO Data

The Solar Dynamics Observatory (SDO) is a NASA mission that has observed the Sun since 2010. The spacecraft includes three instruments: 1) a Helioseismic and Magnetic Imager (HMI), 2) Atmospheric Imaging Assembly (AIA), and 3) Extreme Ultraviolet Variability Experiment (EVE). In our analysis, we used HMI data. HMI (Scherrer *et al.* 2012), (Schou *et al.* 2012), (Liu *et al.* 2012), (Wachter *et al.* 2011) is designed to study oscillations and the magnetic field on the visible hemisphere of the solar surface by observing the entire solar disk at 6173 Å with a resolution of 1 arc second using a CCD of 4096×4096 square pixels. We have used HMI line of sight magnetograms with a cadence of 45 seconds and HMI Continuum intensities with limb darkening removed with 720 seconds cadence.

2.5 Spectroscopic Data Reduction

The archive data used in the thesis (LAMOST & HARPS-N) are already reduced. The data taken from HCT using HFOSC and HESP are reduced using IRAF and HESP data pipeline. The Keck-HIRES data is partially reduced in IRAF and partially downloaded from KOA. The pre-processing of low and high-resolution spectroscopy are essentially the same. Converting the 2D image into a 1D image for single-order slit spectra and multi-order echelle spectra are similar except for the multi-order nature of the data; additional care has to be taken, and the wavelength calibration involves 2D functional form.

A two-dimensional CCD image from a typical high-resolution echelle spectrograph and a low-resolution slit spectrograph is shown in Figure 2.8 and Figure 2.9. The basic data reduction follows similar steps for both low and high-resolution spectroscopy. That includes

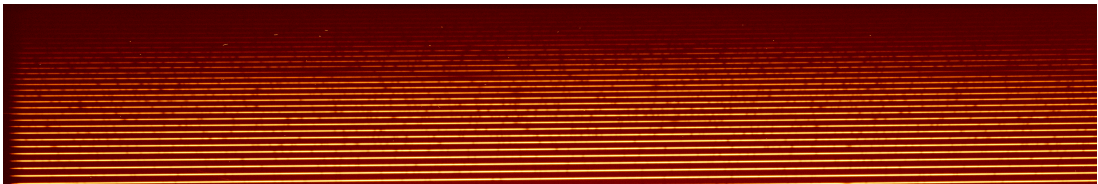


FIGURE 2.8: 2D stellar image and sky from a high-resolution echelle spectrograph from Keck/HIRES (CCD1).

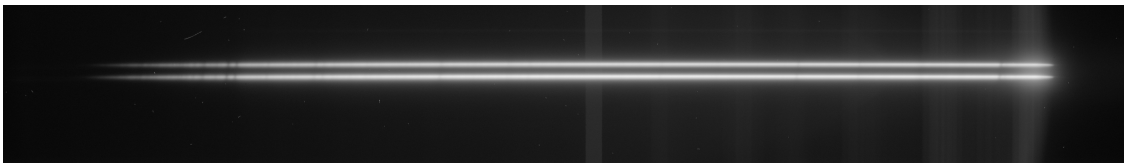


FIGURE 2.9: 2D stellar image and sky from a low-resolution long slit observation of two stars from HCT/HFOSC.

- **Bias subtraction** : Bias is a DC offset in the counts for individual pixels due to the applied voltage to each pixel, this changes due to input voltage (could cause due to fluctuation in the grounding voltage). A bias frame is

obtained using zero exposure with the CCD shutter closed. The bias frame is subtracted from the science frame for bias correction. Normally, a master bias frame is obtained by combining several bias frames taken during the night. The master bias frame subtracts from all the science and calibration frames (*master bias*). Generally, an observer will take about ten bias frames in a night (or more in the case of high-precision observations).

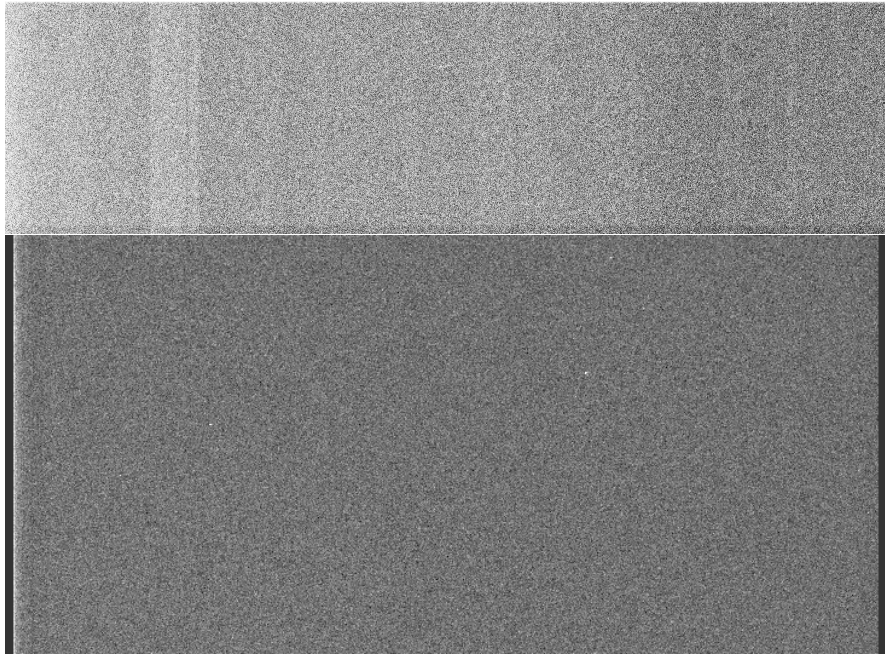


FIGURE 2.10: The top panel is a typical bias frame from Keck/HIRES (CCD1, one of the mosaics). The bottom panel is a bias frame for HFOSC CCD.

- **Dark frame** is an exposure to correct for the thermal electrons. Hence it with the same exposure time as the science frame with the shutter closed. This count is mainly generated because of the increased thermal fluctuation in the CCD during the exposure time. Modern spectrographs usually use thermally stable environments, so dark current observations are unimportant.
- **Flat normalization** : The light sensitivity of each pixel in a CCD will be different. To address this issue, the observer will illuminate a uniform Halogen lamp to the CCD for a short exposure, combine three or five exposures

to *master flat frame*, and characterize the sensitivity of each pixel by normalizing it. And divide this normalized *master flat frame* from the science frame.

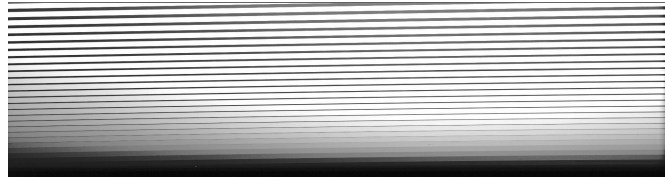


FIGURE 2.11: Typical flat frame from HIRES spectrograph CCD1. The exposure time is in the order of seconds.

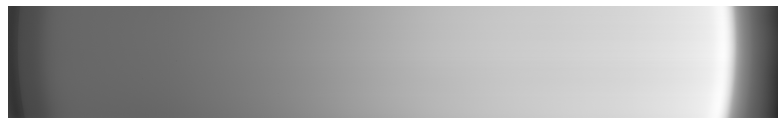


FIGURE 2.12: Typical flat frame from HCT/HFOSC. The exposure time is in the order of seconds.

- **Aperture extraction** : Each order of the two-dimensional image is extracted to get the flux Vs. pixel information. First, one has to define each aperture's lower and upper limit and the corresponding sky background. Subtract the sky background and trace each order by fitting a function to extract the sky-subtracted stellar spectra.
- **Wavelength calibration** : The observer will take three or five exposures of the wavelength calibration lamp (ThAr, FeNe, FeAr based on the wavelength coverage the spectrograph is designed for) median, combine the exposures, and apply bias and flat correction. After aperture extraction, identify the emission lines compared with the Atlas provided by the telescope facility and do the pixel-to-wavelength conversion. Finally, apply this conversion to the science frame (Figure 2.15).

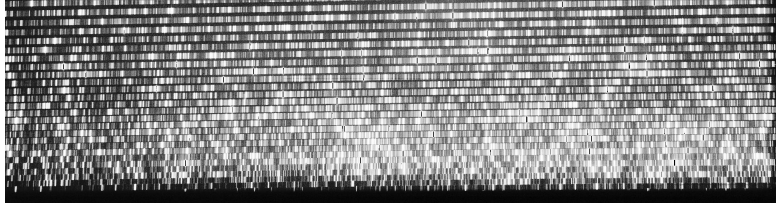


FIGURE 2.13: Typical ThAr frame from HIRES CCD1. The typical exposure time is in the order of seconds.



FIGURE 2.14: Typical FeAr frame HCT/HFOSC. The typical exposure time is in the order of seconds.

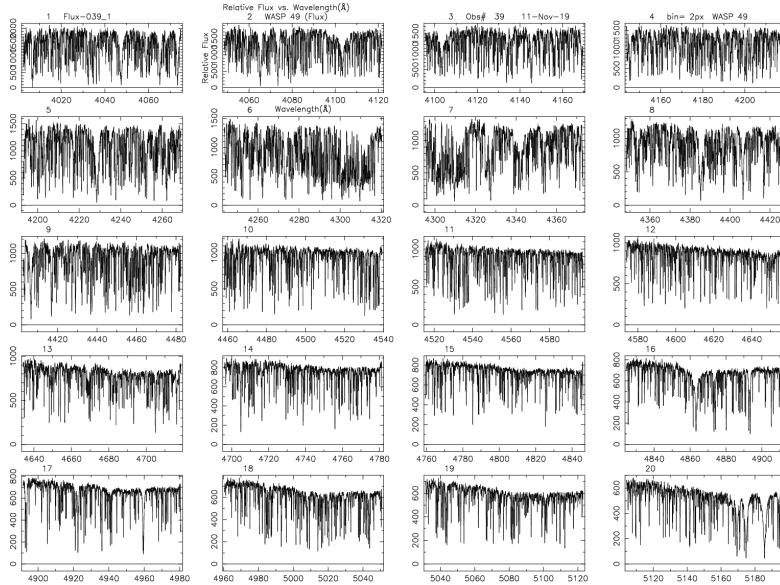


FIGURE 2.15: Typical wavelength calibrated high-resolution spectra cover different orders from Keck/HIRES.

2.6 Stellar chemical abundances

The standard methodology includes reducing the data, compiling line lists, choosing the correct model for a stellar atmosphere, and deriving the stellar parameters (Figure 2.17). Describing the reduction of data in detail is beyond the scope of the thesis. Detailed data reduction of high-resolution Echelle spectra is explained by [Wako Aoki](#) using IRAF modules. This section will discuss primary data reduction

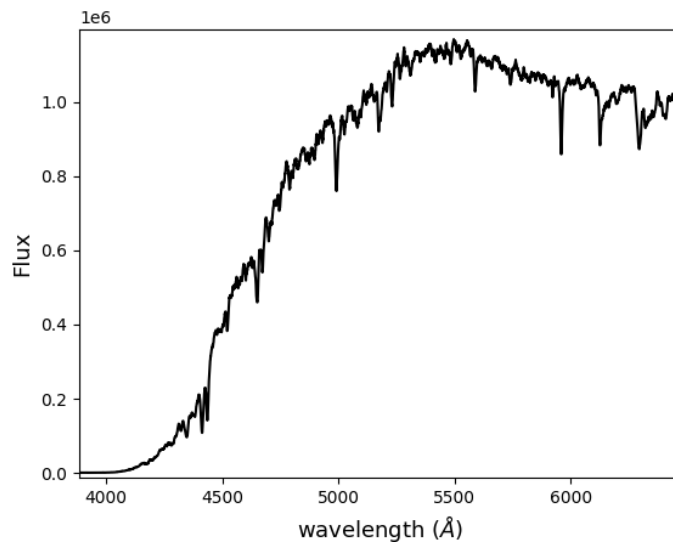


FIGURE 2.16: Typical wavelength calibrated low-resolution spectra from HCT/HFOSC grism 7.

briefly, a compilation of line lists, stellar modeling, and spectrum synthesis.

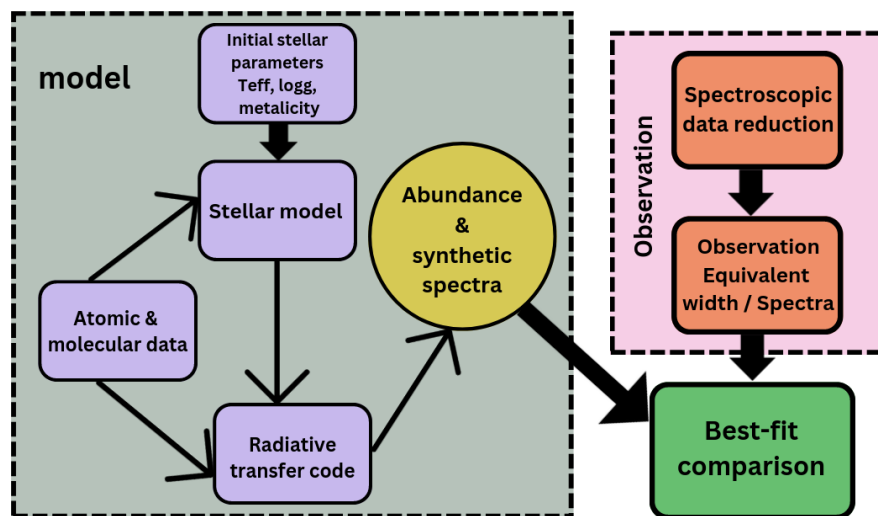


FIGURE 2.17: The diagram shows the main steps included in the calculation of stellar abundance by combining observation and modeling.

2.6.1 Stellar parameters

Stellar parameters define the basic properties of a star, including

- **Effective temperature (T_{eff})** : Even though the temperature of the star varies with optical depth, T_{eff} is defined as the temperature of a black body emitting the same flux as coming from the star. T_{eff} can be calculated using the famous Stefan-Boltzmann law

$$L = 4\pi R^2 \sigma T_{eff}^4$$

$\sigma = 5.6705 * 10^5 \text{ erg cm}^2 \text{ K}^4 \text{ s}^{-1}$. Absorption lines are formed by the transition of an electron from one bound state to another bound state. The continuous absorption in the optical part of the stellar spectra, except for hotter stars, is caused by the bound-free transition of the electron (H^-). If the number of absorbing atoms increases, the line depth also increases proportionally, making an absorbing line optically thick. Still, the wings of the lines are optically thin, so if the number of absorbing atoms increases, the line becomes broader. As the temperature increases, the transition probability of the Balmer lines also increases until the temperature reaches the ionization potential of Hydrogen. Even though all the lines are temperature sensitive, Balmer lines are considered to be a better indicator of the T_{eff} (Figure 2.18).

- **logg** is defined as the acceleration due to gravity by a test particle on the stellar surface. $1/R^2$ nature indicates that the higher the logg value more compact the star is. Pressure-broadened wings of Mg I b are used as a surface gravity diagnostic for cool stars, even if the intensity of the line is temperature-dependent. Mg Ib at 5167, 5172, 5183 Å is observable in stars from A -K spectral type with a wide range of metallicity. In hydrostatic equilibrium, the gas pressure $P_g \propto g^{2/3}$ as well as $P_g \propto P_e^2$ (P_e is the electron pressure). If a species has most of its element in the same ionization state, then the strength of the absorption line is proportional to $P_e^{-1} \propto g^{-1/3}$. That is, the strength of the absorption line is inversely proportional to g, and it will be more evident in the wings of the strong lines (Figure 2.19).

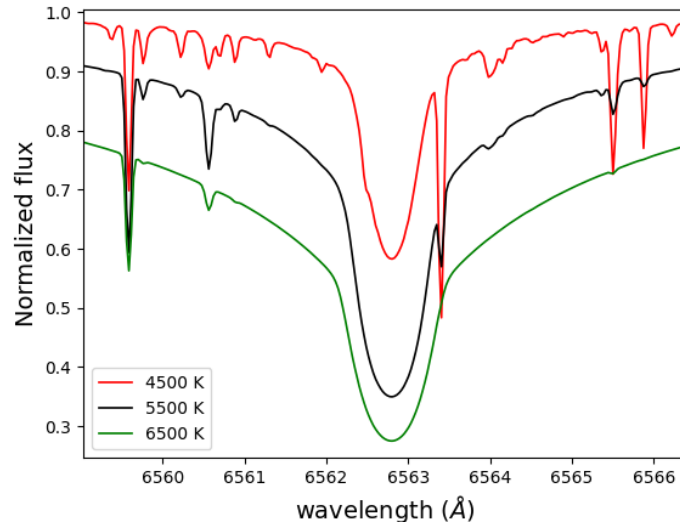


FIGURE 2.18: Synthetic spectra around $H\alpha$ region with different T_{eff} . All the other parameters are fixed.

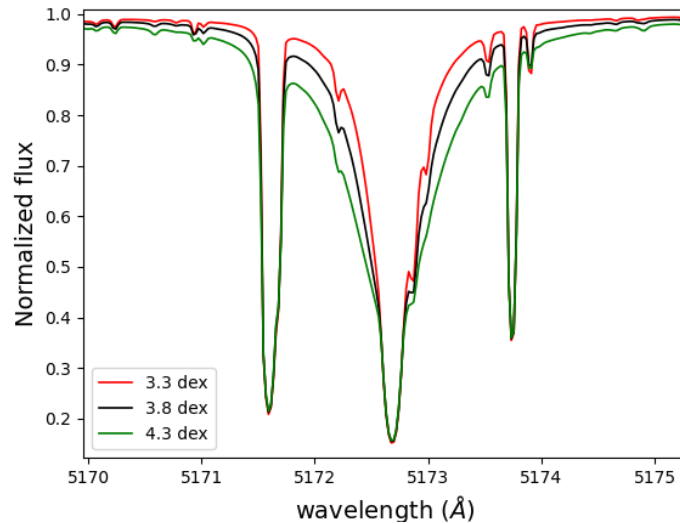


FIGURE 2.19: Synthetic spectra around one of the Mg triplet regions with different $\log g$ values. All the other parameters are fixed.

- **Metallicity** : Astronomers usually denote all the elements above H and He as *metals*. In stellar physics, the abundance of Fe is considered as metallicity (denoted as $[Fe/H]$) as the Fe absorption lines are ubiquitous in the optical region of the spectra, and this can be used to estimate the stellar parameters of the star with less uncertainty. The metallicity, defined as the logarithmic

iron abundance with respect to the Sun,

$$[Fe/H] = \log A_{Fe} - \log A_{Fe, \odot}.$$

- **Microturbulent velocity** is defined as the non-thermal velocity component of a single particle in the stellar surface, which broadens the absorption lines in the stellar surface.

2.6.2 Atomic and molecular data

Detection of a line in the spectrum provides detailed information about the physical conditions and the chemical nature of the photosphere where the transition occurs. The line list contains all the possible transitions in the optical region from the laboratory experiments. The linelist contains information regarding the wavelength in vacuum, transition details, oscillatory strength, lower excitation potential, etc. We have used NIST, VALD, and KURUZ linelist with updated oscillatory strength values.

2.6.3 Stellar model atmospheres

The main assumption applied for stellar photospheric modeling includes plane parallel geometry; that is, the thickness of the photosphere is usually very small ($\Delta R/R \ll 1$), hydrostatic equilibrium, and assuming the photosphere is homogeneous.

We have used **Kurucz ATLAS9 atmospheric models** (Castelli and Kurucz 2003a) with 72 opacity layers of different temperatures, pressure, electron density, etc., assuming there is no relative motion between the layers and entirely balanced by gravity. The stellar model grid contains $3500 \leq T_{eff} \leq 50000$ K, $0.0 \leq \log g \leq 5.0$ and $-0.5 \leq [Fe/H] \leq 0.5$ with a step size of 250 K, 0.5 dex and 0.1 dex respectively. ATLAS9 requires an input model atmosphere as an initial guess then the code will undergo multiple iterations to produce the best model.

Stellar model spectra synthesized using **TURBOSPECTRUM** Alvarez and Plez (1998a); Plez (2012). TURBOSPECTRUM requires a model atmosphere and a line list as input. The model atmospheres were provided by the ATLAS9 atmospheres. This can be useful for any temperature-pressure stratification and the execution time is relatively short even if the input linelist has millions of lines.

2.6.4 Equivalent width measurement and abundance calculation

Equivalent width is a common term used in stellar spectroscopy, defined as the width of a rectangle having the same height and area as an absorption line of the star (Figure 2.20).

$$W_\lambda = \int_{\lambda_1}^{\lambda_2} \frac{F_{\lambda_c} - F_\lambda}{F_{\lambda_c}} * d\lambda$$

F_{λ_c} is denoted by the flux level at continuum and F_λ is the flux at λ .

2.6.5 Estimating stellar parameters

The stellar parameters for the reference star are determined using the absolute excitation and ionization equilibrium for both Fe I and Fe II lines using Boltzmann

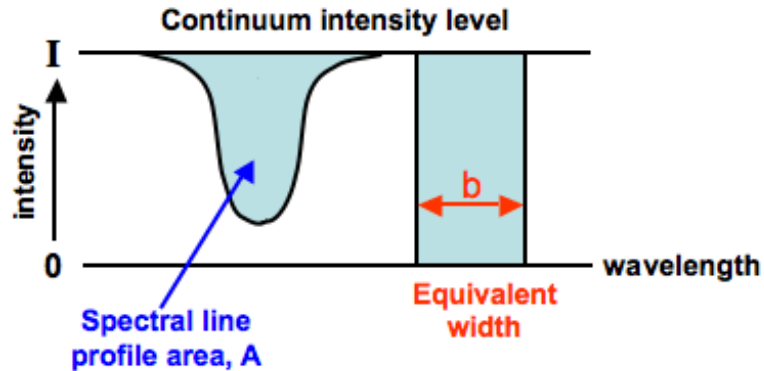


FIGURE 2.20: Area under the absorption line and the area of the rectangle are the same. Equivalent width is the width (b) of the rectangle. Image credit: Cosmos

and Saha's equation.

Boltzmann equation gives the number of atoms in each energy level at thermodynamic equilibrium. The number of atoms present at a lower excitation level at thermodynamic equilibrium indicates the strength of the stellar absorption line. The thermodynamic equilibrium is achieved when the net number of excitation and de-excitation events equals.

$$\frac{n_u}{n_l} = \frac{g_u * \exp\left(\frac{E_u}{K T}\right)}{g_l * \exp\left(\frac{E_l}{K T}\right)}$$

n_u, n_l = number of atoms per unit volume in the upper and lower level, respectively.

E_u, E_l = upper and lower energy level respectively.

K = Boltzmann constant

T = gas temperature

g_u, g_l = statistical weight applied at the upper and lower energy levels, respectively.

As the number of atoms present at different energy levels can be obtained from the spectra, one can calculate the 'T' that is the T_{eff} from the Boltzmann equation.

Saha's equation is defined as at thermodynamic equilibrium, the rate of recombination and ionization are equal. And the equation can be represented as

$$\log_{10} \frac{n_{i+1}}{n_i} = -0.1761 - \log_{10} P_e + \log_{10} \frac{Z_i}{Z_{i+1}} + 2.5 \log_{10} * T - \frac{5040}{T} * \chi_i$$

T = ionization temperature

χ_i = ionization energy

P_e = electron pressure which is proportional to the gravity ($g^{\frac{1}{3}}$)

Saha's equation can be used to measure the surface gravity of a star.

2.6.6 Abundance estimation

The relation which converts the equivalent width to the number of atoms present in the absorption line is called the *Curve of growth* shown in Figure 2.21. And the relation is given by

$$\log\left(\frac{W_\lambda}{\lambda}\right) = \log(C) + \log(gf\lambda) - \frac{5040}{T_{ex}} * \chi + \log(N) - \log(\kappa_c)$$

T_{ex} = excitation temperature

χ = lower excitation potential

gf = statistical weight times the oscillatory strength

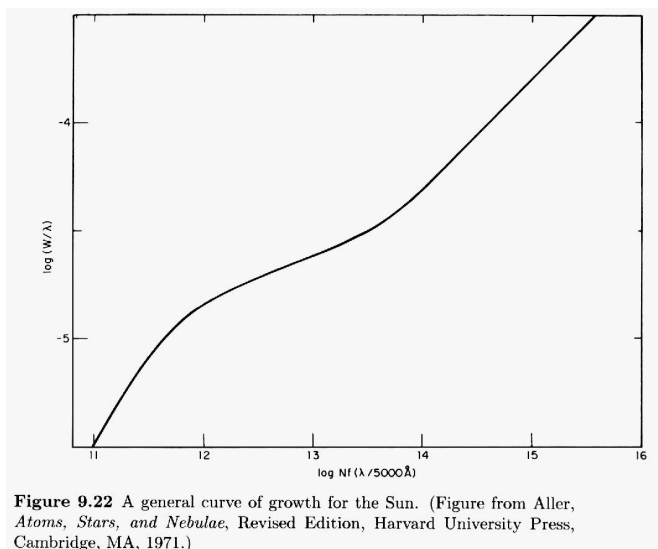


FIGURE 2.21: Number of atoms present as a function of the equivalent width of the absorption line from *Aller, Atoms, Stars and Nebulae, Revised edition, Harvard University Press, Cambridge, MT, 1971.*

$C = \text{constant}$

$\kappa_c = \text{continuum opacity}$ $N = \text{abundance}$

Finding the combination of T_{eff} , $\log g$, and $[\text{Fe}/\text{H}]$ that simultaneously minimized the slopes of Saha's and Boltzmann equations for both Fe I and Fe II will give the best stellar parameters. All our samples are metal-rich main-sequence dwarf stars. So plenty of Fe lines will be there in the observed spectra. We chose equivalent width less than 120 \AA since they are on the linear part of the curve of growth and are sensitive to the choice of micro-turbulence. Multiple measurements of the equivalent widths of each spectral line are taken, and the median is chosen to reduce measurement error.

- Absolute Fe abundance and the differential Fe abundance should be independent of the lower excitation potential. The slope should be minimum. Demanding no trend in Fe I abundances with the lower excitation potential allowed for the iterative derivation of the T_{eff} .

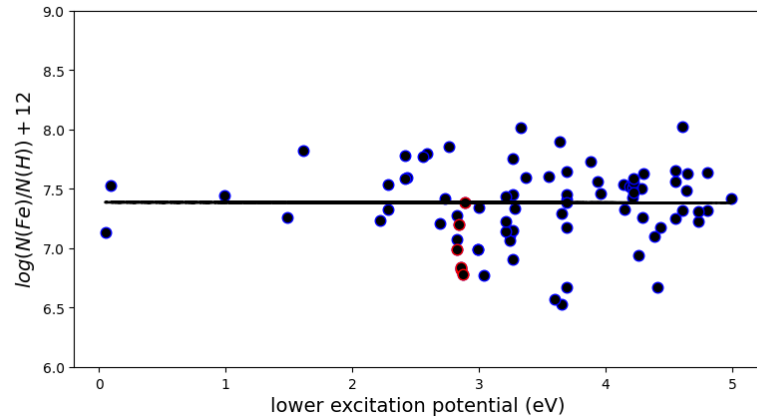


FIGURE 2.22: Best fit model (solid black line) for the abundance of both Fe I (blue) and Fe II (red) lines independent of lower excitation potential. for HD 202772 B using Keck/HIRES observations.

- Absolute Fe abundance and the differential Fe abundance should be independent of the reduced equivalent width. The micro-turbulent velocity was derived by requiring no trend of Fe I abundances with the reduced equivalent width.

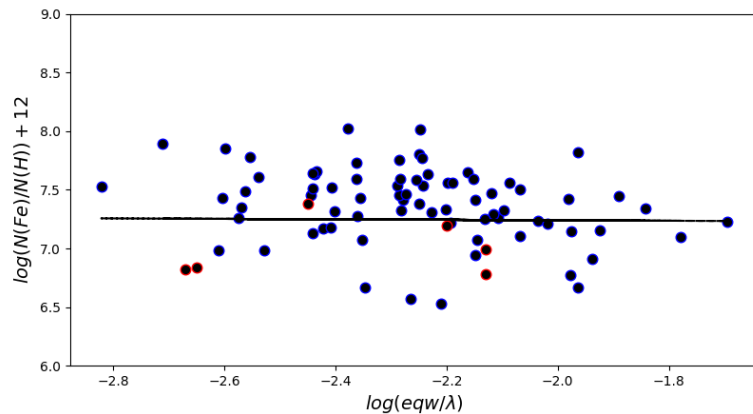


FIGURE 2.23: Best-fit model (solid black line) for the abundance of both Fe I (blue) and Fe II (red) lines independent of reduced equivalent width for HD 202772 B using Keck/HIRES observations.

- Absolute Fe I, Fe II abundance and the differential Fe I and Fe II abundance should be same. The logg of the star is fixed by applying this condition.
- Input metallicity should match with the derived iron abundance.

2.7 Methodology: Exoplanet atmospheric characterization with spectroscopy

Transit spectroscopic observations usually have a time series of continuous observations of the exoplanet host star covering some exposures before ingress, during ingress, during transit, during egress, and after egress. All these time series of spectra have to follow the primary data reduction mentioned in the section 2.5.

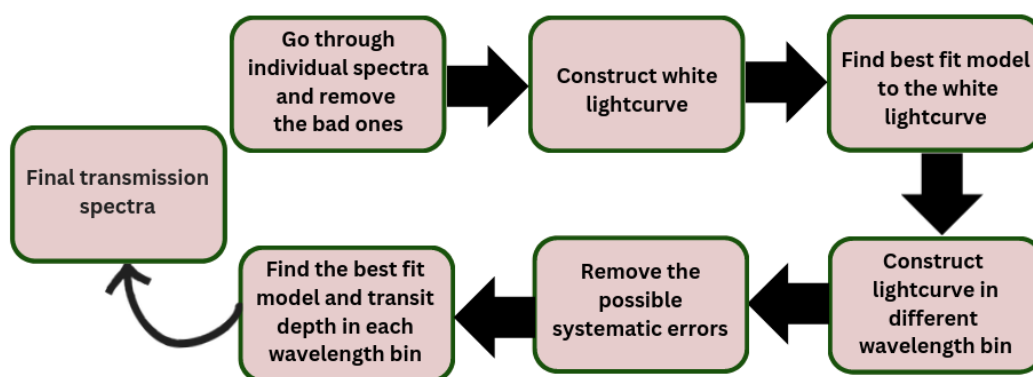


FIGURE 2.24: Step-by-step data analysis procedure of the low-resolution transmission spectroscopy.

Figure 2.24 indicates the data analysis flow of the **low-resolution transmission spectroscopy**. Removing the low SNR spectra from the complete data is important. Then obtain the white light curve to find the transit depth by calculating the mean flux of each exposure in the entire wavelength band as a function of time. Also, obtain the lightcurve in different wavelength bins. Find the best-fitting model for the observed lightcurve and remove all the possible systematic errors. And try to improve the fit to obtain the best transit depth in each wavelength bin, called low-resolution transmission spectra. Finally, model the observed transmission spectra with the available exoplanet atmospheric models. Detailed discussion is presented in Chapter 5.

2.7.1 High-resolution transit spectroscopy with Keck/HIRES

The instrument details of Keck/HIRES are explained in Section 2.2. Once we have the wavelength-calibrated time series spectra of the target star after following the data reduction explained in Section 2.5, visually check each spectra along with SNR achieved for each exposure and remove the bad ones from that. The steps included in the data analysis of a typical High-resolution transit spectroscopy are as follows

- Normalize the spectra by fitting a lower order Spline3 function to the required spectral region.
- Check the stability of the wavelength solution in all the exposures. If needed, do an additional wavelength re-calibration.
- Once the wavelength solution of all the exposures matches within the error, then shift all the wavelength solutions of all the exposures uniformly to the Stellar Rest Frame (SRF).

$$V_{SRF} = -V_{ber} - V_{sys} + V_{star}$$

(+ve means moving towards us, and -ve means moving away from us.). V_{ber} is the barycentric Earth radial velocity, V_{sys} is the velocity with which the planetary system moves with respect to the barycentre of our solar system, and V_{star} is the 1D relative velocity of the star at each exposure (Keplerian).

- Telluric correction is very important as we are looking for an exoplanetary signal in the order of the Earth's atmospheric variation. The standard star observed during the same night can be used as a telluric standard. There are well-performed telluric models available to replicate Earth's atmospheric variations as a function of time. Figure 2.25 shows typical telluric lines present in the optical part of the spectra.

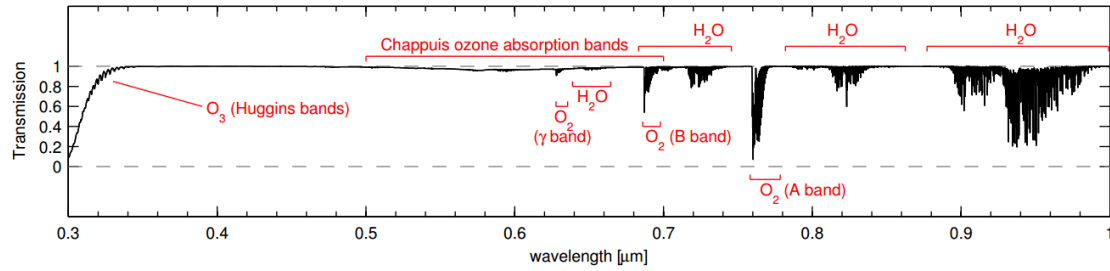


FIGURE 2.25: Possible telluric lines present in the Earth’s atmosphere, in the optical part of the spectra (Smette *et al.* 2015).

- Segregate all the exposures taken during transit and those taken without the transit event. Then median combine all the spectra observed during the out-of-transit to get the *master out of transit spectra*.
- Divide each of the in-transit spectra using the *master out of transit spectra* to get the *residual spectra* around the sodium doublet.
- Shift each of the residual spectra to the planetary rest frame (PRF). Here we have to calculate the planet’s relative velocity as a function of time. This is also known as cross-correlation and is a powerful tool to confirm the exoplanetary origin of the detected atmospheric composition.

$$V_{PRF} = V_p(t) - V_{star}$$

V_p is the Keplerian velocity.

- Combine all the shifted residual spectra and then normalize to get the final transmission spectra around the required region.

The detailed discussion is explained in Chapter 6.

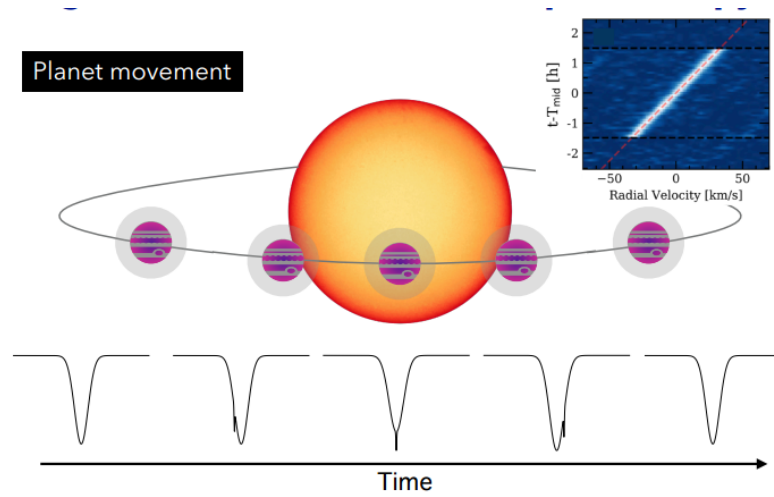


FIGURE 2.26: Pictorial representation of expected velocity shift in the absorption line during transit.

Chapter 3

Carbon abundance of stars in the LAMOST-Kepler field

Abstract

The correlation between host star iron abundance and the exoplanet occurrence rate is well established and arrived at in several studies. Similar correlations may be present for the most abundant elements, such as carbon and oxygen, which also control the dust chemistry of the protoplanetary disk. In this chapter, using a large number of stars in the Kepler field observed by the LAMOST survey, it has been possible to estimate the planet occurrence rate with respect to the host star carbon abundance. Carbon abundances are derived using synthetic spectra fit of the CH- G-band region in the LAMOST spectra. The carbon abundance trend with metallicity is consistent with the previous studies and follows the Galactic chemical evolution (GCE). Similar to $[\text{Fe}/\text{H}]$, we find that the $[\text{C}/\text{H}]$ values are

higher among giant-planet hosts. The trend between $[C/Fe]$ and $[Fe/H]$ in planet hosts and single stars is similar; however, there is a preference for giant planets around host stars with a subsolar $[C/Fe]$ ratio and higher $[Fe/H]$.

3.1 Introduction

Planets and their host stars are formed together from the same molecular cloud. Naturally, the planet's chemical composition is expected to correlate with the host star. Hence, studies of the host star's chemical abundance could constrain the planet's bulk composition and formation processes. Host star metallicity and giant planet connection were first observed by [Gonzalez \(1997b, 1998\)](#) and confirmed by [Santos *et al.* \(2001, 2004a\)](#) with a larger sample. These authors also showed that the frequency of giant planet hosts increases steeply above solar metallicity. This rapid rise in giant planet ($R_p > 4R_\oplus$) occurrence of 3% at solar metallicities and up to 25% at $[Fe/H]=0.3$ was again shown by [Fischer and Valenti \(2005b\)](#). [Johnson *et al.* \(2010b\)](#) observed giant planet-metallicity correlation in a wide range of stellar masses, and the occurrence increased from 3% in M dwarfs to 14% in A dwarfs at solar metallicity. Although the metallicity trend was absent for stars that host smaller planets, a large spread in metallicities is observed among them ([Sousa *et al.* 2008](#); [Neves *et al.* 2009](#)), and the low-mass planet-bearing stars at low metallicity were found to be rich in α elements ([Adibekyan *et al.* 2012a,b,c](#); [Mulders 2018](#)). [Adibekyan *et al.* \(2012a\)](#) suggested terrestrial planets could form early in the Galaxy among the thick disk stars due to their enhanced α abundances. A recent study by [Swastik *et al.* \(2022\)](#) showed that $[\alpha/Fe]$ ratio shows a negative trend with respect to planetary mass, indicating possible conditions for the formation of low-mass planets before Jupiter-like planets.

The enhanced abundance of volatile elements as compared to refractory elements

was first observed in the solar atmosphere (Meléndez *et al.* 2009a); this could be used as a possible signature of the solar system among solar twins (Ramírez *et al.* 2009; Meléndez *et al.* 2012). However, high precision differential abundances of solar analogs and stellar twins in binary systems did not show a significant difference in the trend of stellar abundance and condensation temperatures among planet hosts and non-hosts (Gonzalez *et al.* 2010; González Hernández *et al.* 2010, 2013; Mishenina *et al.* 2016b). Adibekyan *et al.* (2014) noticed a significant correlation of the stellar abundances versus condensation temperature slope with stellar age and Galactocentric distance among Sun-like stars, which could be a cause for the observed difference in the volatile and refractive element abundances. Stellar lithium abundance could be a sensitive indicator of planet pollution. However, the results were inconclusive, shows a large spread in Li even among stars of very similar stellar parameters (Pollack *et al.* 1996a; Israelian *et al.* 2009; Gonzalez *et al.* 2010; Figueira *et al.* 2014; Gonzalez 2014; Mishenina *et al.* 2016a; Delgado Mena *et al.* 2014, 2015). Carbon is produced in massive stars similar to α elements at low metallicities, but low-mass AGB (Asymptotic Giant Branch) stars could also make carbon (Gustafsson *et al.* 1999; Kobayashi *et al.* 2020) at higher metallicities, and hence the C/O ratio can change with time. Bond *et al.* (2010) showed the importance of the C/O ratio in the formation of carbide and silicates in the planet formation and determined the planet mineralogy (Madhusudhan 2012).

Ecuivillon *et al.* (2004) studied 91 planet hosts and 31 non-host solar-type dwarf stars using atomic carbon lines and found no significant difference in $[C/Fe]$ for the planet host and the non-host stars. Delgado Mena *et al.* (2010) also found no difference between carbon abundance between giant planet hosts and non-host stars. Suárez-Andrés *et al.* (2017) used the CH band at 4300 Å for deriving the carbon abundance instead of the atomic lines at 5380.3 Å and 5052.2 Å to study the carbon abundance of HARPS FGK stars with 112 giant planet hosts and 639 stars without known planets. Furthermore, they found that $[C/Fe]$ is not varying as a function of the planetary mass, indicating the absence of a significant

contribution of carbon in the formation of planets.

Here we present the occurrence rate analysis of carbon abundance based on a large number of Kepler-LAMOST (The Large Sky Area Multi-Object Fiber Spectroscopic Telescope) samples of main-sequence FGK stars to understand the importance of carbon abundance in the planet formation process as well as Galactic chemical evolution using CH G band at 4300 Å. The sample contains 825 confirmed planet host stars and 214 stars with planet candidates from the Kepler catalog, and 49215 stars without detected planets.

3.2 Data acquisition and target selection

As we are interested in the statistical analysis of the different populations of planet-host stars, we require the largest sample possible. So we combined LAMOST, the largest low-resolution spectroscopic survey in the Kepler field, called the LK project.

Kepler is a dedicated mission for detecting Earth-like exoplanets around the Solar neighborhood. More than half of the known planets are detected using the Kepler mission using the transit method. Kepler has a wide field of view > 100 deg with a primary aperture of 0.95m. Moreover, it can simultaneously take the photometric observation of 100000 stars using a broad band pass filter (420 - 865 nm) (Koch *et al.* 2004).

LAMOST is a wide-field spectroscopic survey facility using a telescope with a 4m clear aperture and 5 deg field of view. The survey obtains 4000 spectra in a single exposure to a limiting magnitude of $r=19$ at the resolution $R=1800$ and simultaneous wavelength coverage of 370 - 900 nm (Zhao *et al.* 2012). A detailed

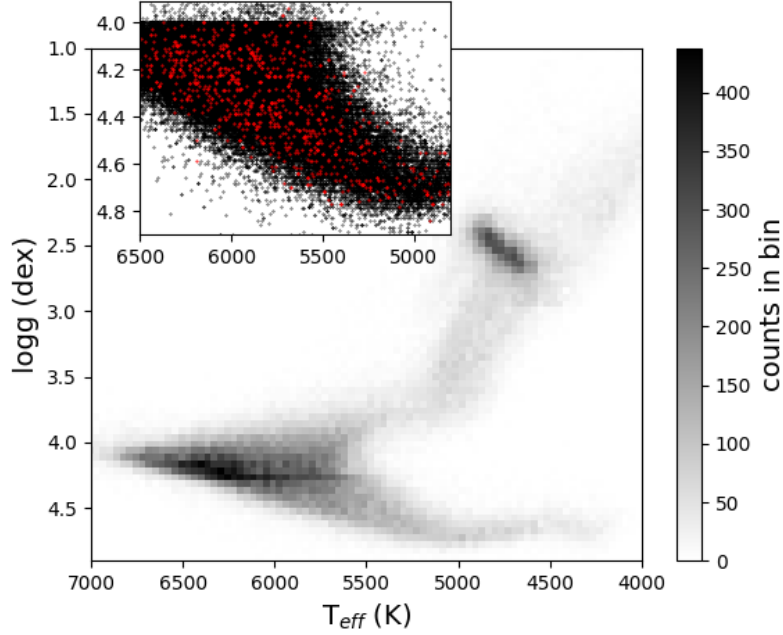


FIGURE 3.1: The entire sample from the LAMOST-KEPLER field is shown as a density plot. And the selected samples within the restricted stellar parameters for the current study are shown as an inset. The black and red dots indicate the field and the planet host stars, respectively.

explanation of the instrument is given in Chapter 2. We have used the LAMOST-Kepler project [Zong *et al.* \(2018\)](#) Public Data Release 4 (<http://dr4.lamost.org>) data for the current study. The observations were carried out between 2012 and 2017 and covered the entire Kepler field. A total of 227870 spectra belonging to 156390 stars were available in the database and out of which the spectroscopic parameters for 126172 stars were available from the LASP pipeline ([Luo *et al.* 2014](#)). The spectra and the corresponding stellar parameters (e.g., T_{eff} , $\log g$, $[Fe/H]$, and radial velocity) were obtained from the LAMOST database. Additional parameters such as the mass and the radius of the planets are taken from the NASA Exoplanet archive [NASA exoplanet archive](#)([Akeson *et al.* 2013](#)). We restricted the analysis to the main sequence dwarf stars, leading to a final sample of 49215 field stars and 1039 host stars with confirmed exoplanets and potential candidates. Figure 3.1 shows the parameter range of the final LAMOST-Kepler sample. Figure 3.2 indicates the SNR (Signal to Noise Ratio), $\log g$, and T_{eff} histogram distribution of the final sample.

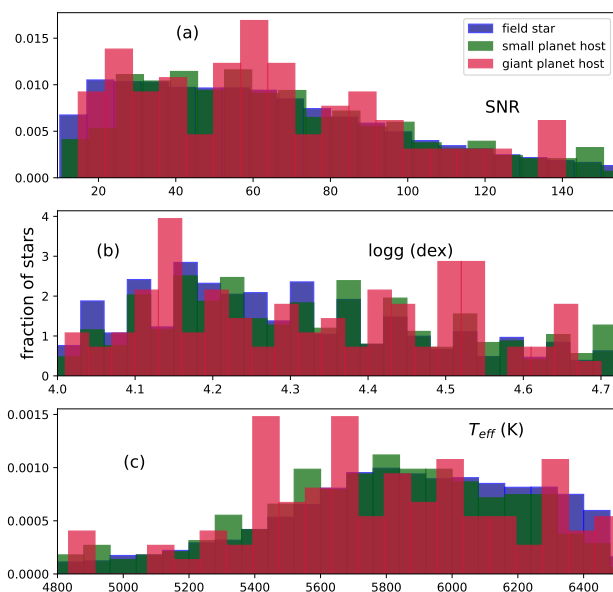


FIGURE 3.2: Distribution of SNR, T_{eff} and $\log g$ of the final sample ($4800 \leq T_{eff} \leq 6500$ K and $\log g > 4.0$). The small planet host with planet radius $R_p \leq 4R_{\oplus}$, giant planet ($R_p > 4R_{\oplus}$) host stars, and field stars are in green, red and blue respectively.

3.2.1 Estimation of carbon abundances

The methodology for estimating the carbon abundance uses a grid of synthetic spectra of varying carbon abundances across various stellar parameters and interpolates the model spectra to match the observed spectra. In this work, we used Kurucz ATLAS9 NEWODF (Castelli and Kurucz 2003c), stellar atmospheric models, by Castelli and Kurucz (2003b) and Turbospectrum (Alvarez and Plez 1998b) spectrum synthesis code V19.1 (Plez 2012) for generating the synthetic spectra. The atomic and molecular line lists are the same as that of Lee *et al.* (2008) and Carollo *et al.* (2012) with minor updates to the hyperfine structure and inclusions of isotopes for the heavy elements. The synthetic grid covers a wavelength range of 4200-4400 Å, which covers the CH molecule of the G-band region, which

is sensitive to carbon abundance. The synthetic spectra cover a range in effective temperatures between $T_{eff} = 3500 - 7000$ K, with an increment of 250 K, and the logg range is between 0.0 – 5.0 dex with an increment of 0.5 dex and $[Fe/H] = -1.0 - +0.5$ dex (with 0.5 dex increment). Carbon abundance was varied over this stellar parameter range at every 0.1 dex step size. We used a python script for interpolation and χ^2 minimization between the observed and the model spectra. Since the wavelength coverage of the grid is limited, stellar parameters from LAMOST were used, and only the carbon abundances were varied for estimating the best fit between observed and synthetic spectra. Figure 3.3 shows an example of a best-fit spectrum. Solar scaled abundances are used for the stellar model atmospheres and synthetic spectra generation in the range $[Fe/H] = +0.0 - +0.5$ and for the metal-poor range, $[Fe/H] = -1.0 - -0.5$ dex an alpha enhanced abundances of $[\alpha/Fe] = 0.4$ dex was used. Solar abundances values are taken from [Grevesse *et al.* \(2007\)](#) where $\log(N(C)/N(H)) + 12 = 8.39$ and $\log(N(O)/N(H)) + 12 = 8.66$ were used. The synthetic spectra grid uses an oxygen abundance ($[O/H]$) that scales with the metallicity for the metal-rich models ($0.0 < [Fe/H] < 0.5$) and follows the alpha abundance in the metal-poor models ($[Fe/H] < 0.0$), as expected by the Galactic chemical evolution. We checked the sensitivity of the derived carbon abundances to the assumed oxygen abundance and found it has less impact on the current sample, as the targets have $T_{eff} > 4800$ K and $C/O < 1.0$. We also visually inspected the goodness of the spectral fit for the entire planet host stars, using plots similar to Figure 3.3. Figure 3.4 represents the goodness of the fit at two extreme T_{eff} regimes.

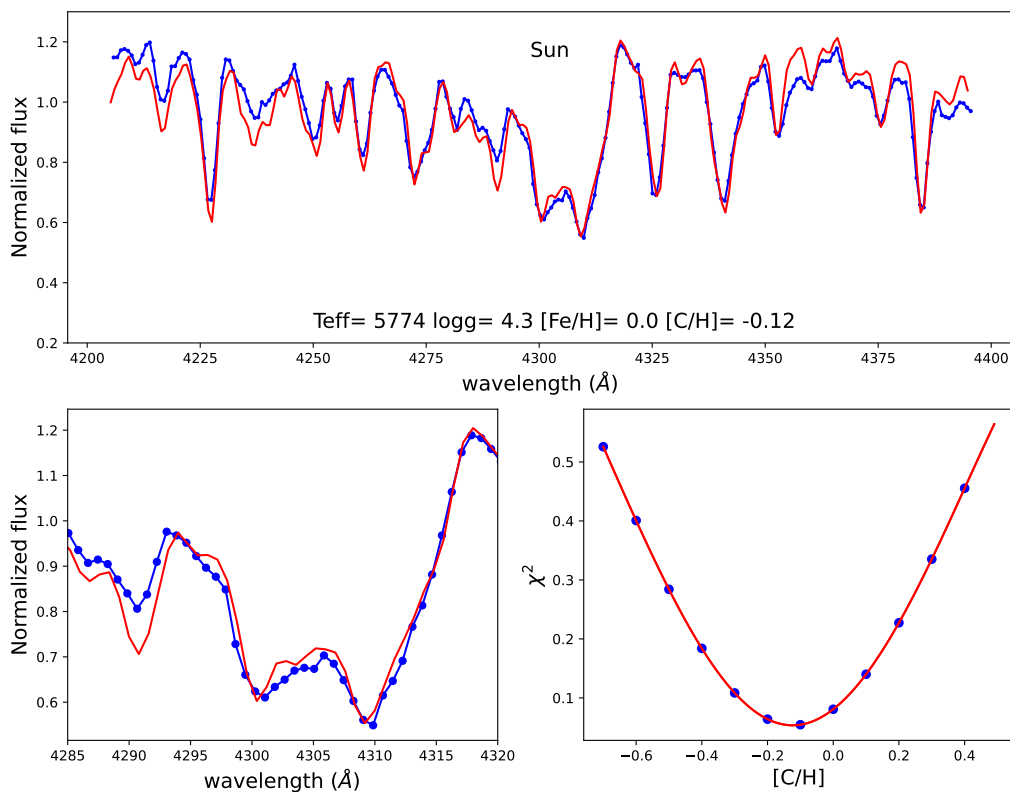


FIGURE 3.3: Observed spectra of Sun (blue) and the synthetic spectra (red). The top panel shows the best fit with input parameters from LAMOST. The bottom-left panel shows an enlarged view of the CH G-band region. Bottom right panel shows the χ^2 variation with $[C/H]$ for obtaining the best fit $[C/H]$ value for the Sun with $T_{eff} = 5774$ K and SNR= 76.

3.2.2 Scaling the derived carbon abundances

The carbon abundances derived in this work use low-resolution spectra fitting the strong CH feature. This spectral region is prone to be affected by continuum fitting error. However, accurate stellar abundances use high-resolution spectroscopy of carefully selected weak lines (mostly atomic CI lines) in the linear part of the curve of growth. Hence, our derived abundance will be different from high-resolution abundances. We corrected the LAMOST carbon abundances using

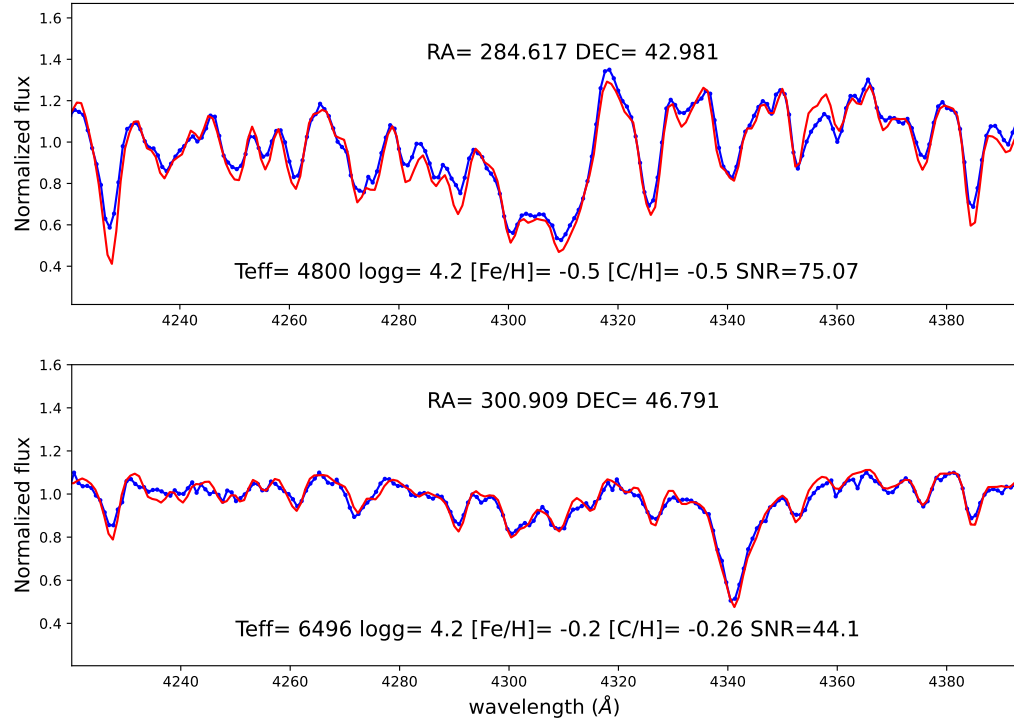


FIGURE 3.4: Observed spectra (blue) and synthetic spectra (red). The top panel shows the best fit for a star of $T_{eff} = 4800$ K and $SNR = 75.07$. The bottom-left panel shows the best fit for a star with $T_{eff} = 6496$ K and $SNR = 44.10$

common samples from the California Kepler Survey (CKS) *(Brewer and Fischer 2018) observed using high-resolution ($R=65000$), Keck-HIRES (High-Resolution Echelle Spectrograph) spectra. We used 1025 common targets from CKS for deriving the corrections. As shown in Figure 3.5, the temperature scale between CKS and LAMOST common samples matches well after removing the 5σ outliers.

First, we made corrections to the CKS and LAMOST $[Fe/H]$ estimates (from the LAMOST catalog), which is not significantly different (Figure 3.6). The LAMOST and CKS, $[C/H]$ values show some dependency with effective temperature (Figure 3.7). So, in the next step, we derive corrections for $[C/H]$ values as a

*The CKS sample is available from <https://doi.org/10.3847/1538-4365/aad501>

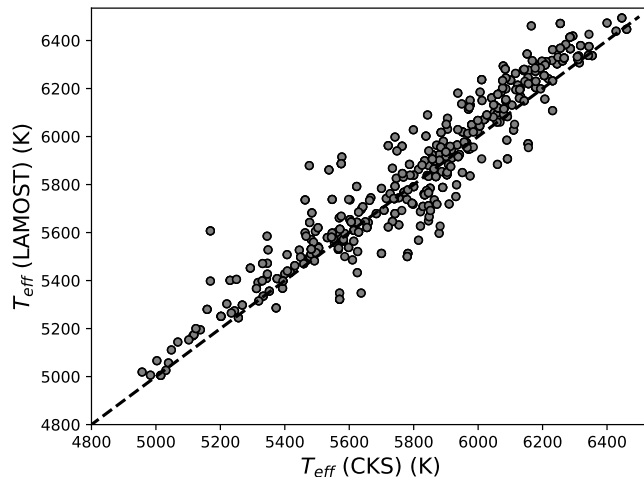


FIGURE 3.5: Comparison of the derived T_{eff} values from CKS and the LAMOST. The black line is the 1:1 line.

function of T_{eff} (Figure 3.8). We verified the correction for Sun using HARPS solar spectra. We have used Sun as star spectra from HARPS and convolved and re-binned to LAMOST resolution. We also added Gaussian noise to the data with an SNR=76, which is the mean SNR of the final sample. The stellar parameters we adopted for Sun are, $T_{eff} = 5774$ K, $\log g = 4.3$ dex and $[Fe/H] = 0.0$. We found an offset of $[C/H]_{LAMOST} = -0.12$ at solar temperature, which is consistent with CKS corrections. The derived solar carbon abundance with CKS correction is $[C/H]_{LAMOST} = 0.09$ (Figure 3.3). In the following sections, we only use the CKS corrected LAMOST $[Fe/H]$ and $[C/H]$ values.

3.2.3 Searching for systematic trends

We plotted the derived carbon abundances with respect to the stellar parameters to infer any systematic trends among them. Figure 3.9 indicates no obvious correlation between the derived carbon abundances with T_{eff} and $\log g$. Figure 3.9 (a) and (b) also shows no systematic difference in the T_{eff} and $\log g$ distribution between giant planet host stars, small planet host, and the field stars. The derived

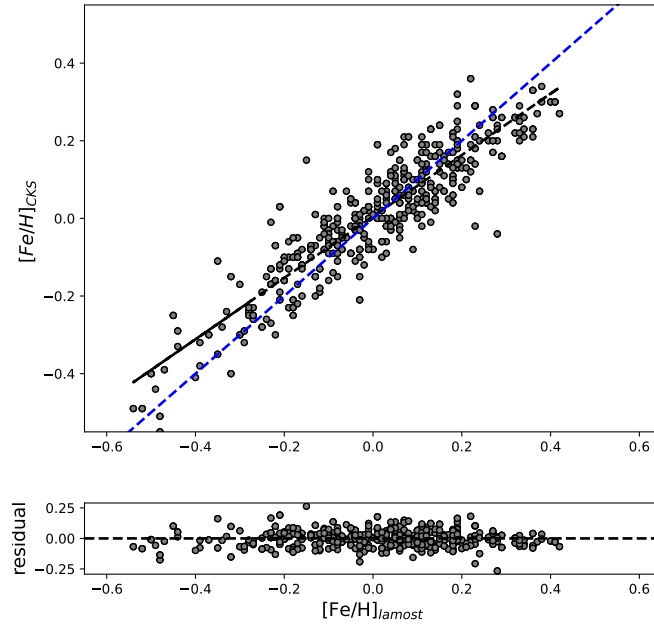


FIGURE 3.6: Comparison of the derived $[Fe/H]$ values from CKS and the LAMOST pipeline. A linear fit is established between the CKS and the LAMOST $[Fe/H]$ values. The best fit coefficients are $[Fe/H]_{new} = [Fe/H]_{lamost} * 0.791 + 0.005$. The blue dashed line is the 1:1 line, and the black dashed line is the best-fit line.

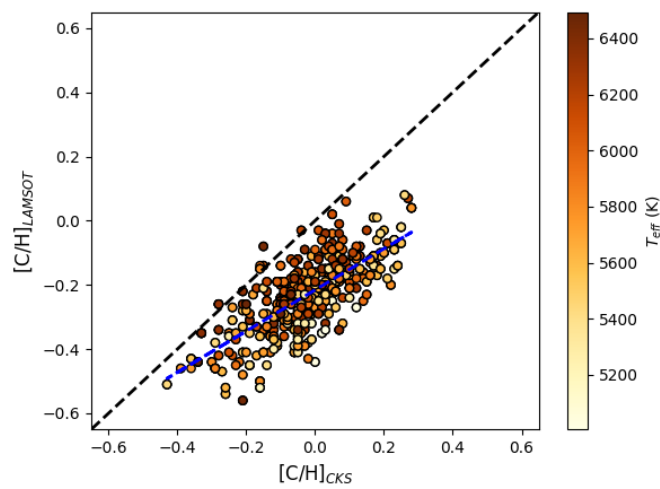


FIGURE 3.7: Comparison of the derived $[C/H]$ values from CKS and the LAMOST as a function of T_{eff} . The black dashed line is the 1:1 line, and the blue dashed line is the best-fit line.

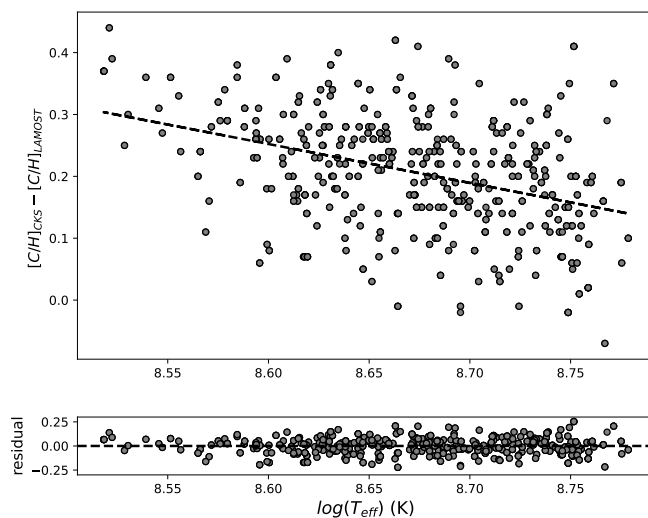


FIGURE 3.8: Comparison of $\delta[C/H] = [C/H]_{CKS} - [C/H]_{LAMOST}$ as a function of T_{eff} . A linear fit is established, and the best fit coefficients are $\delta[C/H] = -0.762 * \log(T_{eff}(lamost)) + 6.820$

mean errors in the carbon abundances across different stellar parameters are also shown in the plots. The error in the carbon abundance is estimated from the χ^2 difference for a fixed difference $\delta[C/H] = \pm 0.1$ dex in the carbon abundance around the minimum χ^2 . Figure 3.9 (c) represents $[C/H]$ as a function of $[Fe/H]$, which shows a positive trend between $[Fe/H]$ and $[C/H]$ as expected due to the Galactic chemical evolution (GCE) effect. Both $[Fe/H]$ and $[C/H]$ increase linearly from the low metallicity close to the solar value and then flatten. This is the typical behavior of α elements that indicate carbon is primarily produced due to massive stars. Carbon may increase slightly at the very metal-rich end due to carbon production from the AGB stars; however, it is not very clear. Figure 3.9 (d) represents the trend of $[C/Fe]$ as a function of $[Fe/H]$, which also represents the GCE effect of carbon with respect to iron. Both field stars and host stars follow a similar trend.

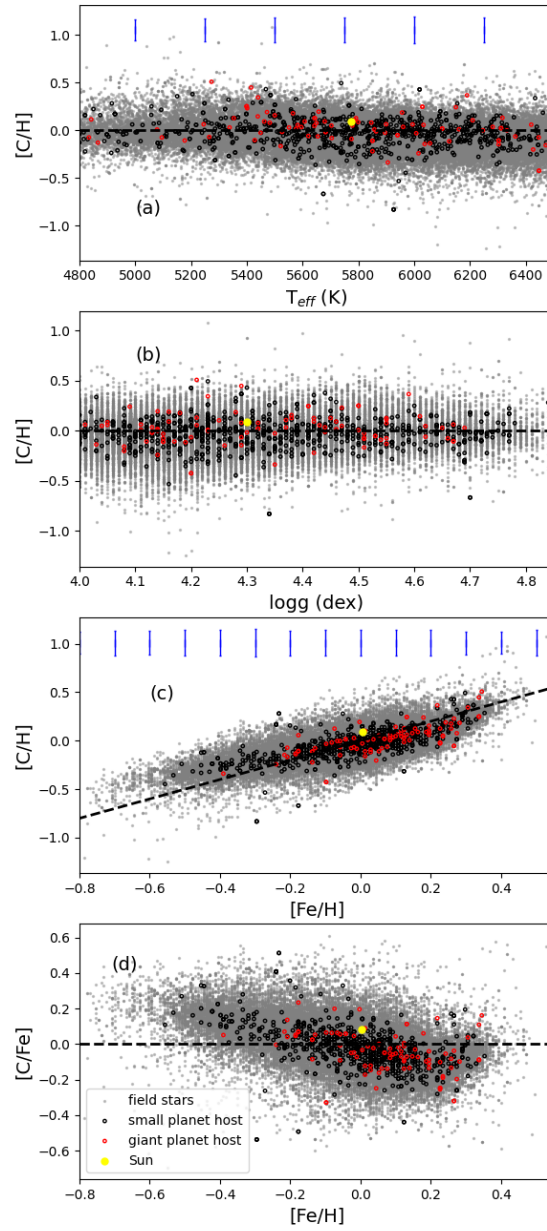


FIGURE 3.9: Variation in $[C/H]$ as a function of T_{eff} (a), $\log g$ (b) and $[Fe/H]$ (c) after CKS correction. Giant planet host stars (red), Small planet host stars (black), field stars (grey), and Sun (yellow). Variation in $[C/H]$ error (shifted for the visual purpose at different x values) plotted in blue. In Figure 3.9 (c), the black dashed line shows the 1:1 correlation. (d) shows $[C/Fe]$ as a function of $[Fe/H]$

3.3 Results

We study the distribution of carbon abundance for planets of different radii and the occurrence rates with respect to the metallicity and carbon abundances. Using Galactic velocity dispersion, we infer the ages of the sample independent of the chemical abundances to understand the role of planet formation on the chemical composition.

3.3.1 Elemental abundance of the host stars as a function of planet population

We examined the elemental abundance distribution of three distinct stellar populations: (i) host stars of the smaller planet ($R_p \leq 4R_\oplus$), (ii) host stars with giant planets ($R_p > 4R_\oplus$) and, (iii) Kepler field stars with no known planet detection. Distributions of $[Fe/H]$, $[C/H]$ and $[C/Fe]$ as a function of planetary radius is shown in Figure 3.10. We find that (a) giant planet hosts, on average, have a higher value of $[Fe/H]_{mean}$ as compared to the host stars of small planets and field stars. This indicates that the giant planets are preferentially found around metal-rich host stars, similar to previous studies (Mulders *et al.* 2016; Petigura *et al.* 2018a; Narang *et al.* 2018). And even the smaller planet hosts have a slightly higher $[Fe/H]_{mean}$ as compared to the field stars, perhaps indicating that the formation of small planets $[Fe/H]$ could have some role (Schlaufman and Laughlin 2011).

Similarly in figure 3.10 (b), the distribution of $[C/H]$ also follows similar trend as that of $[Fe/H]$. The giant planet host stars are carbon-rich compared to field stars and small planet host stars. The resulting $[C/H]$ trend is expected because $[C/H]$ increases with $[Fe/H]$ due to GCE. However, the difference between the $[C/H]$ distribution for small planet hosts and field stars is insignificant. Figure 3.10 (c)

shows the distribution of $[C/Fe]$ for host stars of different planet radii. We find $[C/Fe]$ peaks at a higher value for the field stars compared to the planet hosts, which could be again due to the effect of GCE. Since most of the field stars are $[Fe/H]$ poor compared to the planet hosts, the $[C/Fe]$ at lower metallicities are expected to be higher, as most of the carbon in the Galaxy seems to have come from massive stars and hence the $[C/Fe]$ is high than solar values at lower metallicities (Kobayashi *et al.* 2020). Beyond solar metallicities, the rate of increase of iron is higher compared to carbon; hence the $[C/Fe]_{mean}$ value for the giant planet host star is low compared to stars host small planets and field stars. The results are shown in Table 3.1.

TABLE 3.1: Each column represents the different category of stars, mean $[Fe/H]$, mean $[C/H]$, and mean $[C/Fe]$ values from the histogram distribution.

category	$[Fe/H]_{mean}$	$[C/H]_{mean}$	$[C/Fe]_{mean}$
field star	-0.034 ± 0.001	-0.036 ± 0.001	-0.006 ± 0.001
small planet host	-0.006 ± 0.005	-0.025 ± 0.005	-0.019 ± 0.004
giant planet host	0.068 ± 0.016	0.023 ± 0.016	-0.044 ± 0.012

3.3.2 Occurrence rate of planets and the host star abundance

The analysis described in the previous sections does not take the completeness of the Kepler survey, the detector efficiency, or the probability of detecting a planet into account. The real trend can not be inferred from histograms. In order to derive the correlation between the host star elemental abundance and the planet radius that is free of selection effects and observational biases, we use the final Kepler DR25 data release Mathur *et al.* (2017) to compute the occurrence rate of exoplanets as a function of radius and host star $[Fe/H]$ and $[C/H]$. We updated

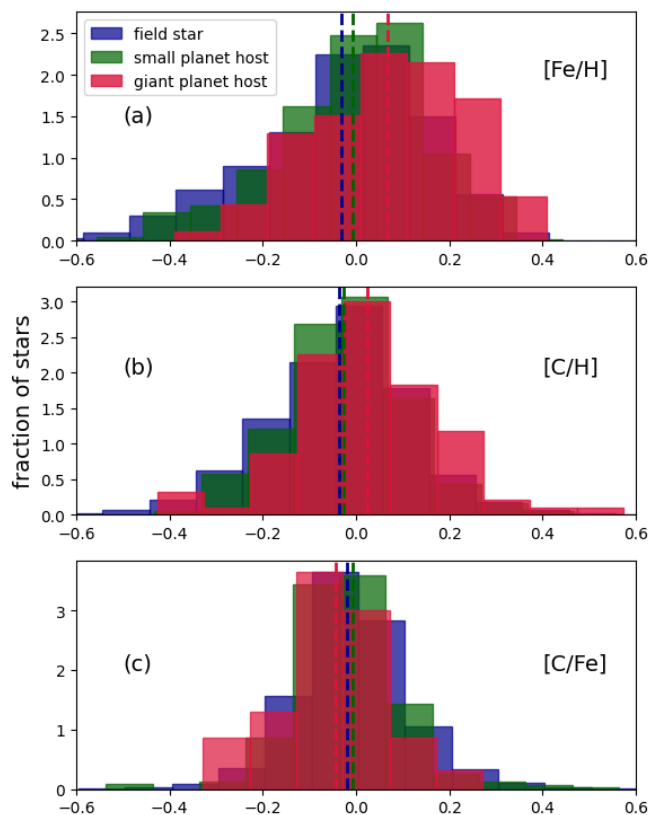


FIGURE 3.10: Distribution of carbon among small planet($R_p \leq 4R_\oplus$) host, giant planet($R_p > 4R_\oplus$) host stars and field stars. A dashed vertical line represents the mean value of each distribution.

the Kepler DR25 catalog with updated stellar and planetary radius based on Gaia DR2 from [Berger *et al.* \(2018\)](#). Since the LAMOST metallicity and the derived carbon abundances are calibrated with respect to the CKS values, we combine CKS samples ([Petigura *et al.* 2018b](#); [Brewer and Fischer 2018](#)) that have metallicities and carbon abundances. This also added additional samples for the occurrence rate estimation. To compute the occurrence rate as a function of planetary radii, we followed the prescription presented in [Youdin \(2011\)](#); [Howard *et al.* \(2012\)](#); [Burke *et al.* \(2015\)](#); [Mulders *et al.* \(2016\)](#).

Similar to [Narang *et al.* \(2018\)](#), we have divided the sample into three $[Fe/H]$ bins; (i) sub-solar metallicity ($-0.8 < [Fe/H] < -0.2$), (ii) solar metallicity ($-0.2 < [Fe/H] < 0.2$) and (iii) super-solar metallicity ($0.2 < [Fe/H] < 0.8$). In Figure 3.11 (a), the occurrence rate of the sample is shown as a function of planet radius and host star $[Fe/H]$. We also calculated the occurrence rate (for the exoplanet sample used in Figure 3.11 (a)) as a function of planet radius Figure 3.11 (b). The 3.11 (a) is both a function of host star $[Fe/H]$ and radius. Similar to [Narang *et al.* \(2018\)](#), we normalized the occurrence rate in Figure 3.11 (a) with the total occurrence rate as a function of radius Figure 3.11 (b) to produce the normalized occurrence rate. The normalized occurrence rate Figure 3.11 (c) is only a function of the host star $[Fe/H]$. From Figure 3.11 (a) and Figure 3.11 (b) it can be seen that smaller planets $R_P \leq 4R_\oplus$ have similar occurrence rate for the three $[Fe/H]$ ranges, while giant planets $R_P > 4R_\oplus$ have a higher occurrence rate for the solar and super-solar $[Fe/H]$. This is consistent with the previous works in literature (e.g., [Mulders *et al.* 2016](#); [Petigura *et al.* 2018a](#); [Narang *et al.* 2018](#)). To compute the occurrence rate of planets as a function of $[C/H]$, we divided the sample into three $[C/H]$ bins since we found that the $[C/H]$ is a strong function of $[Fe/H]$ (see Figure 3.13c) we converted the $[Fe/H]$ bins to $[C/H]$ bins. Based on equation

$$[C/H] = 0.657 * [Fe/H] - 0.165 \quad (3.1)$$

we define the bins as (i) sub-solar $[C/H]$ ($-0.7 < [C/H] < -0.3$), (ii) solar $[C/H]$ ($-0.3 < [C/H] < 0.0$) and (iii) super-solar $[C/H]$ ($0.0 < [C/H] < 0.2$). Figure 3.12 (a) shows the occurrence rate as a function of host star carbon abundance and planetary radius. Similar to Figure 3.11 (a), Figure 3.12 (a) is a strong function of both planetary radius and $[C/H]$. In Figure 3.12 (b), the normalized occurrence rate of planets (using Figure 3.11 (b)) as a function of $[C/H]$ is shown. From Figure 3.12, we find that similar to Figure 3.11, the occurrence rate of giant planets is higher for stars with solar and super-solar $[C/H]$.

We further analyzed the occurrence rate of planets as a function of $[C/Fe]$. We divide the sample again into three bins (i) $[C/Fe]$ between -0.4 to -0.1, (ii) $[C/Fe]$ between -0.1 to 0.1, and (iii) $[C/Fe]$ between 0.1 to 0.4. In Figure 3.13 (a), the occurrence rate as a function of host star $[C/Fe]$ and planetary radius is shown. We found that the occurrence rate for smaller planets ($R_P \leq 4R_\oplus$) is similar in all the three $[C/Fe]$ bins, while the occurrence rate of the giant planets ($R_P > 4R_\oplus$) is much higher for $[C/Fe] < 0.1$. This might indicate that volatile elements such as carbon do not play a significant role in forming giant planets, even though they are more abundant than iron. The overall metallicity may be important, and the formation of giant planets started only in the later stage of GCE.

3.3.3 Galactic space velocity dispersion

The increase in (normalized) occurrence rate as a function of $[C/H]$ indicates that carbon enhancement is necessary for the Galactic context of planet formation. However, it might play a weaker role than that of $[Fe/H]$ in determining the size/radius of the planet. To further understand the planet population in the Galactic context, we need to understand the dependence and evolution of planetary and host star properties as a function of the Galactic age. In Narang et al. (under review), we have established that the critical threshold of $[Fe/H]$ in ISM that was necessary to form Jupiter-like planets was only achieved in the last 5-6 Gyrs indicating that the Jupiters only started forming in the last 5-6 Gyrs. Since the $[C/Fe]$ values are expected to change over the timescale of the Galactic thin disk, we further investigated if probing the Galactic evolution of the $[C/H]$ and/or the $[C/Fe]$ might provide us with clues about the Galactic evolution of planetary systems. Similar to [Binney et al. \(2000\)](#); [Manoj and Bhatt \(2005\)](#); [Hamer and Schlaufman \(2019\)](#) and Narang et al. (under review), we used the dispersion in the peculiar velocity of the stars as a proxy for the age of the stars in the Kepler

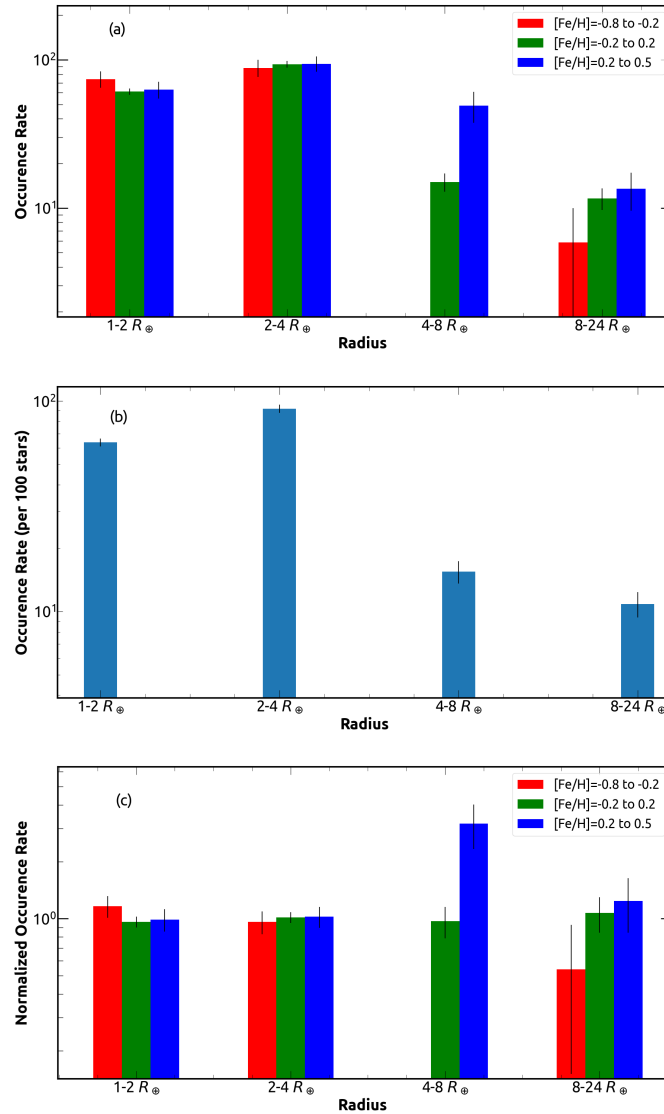


FIGURE 3.11: (a) Occurrence rate of exoplanets as a function of the planetary radius and the host star metallicity. (b) The total occurrence rate of the sample without subdividing it into different metallicity bins. (c) The normalized occurrence rate of the exoplanets as a function of the planetary radius and the host star metallicity. The error bars in these plots are the Poissonian errors based on the number of planets in each bin.

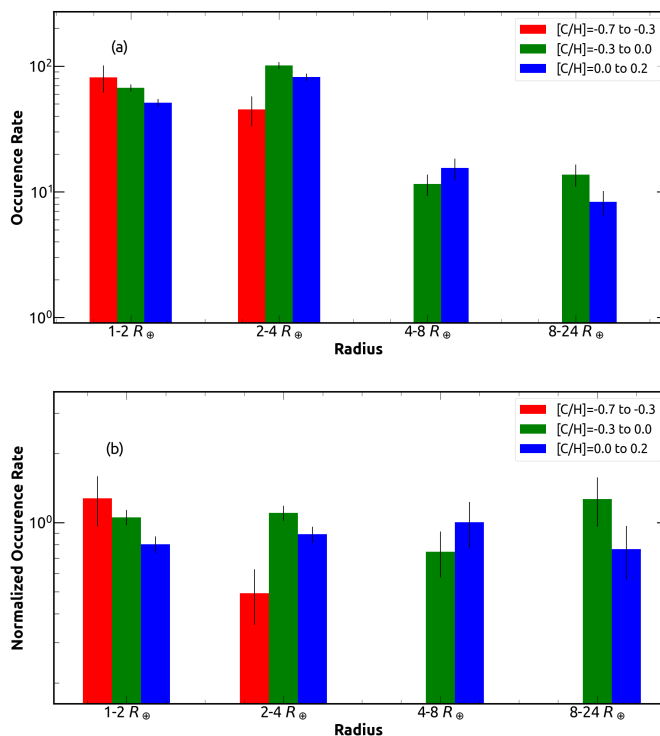


FIGURE 3.12: (a) Occurrence rate of exoplanets as a function of the planetary radius and the host star $[C/H]$. (b) The normalized occurrence rate of the exoplanets as a function of the planetary radius and the host star $[C/H]$.

field. We estimated the velocity dispersion (a proxy for age) as a function of $[Fe/H]$, $[C/H]$, and $[C/Fe]$ with the help of Gaia DR2.

To compute the velocity dispersion, we first calculated the Galactic space velocity in terms of the U, V, & W space components following [Johnson and Soderblom \(1987\)](#); [Ujjwal *et al.* \(2020\)](#) using the proper motion and parallax information from Gaia as well as the radial velocity information from LAMOST. The total velocity dispersion (σ_{tot}) for a particular ensemble of stars is then given as the quadratic sum of the individual components of the velocity dispersion in that given ensemble such that

$$\sigma_{tot} = \sqrt{\sigma_U^2 + \sigma_V^2 + \sigma_W^2} \quad (3.2)$$

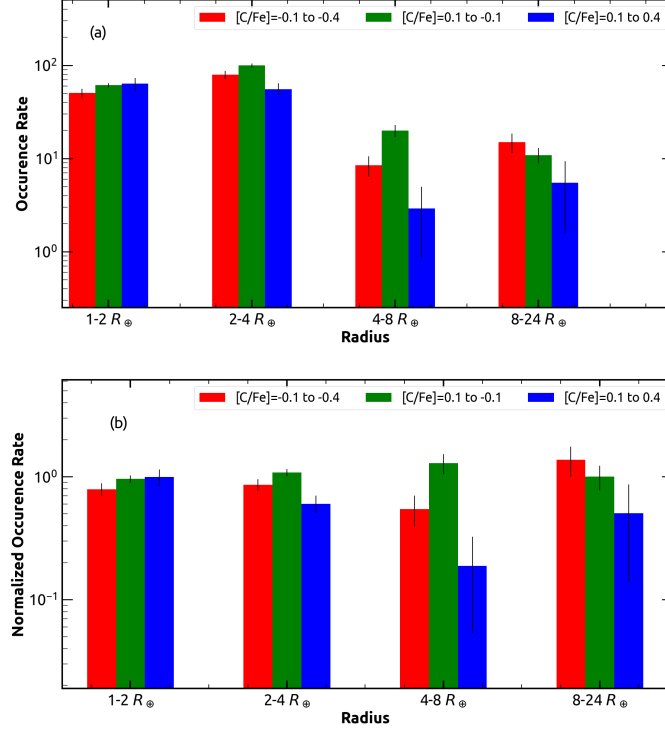


FIGURE 3.13: (a) Occurrence rate of exoplanets as a function of the planetary radius and the host star $[C/Fe]$. (b) The normalized occurrence rate of exoplanets as a function of the planetary radius and the host star $[C/Fe]$.

where σ_U , σ_V , and σ_W are the velocity dispersion of the U , V , and W components given in the same manner as:

$$\sigma_U^2 = \frac{1}{N} \sum_{i=0}^N (U_i - \bar{U})^2 \quad (3.3)$$

where N is the number of stars.

Furthermore, velocity dispersion can then be converted to an average age of the stars following the formalism from Narang et al., (under review):

$$\sigma_{tot}(\tau) = A \times \tau^\beta \quad (3.4)$$

where τ is the average age of the host stars in a bin, A is a constant and is equal to $21.5 \text{ km s}^{-1} \text{ Gyr}^{-0.53}$ and $\beta = 0.53$.

In Figure 3.14, we illustrate the velocity dispersion of the Kepler field as a function of $[Fe/H]$. As the average field $[Fe/H]$ increases, the total velocity dispersion σ_{tot} decreases. This indicates that $[Fe/H]$ rich stars ($[Fe/H] > -0.2$) are younger. Similar behavior is seen for the σ_U , σ_V , and σ_W as well. Using equation 3.4, we can further convert σ_{tot} to the average age of the stars. We find that $[Fe/H]$ rich stars ($[Fe/H] > -0.2$) have an average age between ~ 4 -6 Gyrs. Further from Figure 3.11, we find that most giant planets are around $[Fe/H]$ rich stars. Hence from Figure 3.11 and Figure 3.14, we conclude that most of the giant planets ($R_P > 4 R_\oplus$) in the Kepler field are of an average age between ~ 4 -6 Gyrs, while smaller planets have a much larger spread in host stars $[Fe/H]$ and hence even in the age.

Similarly, by combining the results of velocity dispersion as a function of $[C/H]$ from Figure 3.15 and the occurrence rate of planets in the Kepler field as a function of $[C/H]$, we find that the average age of host stars of giant planets $R_P > 4R_\oplus$ is between 4-5 Gyrs. Similar age ranges are obtained based on $[C/Fe]$ as well (Figure 3.16).

3.4 Discussion

We have calculated the planet occurrence rate as a function of the metallicity of the host star and carbon abundance. The distribution of $[Fe/H]$ and $[C/H]$ with respect to the planet radii show that planets with $R_p > 4R_\oplus$ are mostly found around stars with solar and super-solar metallicities. At these preferred high metallicities, the GCE trend shows lower $[C/Fe]$ ratios, and planet hosts also follow a similar trend as the field stars, as shown in Figure 3.9. With the current

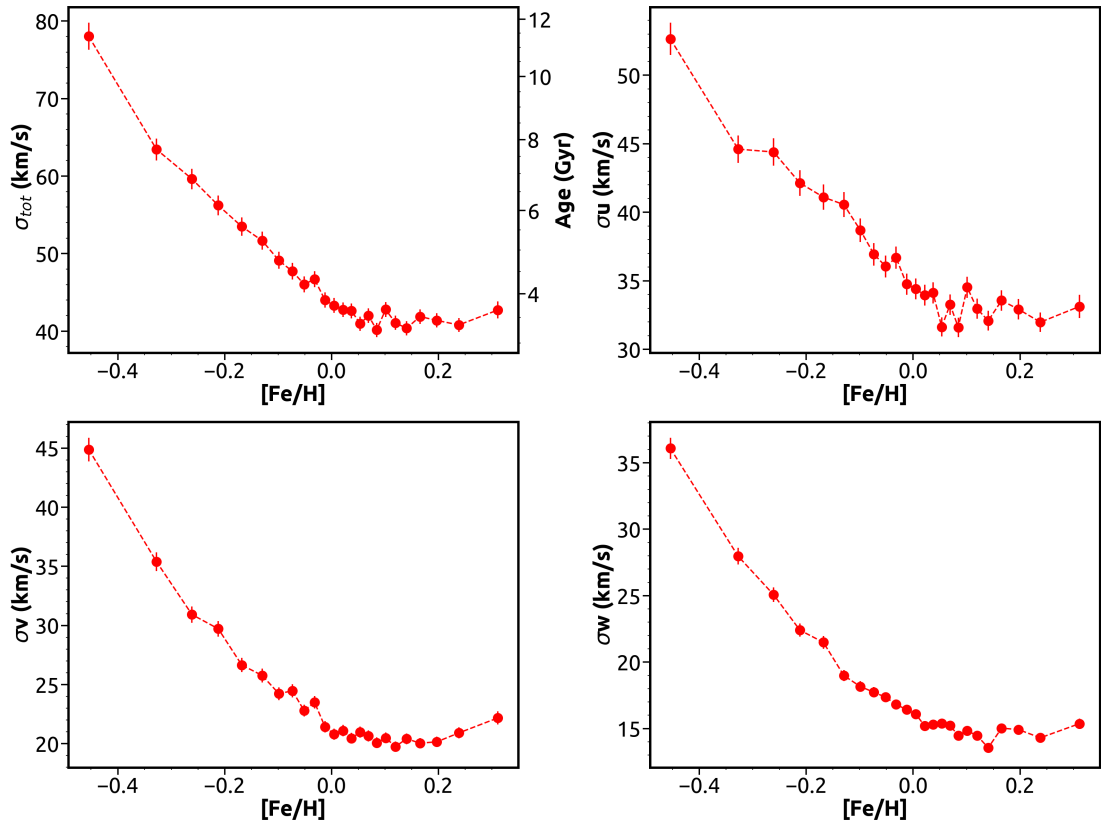


FIGURE 3.14: The total velocity dispersion and the velocity dispersion of the individual components (σ_U , σ_V , and σ_W) as a function of $[Fe/H]$. We have used a running average with a bin size of 1000 and a step size of 200. The error bar on the velocity dispersion is computed following Binney *et al.* (2000). On the right-hand y-axis are the corresponding ages computed using Equation 3.4. The same axis and error bar, as well as the binning scheme, are followed for all subsequent figures.

sample, we do not find a significant difference in the $[Fe/H]$ versus $[C/Fe]$ trend above solar metallicities between the field stars and planet hosts. We explored the difference in $[C/Fe]$ within a narrow bin in metallicity to remove the GCE trend; however, this has significantly reduced the number of samples. A simple mean gives a $[C/Fe]$ value of -0.09 for field stars and -0.13 for giant planet hosts for $[Fe/H] > 0.28$. However, at lower metallicities (where mostly low-mass planet hosts are present), the planet hosts may have slightly higher $[C/Fe]$ values than the field stars, which is similar to what is observed in alpha elements (Adibekyan *et al.* 2012a). Hence, there may be a general preference for planet hosts to have higher abundances of metals. Since planet hosts and field stars follow the GCE trends

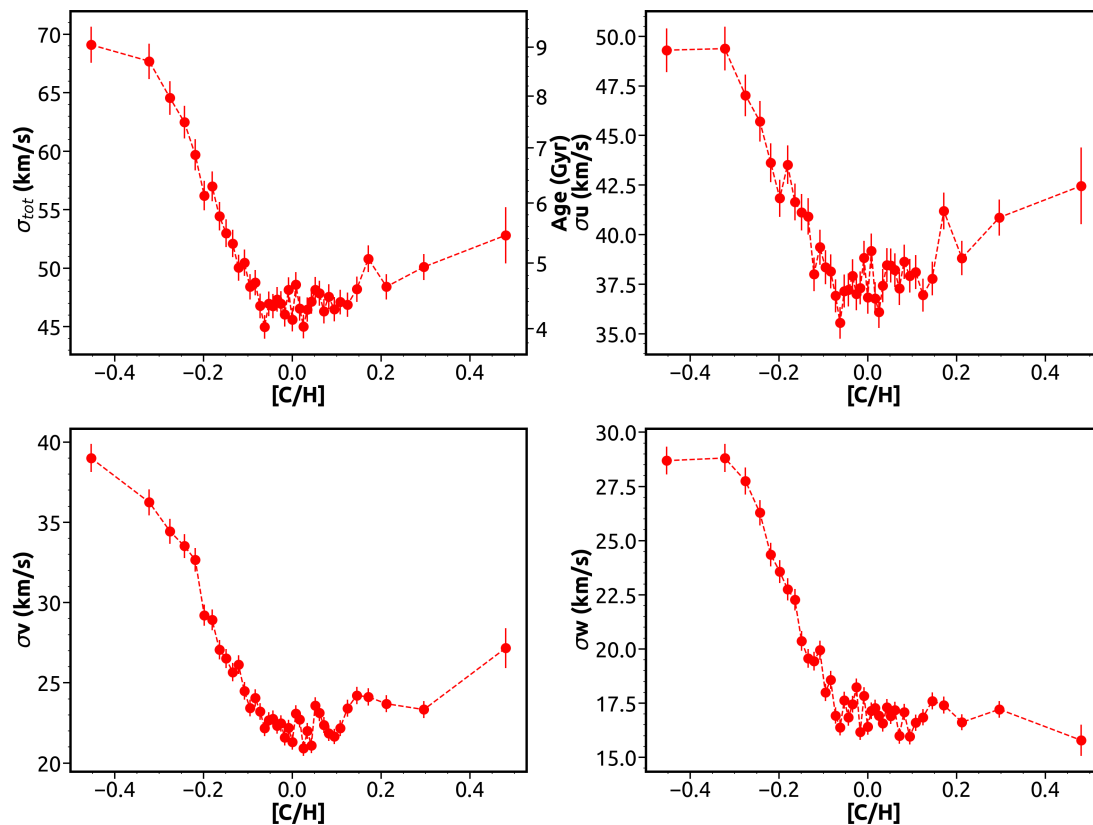


FIGURE 3.15: The total velocity dispersion and the velocity dispersion of the individual components (σ_U , σ_V and σ_W) as a function of $[C/H]$.

in elemental abundance, it is difficult to test the preference of a higher $[C/Fe]$ among planet hosts at solar and super solar metallicities. A stellar population with different abundance ratios with overlapping metallicity, similar to a thick and thin disk, is not present at higher metallicity. Giant planet frequency at a different Galactic distance from future microlensing surveys can cover a range of stellar metallicities and possibly with different abundance ratios.

To remove the Galactic chemical evolution trend of carbon with metallicity, we looked at a narrow bin in metallicity and tried to find the difference in the carbon abundance among planet hosts and field stars; however, this has reduced the number of samples significantly. From Figure 3.9(c), we can say that the planet hosts above $[Fe/H] > 0.0$ and occupy a slightly lower value of $[C/H]$ compared to the field stars. The mean $[C/Fe]$ for planet hosts in the metallicity range

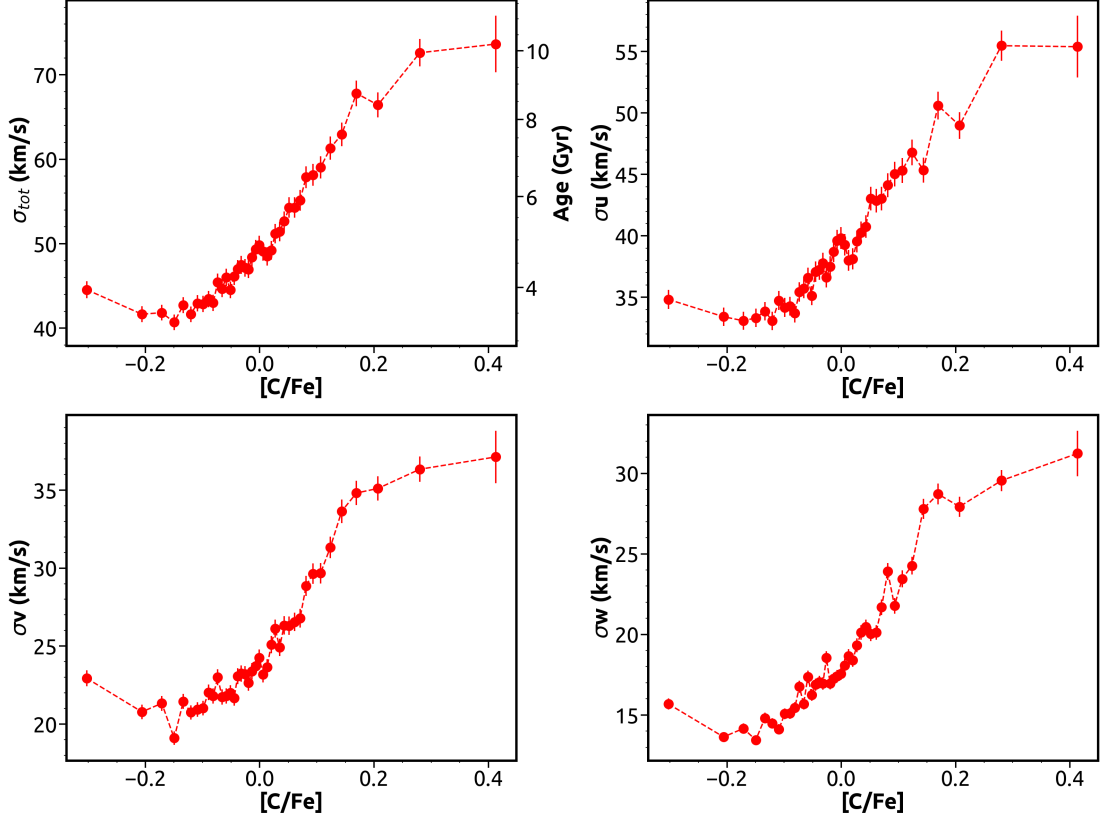


FIGURE 3.16: The total velocity dispersion and the velocity dispersion of the individual components (σ_U , σ_V and σ_W) as a function of $[C/Fe]$.

$0.0 < [Fe/H] < 0.2$ is -0.285 and for the field stars in the same metallicity range is -0.272 .

3.5 Conclusion

We have used LAMOST-Kepler data of main-sequence dwarfs to derive the carbon abundance and compare the planet hosts and the field stars. We constrained the sample to the main sequence dwarf stars to avoid effects due to stellar evolution. The distribution of carbon and iron with the planet radii and the occurrence rate analysis showed the giant planet hosts are iron-rich and carbon-rich compared to the field stars and the stars with smaller planets. However, at super-solar

metallicities, the $[C/Fe]$ values are lower than the solar ratio. Iron increases at a faster rate at the metal-rich end compared to carbon, which may be crucial for increasing the abundance of the refractory elements. Based on the Galactic space velocity dispersion, we found that the Jupiter host stars are younger, only about 4-5 Gyrs old. Even though the number density of carbon is higher than iron at super-solar metallicities, the giant planet formation may require a critical abundance of refractory elements and could reach it only 4-5 Gyrs ago. From the detailed occurrence rate analysis, we found that carbon is not a significant contributor to the mineralogy of planet formation as compared to iron.

Appendix

RA(degree)	DEC(degree)	T_{eff}	logg	[Fe/H]	[C/H]
12.9681	10.1142	5843.0	4.09	-0.5487	-0.2814
13.1028	8.7679	6058.0	4.34	0.0207	-0.0390
13.1220	9.1860	5044.0	4.57	-0.4775	-0.2193
13.1915	9.5228	5562.0	4.25	0.0681	0.0960
13.2336	8.7201	5401.0	4.57	-0.4854	-0.1415
13.2383	10.6629	5024.0	4.46	-0.0979	0.2636
13.2399	9.5898	5444.0	4.44	0.0444	-0.0075
.....
.....
167.630188	0.307838	4261	4.6999998	-0.47	-0.57
167.6458588	-0.851329	5044	4.5900002	-0.32	-0.43
167.6579895	-0.223648	4687	4.6599998	-0.05	-0.4
167.6629944	-0.131331	5304	4.6799998	-0.21	-0.43
167.6772461	0.038034	4986	4.54	-0.36	-0.45
167.6934814	1.625792	6054	4.1700001	-0.03	-0.19
167.699646	0.259866	5063	4.6399999	-0.19	-0.39
167.7208862	0.060551	6122	4.1199999	-0.46	-0.39
167.7237549	-0.303719	4499	4.5799999	-0.19	-0.51
167.7408295	-1.480244	5119	4.6100001	0.12	-0.31
167.7738342	0.058243	4228	4.75	-0.48	-0.7
167.7752838	2.2649209	4730	4.5599999	-0.75	-0.72
167.7816772	0.325315	5979	4.4200001	-0.05	-0.33
167.8115997	-1.016991	4577	4.6300001	-0.26	-0.52
167.8118439	2.2391789	5980	4.3299999	0.03	-0.11
.....
.....

TABLE 3.2: Sample data of LAMOST-Kepler field stars. Each column represents RA, DEC, effective temperature of the star, logg, [Fe/H], and the [C/H]

RA(degree)	DEC(degree)	T_{eff}	logg	[Fe/H]	[C/H]
.....
279.8469238	44.1596909	5604	4.56	0.03	-0.22
279.8469238	44.1596909	5604	4.56	0.03	-0.22
279.847168	43.0251808	4635	4.74	0.12	-0.34
279.847168	43.0251808	4635	4.74	0.12	-0.34
279.8475342	47.7032356	6024	4.25	-0.2	-0.24
279.8491211	46.4808731	5613	4.01	0.08	-0.17
279.8659058	46.9793854	5795	4.21	0.02	-0.2
279.866394	47.1573563	5379	4.23	-0.12	-0.4
279.866394	47.1573563	5379	4.23	-0.12	-0.4
279.866394	47.1573563	5379	4.23	-0.12	-0.4
279.8666077	41.9319344	5528	4.48	-0.33	-0.46
.....
291.1022034	50.5369301	6018	4.1799998	-0.31	-0.46
291.1022034	50.5369186	5991	4.1300001	-0.31	-0.43
291.1026611	41.6170769	5620	4.54	0.24	-0.17
291.1026611	41.6170769	5620	4.54	0.24	-0.17
291.1028748	45.4185829	6075	4.0799999	0.22	-0.11
291.1028748	45.4188957	6079	4.1300001	0.2	-0.07
291.1028748	45.4185715	6055	4.0900002	0.2	-0.05
291.1038208	43.7535019	6245	4.29	-0.16	-0.2
291.104187	48.0426292	5896	4.25	0.01	-0.19
291.104187	44.0601997	6090	4.2199998	-0.23	-0.41
291.1042175	44.0601921	5984	4.3899999	-0.17	-0.36
.....

TABLE 3.3: Sample data of LAMOST-Kepler field stars. Each column represents RA, DEC, effective temperature of the star, logg, [Fe/H], and the [C/H]

RA(degree)	DEC(degree)	T_{eff}	logg	[Fe/H]	[C/H]
.....
291.1053467	48.2742767	5243	4.6500001	0.16	-0.22
291.1053772	49.1808281	5918	4.21	-0.34	-0.45
291.1054688	44.4811096	6049	4.3299999	-0.03	-0.39
291.1054688	44.4810982	6015	4.3299999	-0.05	-0.15
291.1057434	42.3970184	5758	4.1900001	-0.37	-0.4
291.1072998	42.2459106	5731	4.3400002	0.06	-0.18
.....
.....
299.459137	45.91679	6028	4.04	-0.05	-0.23
299.4594421	43.9097595	6211	4.15	0.33	-0.37
299.4607544	43.8092232	6289	4.21	-0.12	-0.32
299.462677	47.3565826	5981	4.13	0.02	-0.52
299.4630737	42.5211487	6404	4.15	0.05	-0.41
299.4630737	42.5211487	6404	4.15	0.05	-0.41
299.4639282	46.16819	5656	4.36	0.1	-0.11
299.4639282	46.1681938	5591	4.25	0.08	-0.22
299.4649963	45.5816193	6264	4.23	-0.31	-0.25
299.4655457	45.5748405	5823	4.42	-0.12	-0.21
299.4665833	47.0244179	6354	4.0	-0.31	-0.34
299.4670715	42.4379234	6468	4.19	0.08	-0.04
299.4685059	44.25214	6193	4.02	0.05	-0.25
299.4685059	45.2125015	6322	4.21	0.04	-0.17
299.4685059	45.2125015	6322	4.21	0.04	-0.17
299.4686279	45.2126846	6310	4.21	0.02	-0.09
299.468689	41.3595695	5899	4.44	0.07	-0.27
.....
.....

TABLE 3.4: Sample data of LAMOST-Kepler field stars. Each column represents RA, DEC, effective temperature of the star, logg, [Fe/H], and the [C/H] (continue)

RA(degree)	DEC(degree)	T_{eff}	logg	[Fe/H]	[C/H]
.....
.....
299.9935913	44.6848068	6273	4.21	-0.48	-0.51
299.9935913	44.6848068	6273	4.21	-0.48	-0.51
299.9957886	47.1198616	5178	4.5900002	0.11	-0.24
299.9957886	47.1198616	5178	4.5900002	0.11	-0.24
299.997345	44.2460709	5218	4.6199999	-0.07	-0.41
299.9992371	40.8527718	6421	3.99	0.1	-0.16
299.9999695	45.2290382	5258	4.6500001	0.07	-0.33
300.0004883	46.8639984	5869	4.1100001	0.09	-0.18
300.000885	46.8380394	5840	4.0	-0.21	-0.33
300.0009155	46.838028	5850	4.04	-0.2	-0.34
300.0009766	44.8284988	5345	4.6700001	-0.08	-0.34
300.0010376	40.9790421	5271	4.54	0.28	-0.16
300.0010376	40.9790421	5271	4.54	0.28	-0.16
300.0012207	44.4470215	6082	4.5500002	-0.03	-0.04
300.0012817	41.9199257	5851	4.02	0.32	0.045
300.0039062	41.7315407	6476	4.2199998	0.03	-0.25
300.0039062	41.7315407	6476	4.2199998	0.03	-0.25
300.0039062	41.7315407	6476	4.2199998	0.03	-0.25
300.0039978	44.1375313	5664	4.5900002	-0.13	-0.44
300.0046997	45.3192711	5542	4.5900002	0.05	-0.34
300.0054932	48.1293755	5217	4.6100001	0.0	-0.45
300.0058289	44.7187805	4251	4.5599999	-0.03	-0.57
300.0065613	42.0198364	5496	4.3200002	-0.36	-0.57
.....
.....
303.3804	45.6495	5788.0	4.40	0.1077	-0.1142
303.3810	45.7701	6286.0	4.23	-0.0188	-0.2871
303.4039	45.6290	5910.0	4.25	-0.0109	0.1798

TABLE 3.5: Sample data of LAMOST-Kepler field stars. Each column represents RA, DEC, effective temperature of the star, logg, [Fe/H], and the [C/H] (continue)

Chapter 4

Differential Abundance Analysis of Planet Host Visual Binary Systems

Abstract

Differential abundance analysis among planet-hosting stars in a binary system can probe the primordial versus the self-enrichment scenario on the origin host star abundance difference. Here we perform the differential abundance analysis of two binary systems, HD 80606/ HD 80607 and HD 202772 A/ HD 202772 B. The primary and secondary have similar stellar parameters. In the binary system, one of the companions hosts a giant planet, and the other does not. Precise line-by-line differential analysis shows an overall enhancement in all elements to a level

0.01dex. There is no significant trend as a function of condensation temperature and the abundance difference.

4.1 Introduction

The formation and evolution of exoplanets can alter the chemical composition of the host star as they are formed from the same initial molecular cloud. The metal-rich nature of the giant planet host star is supported by the core accretion model of planet formation by [Pollack *et al.* \(1996b\)](#) and later supported by the observations ([Gonzalez 1997a, 1998](#); [Santos *et al.* 2001, 2004b](#); [Fischer and Valenti 2005a](#); [Johnson *et al.* 2010a](#)). In the core accretion model, the metal-rich environment helps the formation of the planetary core of mass around $10M_{\oplus}$ in a faster way. It can accrete the gaseous envelope before the gas dissipation timescale. However, this correlation is seen only for the giant planet ($R_P > 4R_{\oplus}$) host stars. [Meléndez *et al.* \(2009b\)](#) introduced the differential abundance analysis by comparing the Sun and other Sun-like field stars which do not host a planet. He found that the Sun is deficient in refractory elements ($T_c > 900$) K as a function of condensation temperature (T_c) compared to the volatile elements ($T_c < 900$) K and they proposed the refractory elements are mainly used for the formation of the rocky planets. [Liu *et al.* \(2016\)](#) also supported this result by observing planet host stellar binary twins in the open cluster M67. As we know, the local and global composition of the protoplanetary disk and the Galactic Chemical Evolution (GCE) trend is different in different parts of the sky. So some other studies justified the observed abundance difference can be due to the difference in the stellar age or the difference in the Galactocentric distance [Adibekyan *et al.* \(2014\)](#); [Nissen \(2015\)](#). The accretion of post-formation of planets can also alter the photospheric composition of the host star photosphere based on the mass of the planet ([Liu *et al.* 2018](#)).

The binary stars are important for these studies because they are formed from the same initial molecular cloud (Kratte 2011; Vogt *et al.* 2012). A differential abundance analysis of binary stars can give better results, excluding all the model-dependent uncertainties and the GCE effects. So planet-host binary systems are ideal cases to study the impact of planet formation and evolution on the host star. Recently many studies have been focusing on this aspect using high-resolution and high signal-to-noise ratio spectroscopic observations. The study based on the binary system XO-2N/XO-2S (Teske *et al.* 2015), 16 Cyg A/B (Tucci Maia *et al.* 2014), and HD 20807/20766 system where one of the binary star host a debris disk (Saffe *et al.* 2016) or a planet shows that planet host is deficient in refractory elements compared to volatile elements supporting the observation by Meléndez *et al.* (2009b) for Sun. Meanwhile, HD 240430/240429 (Oh *et al.* 2018) and HAT-P-4 A/B (Saffe *et al.* 2017) showed that refractory elements are enhanced in the planet host star compared to the volatile elements, which probably indicates engulfment of a close-in terrestrial planet. In some other systems like WASP-94 A/B (Teske *et al.* 2016a) and HD 133131 A/B (Teske *et al.* 2016b), even though a significant elemental abundance difference was derived, as there is no trend with condensation temperature. However, Bitsch *et al.* (2018) proposed the observed abundance difference can be related to the planet formation location in the disk. For HAT-P-1 (Liu *et al.* 2014), HD80606 (Liu *et al.* 2018), and HD 20781/20782 (III *et al.* 2014) show no significant difference in the abundance among the binary companions. Liu found no relation between the observed difference in the abundance and the planet occurrence rate based on the study on nine binary planet host systems, which implies the presence of a planet may not alter the photospheric chemical composition of the host star. Based on the observational evidence we have so far, the results are not converging to a common conclusion about how different populations of planets can alter the host star's chemical composition. So we require more samples for the analysis.

Here we are presenting the detailed differential abundance analysis of the co-moving wide visual binary system HD 80606 (09:22:37.576,+50:36:13.435) and HD 80607 (09:22:39.736,+50:36:13.952) with an angular separation of 20" and a projected separation of 1200 AU. Both are solar-type stars with spectral type G5V, with apparent V magnitudes of 9.06 and 9.17, respectively. HD 80606 hosts a massive gas giant planet with a mass of $4M_J$ and radius R_J on a highly eccentric orbit ($e=0.93$) at a distance 0.05 AU from the host star (Naef *et al.* 2001). All the parameters make HD 80606/HD 80607 a good target for studying the influence of how close-in massive planets in highly eccentric orbit can alter the host star photospheric composition Saffe *et al.* (2015). Mack *et al.* (2016) and Liu *et al.* (2018) done a detailed differential analysis on this aspect of this system. However, here we are presenting an independent study using our observations.

We are also presenting the differential abundance analysis of another visual binary HD 202772 A (21:18:47.901,-26:36:58.95) and 202772 B (21:18:47.813,-26:36:58.42) for the first time using the Keck/HIRES data. Both stars HD 202772 A/B are main sequence dwarf stars with apparent V magnitudes of 8.3 and 10.1, respectively, and separated by 1.3" (149.5 pc). HD 202772 A hosts a highly irradiating inflated gas giant planet with a mass of $1.0M_J$ and radius $1.5R_J$ on a nearly circular orbit ($e=0.04$) at a distance 0.05 AU from its host star (Wang *et al.* 2019).

4.2 Observation and Data reduction

HD 80606/ HD 80607 are observed using the Hanle Echelle SPectrograph (HESP) mounted on 2m Himalayan Chandra Telescope (HCT) (Sriram *et al.* 2018) (PI: Sivarani Thirupathi). The observation was carried out on 2016-01-26, with an exposure time of 40 minutes. Three exposures for each star are taken to increase the signal-to-noise ratio. The airmass varied from 1.60 to 1.05 during the beginning

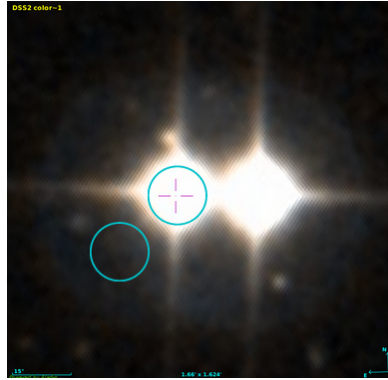


FIGURE 4.1: HD 80606/HD 80607 visual binary system from *Aladin*. Two circles illustrate two pinholes of HESP to observe stars and sky simultaneously.

and end of the observation. We have used high-resolution observation with the star-sky mode. Figure 4.1 indicates the image of both stars taken from *Aladin*.

We visually inspected the quality of the 2d image obtained. Initial data reduction to the raw data has been performed using the IRAF (Image Reduction and Analysis Facility) package. Then median combined the five bias frames taken during the observation and made the master bias frame. The three exposures of science frames for each star are median combined. Then we performed the bias subtraction from the median combined science frame. We followed the optimal extraction of the aperture using the *apall* package in IRAF. Wavelength calibration is performed using the ThAr lamp taken during the night of observation and the ThAr atlas provided by the IAO (Indian Astronomical Observatory). Continuum normalization has been done using the *continuum* package with *Spline 3* function of lower order. Figure 4.2 represents different wavelength regions overplotted for both the stars HD 80606/HD 80607. The spectral features at other wavelength regions match well, indicating the possibility of having similar physical parameters for both stars.

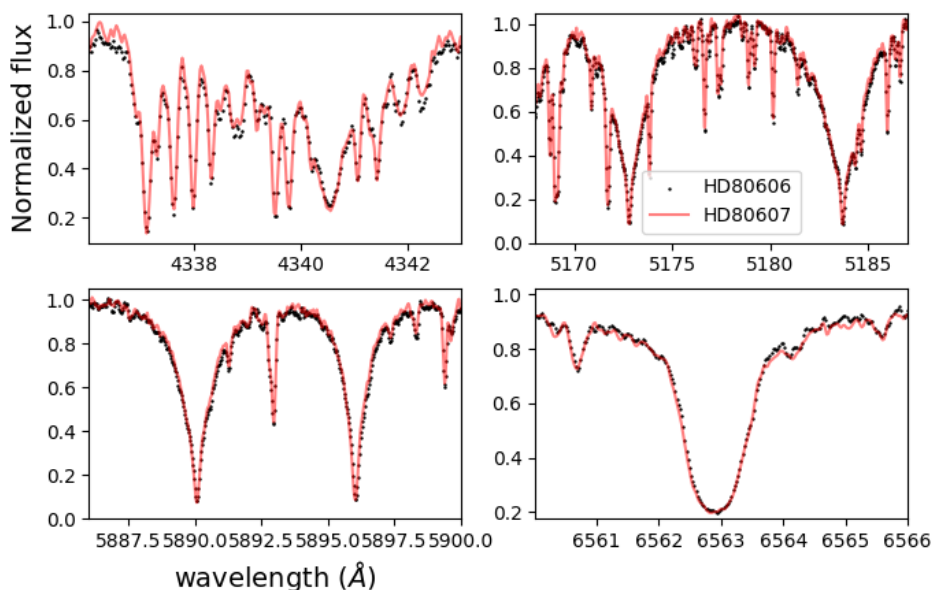


FIGURE 4.2: Overplotted different regions of the spectra of both the planet host star (HD80606) in black and companion star (HD80607) in red.

4.3 Determining stellar parameters

Initial parameter guesses for the stars are taken from Wang *et al.* (2019). We used clean Fe I and Fe II lines common to both the stars having equivalent widths below $200 \text{ m}\text{\AA}$ for the parameter estimation. Equivalent widths are measured interactively using the *Splot* package in IRAF by carefully taking the nearby continuum close to the clean absorption line. The required line lists are taken from VALD and Kurucz with updated oscillatory strength values (complete linelist is added to the Appendix Table 4.10 and Table 4.12 for both systems). We used Kurucz ATLAS9 NEWODF (Castelli and Kurucz 2003c), stellar atmospheric models, by Castelli and Kurucz (2003b) with plane parallel approximation and Local Thermodynamic Equilibrium (LTE) and Turbospectrum (Alvarez and Plez 1998b) spectrum synthesis code V19.1 (Plez 2012) for generating the synthetic spectra. The stellar parameters for the reference star are determined using the absolute excitation and ionization equilibrium for both Fe I and Fe II lines using Boltzmann and Saha's

equation by finding the combination of T_{eff} , $\log g$, and $[Fe/H]$ that simultaneously minimized the slopes. That is

- Absolute Fe abundance and the differential Fe abundance should be independent of the lower excitation potential. The slope should be minimum.
- Absolute Fe abundance and the differential Fe abundance should be independent of the reduced equivalent width.
- Absolute Fe I, Fe II abundance and the differential Fe I and Fe II abundance should be same.
- Input metallicity should match with the derived iron abundance.

Furthermore, stellar abundance for the object star is determined using the line-by-line differential excitation and ionization equilibrium with respect to the reference star. Figure 4.3 and Figure 4.4 represent the excitation and ionization balance for determining the effective temperature, $\log g$, and micro turbulent velocity of the stars. We have confirmed the calculated T_{eff} by overplotting the model with observed spectra in the $H\alpha$ region. The wings of the $H\alpha$ absorption line are sensitive to the T_{eff} of the star. Similarly, the $\log g$ of the stars is confirmed by overplotting the Mg region of the spectra. Our analysis shows that the effective temperature of both the binary stars differs by 37 K, and $\log g$ differs by 0.03 dex. The planet host star is metal-rich by a factor of 0.012 dex compared to the binary companion star. The final adopted stellar parameters for both the binary systems are given in Table 4.1 along with the parameters obtained from the literature.

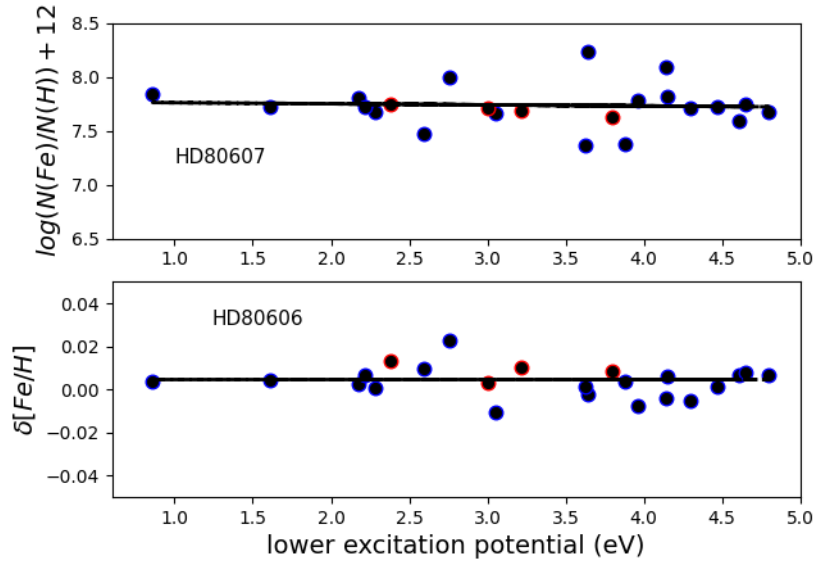


FIGURE 4.3: The top panel indicates the zero-slope model for abundance versus lower excitation potential for the companion star using the absolute method. The bottom panel represents the stellar parameters of the planet host star using differential equilibrium (Fe I lines in blue and Fe II lines in red dots) for HD 80606/HD80607.

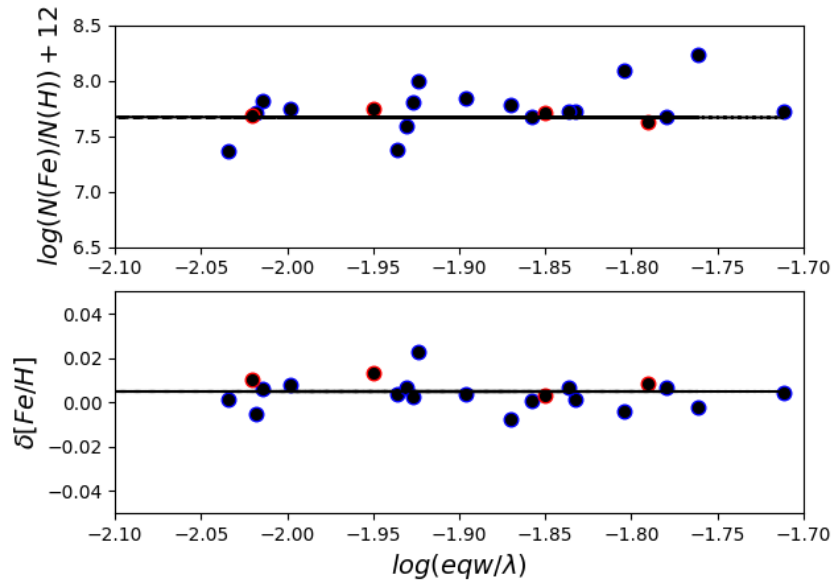


FIGURE 4.4: The top panel depicts the zero-slope model for abundance versus reduced equivalent width for the companion star using the absolute method. The bottom panel shows the stellar parameters of the planet host star using differential equilibrium (Fe I lines in blue and Fe II lines in red dots) for HD80606/HD80607.

TABLE 4.1: Estimated stellar parameters for HD 80606/HD 80607

Parameters	HD 80606	HD 80607	Reference
T_{eff} (K)	5613	5650	(this work)
T_{eff} (K)	5584	5506	Liu <i>et al.</i> (2018)
logg	4.43	4.4	(this work)
logg	4.4	4.38	Liu <i>et al.</i> (2018)
[Fe/H]	0.332	0.32	(this work)
[Fe/H]	0.316	0.303	Liu <i>et al.</i> (2018)
V_{turb} (Km/S)	1.0	1.38	(this work)

4.4 Deriving the abundances of all the elements

Once the stellar parameters are established, we derive the differential abundance of alpha elements and iron peak elements. We derived the abundance of C, O, Y, Zr, Ce, La, and Ba by synthesizing the absorption lines. The details are given in the Appendix 4.12. The elements and the differential abundance derived are presented in Table 4.2.

As we are doing a strictly differential abundance analysis, the uncertainty mainly comes from the signal-to-noise ratio at different wavelength regions of the spectra. The mean abundance difference of all elements between the planet host and the binary companion is 0.013 dex, with no elemental abundance differing by more than 0.019 dexes. Figure 4.5 indicates the differential abundance (The average abundance of each element in different ionization states) obtained for all the derived abundance for HD 80606/HD 80607 as a function of atomic number.

Figure 4.6 and Figure 4.7 depict the different absorption lines of both the stars in the system where one can justify the derived abundances.

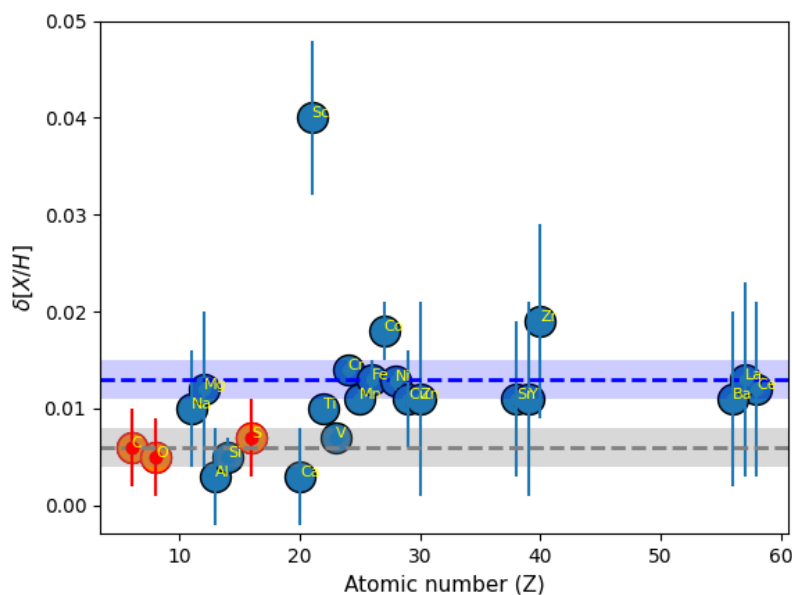


FIGURE 4.5: Differential abundance as a function of atomic number for HD 80606/HD 80607. The mean abundance and the error of volatile elements C, O, and S are presented in grey, and the mean abundance and the error of refractory elements are presented in blue.

4.5 Discussion

The main motive of this section is to understand the difference in the chemical abundance of the planet host star with respect to the binary companion and the possible connection with planet formation. As discussed in the introduction, [Meléndez *et al.* \(2009b\)](#) shows that the difference in the abundance derived for Sun with respect to other solar twin stars is correlated with the condensation temperature (T_c) [Lodders \(2003\)](#), which gives the 50% temperature at which the element starts to condense. That is, the refractory elements ($T_c \geq 900$ K) seem to be deficient in Sun compared to the volatile elements ($T_c < 900$ K), and they are suggesting that this could be connected with the presence of terrestrial planets in the solar system. However, [Önehag *et al.* \(2014\)](#) studied 14 stars in the open cluster M67 and suggested that this abundance difference observed in the Sun is mainly because of the dust-gas separation in the Inter-Stellar Medium (ISM) before

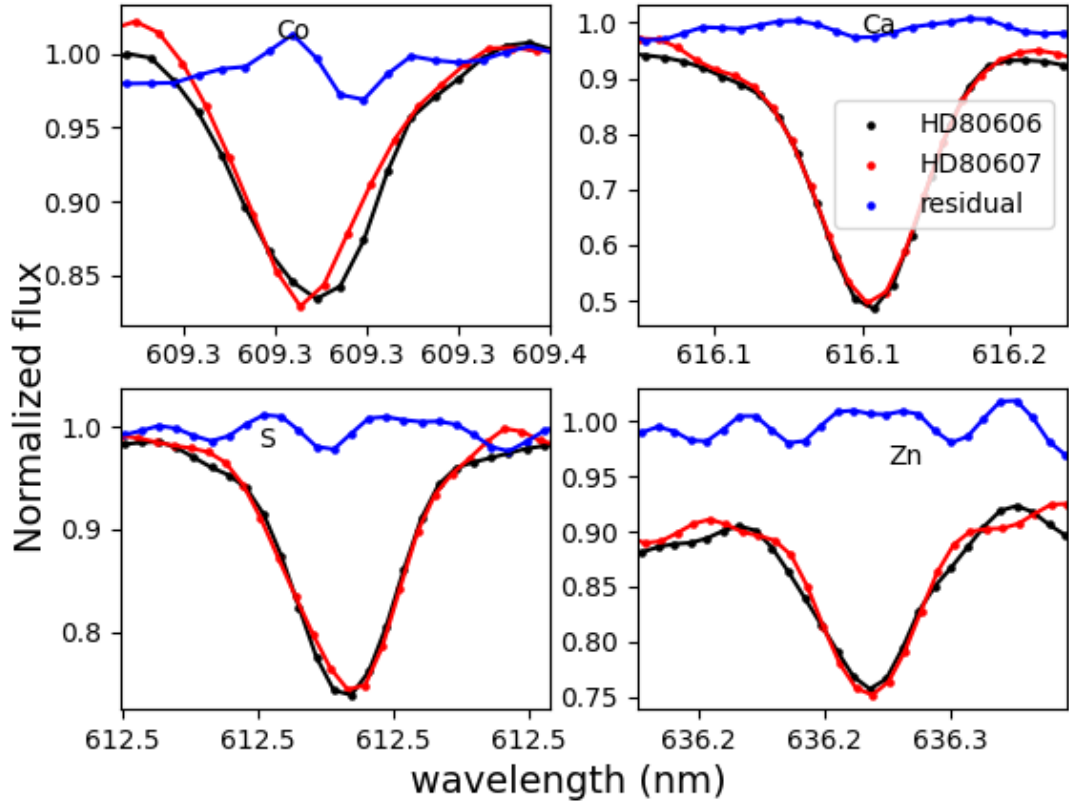


FIGURE 4.6: The absorption lines of Co, Ca, S, and Zn of HD 80606 (solid black line) overplotted with HD 80607 (solid red line). The blue line is the residual spectra.

the star formation takes place. Irrespective of the condensation temperature, the abundance of all the elements is enhanced in the planet host star compared to the field star, except the derived abundance of C, N, and O are the same within the errorbar (Figure 4.5).

Our analysis of $\Delta[X/H]$ as a function of T_c shows that the abundance of refractory elements is slightly higher than the volatile elements in the planet host star (HD 80606) compared to the binary companion (Figure 4.8). As the planet has a highly eccentric orbit, the enhanced refractory abundance can be explained by the rocky planet engulfment, also suggested by Mack *et al.* (2016). This work supports the results discussed in Chapter 3. The $\Delta[Fe/H] = 0.013$ for the planet host star can

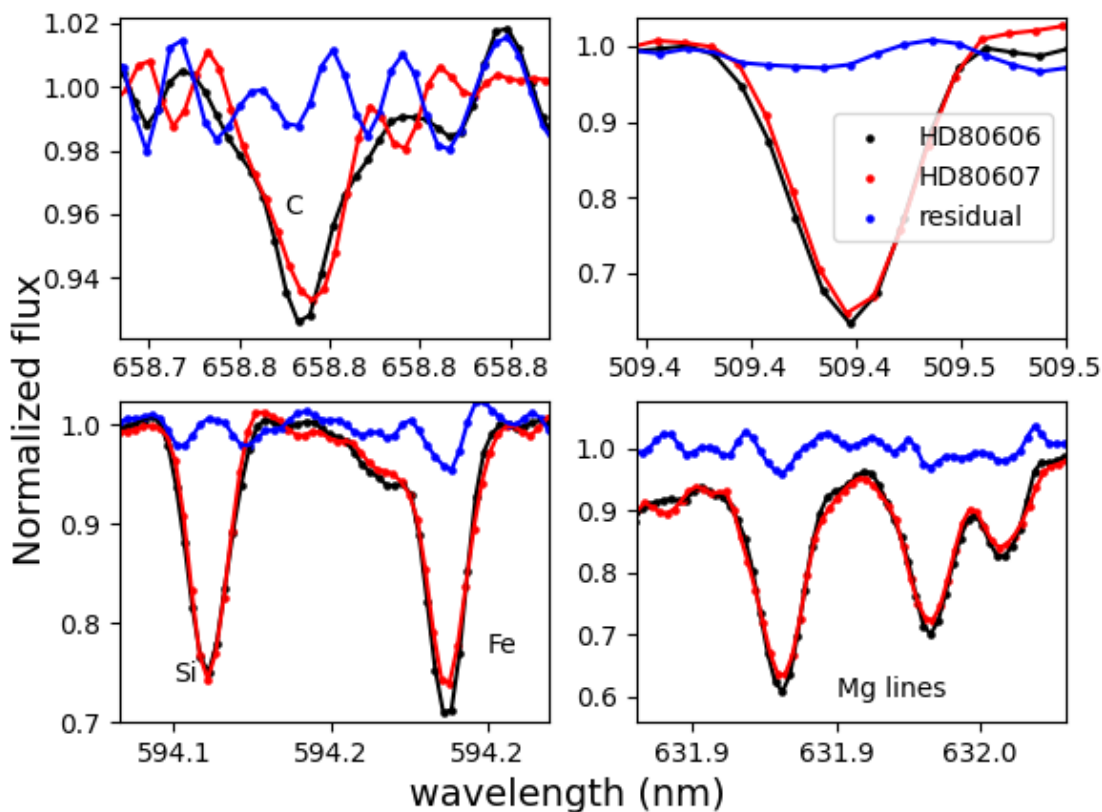


FIGURE 4.7: The absorption lines of C, Sc, Si, Fe, and Mg of HD 80606 (solid black line) overplotted with HD 80607 (solid red line). The blue line is the residual spectra.

unlikely explain the inhomogeneities in the initial cloud where both the stars are born. This leads to the conclusion by adding the previous works along with this study is (Liu *et al.* 2014; III *et al.* 2014; Liu *et al.* 2018), that the formation of (gas) giant planet does not necessarily imprint chemical signatures and the mass of a planet does not necessarily produce the corresponding scale of abundance differences. We cannot make a general statement based on the number of systems studied. However, we need more systems and observations to confirm it further.

We also tried the differential abundance analysis of HD 202772 A/ HD 202772 B using archival data obtained from HIRES (HIgh-Resolution Spectrograph)/Keck (Vogt *et al.* 1994a), observed by Wang *et al.* (2019) (Program ID: H241). The

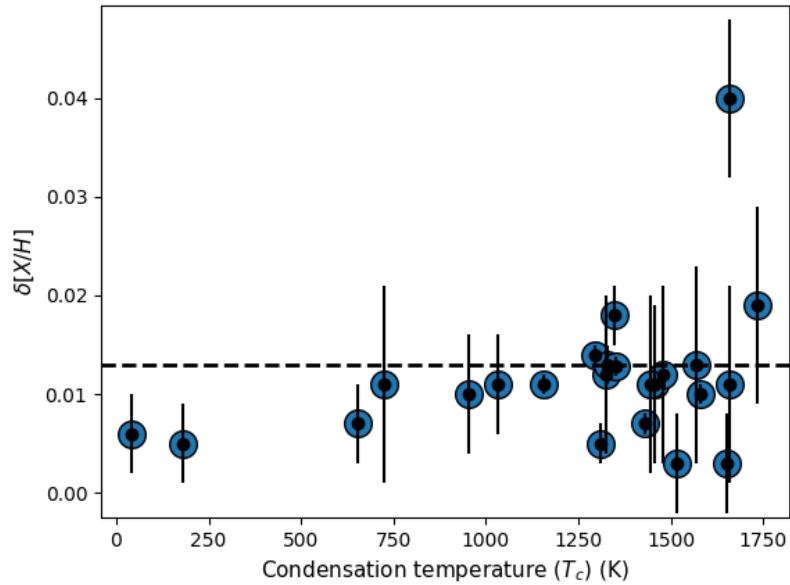


FIGURE 4.8: Condensation temperature as a function of differential abundance for HD 80606/HD 80607.

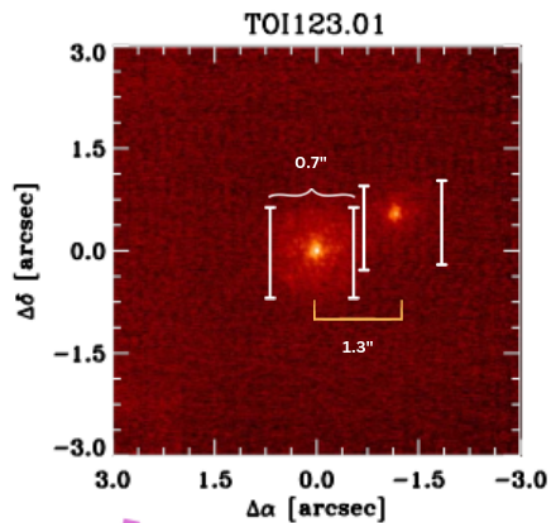


FIGURE 4.9: AO image from KECK/NIRC2 of the binary system. A companion is separated by 1.3'' (Wang *et al.* 2019). The entrance slit width of Keck/HIRES is 0.7''.

observation was carried out on 2018-09-24, with a single exposure of 54s and 164s each for HD 202772 A and HD 202772 B, respectively. The spectrograph covers wavelengths starting from 380-800 nm using three different CCDs with a spectral resolution of 65000 at 5500 Å. The separation between the stars is 1.3'',

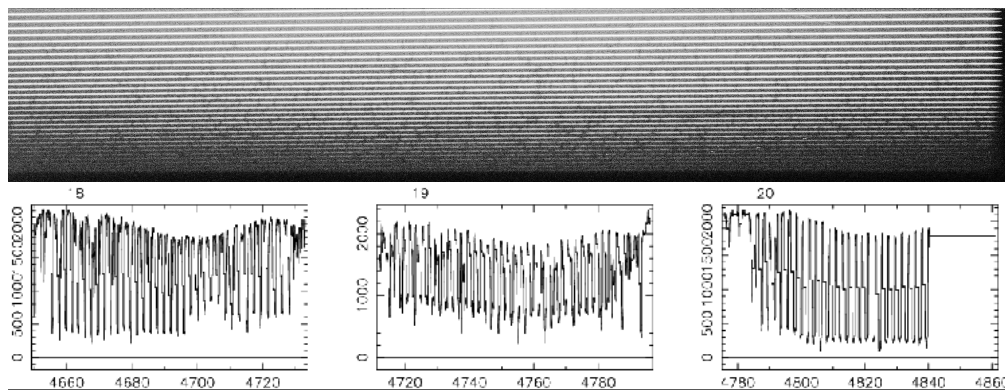


FIGURE 4.10: CCD1 raw image and extracted spectra from KECK/HIRES pipeline (MAKEE).

making (Figure 4.9) the observation difficult. The HIRES slit (slit width= $0.7''$) is aligned perpendicular to both the stars separately during observation to minimize contamination. The average seeing of the observing night was $0.7''$, and the data has a signal-to-noise ratio of 150 at 5000 \AA . We have noticed that the extracted data in the Keck archive had some issues, and the extracted data for the CCD3 was also unavailable. However, the 2D image of the raw data looks fine. For example, Figure 4.10 shows the raw CCD1 images and the corresponding extracted spectra of orders 18, 19, and 20. So we used the raw data for the analysis. Figure 4.11 indicates the normalized spectra of both the stars in the similar wavelength region shown in Figure 4.10. However, it looks like the strength of the spectral features of both stars is very different. However, by closely watching other wavelength regions, we could understand that the bluer part of the spectra (CCD1) is contaminated (Figure 4.12). We derived the stellar parameters of the stars, in the same way explained for HD 80606 system, excluding the absorption lines from CCD1.

Figure 4.13 and Figure 4.14 illustrate the excitation and ionization balance for Fe I and Fe II. And the best fit T_{eff} and $\log g$ are re-confirmed by overplotting the $H\alpha$ and Mg region of the spectra.

The derived stellar parameters and comparison with previous studies are presented in Table 4.3. The abundance of 17 elements is derived (Table 4.4), and the

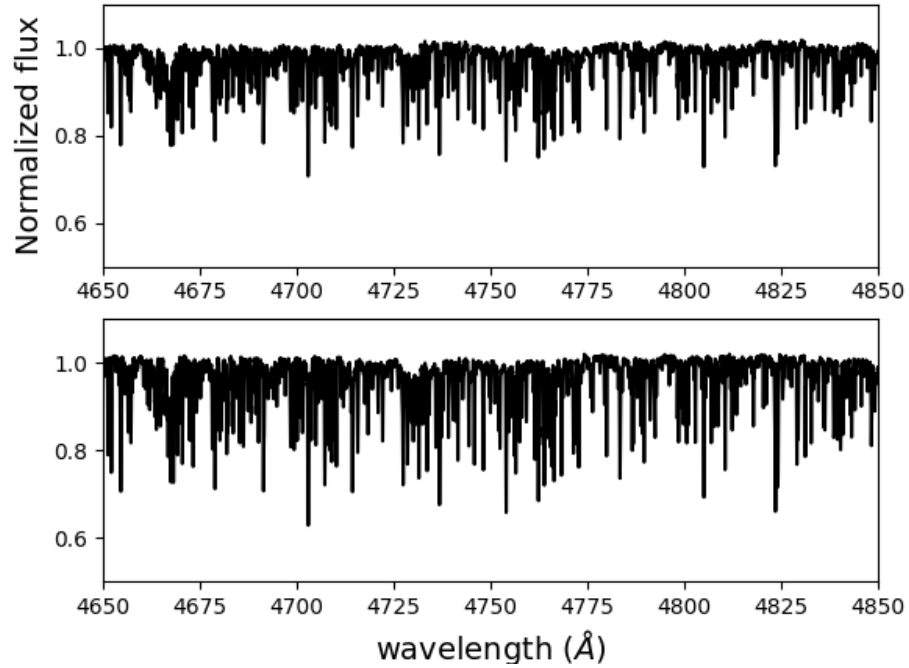


FIGURE 4.11: Normalized spectra of planet host star (HD 202772 A) and the binary companion star (HD 202772 B) in the wavelength range of 4500 Å- 4580 Å.

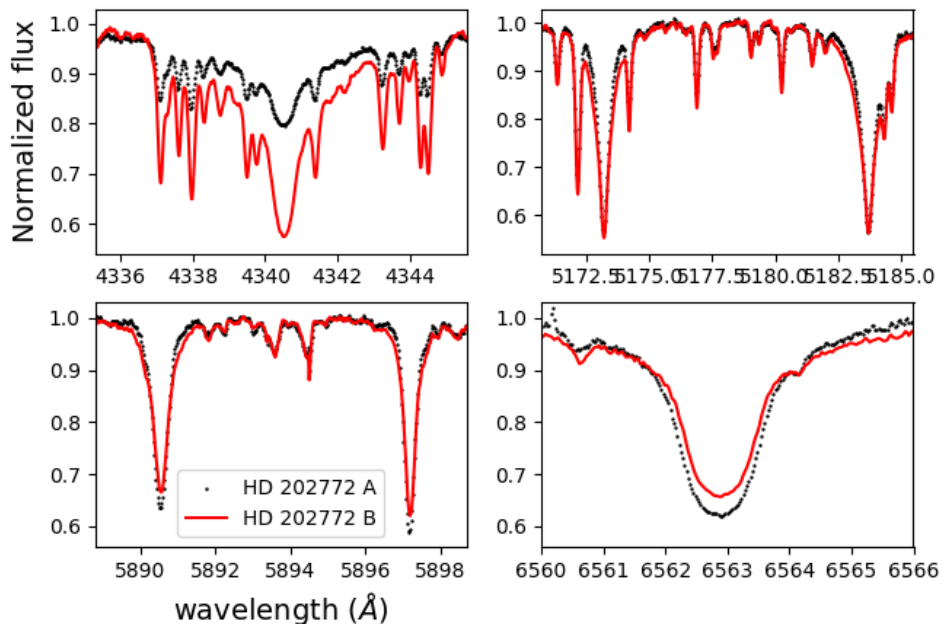


FIGURE 4.12: Figure indicates different regions of the spectra of both the planet host star HD202772 A (red) and HD202772 B (black).

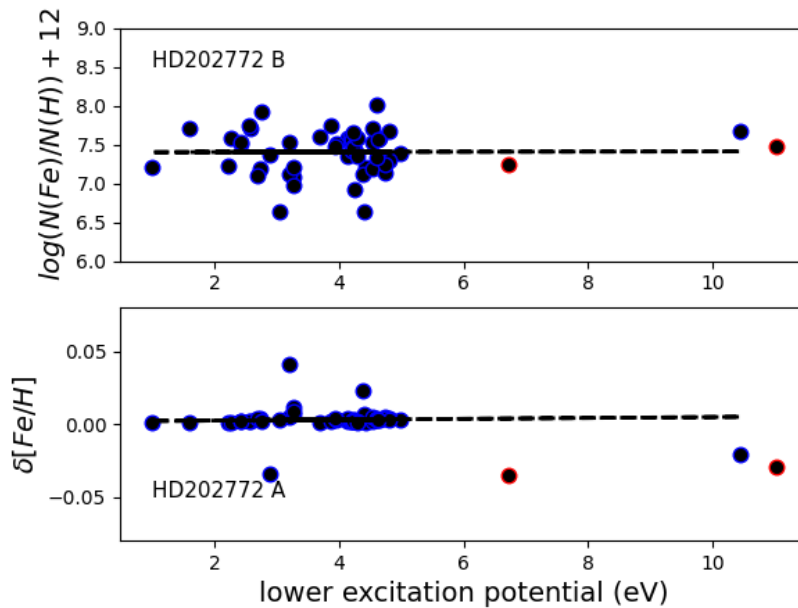


FIGURE 4.13: The top panel represents the best fit zero slope model for abundance as a function of lower excitation equilibrium for the companion star using the absolute method. The bottom panel shows the stellar parameters of the planet host star using differential equilibrium (Fe I lines in blue and Fe II lines in red dots) for HD202772A/B.

differential abundance of the planet host star is plotted against condensation temperature to check the possible correlation (Figure 4.15). Even if there is no trend of abundance difference and condensation temperature, the abundance of all the elements is enhanced in the planet host star. As we couldn't make any corrections for the contamination, the results are biased, and we need better observations for the system.

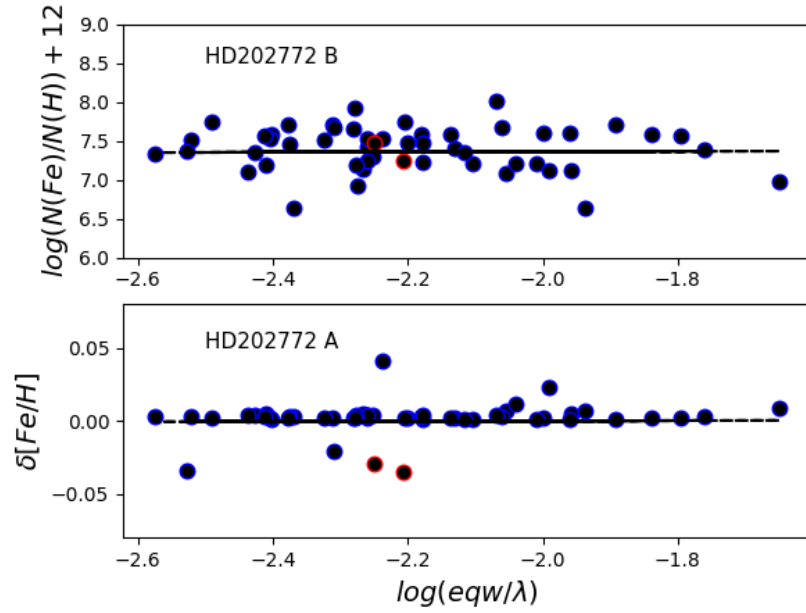


FIGURE 4.14: The top panel illustrates the best fit zero slope model for abundance as a function of reduced equivalent width for the companion star using the absolute method. The bottom panel shows the stellar parameters of the planet host star using differential equilibrium (Fe I lines in blue and Fe II lines in red dots) for HD 202772 A/B.

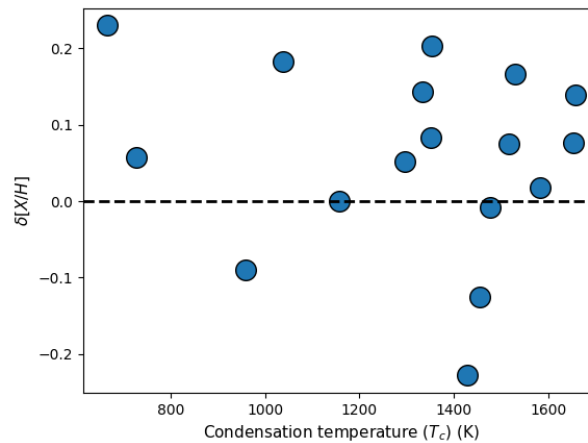


FIGURE 4.15: Condensation temperature as a function of differential abundance for HD 202772 A/B.

Appendix

TABLE 4.2: Differential abundance of HD80606/ HD80607.

Element	δ [X/H]
[C/H]	0.006
[O/H]	0.005
[Na/H]	0.01
[Mg/H]	0.012
[Al/H]	0.003
[Si/H]	0.005
[S/H]	0.007
[Ca/H]	0.003
[Sc/H]	0.04
[Ti/H]	0.01
[V/H]	0.007
[Cr/H]	0.014
[Mn/H]	0.011
[Fe/H]	0.013
[Co/H]	0.018
[Ni/H]	0.013
[Cu/H]	0.011
[Zn/H]	0.011
[Sr/H]	0.011
[Y/H]	0.011
[Zr/H]	0.019
[Ce/H]	0.012
[Ba/H]	0.011
[La/H]	0.013

TABLE 4.3: Estimated stellar parameters fo HD 202772A/B

Paramters	HD 202772 A	HD 202772 B	Reference
T_{eff} (K)	6955 ± 10	6950	(this work)
T_{eff} (K)	6330	6156	Wang et al. (2019)
logg	4.24 ± 0.01	4.24	(this work)
logg	4.03	4.24	Wang et al. (2019)
$[Fe/H]$	7.402	7.400	(this work)
$[Fe/H]$	0.29	0.25	Wang et al. (2019)
V_{turb} (Km/S)	1.0	1.0	(this work)

TABLE 4.4: Differential abundance of HD202772 A/B

Element	δ [X/H]
[Na/H]	-0.090
[Al/H]	0.075
[Si/H]	0.166
[S/H]	0.230
[Ca/H]	0.074
[Sc/H]	0.138
[Ti/H]	0.017
[V/H]	-0.228
[Cr/H]	0.051
[Mn/H]	0.000
[Fe/H]	0.142
[Co/H]	0.082
[Ni/H]	0.203
[Cu/H]	0.183
[Zn/H]	0.057
[Ce/H]	-0.008
[Ba/H]	-0.125

TABLE 4.5: The complete linelist used for the analysis HD 202772A/B. The Wavelength, element, and equivalent width of both stars are represented in each column.

wavelength (\AA)	Element	Eqw(HD 202772 A) (m\AA)	Eqw(HD 202772 B) (m\AA)
4497.7	Na1	14.4	21.5
6696	Al1	27	28.3
6698.7	Al1	9.8	11.2
5690.4	Si1	29.8	25.6
5772.1	Si1	36.9	36.6
6555.5	Si1	24.4	22.7
6721.8	Si1	34.8	31.3
6748.8	S1	35.5	26.5
6757.2	S1	33.7	19.6
4425.4	Ca1	38.7	69.6
4578.6	Ca1	34.9	48.6
4685.3	Ca1	34	37.1
5582	Ca1	55.4	49.5
5590.1	Ca1	58.8	49.6
5601.3	Ca1	65.5	56.5
6717.7	Ca1	74.8	64.7
5239.8	Sc2	49.1	39.9
5669	Sc2	45.2	30.7
6604.6	Sc2	35.2	24.6
4449.1	Ti1	25.2	38.1
4512.7	Ti1	20	34.2
4758.1	Ti1	14.3	18.8
4759.3	Ti1	16.1	20
4820.4	Ti1	16.6	19.2
4411.9	Ti2	25.2	42.6
4417.7	Ti2	40.8	73.1
4418.3	Ti2	30.2	55.4
4443.8	Ti2	56.9	97.4
4468.5	Ti2	60	97.8
4493.5	Ti2	20.2	35

TABLE 4.6: The complete linelist used for the analysis (HD 202772A/B) (continue)

wavelength (\AA)	Element	Eqw(HD 202772 A)	Eqw(HD 202772 B)
4544	Ti2	26	38
4590	Ti2	46.3	59.9
5185.9	Ti2	52	40.8
5188.7	Ti2	111.5	102.8
5336.8	Ti2	61.7	48.7
5418.8	Ti2	43.5	33.9
4379.2	V1	26.9	50.1
4406.6	V1	16.7	35.8
4511.9	Cr I	13.1	20.3
4545.9	Cr I	28.3	39.9
4591.4	Cr I	33.8	48.6
4651.3	Cr I	31.8	39.9
4652.2	Cr I	38.2	48.9
4689.4	Cr I	25.2	34.2
4718.4	Cr I	23.2	29.7
5225	Cr I	33.6	38
5296.7	Cr I	41.9	41.9
5297.4	Cr I	42	41.9
5329.1	Cr I	35.6	35.2
5348.3	Cr I	45.7	44.2
4558.6	Cr II	55.8	72.9
4634.1	Cr II	42.9	53.1
4848.2	Cr II	37.8	38.4
5237.3	Cr II	52	40.3
5305.9	Cr II	29.3	22.7
5308.4	Cr II	30.4	21.3
5334.9	Cr II	34.9	23.5
4502.2	Mn I	18.6	25.9
4709.7	Mn I	24.7	31.1
4739.1	Mn I	24.6	31.4
4754	Mn I	55.5	66.6

TABLE 4.7: The complete linelist used for the analysis (HD 202772A/B) (continue)

wavelength (\AA)	Element	Eqw(HD 202772 A)	Eqw(HD 202772 B)
4348.9	Fe I	12.9	27.5
4365.9	Fe I	10.7	23.1
4376.8	Fe I	8.5	19.9
4389.2	Fe I	15.9	31.1
4433.2	Fe I	27.3	54.6
4438.3	Fe I	16.8	30.3
4445.5	Fe I	6.7	12.9
4484.2	Fe I	24.4	42.3
4485.7	Fe I	20.2	36.1
4504.8	Fe I	16.2	27.7
4574.2	Fe I	11.4	16.7
4625	Fe I	39.5	51.9
4630.1	Fe I	29.1	40
4683.6	Fe I	20.4	28.4
4690.1	Fe I	24.7	34
4700.2	Fe I	24.4	32.2
4704.9	Fe I	26.5	31.4
4705.5	Fe I	13.6	18.2
4733.6	Fe I	36.9	44
4741.1	Fe I	26.8	35.5
4741.5	Fe I	33.9	39.6
4745.8	Fe I	36.3	43.2
4757.6	Fe I	24.7	29.7
4787.8	Fe I	12.9	16.5
4788.8	Fe I	21.2	26.1
4807.7	Fe I	20.9	27.7
4834.5	Fe I	13.5	16
4845.6	Fe I	15.5	17.9
5159.1	Fe I	44.2	38.1

TABLE 4.8: The complete linelist used for the analysis (HD 202772A/B) (continue)

wavelength (\AA)	Element	Eqw(HD 202772 A)	Eqw(HD 202772 B)
5162.3	Fe I	81.7	75
5187.9	Fe I	26.7	27.6
5196.1	Fe I	36.9	34.5
5198.7	Fe I	48	45.9
5215.2	Fe I	62.2	57.5
5217.4	Fe I	55.3	52.3
5236.2	Fe I	20.5	22.4
5281.8	Fe I	55.6	48.2
5302.3	Fe I	76.2	67.9
5307.4	Fe I	57.7	51.9
5321.1	Fe I	20.8	21.1
5322	Fe I	30.4	30.8
5324.2	Fe I	107.4	119.6
5339.9	Fe I	61.6	61.8
5367.5	Fe I	58.4	54.8
5415.2	Fe I	90.1	86.7
5472.7	Fe I	19.8	20.5
5473.9	Fe I	43.8	43.1
5506.8	Fe I	71	60.4
5543.1	Fe I	38.2	35
5543.9	Fe I	35.2	30.5
5586.8	Fe I	92.3	97.2
5618.6	Fe I	24.8	23.7
5633.9	Fe I	40	37.2
5638.3	Fe I	42.9	41.1
5679.0	Fe I	33.1	29.7
5691.5	Fe I	20.8	18.4
5775.1	Fe I	30.1	31.7

TABLE 4.9: The complete linelist used for the analysis (HD 202772A/B) (continue)

wavelength (\AA)	Element	Eqw(HD 202772 A)	Eqw(HD 202772 B)
5809.2	Fe I	25.2	24.3
5816.4	Fe I	47.6	44.4
5852.2	Fe I	21.5	22.7
5856.1	Fe I	15.6	17.6
5859.6	Fe I	43.3	38.8
5883.8	Fe I	31.3	31.8
5976.8	Fe I	38.7	33.5
5984.8	Fe I	38.4	32.8i
5987.1	Fe I	31.3	29.2
6569.2	Fe I	38.9	34.8
6575	Fe I	37	31.2
6592.9	Fe I	69	57.2
6593.9	Fe I	46.4	41.1
6597.6	Fe I	23.9	24.1
6609.1	Fe I	37.6	34.7
6678	Fe I	64	57
6703.6	Fe I	16.9	17.8
6705.1	Fe I	28.1	26.4
6726.7	Fe I	26.7	26
6750.2	Fe I	37.6	33.1

TABLE 4.10: The complete linelist used for the analysis (HD 202772A/B) (continue)

wavelength (\AA)	Element	Eqw(HD 202772 A)	Eqw(HD 202772 B)
6810.3	Fe I	25.9	25.9
6752.7	Fe I	18.5	20
4491.4	Fe II	42	59.9
4508.3	Fe II	50.3	74.9
4515.3	Fe II	53.2	80.9
4576.3	Fe II	41.7	56.3
4620.5	Fe II	36.6	43.6
5234.6	Fe II	76.3	55.8
5256.9	Fe II	25.2	19.7
5325.6	Fe II	44.2	33.1
5425.3	Fe II	38.9	30.5
4813.5	Co I	16.1	20.3
5342.7	Co I	9.5	17.1
4732.5	Ni I	29	22.6
4754.8	Ni I	20.6	26.3
4807	Ni I	29.8	32.3
6643.6	Ni I	45.1	38.9
6767.8	Ni I	39.8	37
6772.3	Ni I	25.1	22.7
4831.2	Ni I	38.3	44.4
4852.5	Ni I	12.1	14.9
5578.7	Ni I	28.2	26.3
5593.7	Ni I	20.5	22.6
5105.5	Cu I	34.5	38.6
4722.2	Zn I	27.8	33.3
4810.5	Zn I	44.6	49.5
4554	Ba II	71.8	99.8
4628.2	Ce II	9.3 1	3.7
4562.4	Ce II	12.5	17.3

TABLE 4.11: The complete linelist used for the analysis (HD 80606/HD80607). The Wavelength (\AA), element, and equivalent width ($\text{m}\text{\AA}$) of both stars are represented in each column.

wavelength (\AA)	Element	Eqw(HD80606)	Eqw(HD80607)
6154.25	Na 1	57.23	54.98
5711.10	Mg 1	58.12	55.21
6696.0	Al 1	45.43	42.21
6125.021	Si1	48.10	53.40
6166.43	Ca 1	92.8	90.90
6455.598	Ca1	80.1	79.50
5526.790	Sc 2	86.00	84.1
4758.118	Ti 1	57.40	55.90
5219.702	Ti 1	58.70	57.50
5336.771	Ti 2	77.80	80.70
4428.504	V1	91.70	93.90
4577.174	V1	81.00	71.1
6090.214	V1	68.80	64.3
6330.093	Cr1	55.30	51.3
5334.946	Cr 2	44.30	44.50
4257.669	Mn I	78.60	75.40
4457.04	Mn 1	60.2	62.70
4243.816	Fe 1	48.90	47.4
4360.803	Fe 1	74.00	76.7
4439.634	Fe 1	30.30	34.60
4439.881	Fe 1	62.10	61.30
4602.001	Fe 1	89.40	87.50
5187.914	Fe 1	79.90	84.10

TABLE 4.12: The complete linelist used for the analysis (HD 80606/HD80607) (continue)

wavelength (\AA)	Element	Eqw(HD80606)	Eqw(HD80607)
5223.185	Fe 1	48.20	47.40
5373.709	Fe 1	77.70	78.20
5386.334	Fe 1	52.20	48.70
5705.465	Fe 1	54.20	57.60
5848.123	Fe 1	67.60	64.20
5883.817	Fe 1	79.30	84.40
5956.694	Fe 1	75.70	74.0
6005.543	Fe 1	43.40	37.7
6078.491	Fe 1	99.00	95.40
6079.009	Fe 1	61.10	56.6
6085.259	Fe 1	72.50	60.83
6151.618	Fe 1	73.90	71.40
6173.336	Fe 1	87.40	86.56
5234.625	Fe2	83.20	84.50
5094.406	Ni1	47.20	44.80
5103.029	Ni1	74.80	72.5
6186.709	Ni1	55.00	52.10
6327.593	Ni1	68.80	65.20
5700.20	Cu 1	47.78	45.2
5218.20	Cu 1	76.7	72.0
6141.56	Zr1	60.0	72.5
6496.90	Ba 2	45.56	48.0
6141.20	Ba 2	58.6	55.0

Chapter 5

Transit Spectrophotometry of Hot Jupiters Using 2m Himalayan Chandra Telescope

Abstract

In this chapter, we present transmission spectrophotometry of three hot Jupiters with the 2m Himalayan Chandra Telescope (HCT) covering the entire optical and up to 900nm region. We choose targets with suitable reference stars for accurately tracking slit losses, even for long cadence observations, to reach the required signal-to-noise ratio. Typical individual exposures are between 300-500s over 5-6 hours covering a transit. We use common mode rejection (CMR) technique using a white light transit curve. We obtain complete transit for three stars, HAT-P-1,

KELT-18, and WASP-127, that host a giant planet. We confirm NaD detection and Rayleigh slope in the blue for WASP-127b. In addition, we detect a feature near 4227Å in HAT-P-1b, and, for the first time, we present a low-resolution transmission spectrum for KELT-18b that shows a flat spectrum.

5.1 Introduction

Exoplanet transit spectroscopy using low spectral resolution observations is constructed by taking time series of spectrophotometric observations during the planet transit and measuring the transit depth as a function of different wavelength bins. The wavelength-dependent transit depth can probe the chemical composition of the exoplanet atmosphere (Seager and Sasselov 2000; Brown 2001). Early low-resolution transit spectroscopic observations were from space-based telescopes, which are free from Earth’s telluric features (Charbonneau *et al.* 2002a; Bean *et al.* 2010; Snellen *et al.* 2010; Sing *et al.* 2016). Ground-based multi-object (Bean *et al.* 2010; Bean *et al.* 2011; Gibson *et al.* 2013; Stevenson *et al.* 2014; Nikolov *et al.* 2016; Rackham *et al.* 2017; Espinoza *et al.* 2019; Todorov *et al.* 2019; Wilson *et al.* 2020; Panwar *et al.* 2022) and long-slit spectrophotometric observations (Sing *et al.* 2012; Nortmann *et al.* 2016; Palle *et al.* 2017; Murgas *et al.* 2019) enabled accurate differential spectrophotometry by simultaneously observing a reference star to track variable slit loss during transit. Features due to alkali elements such as NaD (589 nm) and K I (767 nm) doublets are detected in the visible wavelength region (Brown 2001; Seager and Sasselov 2000) among hot Jupiters. Other features in the visible wavelengths are a steep slope in the blue due to Rayleigh scattering of aerosols and absorption due to TiO and VO (Tennyson and Yurchenko 2012). Observations from different instruments or repeated observations for the same planet over multiple transits have sometimes revealed different results, and stellar disk inhomogeneity could be a possible cause (Rackham *et al.* 2018).

Here we present transit spectrophotometric observations for the first time using the 2m Himalayan Chandra Telescope for three hot Jupiters. The ground-based transit spectrophotometric observations suffer from contamination of telluric lines and variable slit losses, which are comparable to the amplitude of variations due to the planetary atmosphere itself. Simultaneous multi-object observation can minimize these errors. That is, by simultaneously observing the target star and a reference star in the field of view and doing differential spectrophotometry with respect to the reference star. Differential photometric corrections work well when the brightness and spectral type of the comparison stars are similar to the target stars (Nascimbeni *et al.* 2013). Out of the three targets presented here, HAT-P-1b (Todorov *et al.* 2019) and WASP-127b (Lam *et al.* 2017; Palle *et al.* 2017) were already studied using low-resolution spectrophotometry; however, low-resolution transit spectroscopy for KELT-18b is performed for the first time in this work.

5.2 Observations and analysis

Observations are obtained from the Indian Astronomical Observatory (IAO) at Hanle, the Ladakh region of the Himalayas, operated by the Indian Institute of Astrophysics. We use the Faint Object Spectrograph Camera (HFOSC) mounted on the 2m Himalayan Chandra Telescope. HFOSC is a low-resolution slit spectrograph uses different gratings and slits of different widths and lengths. The instrument configuration allows coverage of 350-1000nm and spectral resolution of $R=150-4500$ (refer Chapter 2.3). We used grism-8 and grism-7 to cover the wavelength range from 3800 - 6500 Å and 5800 - 8350 Å, which provides a resolution of 1300-2100 for a narrow slit width. So, in a given transit, we only use one of the grism settings; hence the entire optical wavelength range is not covered simultaneously. We use the longest and widest slit available 11' X 15.41" to minimize the slit loss and maximize the FOV to allow suitable reference target stars. We

performed differential spectrophotometry with HFOSC. The slit had to be aligned in the direction connecting the two objects to observe the target and a reference star simultaneously. HFOSC does not have an atmospheric dispersion corrector, and we need to align the slit along the position angle connecting the star and reference instead of the parallactic angle. To minimize differential slit loss between the target and reference due to atmospheric dispersion, we selected targets with a reference star nearby with a similar spectral type, ideally a well-separated visual binary stellar twin. We selected targets based on the following criteria to be suitable for observations with 2m HCT and HFOSC.

- Due to the required sensitivity of detection with a 2m class telescope, we limited targets to $V_{mag} \leq 12.0$ and planetary system with large transit depth 0.04 %. A magnitude limit of 12 gives S/N greater than 1000 per wavelength sampling (at the grating blaze peak) for an exposure of 15min for a seeing of 2 arcsec.
- Planetary system with a short orbital period of a few days and transit duration of a few hours are chosen. This will enable coverage of the full transit light curve on the same night, including the ingress and egress. A full transit curve allows using a white light curve for common mode correction (discussed in section 5.3.1). A shorter orbital period allows multiple transits to observe in the thesis project duration.
- Finding a suitable reference star is also important, as discussed earlier, to minimize differential slit loss between target and reference due to atmospheric dispersion, seeing, and other environment and instrument effects. A suitable reference star should have a similar T_{eff} and brightness as that of the target star. The separation between the target and reference star should not exceed $11'$ because the longest slit available for the instrument is $(5'' \times 11')$.

TABLE 5.1: **Observational details:** Name of the object, Date of Observation, Signal to Noise Ratio, Exposure time, Parallactic angle, and airmass at the beginning and end of the observation are listed.

Object	DoO	SNR	Exp.time	No.Exp	parallactic angle	airmass
WASP-127	09 – 03 – 2019	909	420s	62	339.19	1.99-1.99
HAT-P-1 A	02 – 07 – 2018	344	180s	57	272.45	1.55-1.02
KELT-18	10 – 06 – 2019	1075	420s	55	125.34	1.15-1.74

During observation, we aligned the target star and the reference star along the slit by changing the position angle of the instrument cube in the Cassegrain unit so that simultaneous observations of the target and reference are possible. Differential spectrophotometry with respect to the reference star can minimize errors due to seeing variations, telluric contribution, and the possible instrumental shift during the observation. Here we present transit observations of three objects. Among them, HAT-P-1 is a visual binary with a twin companion. HAT-P-1A hosts a Jupiter sized planet with $R_p = 1.2R_J$ and $M_p = 0.52M_J$ (Bonomo *et al.* 2017). WASP-127 is also a part of a binary system and hosts a planet with $R_p = 1.37R_J$ and $M_p = 0.18M_J$ (Lam *et al.* 2017). Out of three objects, KELT-18 is a single-star hosting a massive planet of $R_p = 1.57R_J$ and $M_p = 1.18M_J$ (McLeod *et al.* 2017). In the case of HAT-P-1 and WASP-127, we used the binary companion star as the reference star, and for KELT-18, we used the nearby bright field star as a reference star. The observational details and object details are given in Table 5.1 and Table 5.2.

TABLE 5.2: **Stellar parameters:** Name of the object, Visual magnitude, Effective temperature, the logarithm of gravity, and metallicity and separation between the object star and the reference star are given below.

Object	Vmag	T_{eff}	$\log(g)$	[Fe/H]	Separation
WASP-127	10.20	5750 ± 100	3.90 ± 0.1	-0.18 ± 0.06	41.8''
TYC 4916-897-1	11.0	5733	4.480	...	
HAT-P-1 A	10.4	6047 ± 56	4.13 ± 0.10	0.12 ± 0.05	11.2''
HAT-P-1 B	9.87	5975 ± 45	4.45 ± 0.06	0.13 ± 0.02	
KELT-18	10.4	6670 ± 120	4.034 ± 0.083	0.08 ± 0.13	5.79'
TYC 3865-1339-1	9.92	6787	3.976	...	

5.3 Data reduction

Figure 5.2 represents the image of the target and the reference star, and Figure 5.3 indicates the 2D image of the spectra for all three objects. Initial data reduction was carried out using the IRAF, which includes bias correction, flat fielding, and aperture extraction. Wavelength calibration was done using the calibration lamp exposure taken at the beginning and end of the transit observations. A detail of data reduction is presented in Chapter 2, section 6.3). Since the on-sky observations were taken continuously (without wavelength calibration) for several hours, a wavelength drift of the spectra is expected due to instrument flexure, temperature changes, or other possible reasons. So we applied possible wavelength shifts using the telluric lines for each exposure (The wavelength shift from first to last exposure of for HAT-P-1, KELT-18, and WASP-127 was 2.7 Å, 2.1 Å, 1.8 Å, respectively). Figure 5.4 represents the wavelength-calibrated spectra of the target star and reference from the same exposure.

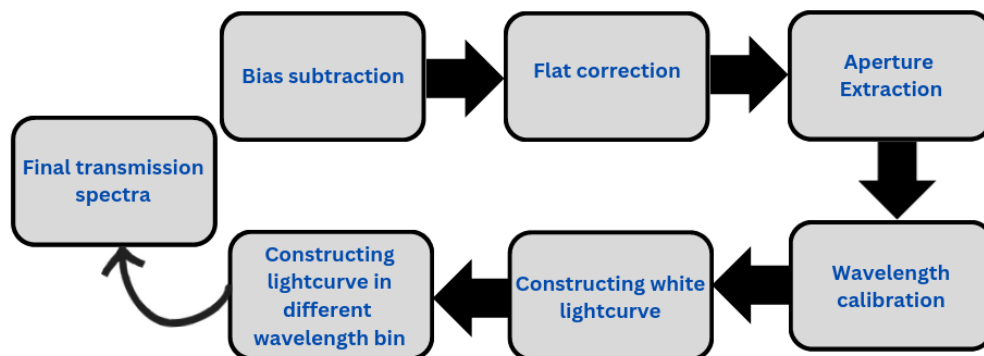


FIGURE 5.1: The figure depicts the schematic diagram explaining the steps included in the data analysis for low-resolution transmission spectroscopy.



FIGURE 5.2: The figure shows the object and reference stars (connected with a red line in the figure) selected for the observation. Images from left to right are HAT-P-1, WASP-127, and KELT-18. (Image credit: *Aladin*)

5.3.1 Constructing light curve

A transit white light curve was constructed for the target and the reference star by integrating the entire spectra, and a differential light curve with respect to the reference star was derived. We avoided the dominant telluric line region while constructing the white light curve. The best fit model to the lightcurve was obtained using the open source code *PyLightcurve** (Tsiaras *et al.* 2016). The primary input to the code is the normalized flux in the defined wavelength region, the mean error of the flux, and the observation time. The model will take care of a quadratic limb darkening correction and provide a best-fit model with all the transit parameters. Figure 5.5 shows the white lightcurve for HAT-P-1b, WASP-127 b, and KELT-18

*Light curve fitting open source code by University College London team.

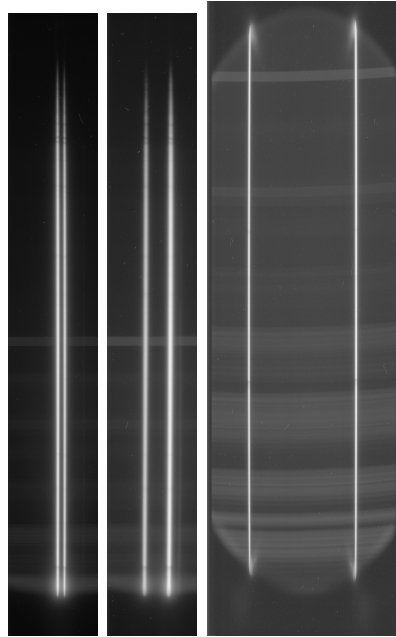


FIGURE 5.3: CCD images of HAT-P-1, WASP-127, and KELT-18, along with the reference star from left to right observed using HCT/HFOSC single exposure.

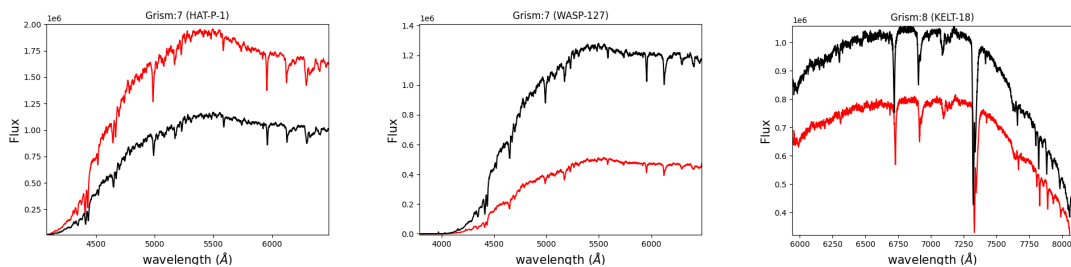


FIGURE 5.4: Single exposure, wavelength calibrated spectra of HAT-P-1 (Grism 7), WASP-127 (Grism 7), and KELT-18 (Grism 8) from left to right. The solid black line is the object star, and the solid red line is the reference star.

b, along with the best fit model. Table 5.3 compares the transit depth measured from the observed white lightcurve and the literature. And they both are in good agreement with each other.

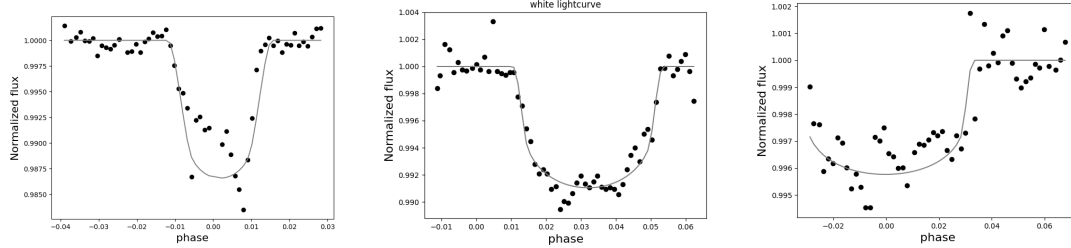


FIGURE 5.5: Observed white lightcurve of HAT-P-1b, WASP-127 b, and KELT-18 b from left to right with the best fit model.

TABLE 5.3: Comparison of observed transit depth from the white lightcurve and from literature.

Object	R_p/R_* (obs)	R_p/R_* (liter)
WASP-127	$0.085^{+0.006}_{-0.004}$	0.09992 ± 0.0018
HAT-P-1 A	$0.105^{+0.006}_{-0.006}$	0.11238 ± 0.0001
KELT-18	$0.041^{+0.008}_{-0.002}$	0.08462 ± 0.0009

5.3.2 Constructing low-resolution transmission spectra

Figure 5.6 illustrates the major steps included in the lightcurve analysis. We applied the Common Mode Correction technique (Wilson *et al.* 2020) to remove dominant time-dependent systematics. Using common mode correction, we lose information on the absolute value of transit depths and obtain relative transit depths (Wilson *et al.* 2020). We divided the data into equal wavelength bins of 150 \AA . Then the white lightcurve residual is divided from each wavelength channel to construct the lightcurve. This approach will avoid the majority of the time-dependent scatter in the lightcurve. The light curve is further smoothed using a Kalman filter to reduce high-frequency variations in the lightcurve. We find that doing common-mode correction followed by the Kalman filter before fitting the lightcurves improved the precision of measured transit depths in all the wavelength channels. Figure 5.7, Figure 5.8, Figure 5.9, and Figure 5.10

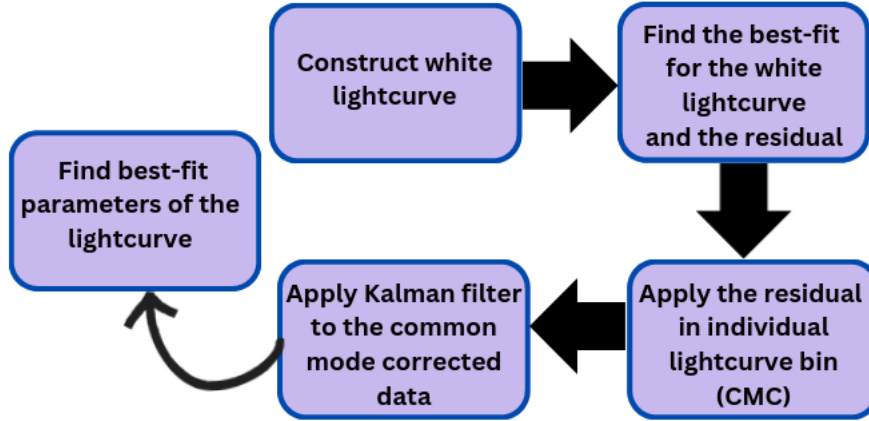


FIGURE 5.6: The figure indicates the schematic diagram explaining the steps included in the lightcurve analysis.

demonstrate the technique used for a lightcurve in a single wavelength channel of WASP-127.

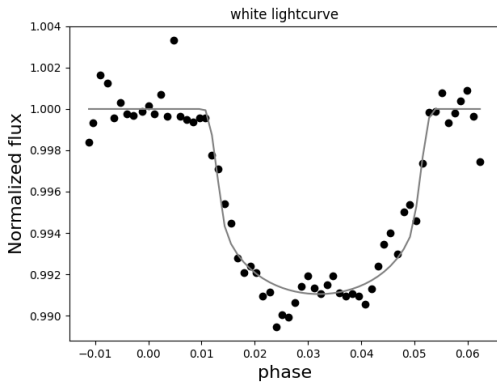


FIGURE 5.7: Observed white lightcurve (scattered point) of WASP-127 with the best fit model (solid line).

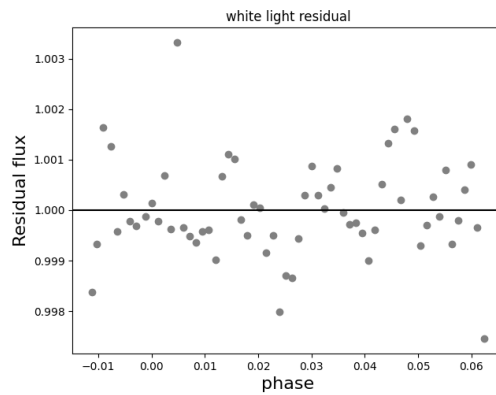


FIGURE 5.8: Residual plot from the Figure 5.7

And Figure 5.11, Figure 5.12, and Figure 5.13 demonstrate the lightcurve at different wavelength bins for three objects after applying all the corrections.

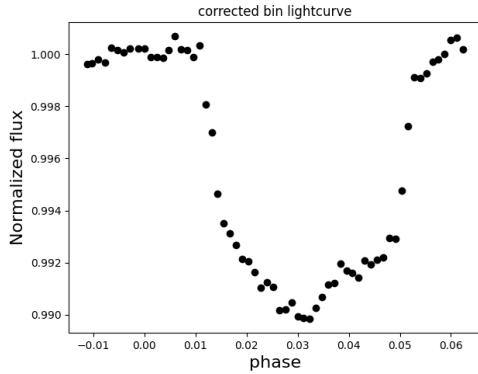


FIGURE 5.9: Lightcurve in a wavelength bin of WASP-127 after common mode correction.

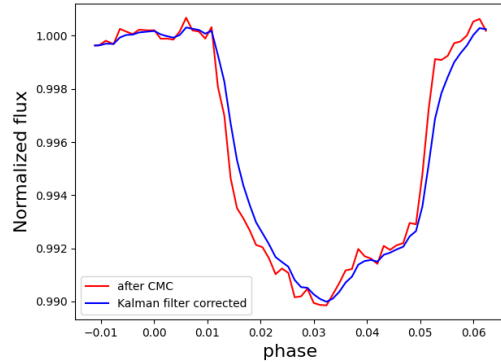


FIGURE 5.10: Lightcurve before (red) and after (blue) applying Kalman filter

5.4 Result and Discussion

The low-resolution transmission spectra are finally constructed using the best-fit transit depth from each wavelength bin. We used the open source code *Exotransmit* (Kempton *et al.* 2017) to interpret the observed exoplanet atmosphere. *Exotransmit* is a forward isothermal model that uses various atmospheric compositions and weather conditions for generating atmospheric models. We have tried different chemical compositions with or without Na, K, TiO, and VO, and clear, hazy, or cloudy weather conditions were considered. Figure 5.14, Figure 5.15, and Figure 5.16 represent the observed transmission spectra with the best fit models. It is seen that none of the transit spectra are flat and shows the presence of different features present in the atmosphere.

WASP-127 b is the puffiest, low-density planet, shows a strong Rayleigh scattering slope in the bluer region of the spectra (Figure 5.14), which indicates the cloud or haze present in the atmosphere. The best fit for the Rayleigh scattering slope using Lecavelier Des Etangs *et al.* (2008) gives a scale height of 450 km for $T_{equ} = 1200K$ and $m_{\mu} = 2.3m_p$. We could detect the presence of sodium at 5890\AA . Our results and derived parameters agree with observations by Palle *et al.* (2017) where they

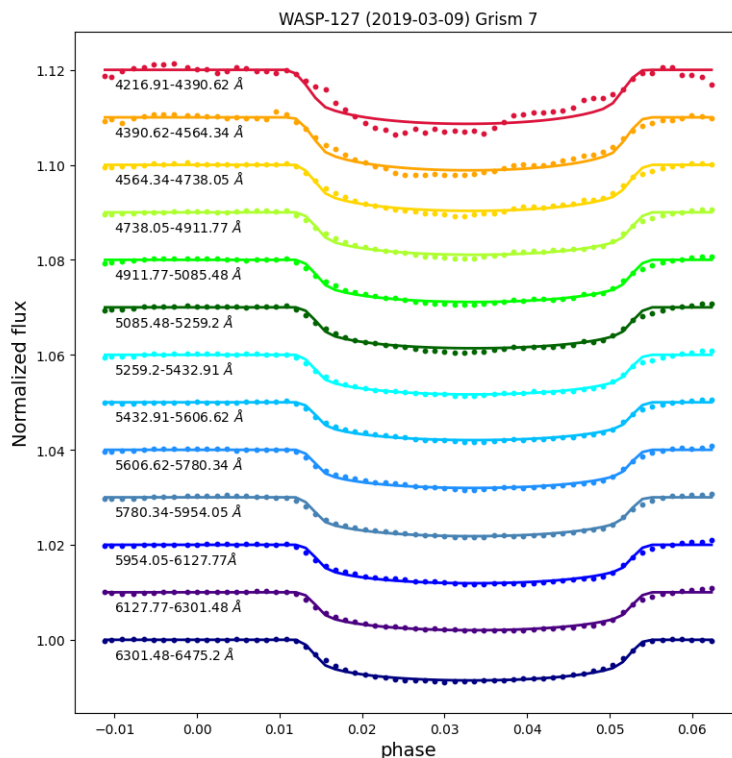


FIGURE 5.11: Grism 7 lightcurves in each wavelength bin (scattered point) and the best-fit transit models (solid line) stacked from top to bottom for WASP-127b and applied a constant scaling factor of 0.01 for visibility.

detected the presence of Rayleigh scattering and Sodium in the atmosphere of WASP-127 b.

Here we report the first low-resolution transmission spectra of highly inflated KELT-18 b. The spectra look flat without any atmospheric detection, and the R_p/R_* varies only 0.06% in the entire optical wavelength. The possible reason for obscured atmospheric features is the clouds in the upper atmosphere of the planet. Rayleigh scattering in the bluer part of the spectra can reveal this. Unfortunately, we need the observations covering the bluer part of the spectra.

The atmosphere of HAT-P-1 b is extensively observed by several high and low-resolution transmission spectroscopic observations (Todorov *et al.* 2019). Here

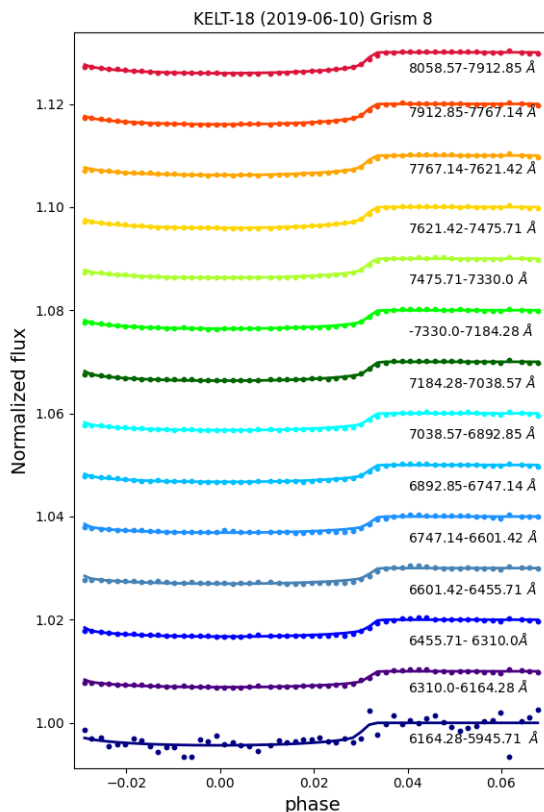


FIGURE 5.12: Grism 8 lightcurves in each wavelength bin (scattered point) and the best-fit transit models (solid line) stacked from top to bottom for KELT-18b and applied a constant scaling factor of 0.01 for visibility.

we could detect calcium in the atmosphere for the first time. However, we need further observation for confirmation.

We estimated the apparent shift in the position of the stars due to differential refraction using Equation 3 in [Sánchez-Janssen *et al.* \(2014\)](#) For the airmass ranges in our study (Table 5.1) and considering the binary separation (Table 5.2) it is coming to be $0.005'' - 0.002''$ for HAT-P-1, $0.03'' - 0.03''$ for WASP-127 and $0.09'' - 0.2''$ for KELT-18 in the beginning and end of the observation. The values are smaller than the slit length of $11'$, so differential refraction is unlikely to play a significant role in the observations. All three object stars and the corresponding

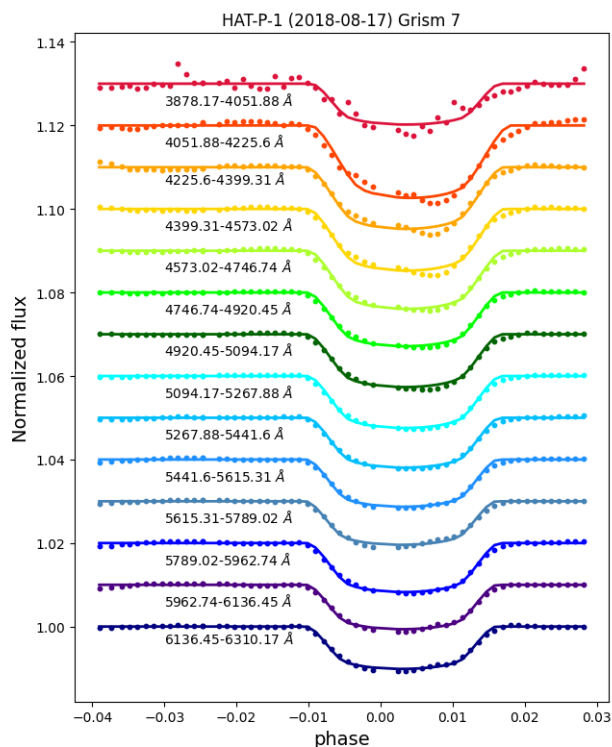


FIGURE 5.13: Grism 7 lightcurves in each wavelength bin (scattered point) and the best-fit transit models (solid line) stacked from top to bottom for HAT-P-1b and applied a constant scaling factor of 0.01 for visibility.

reference stars have the same physical parameters (Table 5.2). It is unlikely that the differential atmospheric dispersion will contribute to the observations. Any variations as a function of time would be due to the instrumental effects.

5.5 Conclusion

Long slit transit spectrophotometry is successfully observed for three hot Jupiter systems using low-resolution 2m HCT/HFOSC. We reproduce the Rayleigh scattering slope in the blue wavelength region and detection of the Na D line in WASP-127 b. For the first time, we performed low-resolution transmission spectroscopy

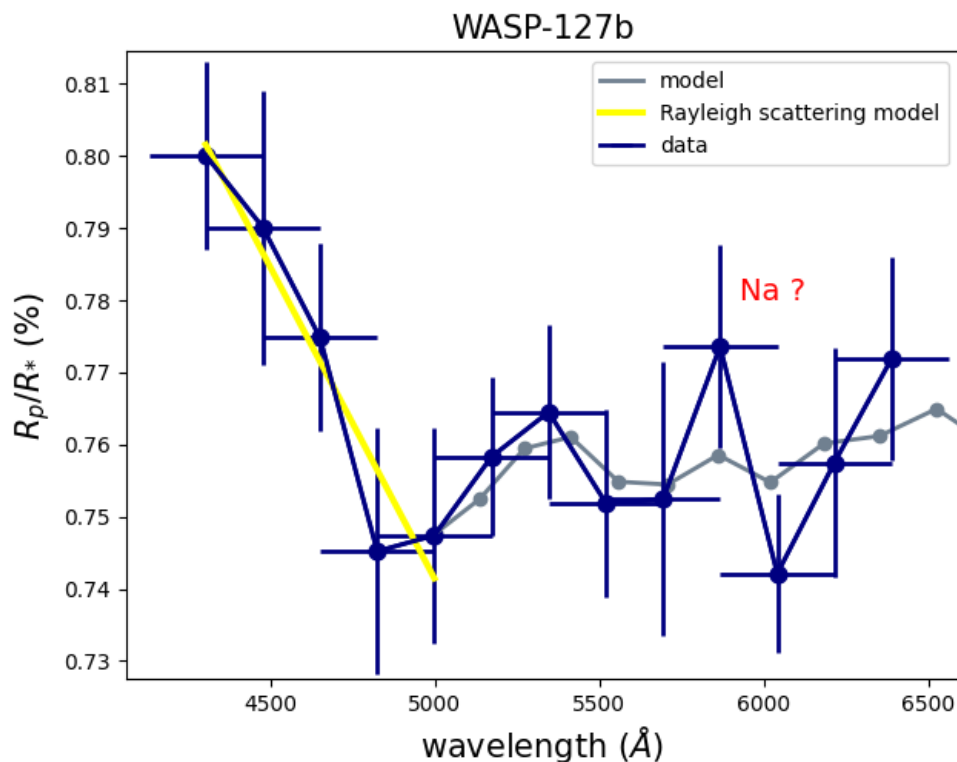


FIGURE 5.14: Observed transmission spectra of WASP-127 b (blue) and the best fit model (grey) computed using *Exo-Transmit* with $1\times$ solar models TiO/VO, Na/K, and $T_{equ} = 1400$ K. We separately calculated the Rayleigh scattering slope (yellow) from Lecavelier Des Etangs *et al.* (2008).

of KELT-18 b, another hot Jupiter system, and showed a flat spectrum between 600-800nm. Further observations covering the bluer part of the optical region will help model the atmosphere. We detect a feature near the calcium 423nm line in the atmosphere of HAT-P-1 b. We were able to show the possibility of using a smaller telescope for exoplanet transmission spectroscopy for a well-selected sample and careful handling of the systematic errors.

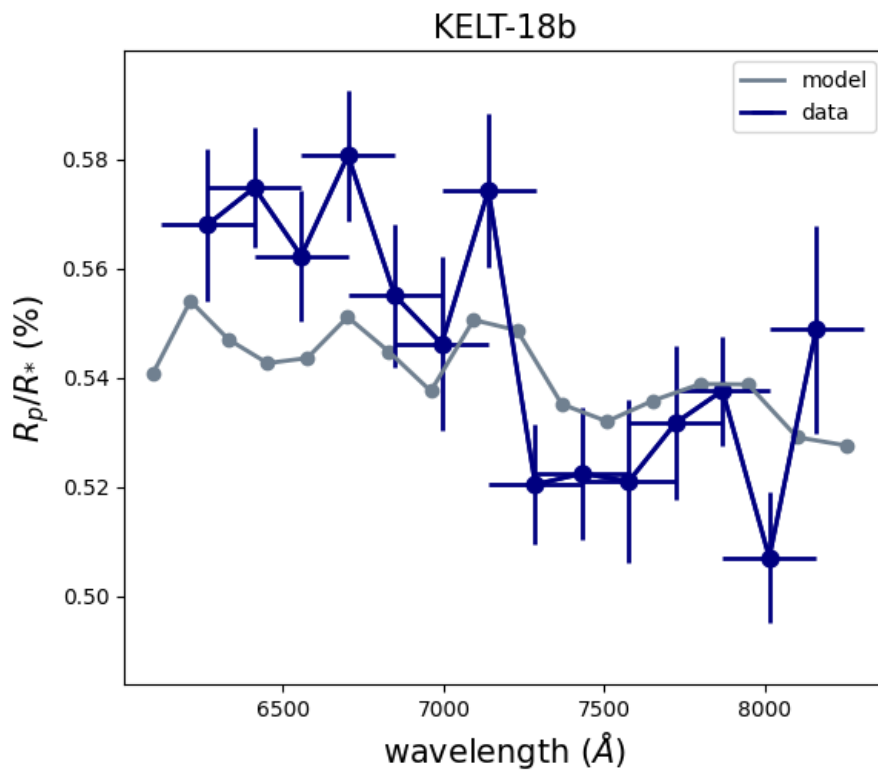


FIGURE 5.15: Observed transmission spectra of KELT-18 b (blue) with the best fit model (teal) using *Exo-Transmit* with $0.1\times$ solar models without TiO/VO and with Na/K and $T_{\text{equ}} = 1400$ K. Binned model spectra represents in grey.

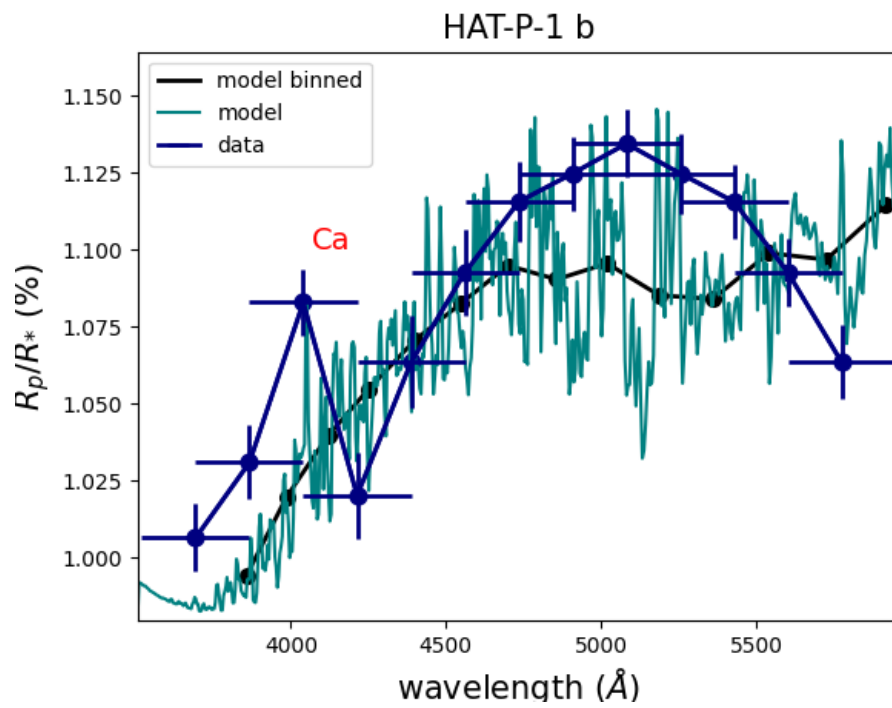


FIGURE 5.16: Observed transmission spectra of HAT-P-1 b (blue) with the best fit model using *Exo-Transmit* with $1.0\times$ solar models without TiO/VO and with Na/K and $T_{equ} = 1500$ K (teal) and binned model in solid black line.

Chapter 6

High-Resolution Transmission

Spectroscopy of WASP-49 b

Using KECK/HIRES

Abstract

WASP-49 b is a highly irradiated giant planet that shows a large optical depth of the sodium D-lines in its atmosphere. Significant optical depth could either be due to supersolar abundance or an extended geometry of the emitting region similar to the Jupiter-Io system. High dispersion transit observations were carried out with the Keck-HIRES spectrograph to estimate the sodium optical depth and possible velocity signature of the exomoon in the transit spectroscopy. Calibration exposures were not taken during the transit observations to over the transit, and

HIRES is not a stabilized spectrograph. So, we performed re-calibration of the wavelength solution with the science data itself, which helped in accurately subtracting the telluric lines and retrieving velocity information of the residual transit spectra. We do not see any transmission feature at the expected planet transit velocity in the Na-D lines. There is an extra residual at a blue-shifted location with respect to the stellar rest frame, possibly due to complex geometry, including possibility of an exomoon system. Light curves from other observations from HARPS and ESPRESSO data indicate variable light curves, which also indicate a complex geometry of the system.

6.1 Introduction

High-resolution transmission spectroscopy is a powerful tool for atmospheric characterization. Using high-resolution transmission spectroscopy, individual atomic and molecular species can be detected without the help of atmosphere retrieval models. Due to the high spectral resolutions, it is also possible to detect signatures of global circulations and auroral emission and identify contamination from stellar chromospheric emission. First, high-resolution exoplanet transit spectra were successfully obtained in 2008 for HD209458b by (Snellen *et al.* 2008) and for HD189733b by (Redfield *et al.* 2008) using High Dispersion Spectrograph (HDS) on the 8.2m Subaru telescope and the High-Resolution Spectrograph (HRS) on the 9.2 m Hobby-Eberly Telescope (HET) respectively.

Sodium is considered the most promising element in the transmission spectra of hot Jupiters (Redfield *et al.* 2008; Snellen *et al.* 2008; Wood *et al.* 2011; Zhou and Bayliss 2012; Murgas *et al.* 2014; Burton *et al.* 2015; Wyttenbach *et al.* 2015a; Nikolov *et al.* 2016; Sing *et al.* 2016; Chen *et al.* 2017; Khalafinejad *et al.* 2017; Wyttenbach *et al.* 2017a; Jensen *et al.* 2018; Seidel *et al.* 2019, 2020a,b). Due

to the large resonance scattering cross-section, even a tiny amount of sodium in the atmosphere leads to detection. The NaD line profiles provide information on the temperature-pressure (T-P) profile (Vidal-Madjar *et al.* 2011a,b; Heng *et al.* 2015) and atmospheric dynamics (Louden and Wheatley 2015; Wyttenbach *et al.* 2015a). Other than the alkali elements Na and K, $H\alpha$ and ionized metals were also detected in several exoplanets based on the irradiation from the host star. Carbon monoxide detection was possible with VLT-CRIRES in HD209458b by Snellen *et al.* (2010).

Here we study the NaD lines of the highly irradiated hot Saturn WASP-49 b using the KECK/HIRES spectrograph. WASP-49 b orbits around a G6V star ($V_{\text{mag}}=11.35$, distance=194.5 pc) (Lendl *et al.* 2012) with a transit duration of 1.87 hours and a mass of $0.37M_J$. First, high-resolution transmission spectra of WASP-49b were obtained using HARPS spectrograph by Wyttenbach *et al.* (2017a), that showed anomalous sodium of 1.99% and 1.83% for D2 and D1 lines even though the host star WASP-49 is a slow rotator and less active ($\log R_{HK} = -5.17$ (Cegla *et al.* 2016; Wyttenbach *et al.* 2017a)). Oza *et al.* (2019); Gebek and Oza (2020) suggested that WASP-49 b can be a promising candidate searching for an exomoon.

HARPS (Mayor *et al.* 2003), ESPRESSO (Pepe *et al.* 2021), and CARMENES (Quirrenbach *et al.* 2014) are the commonly used high-precision spectrographs for exoplanet transmission spectroscopy. High-Resolution Echelle Spectrograph (HIRES) is a general-purpose slit spectrograph mounted on a 10-meter KECK telescope. Though slit spectrographs provide high throughput, the line spread function (LSF) can vary significantly during observations. Due to environmental changes, the wavelength position on the detector shifts, and the wavelength dispersion solution could also change.

The stability of the wavelength dispersion solution is crucial to derive the transmission spectrum from tiny residuals signal from individual residual spectra taken through the transit. Here, we present a successful attempt to minimize wavelength shifts between exposures and derive residual signals from the transit spectra.

6.2 Observation

HIRES is installed on the Nasmyth platform of the Keck-I telescope with an echelle spectrograph that uses grating as a cross-disperser. A wavelength range of 300 - 1000 nm for the spectrograph is achieved using two different cross-dispersers and collimators. Three separate CCDs cover the entire echelle order of the spectra. A spectral resolution of $R=25000-85000$ is possible, and our observations were carried out with $R = \sim 67,000$ (Vogt *et al.* 1994a). One complete transit of WASP-49b was observed with HIRES on 2019-11-11 (PI: de Kleer, Program ID: ID C284). The observation started from UT 10:28:41 (hh:mm:ss) to 16:15:05. The sky was good throughout the night. The transit duration was 1.87 hours, and the mid-transit time was 13.31 UT. A total of 46 exposures of 420s each covered ingress, egress, complete transit, and out-of-transit phases. The airmass varied from 1.30 – 1.50. An overview of the observational details is in table 6.1.

6.3 HIRES data reduction

We reduced the data using the IRAF (Image Reduction and Analysis Facility) echelle data reduction package. There was a strong background emission line at the left edge of both the NaD lines. Hence we carefully selected the background region for extracting spectra and a polynomial fit for the background. We also

TABLE 6.1: Observation details of WASP-49. Ingress, mid-transit and egress are underlined

MJD	SNR (order:56)	Airmass	Seeing
58798.563888	58	1.66	0.6
.....
58798.506149
<u>58798.510222</u>
58798.514301
.....
58798.547244
<u>58798.551311</u>	55	1.30	1.0
58798.559457
.....
58798.596514
<u>58798.612794</u>
58798.621135
.....
58798.650041	59	1.76	1.2

downloaded the [MAKEE](#) pipeline reduced data from the Keck observatory archive (KOA). Reduced spectra from both methods were similar in quality, and for further analysis, we used the data from the MAKEE pipeline and reduced data from KOA. The continuum normalization of each order of all the spectra was performed using IRAF with a cubic spline function. The complete data reduction procedure is explained in Section 2.5.

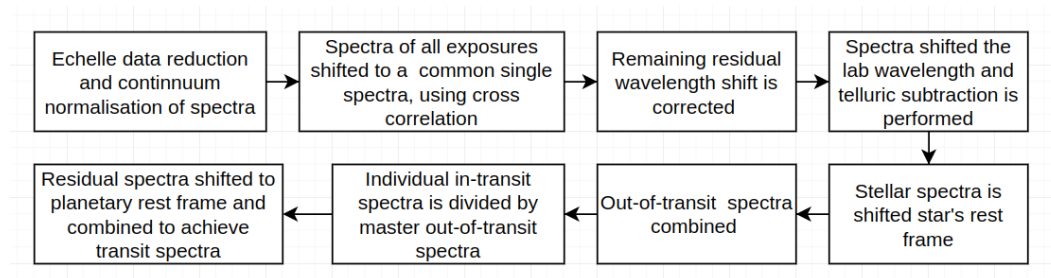


FIGURE 6.1: Various analysis steps are shown in the flow chart

6.3.1 Accurate Wavelength Calibration

HIRES is designed to be a general-purpose spectrograph that provides wide wavelength coverage and spectral resolution by changing the instrument configuration, such as cross-disperser grating, collimator, and slit width. HIRES is not housed inside a thermal or pressure-controlled environment; hence it is expected that there could be instrument drift that will cause a shift in the wavelength or wavelength dispersion solution and a change in blaze function during the observations.

To achieve accurate wavelength calibration, we used the first out-of-transit spectra with a good S/N ratio as a reference and performed cross-correlation of all the exposures and corrected the derived constant velocity shift for all the spectra. Figure 6.2 represents the RV shift across the exposure for the entire duration of the observations, which is about 1km/s . We found a linear increase in instrument drift of about 0.8 km s^{-1} from the start of the observations to the end. This shift is significant for accurate telluric subtraction and estimating the planet's transit velocity signal. Even after correcting the velocity shift and still found a residual wavelength shift of up to $\pm 300\text{m/s}$. The residual shift is not constant across the order (as shown in Figure 6.3), which could arise due to optical distortion caused by aberration and varying anamorphism at the detector. The magnitude of the residual distortion in wavelength was found to scale with overall instrument drift. After correcting the cross-correlation velocity, the first exposures had less

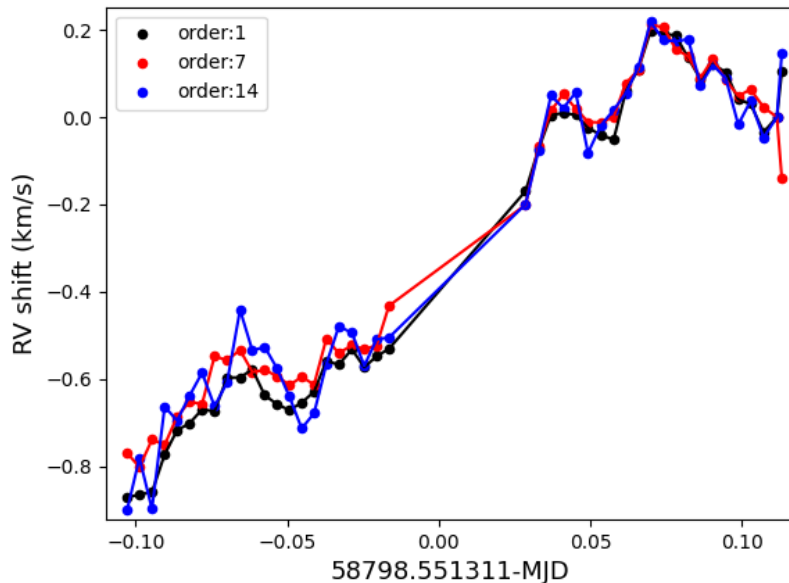


FIGURE 6.2: Radial velocity shift in each exposure with respect to the first exposure as a function of time is shown for three echelle orders. The first order is in black, the last order is in red, and the order containing the sodium doublet around 589 nm is in blue. There is a shift of 0.8 km/s from the first to the last exposure.

residual distortion than the later exposures. It is also worth noting that the ThAr calibration exposure used for deriving the wavelength dispersion solution was taken closer to the first exposure.

6.3.2 Distortion correction

Ideally, re-deriving the wavelength dispersion solution will remove the error due to residual wavelength distortion. However, the ThAr calibration exposures were not taken during transit to maximize the transit coverage. So we used the stellar lines themselves to correct for the residual wavelength distortion errors. We corrected the residual distortion separately for individual orders. For this purpose, we selected ten clean stellar lines in each order and found the centroid of the absorption

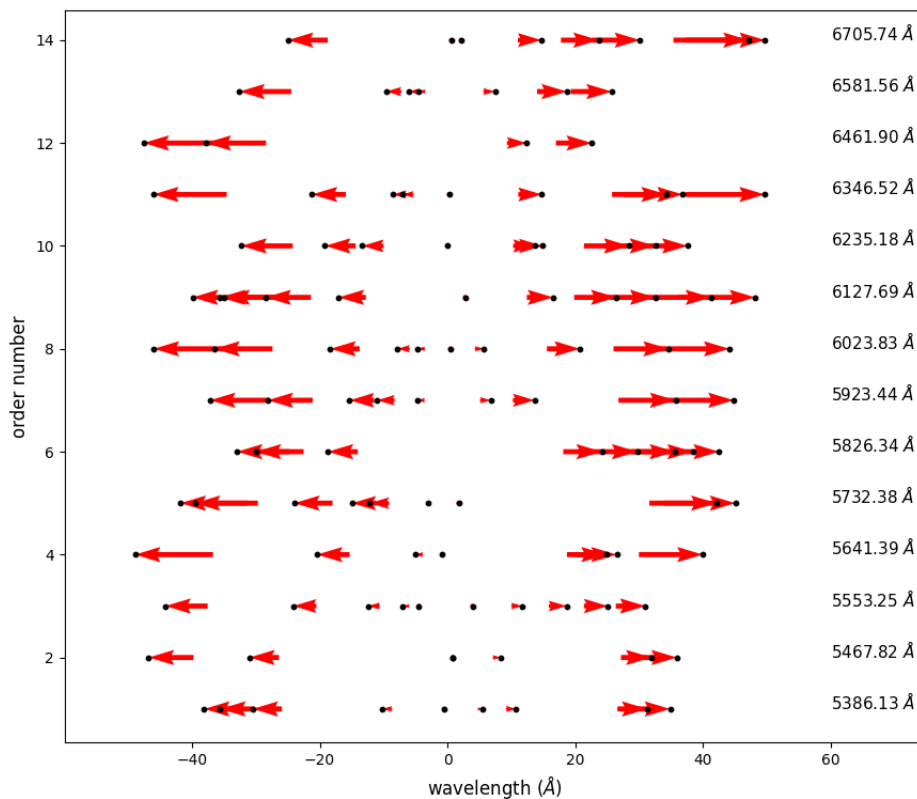


FIGURE 6.3: A residual RV shift vector map across different echelle orders is shown here. The possible residual shift in each exposure is calculated by measuring the centroid of a set of lines in each exposure (Figure 6.4). The calculated the shift in each line (length of the red arrow) with respect to the corresponding line in the first exposure (black dot). The Center wavelength of each order is considered to be zero. And y-axis represents the order number in CCD2.

lines using a gaussian fit (Figure 6.4). The shift in the centroid position compared to the first exposure was considered residual distortion. A correction was applied using a cubic spline polynomial fit between the centroid location of the individual exposures with respect to the first exposure for each echelle order.

Figure 6.5 indicates the cubic spline fitting for a single order. And finally, we could achieve a velocity precision of $\pm 50\text{m/s}$ (Figure 6.6). This is the minimum shift that could achieve using extracted spectra from Keck/HIRES. Once all the

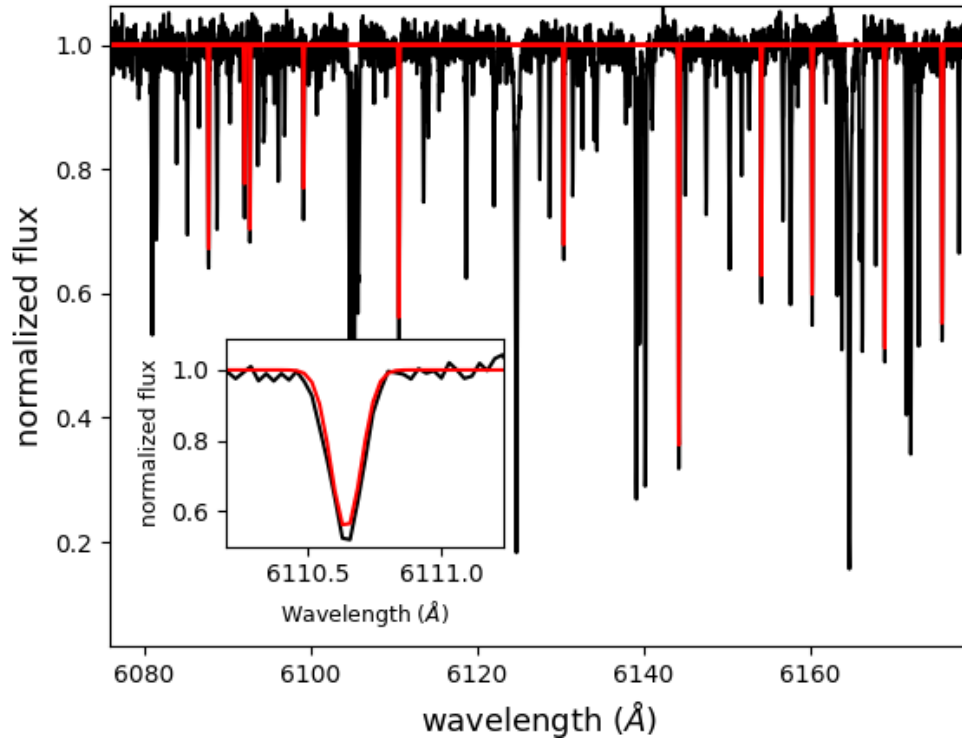


FIGURE 6.4: Observed spectra (in black) and selected clean lines for calculating distortion correction and gaussian fits to the lines are shown in red. Zoomed version of a gaussian fit is shown in the subplot.

shifts are corrected, the next step is to shift all the spectra back to the laboratory rest frame. So we applied a cross-correlation in each exposure with respect to the synthetic solar spectra.

6.3.3 Telluric correction

Earth's atmosphere is the most tricky part of ground-based observations. Even though the telluric contamination is less around the sodium region (590 nm), we have to remove the telluric contamination for each exposure; otherwise, the slight variation in the telluric lines with airmass can mimic the residual planet signal. The telluric correction was performed on the normalized spectra using *molecfit*

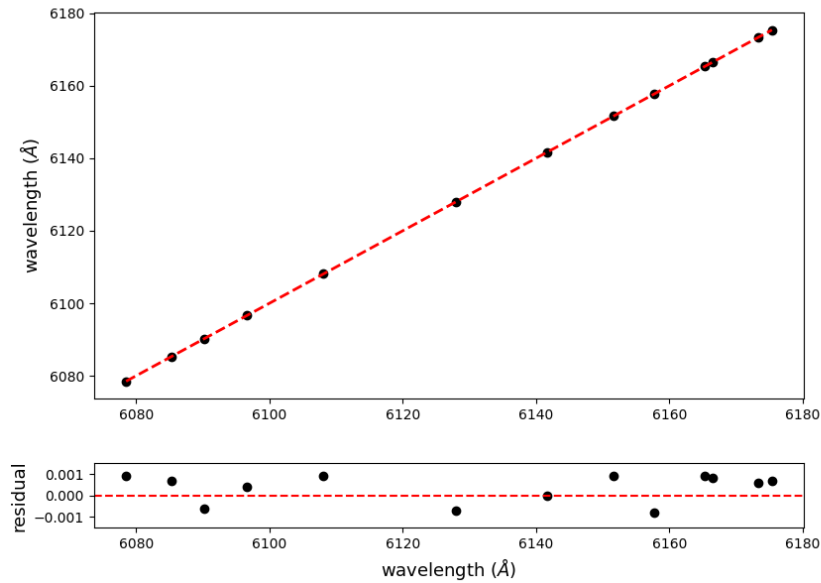


FIGURE 6.5: Distortion (Figure 6.4) correction to the wavelength solution is applied order by order using the first exposure, based on more than ten narrow stellar lines in each order. An example of order five is shown in the top panel. A cubic spline fit to the distortion gives a residual of less than 50 m/s (shown in the lower panel).

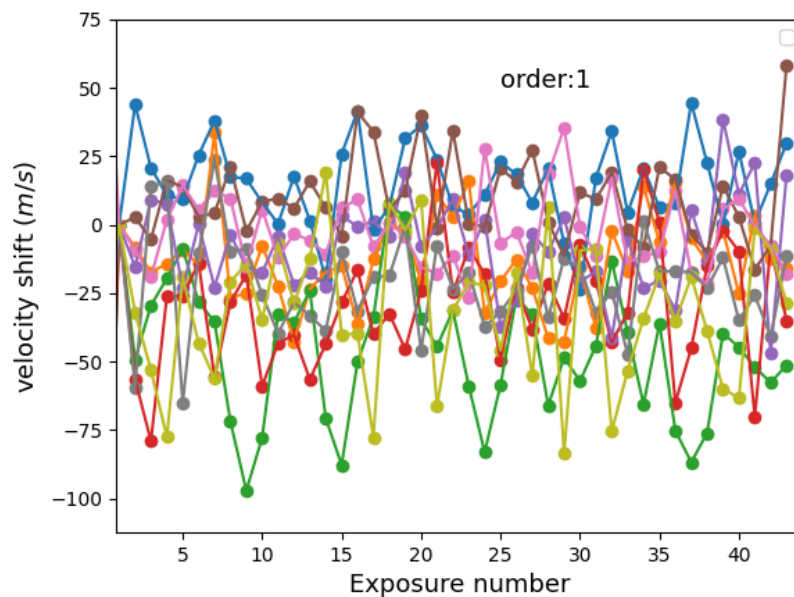


FIGURE 6.6: Final residual in wavelength calibration after distortion correction for all the exposures is shown for the case of order-1.

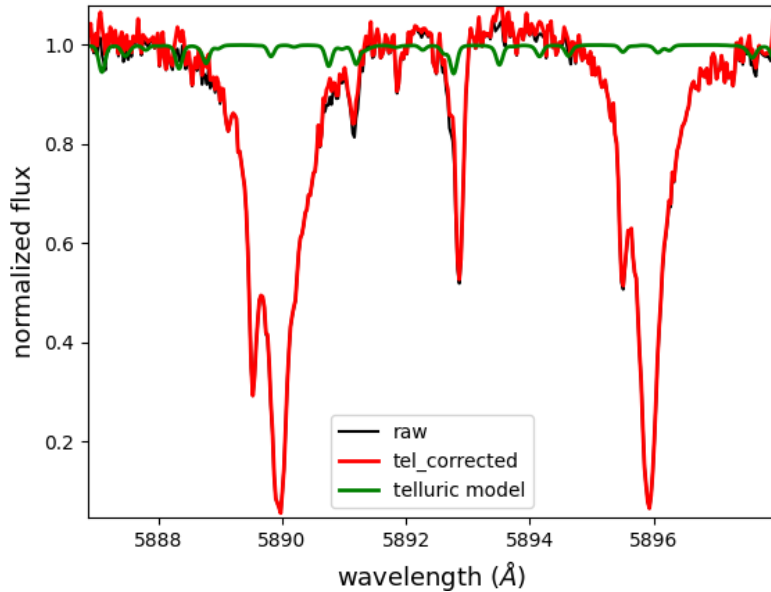


FIGURE 6.7: Telluric corrected spectrum in the synthetic lab frame (red), the telluric model spectrum (green) from *Molecfit* and the spectra before telluric correction (black) close to Sodium region.

(Smette *et al.* 2015; Kausch *et al.* 2015), version 1.5.1, an open source code considering molecular lines of the respective elements as well as local weather conditions at the observing site during the observation. *molecfit* is a well-established tool, successfully used over the years by, e.g., Allart *et al.* (2017); Hoeijmakers *et al.* (2020); Seidel *et al.* (2020a,b); Kawauchi *et al.* (2021); Stangret *et al.* (2021). We followed the steps outlined in Seidel *et al.* (2019) to obtain the transmission spectrum and extract the planetary signal. Figure 6.7 represents the telluric corrected spectra (red), the telluric model used (green), and the data before telluric correction in black.

6.3.4 Final transmission spectra

We segregate the total exposures into exposures taken during transit and observed out-of-transit based on the transit ingress and egress phase ($-0.016 : 0.016$). As

mentioned in table 6.1, we have 13 exposures taken during the transit and 28 spectra taken without transit. Figure 6.8 represents the master out-of-transit spectra by median combining all the spectra taken during out-of-transit.

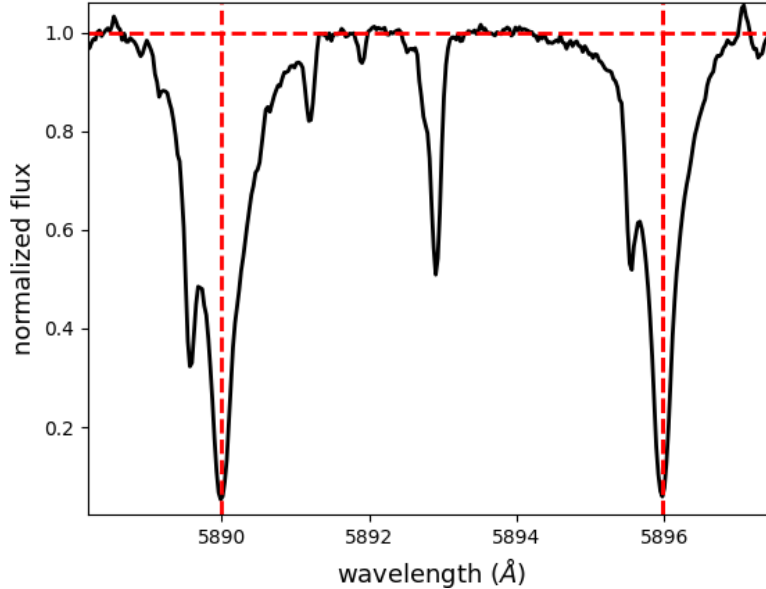


FIGURE 6.8: Master out-of-transit spectra combining all the out-of-transit spectra.

The next step is to divide each in-transit spectra by the master out-of-transit spectra. Figure 6.9 represents the stacked residual spectra as a function of observing time. The residual in each exposure is expected to shift to 0.6 \AA ($\pm 16 \text{ km/s}$) as the planet moves from ingress to egress. But from Figure 6.9, we can observe that the residual is not shifting as expected. We masked some parts of the NaD line profile to avoid stellar and background contamination, and we did not detect residual spectra significantly in the planet rest frame.

Figure 6.10 represents the masked region in the Sodium D1 and D2 lines, where the planet drift velocity coincides with the SRF. Then we combined all the final masked residual spectra in the PRF to get the final transmission spectra (Figure 6.11).

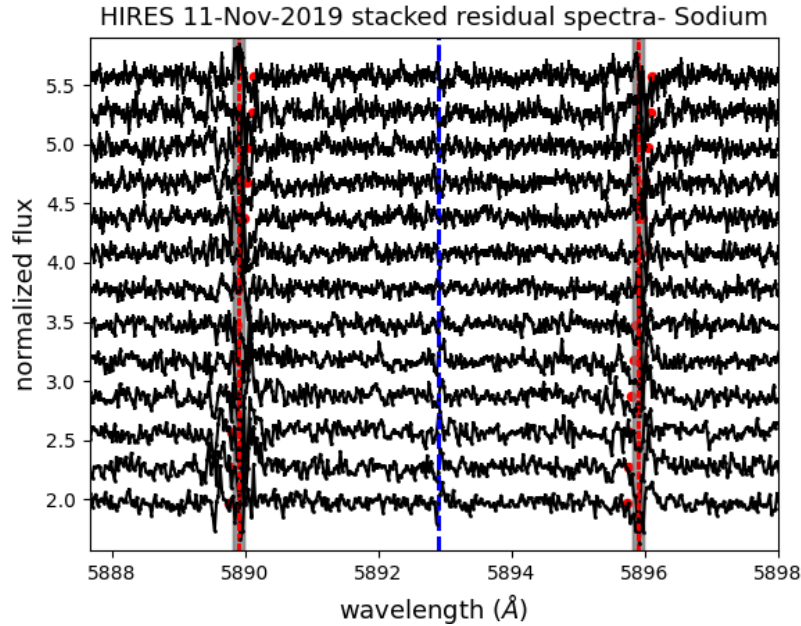


FIGURE 6.9: The figure indicates the transit spectra created by subtracting the master out-of-transit spectra. The first to the last exposures are stacked from bottom to top. The wavelengths are in the stellar rest frame, and we scale the residuals by a factor of 2.3 for visibility. The stellar rest frame location of Na D1 and D2 lines is a red dashed line. The red dots across exposures denote the expected wavelength location of the residual signal due to planet transit. One can also note that there is no residual signal in the location of the stellar Fe I (5892.9 Å) line between the Na-D lines represented by a dashed blue line.

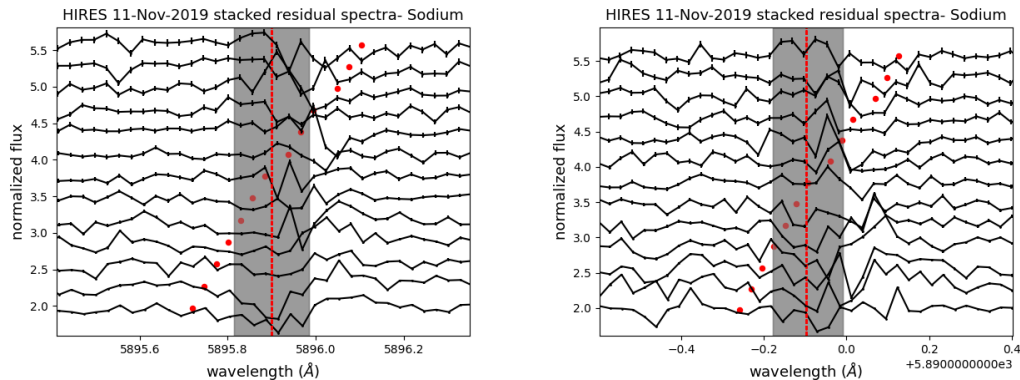


FIGURE 6.10: Stacked residual spectra (scaled for visibility purpose) along with the masked region of 0.15 Å bandpass (grey vertical bar), the central wavelength of the sodium D2 and D1 line in the SRF (dashed red vertical line), and expected planetary signal position (red dot).

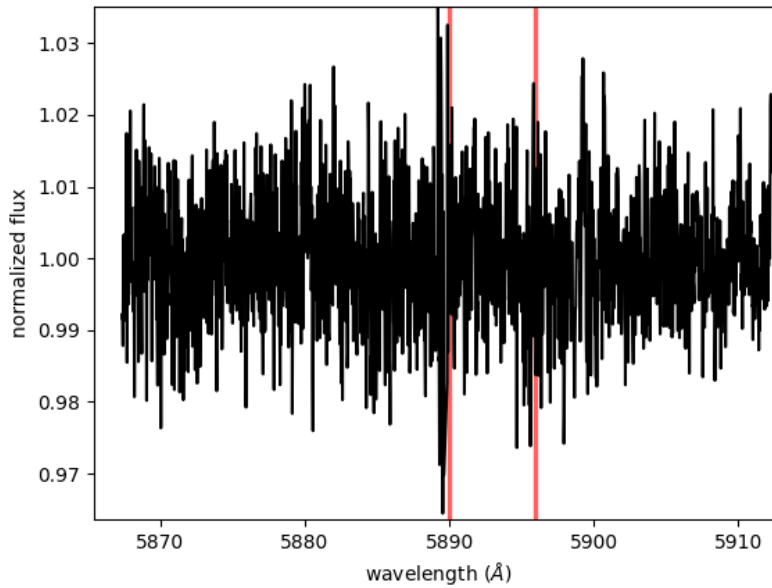


FIGURE 6.11: The residual spectra are shifting back to the planetary rest frame (PRF) and combined to obtain the final transit spectra. There is no detectable Sodium in the PRF. That is the residual what we observed without masking is pure stellar contamination.

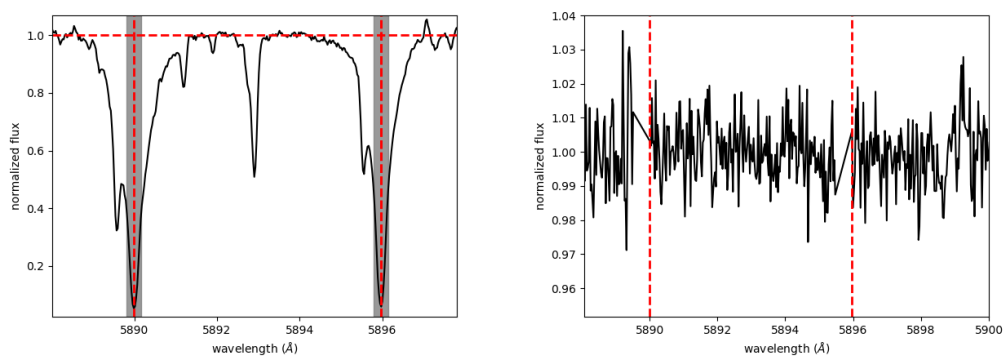


FIGURE 6.12: Left plot shows the region chosen for masking (the region between the vertical red dashed line), and the right plot shows the transmission spectra obtained after masking.

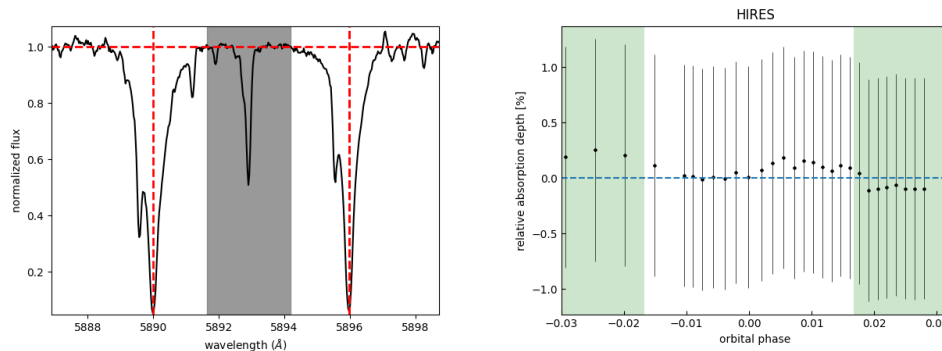


FIGURE 6.13: Left side plot shows the region near the sodium doublet used for lightcurve analysis. The right side plot shows the lightcurve obtained.

We also tried masking the core region of Na D lines of each spectra in case of stellar chromospheric contamination. We did not find clear detection. To assess the expected RMS of the residual spectra, we find the residual transmission spectra (Figure 6.12) as well as analyze a nearby continuum region Figure 6.13. Both this analysis shows no Sodium detection.

6.4 Discussion

After masking, the final transmission spectra around the sodium doublet region are shown in Figure 6.11. There is a sodium detection after masking the central region (Figure 6.12) of the sodium core; still, the individual residual is not following the expected wavelength shift as a function of time (Figure 6.9), indicating a non-stellar origin. We again reconfirmed atmospheric sodium using the lightcurve analysis. Figure 6.14 shows the sodium region selected for the lightcurve analysis and the corresponding lightcurve obtained. We also tried the possibility of detecting K after telluric correction. We could not find any K signature in both the transmission spectra and the lightcurve (Figure 6.15 and Figure 6.16).

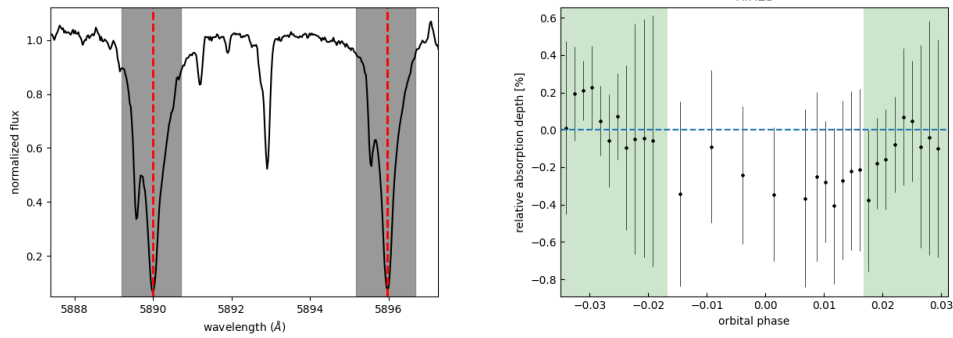


FIGURE 6.14: Left plot shows the region chosen for lightcurve calculation (the region between the vertical red dashed line), and the right plot shows the lightcurve obtained.

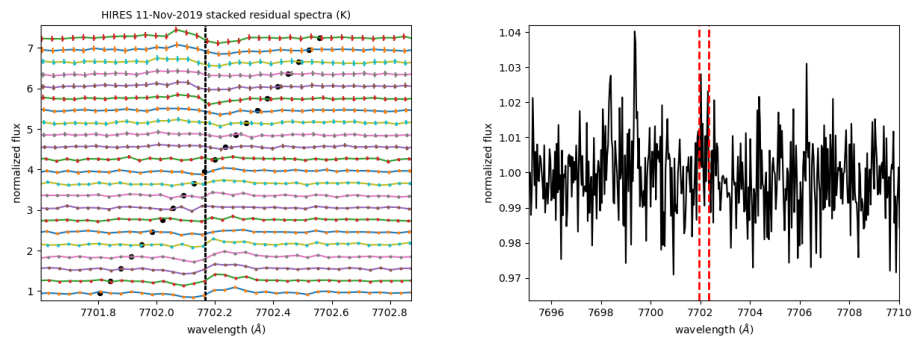


FIGURE 6.15: Left plot shows a stacked residual plot around the K region, and the right plot shows the final transmission spectra.

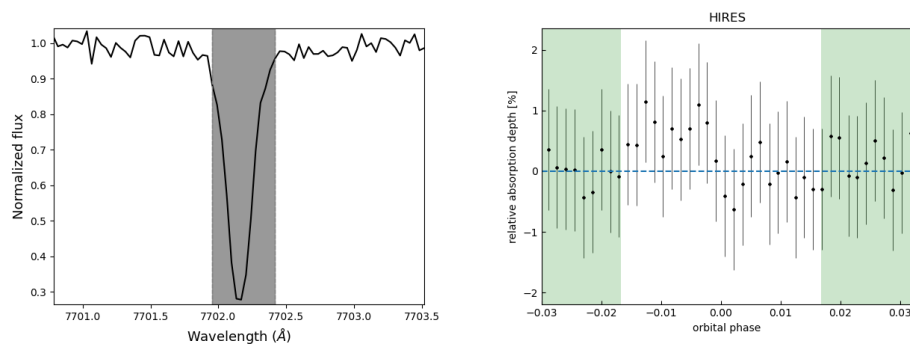


FIGURE 6.16: Left side plot shows the region around K line used for lightcurve analysis. The right side plot shows the lightcurve obtained.

6.5 Conclusion

We could achieve a radial velocity precision of 200 m/s (wavelength shift of 0.006 Å) for KECK/HIRES spectra. For wasp-49b, during the transit, the planetary signal varies 0.3 Å from the mid-transit. So this shift could be detectable using an accuracy of the current wavelength calibration. Using the present study, we cannot prove the origin of the residual sodium. But the sodium detection is not significant as reported in [Wytttenbach *et al.* \(2017a\)](#). We propose further observation for this exciting candidate.

Chapter 7

Characterizing The Solar Disk inhomogeneity From Disk-Integrated Spectra

Abstract

The Sun is the only star for which we can resolve the spatial features of the disk. Current observations can not directly resolve a stellar disk of other main sequence stars. However, a transiting exoplanet indirectly offers a way to probe the spatial inhomogeneity of the host star's disk as the planet transits. The observed transit light curve is a ratio of the flux blocked by the exoplanet atmosphere and the flux from the unocculted stellar disk. Stellar disk inhomogeneity can mimic the transit signal. Hence, we need to model both jointly to characterize a transiting exoplanet. Here, we analyze the disk-integrated solar spectra to explore

possible correlations between different spectral indices and the spot and faculae fill factors of the Sun on the same day. Accuracy of characterizing the stellar disk inhomogeneities may be essential to enable studies of smaller exoplanets. Here, we present some preliminary results that might help in this direction.

7.1 Introduction

Surface inhomogeneities on the Sun, such as Sunspots, have been recorded as early as 800 BC. The Sunspots are regions of lower effective temperature than the photosphere and possess higher magnetic fields. Faculae are the bright features around the Sunspots, and their counterparts in the chromosphere are called plages. Molecular lines of TiO and VO in the Solar spectra indicate the presence of Sunspots because, at average Solar photospheric temperatures, these molecules will dissociate. Temperatures of Sunspots are around 3800 K. The chromospheric region can be traced through the core of Ca II H & K and H α lines at visible wavelengths. The Balmer lines of H and He are very prominent in the spectra of higher layers of the chromosphere. The large bright and dark cloud in the chromosphere is called plages and filaments, respectively, and are more evident in H α and Ca II K filters. Above the chromosphere, the temperature gradually increases to very high values and merges with Corona. Here the temperature reaches around 10^6 K, and highly ionized metallic lines are observed.

Solar images and Sunspots have been routinely recorded for more than 100 years. The time scales and the intensity variations that arise due to the spatial inhomogeneity span between a few minutes to years, and it can impact the detection and characterization of exoplanets around Sun-like (F, G, K, M) stars. [Gomes da Silva *et al.* \(2011\)](#) studied five years of HARPS data of M dwarfs and found the line index of CaII K, H α , and NaD show solar-like variations. They also show H α

- CaII-K line index correlation. There is a renewed interest in observing the Sun as a point source in the context of exoplanet studies. Disk-integrated observations of the Sun and observations of the Sun during the transit of Venus and Mercury are considered valuable to understand exoplanet transit observations. The latest images of the Sun from the Daniel K. Inouye Solar Telescope can resolve spatial scales of 18km on the Sun.

Here, we calculate the line indices of possible activity indicators from Sun as a star high-resolution spectra from HARPS-N to understand how spectral line indices correlate with spots and faculae fraction measured from SOHO images. Estimation of this spatial homogeneity could be helpful in exoplanet atmospheric retrievals.

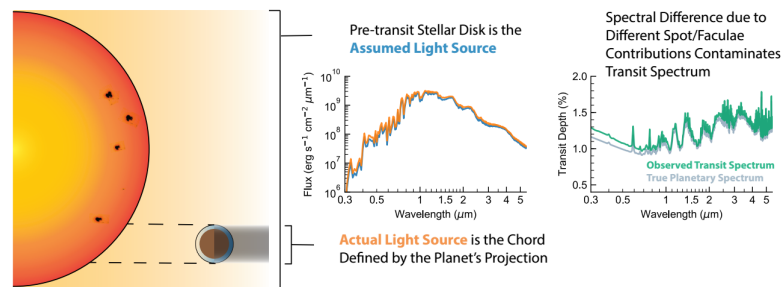


FIGURE 7.1: This illustration shows how the transmission spectra changes in the presents of stellar inhomogeneity (Rackham *et al.* 2018).

7.2 Observation & Data Analysis

We used three years of Sun as a star [archival data](#) provided by the HARPS team. We have chosen two years of data corresponding to different solar activity levels. The data contains at least one spectrum per day from January 2015 to December 2018. The wavelength coverage is 3800-6800 Å with a spectral resolution of 110000 at 5500 Å. Details about the instrument are explained in Chapter 2. We applied the radial velocity correction from the header and used spectral features

of known activity indicators, and the bandpass values are taken from literature for the preliminary analysis (Gomes da Silva *et al.* 2011). We carefully chose clean regions (where no activity indicators are present) on the left and right of the spectral feature and calculated the line indices. We expect the continuum to be stable and not affected by solar activity, and the bandpass for the lines is chosen around the line core so that they will be sensitive to the activity.

7.2.1 Estimating spot and faculae fraction

We have used the SDO/HMI magnetograms and SDO/HMI continuum intensity to disentangle different solar surface features. We extract 24 observations per day (one image per hour), spread from 1st January 2015 to 31st December 2018. For the identification and estimation of feature-specific fill factors and magnetic flux densities, we follow the same basic steps in the preparation and processing of SDO/HMI full-disk images as originally done by Haywood *et al.* (2016) and adopted in various follow up studies (*e.g.*, Milbourne *et al.* (2019); Haywood *et al.* (2020); Milbourne *et al.* (2021)). We have used full-disc continuum intensity with limb darkening removed and the line-of-sight magnetograms from the HMI instrument. We converted SDO images from pixel coordinates to heliographic coordinates (a coordinate system centered on the Sun) (Thompson 2006). Initially, we cropped the HMI images at a center-to-limb distance of $0.96 R_{\odot}$ to avoid the noisy pixels over the edges near the limb. Assuming that much of the magnetic flux on the solar surface is vertically oriented, we convert the line-of-sight magnetic field strength (B_{obs}) to radial magnetic field strength by removing the foreshortening effect (Haywood *et al.* 2016). Foreshortening results from geometric curvature and projection, which causes a decrease in observational spatial resolution as the distance from the solar disc center increases.

The upper left panel of Figure 7.2 indicates the unsigned radial magnetogram after

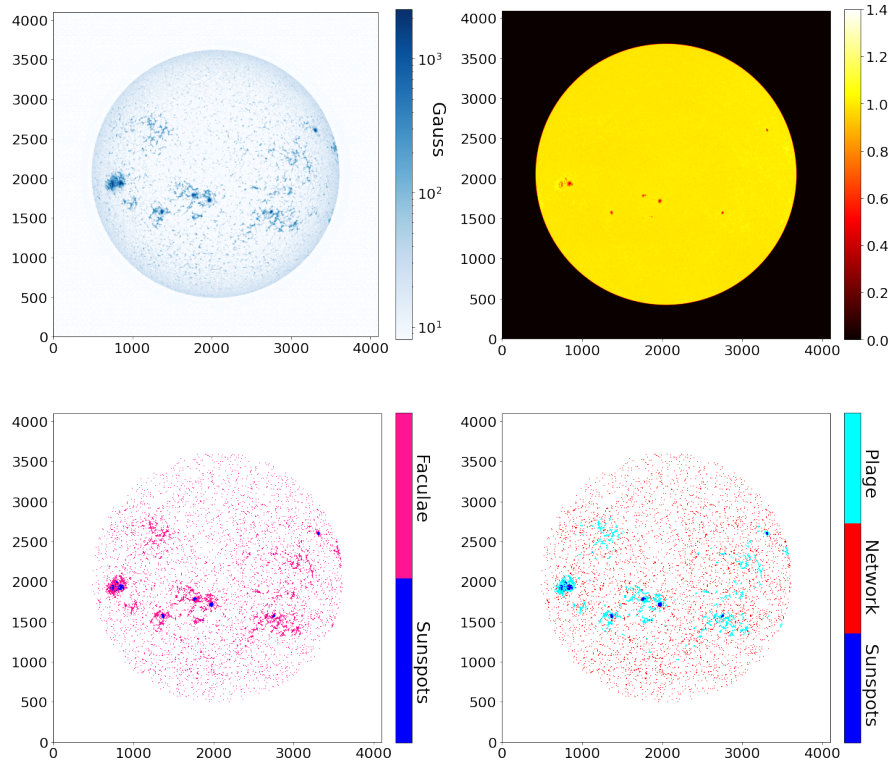


FIGURE 7.2: Upper panels indicate the SDO/HMI radial magnetogram and SDO/HMI flattened continuum intensity, observed on 1st January 2015; Lower panels: show two threshold images on the same date. The left one displays faculae and sunspots separately in different colors, and in the right panel, we have further divided faculae into plage and network fields.

correcting the foreshortening effects. And the upper right panel shows the flattened HMI continuum intensitygram. The noise level in HMI magnetograms is lowest for the pixels near the center of the CCD (around 5G) and increases towards the edges, reaching 8G at the solar limb (Yeo *et al.* 2013). We have applied a threshold in the line-of-sight magnetic field measurement (Haywood *et al.* 2016) and intensity (Yeo *et al.* 2013; Haywood *et al.* 2016). In the bottom panel (left), Figure 7.2 represents a threshold image separating sunspots and faculae in different colors. In the next step, we applied area thresholding to split the stronger magnetic field regions into plages and network fields. Plages are identified as those contiguous pixels occupying an area greater than $A_{thresh} = 0.0315 \text{ arcmin}^2$ (Milbourne *et al.* (2021)), and the rest as network regions. We have illustrated plage and network separately in the last panel of Figure 7.2.

7.3 Line index measurement

We followed the popular method to estimate the activity index in the literature [Gomes da Silva *et al.* \(2011\)](#). We visually inspected the left and right regions of the particular feature and normalized these regions of the spectra. Since HARPS is a stable spectrograph, the blaze function change is insignificant. Integrated the flux over the left (I_{left}), right (I_{right}), and the center (I_{core}) of the line is calculated, and the line index for a single line is defined as

$$Index = \frac{2 * I_{core}}{I_{left} + I_{right}} : \text{singlet}$$

If the line is a doublet, then we have to consider both core fluxes while calculating the index. We also sum up the line cores for the triplet lines, but the continuum region is common for the double and triplet lines.

$$Index = \frac{I_{core1} + I_{core2}}{I_{left} + I_{right}} : \text{doublet}$$

$$Index = \frac{2 * (I_{core1} + I_{core2} + I_{core3})}{3 * (I_{left} + I_{right})} : \text{triplet}$$

The list of line indices are Ca II H & K (3890 Å), H δ 4100 Å, H β 4862 Å, NaD 5890 Å, H α 6562 Å, CH G band (4300 Å), H γ 4340 Å, Mg 4571 Å, Mg triplet 5169 Å, Fe 5250 Å, HeD3 5875 Å, Fe 6173 Å, and He 6678 Å. The initial analysis showed significant changes in the line index for Ca II H&K, H δ , H β , NaD, and H α with respect to the activity. Table 7.1 shows the wavelength range used for line index calculation. We chose these five lines for further analysis, and the bandpass used for spectral index calculations is shown in Figure 7.3, Figure 7.4, and Figure 7.5. We have obtained the line index directly from the HARPS spectra without performing continuum normalization. Since HARPS is a stable spectrograph, the error caused by blaze function change during the observations that could affect line

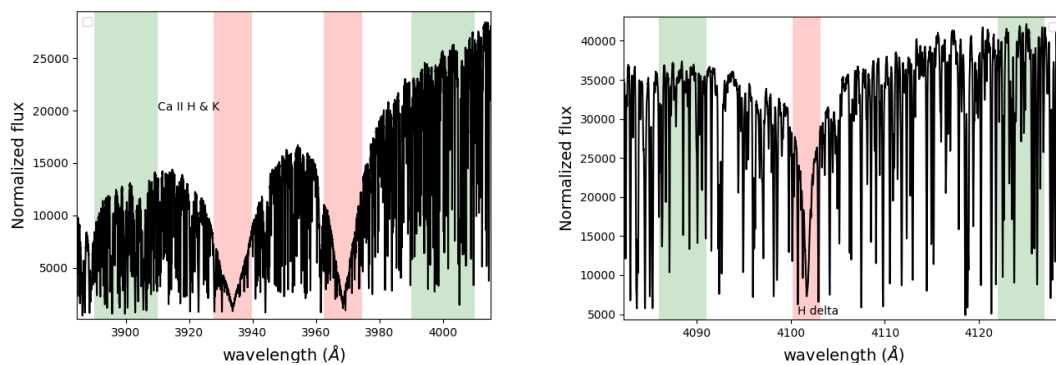


FIGURE 7.3: Left and right continuum (cyan) and the line core regions (red) selected for calculating line index for Ca II H & K (left) and H δ (right).

index estimation is minimal compared to automated continuum normalization.

TABLE 7.1: The reference wavelength region selected left and right of the absorption line and the wavelength region centered around the absorption line used for the line index measurement.

Feature	Reference band (left)	Reference band (center)	Reference band (right)
Ca II H & K	3890.0 – 3910.0 Å	3927.7 – 3939.7 Å 3962.5 – 3974.5 Å	3990.0 – 4010.0 Å
H δ	4086.0 – 4094.0 Å	4100.7 – 4103.7 Å	4122.0 – 4127.0 Å
H β	4846.0 – 4853.0 Å	4860.7 – 4863.7 Å	4877.5 – 4882.5 Å
Na D2 & D1	5800.0 – 5810.0 Å	5895.6 – 5896.1 Å 5889.7 – 5890.2 Å	6080.0 – 6100.0 Å
H α	6545.0 – 6555.0 Å	6562.1 – 6563.5 Å	6575.0 – 6585.0 Å

7.4 Results and Conclusion

We tried to find the possible connection between the line indices and the spot and faculae fraction for the same-day of observations. Figure 7.6 and Figure 7.7 depict the normalized line indices as a function of spot and faculae fraction. 2015

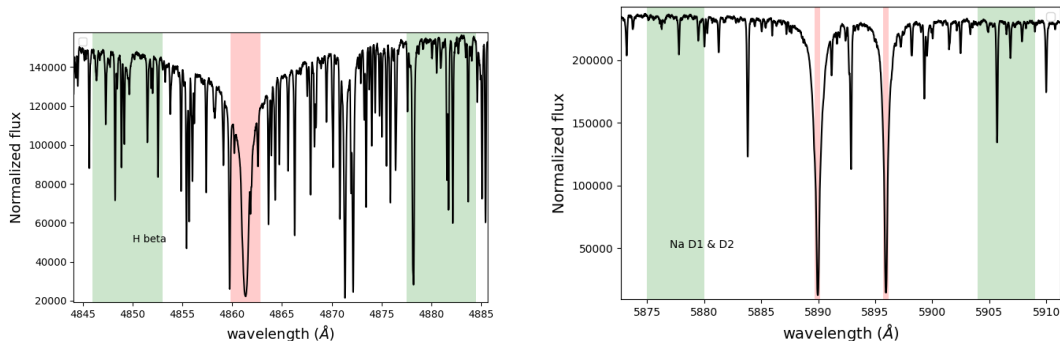


FIGURE 7.4: Left and right continuum (cyan) and the line core regions (red) selected for calculating line index for H β (left) and Na D2 & D1 (right)

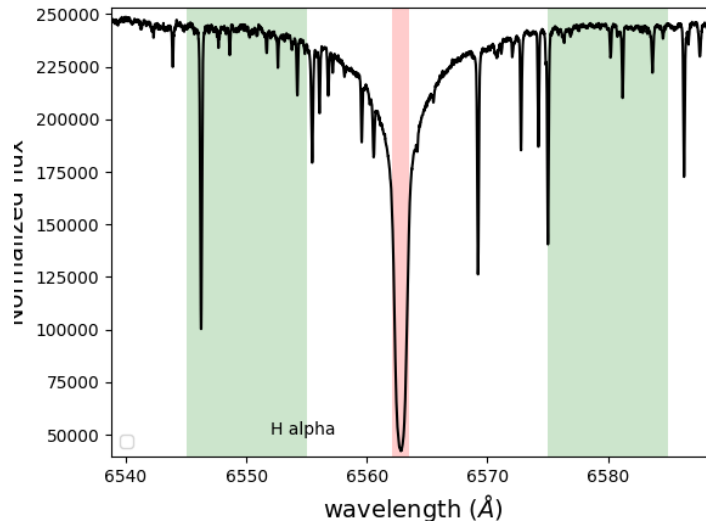


FIGURE 7.5: Left and right continuum (cyan) and the line core regions (red) selected for calculating line index for H α .

is close to the Solar maximum, and 2018 is close to the Solar minimum period. We normalized the line index by the mean value of the line index observed in 2018 to present the variations. Some preliminary results are given below;

- In 2018, the spot activity was low; in 2015, the spot coverage increased to a fraction of a percentage. The area of faculae presented here corresponds to a sum of all magnetic features outside spots. The faculae fraction varied

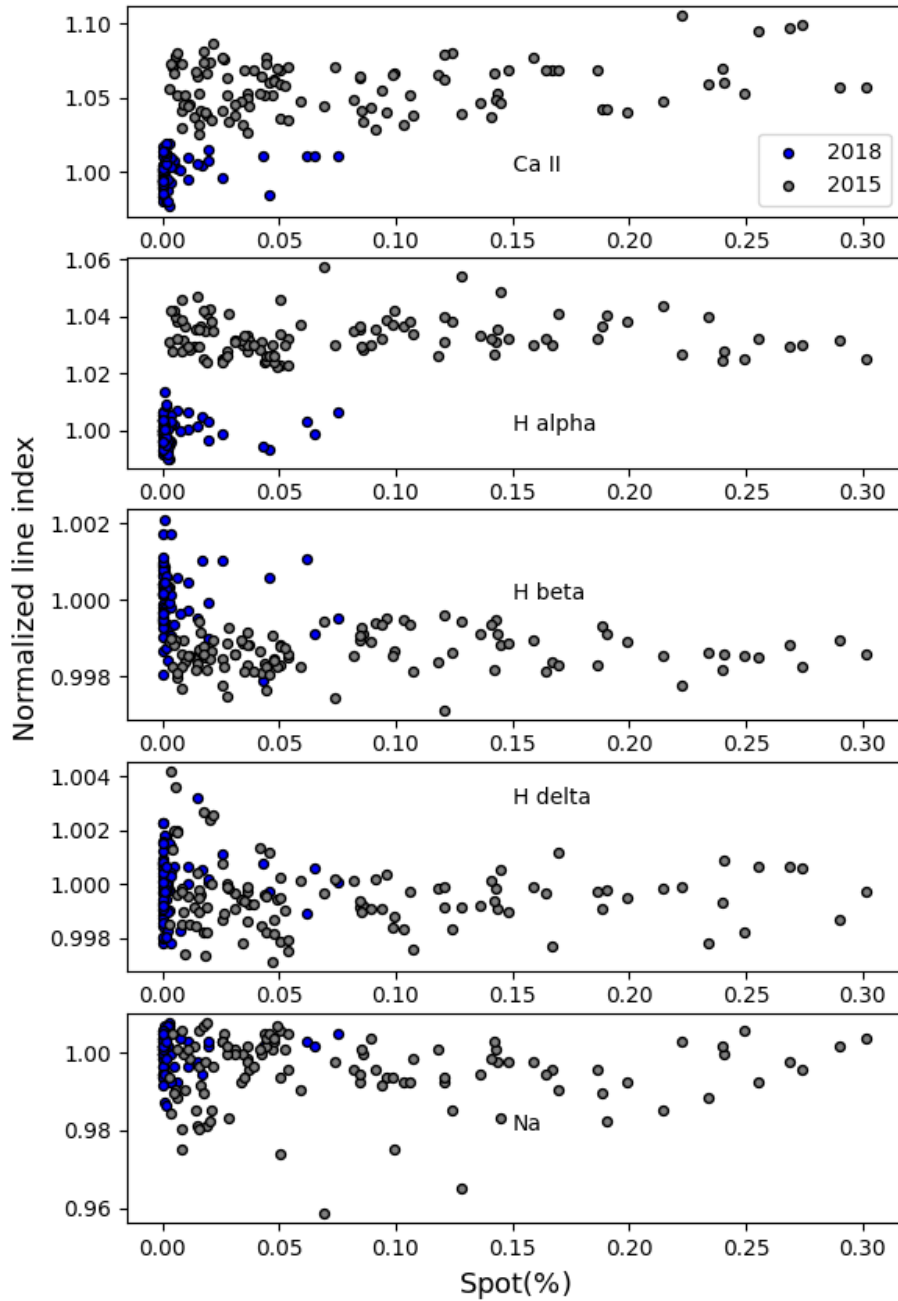


FIGURE 7.6: The image indicates the Sunspot fraction as a function of the normalized line indices of Ca II H & K, H α , H β , H δ , and the Sodium doublet for the years 2015 and 2018.

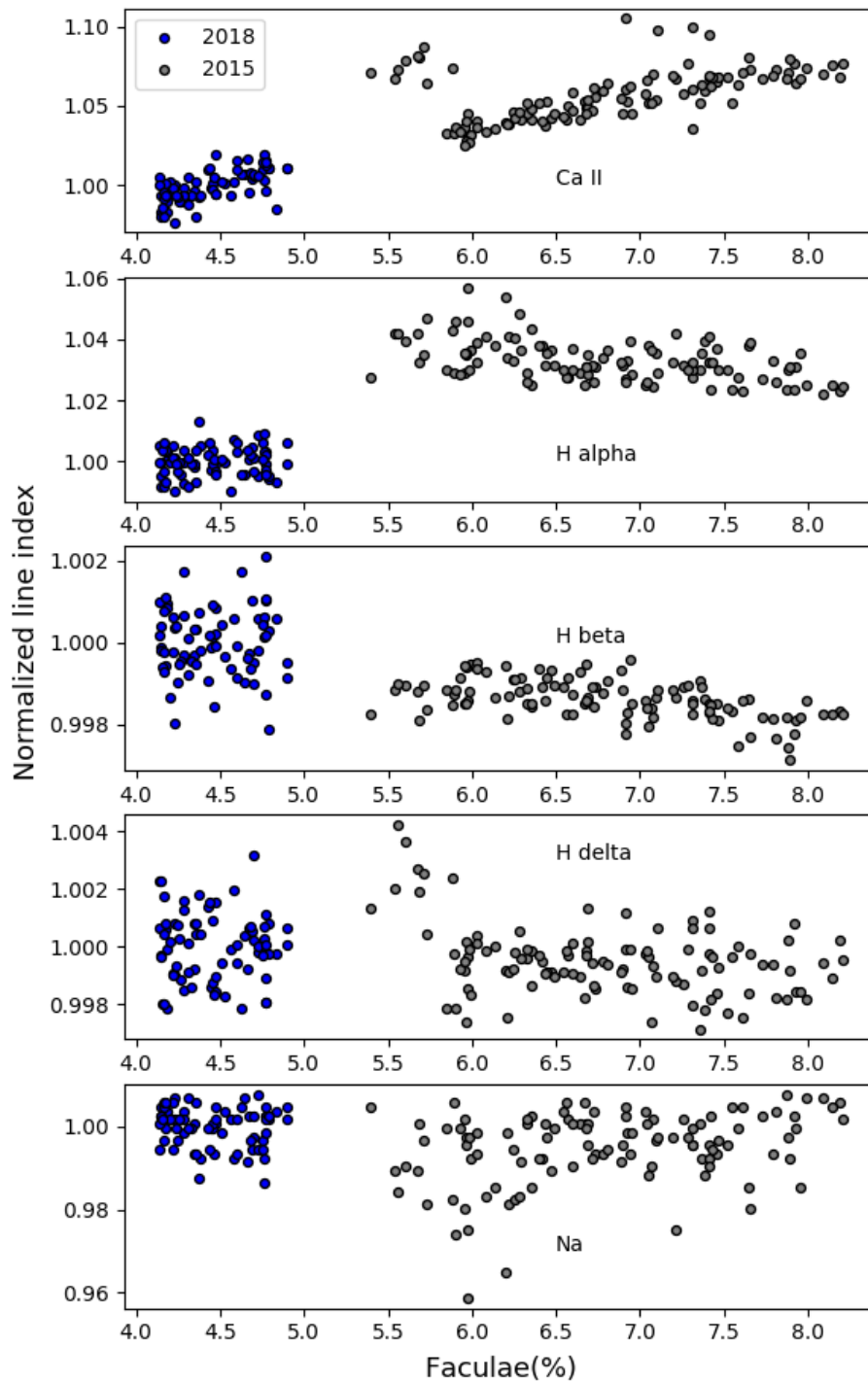


FIGURE 7.7: The Figure represents the normalized line indices of Ca II H & K, H α , H β , H δ , and the Sodium doublet as a function of faculae fraction for the years 2015 and 2018.

about a percent during the quiet period in 2018, and it varied more than 5% during 2015.

- CaII HK line index varies most (about 10%) compared to other lines. The mean line index increased between 2018 to 2015, correlating with overall solar activity. The index shows a positive correlation with the faculae fraction. However, it does not show a clear correlation with spot area fraction.
- H α line index shows different behavior in the active and quiet phases. The index shows an increase with faculae area fraction during the quiet phase but a decrease in the index with faculae area in the active phase.
- H β and H δ index does not vary in the 2018 phase but shows a decline in the line index with respect to the faculae area fraction similar to H α .
- Sodium line index does not show any correlation with spot or faculae fraction.

Chapter 8

Conclusion

In the thesis, we studied exoplanet host star chemical abundances, transmission spectroscopy of hot Jupiters, and characterization of the solar disk inhomogeneity with spectral line indices. Some of the key results from the chapters are presented below.

Chapter 3 discusses the planet occurrence rate and host star carbon abundance from LAMOST & Kepler data. We find, in general, the planet hosts and field stars follow a similar trend in $[C/Fe]$ and $[Fe/H]$ as expected by the Galactic chemical evolution (GCE). Giant planet hosts are generally found among higher $[Fe/H]$ and $[C/H]$ host stars. This may indicate a need for a critical metallicity/abundance to form Jupiter-like planets and may also be for low-mass planets. However, for a narrow range of metallicity among $[Fe/H]$ rich stars, $[C/Fe]$ is low for planet hosts. To further understand the planet population in the Galactic context, we derived the age using Galactic velocity dispersion using Gaia. We found that the hot Jupiter host stars are younger, only about 4-5 Gyrs old, refer to Chapter 3). **Chapter 4** dealing with the differential abundance of stellar twins in visual binary systems was studied to understand the influence of planet formation on

the host star chemical abundance. In the HD80606/HD80607 binary system, the planet host (HD80606) shows an enhanced abundance of refractory elements of about 0.01 dex compared to the binary companion (HD80607). However, C, N, and S show only a mild enhancement. Elements such as Sc show significant enhancement. This shows a correlation between the abundance difference and the condensation temperature. However, a few similar binary systems do not show significant differences. We also estimate the ages of these systems to understand whether this enhancement is diluted in older systems (refer to Chapter 4).

Transit spectrophotometry requires high signal-to-noise observations and accurate tracking of flux losses due to atmospheric and environmental factors and instrument flexure variations. We carried observations with the 2m Himalayan Chandra Telescope (HCT) covering the entire optical band up to 900 nm region. This study is presented in **Chapter 5**. We chose targets with suitable reference stars to accurately track slit losses even for long cadence observations to reach the required signal-to-noise ratio. Typical individual exposures were 300-500s over 5-6 hours covering a transit. We obtained complete transit of three stars, HAT-P-1, KELT-18, and WASP-127, that host a giant planet. We modeled the lightcurves using the Pylightcurve, and best fit atmospheric models are estimated with Exo-transmit (refer to Chapter 5).

High-resolution transmission spectroscopy of WASP-49 b using HIRES/KECK In **Chapter 6**, we study the alkali lines of a highly irradiated hot Jupiter WASP-49 b, first detected with HARPS. The large optical depth of the sodium D-lines in this system could indicate an exomoon around the giant planet. High dispersion transit observations were carried out with the Keck-HIRES spectrograph to estimate the sodium optical depth and possible velocity signature of the exomoon in the transit spectroscopy. As HIRES is not a stabilized spectrograph, we performed a wavelength re-calibration to the HIRES data. The above step helps accurately subtract the telluric lines and retrieve velocity information of the residual transit

spectra. We achieved a velocity accuracy of $\pm 50\text{m/s}$ with a simple polynomial fit of the optical distortion for individual orders. A physically motivated spectrograph model is progress. The lightcurve analysis of HIRES data and other observations from HARPS and ESPRESSO data indicate a variable lightcurve, which may be due to the complex geometry of the system. And we propose further observation for WASP-49 b (refer to Chapter 6).

Chapter 7 presents the possible stellar in-homogeneity in the disk-integrated spectra of the Sun. The main goal of this work is to understand the effect of stellar in-homogeneity in the transmission spectra of exoplanets around Sun-like stars. We have used disk-integrated spectra of the Sun from HARPS-N over a period of 2.9 years, from July 14, 2015, to May 29, 2018, corresponding to the last phase of the solar cycle (refer to Chapter 7) and presented line indices that are sensitive to spot and faculae fraction in the Sun.

“We are stardust brought to life, then empowered by the universe to figure itself out—and we have only just begun.”

- Neil deGrasse Tyson.

Bibliography

- Adibekyan, V. Zh., Delgado Mena, E., Sousa, S. G., Santos, N. C., Israelian, G., González Hernández, J. I., Mayor, M. and Hakobyan, A. A., 2012a, “Exploring the α -enhancement of metal-poor planet-hosting stars. The Kepler and HARPS samples”, *Astron. Astrophys.*, **547**, A36. [DOI], [ADS], [arXiv:1209.6272 [astro-ph.EP]]
- Adibekyan, V. Zh., Santos, N. C., Sousa, S. G., Israelian, G., Delgado Mena, E., González Hernández, J. I., Mayor, M., Lovis, C. and Udry, S., 2012b, “Overabundance of α -elements in exoplanet-hosting stars”, *Astron. Astrophys.*, **543**, A89. [DOI], [ADS], [arXiv:1205.6670 [astro-ph.EP]]
- Adibekyan, V. Zh., Sousa, S. G., Santos, N. C., Delgado Mena, E., González Hernández, J. I., Israelian, G., Mayor, M. and Khachatryan, G., 2012c, “Chemical abundances of 1111 FGK stars from the HARPS GTO planet search program. Galactic stellar populations and planets”, *Astron. Astrophys.*, **545**, A32. [DOI], [ADS], [arXiv:1207.2388 [astro-ph.EP]]
- Adibekyan, V. Zh., González Hernández, J. I., Delgado Mena, E., Sousa, S. G., Santos, N. C., Israelian, G., Figueira, P. and Bertran de Lis, S., 2014, “On the origin of stars with and without planets. T_c trends and clues to Galactic evolution”, *Astron. Astrophys.*, **564**, L15. [DOI], [ADS], [arXiv:1404.4514 [astro-ph.SR]]

- Akeson, R. L., Chen, X., Ciardi, D., Crane, M., Good, J., Harbut, M., Jackson, E., Kane, S. R., Laity, A. C., Leifer, S., Lynn, M., McElroy, D. L., Papin, M., Plavchan, P., Ramírez, S. V., Rey, R., von Braun, K., Wittman, M., Abajian, M., Ali, B., Beichman, C., Beekley, A., Berriman, G. B., Berukoff, S., Bryden, G., Chan, B., Groom, S., Lau, C., Payne, A. N., Regelson, M., Saucedo, M., Schmitz, M., Stauffer, J., Wyatt, P. and Zhang, A., 2013, “The NASA Exoplanet Archive: Data and Tools for Exoplanet Research”, *Pub. Astron. Soc. Pac.*, **125**(930), 989. [DOI], [ADS], [arXiv:1307.2944 [astro-ph.IM]]
- Allart, R., Lovis, C., Pino, L., Wytttenbach, A., Ehrenreich, D. and Pepe, F., 2017, “Search for water vapor in the high-resolution transmission spectrum of HD 189733b in the visible”, *Astron. Astrophys.*, **606**, A144. [DOI], [ADS], [arXiv:1706.00027 [astro-ph.EP]]
- ALMA Partnership, Brogan, C. L., Pérez, L. M., Hunter, T. R., Dent, W. R. F., Hales, A. S., Hills, R. E., Corder, S., Fomalont, E. B., Vlahakis, C., Asaki, Y., Barkats, D., Hirota, A., Hodge, J. A., Impellizzeri, C. M. V., Kneissl, R., Liuzzo, E., Lucas, R., Marcelino, N., Matsushita, S., Nakanishi, K., Phillips, N., Richards, A. M. S., Toledo, I., Aladro, R., Brogiere, D., Cortes, J. R., Cortes, P. C., Espada, D., Galarza, F., Garcia-Appadoo, D., Guzman-Ramirez, L., Humphreys, E. M., Jung, T., Kamenon, S., Laing, R. A., Leon, S., Marconi, G., Mignano, A., Nikolic, B., Nyman, L. A., Radiszcz, M., Remijan, A., Rodón, J. A., Sawada, T., Takahashi, S., Tilanus, R. P. J., Vila Vilaro, B., Watson, L. C., Wiklind, T., Akiyama, E., Chapillon, E., de Gregorio-Monsalvo, I., Di Francesco, J., Gueth, F., Kawamura, A., Lee, C. F., Nguyen Luong, Q., Mangum, J., Pietu, V., Sanhueza, P., Saigo, K., Takakuwa, S., Ubach, C., van Kempen, T., Wootten, A., Castro-Carrizo, A., Francke, H., Gallardo, J., Garcia, J., Gonzalez, S., Hill, T., Kaminski, T., Kurono, Y., Liu, H. Y., Lopez, C., Morales, F., Plarre, K., Schieven, G., Testi, L., Videla, L., Villard, E., Andreani, P., Hibbard, J. E. and Tatematsu, K., 2015, “The 2014 ALMA Long Baseline Campaign: First Results from High Angular Resolution Observations toward the

- HL Tau Region”, *Astrophys. J. Lett.*, **808**(1), L3. [DOI], [ADS], [arXiv:1503.02649 [astro-ph.SR]]
- Alvarez, R. and Plez, B., 1998a, “Near-infrared narrow-band photometry of M-giant and Mira stars: models meet observations”, *Astron. Astrophys.*, **330**, 1109–1119. [ADS], [arXiv:astro-ph/9710157 [astro-ph]]
- Alvarez, R. and Plez, B., 1998b, “Near-infrared narrow-band photometry of M-giant and Mira stars: models meet observations”, *Astron. Astrophys.*, **330**, 1109–1119. [ADS], [arXiv:astro-ph/9710157 [astro-ph]]
- Barge, P., Baglin, A., Auvergne, M., Rauer, H., Léger, A., Schneider, J., Pont, F., Aigrain, S., Almenara, J. M., Alonso, R., Barbieri, M., Bordé, P., Bouchy, F., Deeg, H. J., La Reza, De, Deleuil, M., Dvorak, R., Erikson, A., Fridlund, M., Gillon, M., Gondoin, P., Guillot, T., Hatzes, A., Hebrard, G., Jorda, L., Kabath, P., Lammer, H., Llebaria, A., Loeillet, B., Magain, P., Mazeh, T., Moutou, C., Ollivier, M., Pätzold, M., Queloz, D., Rouan, D., Shporer, A. and Wuchterl, G., 2008, “Transiting exoplanets from the CoRoT space mission. I. CoRoT-Exo-1b: a low-density short-period planet around a G0V star”, *Astron. Astrophys.*, **482**(3), L17–L20. [DOI], [ADS], [arXiv:0803.3202 [astro-ph]]
- Bean, Jacob L., Kempton, Eliza Miller-Ricci and Homeier, Derek, 2010, “A ground-based transmission spectrum of the super-Earth exoplanet GJ 1214b”, *Nature*, **468**(7324), 669–672. [DOI]URL: <https://doi.org/10.1038/nature09596>
- Bean, Jacob L., Désert, Jean-Michel, Kabath, Petr, Stalder, Brian, Seager, Sara, Miller-Ricci Kempton, Eliza, Berta, Zachory K., Homeier, Derek, Walsh, Shane and Seifahrt, Andreas, 2011, “The Optical and Near-infrared Transmission Spectrum of the Super-Earth GJ 1214b: Further Evidence for a Metal-rich Atmosphere”, *Astrophys. J.*, **743**(1), 92. [DOI], [ADS], [arXiv:1109.0582 [astro-ph.EP]]

- Beaugé, C. and Nesvorný, D., 2013, “Emerging Trends in a Period-Radius Distribution of Close-in Planets”, *Astrophys. J.*, **763**(1), 12. [DOI], [ADS], [arXiv:1211.4533 [astro-ph.EP]]
- Berger, Travis A., Huber, Daniel, Gaidos, Eric and van Saders, Jennifer L., 2018, “Revised Radii of Kepler Stars and Planets Using Gaia Data Release 2”, *Astrophys. J.*, **866**(2), 99. [DOI], [ADS], [arXiv:1805.00231 [astro-ph.EP]]
- Binney, James, Dehnen, Walter and Bertelli, Gianpaolo, 2000, “The age of the solar neighbourhood”, *Mon. Not. Roy. Astron. Soc.*, **318**(3), 658–664. [DOI], [ADS], [arXiv:astro-ph/0003479 [astro-ph]]
- Birnstiel, T., Fang, M. and Johansen, A., 2016, “Dust Evolution and the Formation of Planetesimals”, *Space Science Reviews*, **205**(1-4), 41–75. [DOI]URL: <https://doi.org/10.1007%2Fs11214-016-0256-1>
- Bitsch, B, Forsberg, R, Liu, F and Johansen, A, 2018, “Stellar abundance of binary stars: their role in determining the formation location of super-Earths and ice giants”, *Monthly Notices of the Royal Astronomical Society*, **479**(3), 3690–3707. [DOI], [<https://academic.oup.com/mnras/article-pdf/479/3/3690/25162185/sty1710.pdf>]URL: <https://doi.org/10.1093/mnras/sty1710>
- Bond, Jade C., O’Brien, David P. and Laretta, Dante S., 2010, “The Compositional Diversity of Extrasolar Terrestrial Planets. I. In Situ Simulations”, *Astrophys. J.*, **715**(2), 1050–1070. [DOI], [ADS], [arXiv:1004.0971 [astro-ph.EP]]
- Bonomo, A. S., Desidera, S., Benatti, S., Borsa, F., Crespi, S., Damasso, M., Lanza, A. F., Sozzetti, A., Lodato, G., Marzari, F., Boccato, C., Claudi, R. U., Cosentino, R., Covino, E., Gratton, R., Maggio, A., Micela, G., Molinari, E., Pagano, I., Piotto, G., Poretti, E., Smareglia, R., Affer, L., Biazzo, K., Bignamini, A., Esposito, M., Giacobbe, P., Hébrard, G., Malavolta, L., Maldonado, J., Mancini, L., Martinez Fiorenzano, A., Masiero, S., Nascimbeni, V., Pedani, M., Rainer, M. and Scandariato, G., 2017, “The GAPS Programme

- with HARPS-N at TNG . XIV. Investigating giant planet migration history via improved eccentricity and mass determination for 231 transiting planets”, *Astron. Astrophys.*, **602**, A107. [DOI], [ADS], [arXiv:1704.00373 [astro-ph.EP]]
- Borucki, William J., Koch, David, Basri, Gibor, Batalha, Natalie, Brown, Timothy, Caldwell, Douglas, Caldwell, John, Christensen-Dalsgaard, Jørgen, Cochran, William D., DeVore, Edna, Dunham, Edward W., Dupree, Andrea K., Gautier, Thomas N., Geary, John C., Gilliland, Ronald, Gould, Alan, Howell, Steve B., Jenkins, Jon M., Kondo, Yoji, Latham, David W., Marcy, Geoffrey W., Meibom, Søren, Kjeldsen, Hans, Lissauer, Jack J., Monet, David G., Morrison, David, Sasselov, Dimitar, Tarter, Jill, Boss, Alan, Brownlee, Don, Owen, Toby, Buzasi, Derek, Charbonneau, David, Doyle, Laurance, Fortney, Jonathan, Ford, Eric B., Holman, Matthew J., Seager, Sara, Steffen, Jason H., Welsh, William F., Rowe, Jason, Anderson, Howard, Buchhave, Lars, Ciardi, David, Walkowicz, Lucianne, Sherry, William, Horch, Elliott, Isaacson, Howard, Everett, Mark E., Fischer, Debra, Torres, Guillermo, Johnson, John Asher, Endl, Michael, MacQueen, Phillip, Bryson, Stephen T., Dotson, Jessie, Haas, Michael, Kolodziejczak, Jeffrey, Van Cleve, Jeffrey, Chandrasekaran, Hema, Twicken, Joseph D., Quintana, Elisa V., Clarke, Bruce D., Allen, Christopher, Li, Jie, Wu, Haley, Tenenbaum, Peter, Verner, Ekaterina, Bruhweiler, Frederick, Barnes, Jason and Prsa, Andrej, 2010, “Kepler Planet-Detection Mission: Introduction and First Results”, *Science*, **327**(5968), 977. [DOI], [ADS]
- Boss, A. P., 1997, “Giant planet formation by gravitational instability.”, *Science*, **276**, 1836–1839. [DOI], [ADS]
- Brewer, John M. and Fischer, Debra A., 2018, “Spectral Properties of Cool Stars: Extended Abundance Analysis of Kepler Objects of Interest”, *Astrophys. J. Suppl.*, **237**(2), 38. [DOI], [ADS], [arXiv:1804.00673 [astro-ph.SR]]
- Brown, Timothy M., 2001, “Transmission Spectra as Diagnostics of Extrasolar Giant Planet Atmospheres”, *The Astrophysical Journal*, **553**(2), 1006–1026.

[DOI]URL:

<https://doi.org/10.1086%2F320950>

Burke, Christopher J., Christiansen, Jessie L., Mullally, F., Seader, Shawn, Huber, Daniel, Rowe, Jason F., Coughlin, Jeffrey L., Thompson, Susan E., Catanzarite, Joseph, Clarke, Bruce D., Morton, Timothy D., Caldwell, Douglas A., Bryson, Stephen T., Haas, Michael R., Batalha, Natalie M., Jenkins, Jon M., Tenenbaum, Peter, Twicken, Joseph D., Li, Jie, Quintana, Elisa, Barclay, Thomas, Henze, Christopher E., Borucki, William J., Howell, Steve B. and Still, Martin, 2015, “Terrestrial Planet Occurrence Rates for the Kepler GK Dwarf Sample”, *Astrophys. J.*, **809**(1), 8. [DOI], [ADS], [arXiv:1506.04175 [astro-ph.EP]]

Burton, J. R., Watson, C. A., Rodríguez-Gil, P., Skillen, I., Littlefair, S. P., Dhillon, S. and Pollacco, D., 2015, “Defocused transmission spectroscopy: a potential detection of sodium in the atmosphere of WASP-12b”, *Mon. Not. Roy. Astron. Soc.*, **446**(1), 1071–1082. [DOI], [ADS], [arXiv:1410.3702 [astro-ph.EP]]

Carollo, Daniela, Beers, Timothy C., Bovy, Jo, Sivarani, Thirupathi, Norris, John E., Freeman, Ken C., Aoki, Wako, Lee, Young Sun and Kennedy, Catherine R., 2012, “Carbon-enhanced Metal-poor Stars in the Inner and Outer Halo Components of the Milky Way”, *Astrophys. J.*, **744**(2), 195. [DOI], [ADS], [arXiv:1103.3067 [astro-ph.GA]]

Castelli, F. and Kurucz, R. L., 2003a, “New Grids of ATLAS9 Model Atmospheres”, in *Modelling of Stellar Atmospheres*, (Eds.) Piskunov, N., Weiss, W. W., Gray, D. F., 210, [ADS], [arXiv:astro-ph/0405087 [astro-ph]]

Castelli, F. and Kurucz, R. L., 2003b, “New Grids of ATLAS9 Model Atmospheres”, in *Modelling of Stellar Atmospheres*, (Eds.) Piskunov, N., Weiss, W. W., Gray, D. F., 210, [ADS], [arXiv:astro-ph/0405087 [astro-ph]]

Castelli, F. and Kurucz, R. L., 2003c, “New Grids of ATLAS9 Model Atmospheres”, in *Modelling of Stellar Atmospheres*, (Eds.) Piskunov, N., Weiss, W. W., Gray, D. F., 210, [ADS], [arXiv:astro-ph/0405087 [astro-ph]]

- Cegla, H., 2019, “The Impact of Stellar Surface Magnetoconvection and Oscillations on the Detection of Temperate, Earth-Mass Planets Around Sun-Like Stars”, *Geosciences*, **9**(3), 114. [DOI]URL: <https://doi.org/10.3390%2Fgeosciences9030114>
- Cegla, H. M., Lovis, C., Bourrier, V., Beeck, B., Watson, C. A. and Pepe, F., 2016, “The Rossiter-McLaughlin effect reloaded: Probing the 3D spin-orbit geometry, differential stellar rotation, and the spatially-resolved stellar spectrum of star-planet systems”, *Astron. Astrophys.*, **588**, A127. [DOI], [ADS], [arXiv:1602.00322 [astro-ph.EP]]
- Charbonneau, David, Brown, Timothy M., Noyes, Robert W. and Gilliland, Ronald L., 2002a, “Detection of an Extrasolar Planet Atmosphere”, *Astrophys. J.*, **568**(1), 377–384. [DOI], [ADS], [arXiv:astro-ph/0111544 [astro-ph]]
- Charbonneau, David, Brown, Timothy M., Noyes, Robert W. and Gilliland, Ronald L., 2002b, “Detection of an Extrasolar Planet Atmosphere”, *Astrophys. J.*, **568**(1), 377–384. [DOI], [ADS], [arXiv:astro-ph/0111544 [astro-ph]]
- Chen, G., Pallé, E., Nortmann, L., Murgas, F., Parviainen, H. and Nowak, G., 2017, “The GTC exoplanet transit spectroscopy survey. VI. Detection of sodium in WASP-52b’s cloudy atmosphere”, *Astron. Astrophys.*, **600**, L11. [DOI], [ADS], [arXiv:1703.06716 [astro-ph.EP]]
- Cui, Xiang-Qun, Zhao, Yong-Heng, Chu, Yao-Quan, Li, Guo-Ping, Li, Qi, Zhang, Li-Ping, Su, Hong-Jun, Yao, Zheng-Qiu, Wang, Ya-Nan, Xing, Xiao-Zheng, Li, Xin-Nan, Zhu, Yong-Tian, Wang, Gang, Gu, Bo-Zhong, Luo, A. Li, Xu, Xin-Qi, Zhang, Zhen-Chao, Liu, Gen-Rong, Zhang, Hao-Tong, Yang, De-Hua, Cao, Shu-Yun, Chen, Hai-Yuan, Chen, Jian-Jun, Chen, Kun-Xin, Chen, Ying, Chu, Jia-Ru, Feng, Lei, Gong, Xue-Fei, Hou, Yong-Hui, Hu, Hong-Zhuan, Hu, Ning-Sheng, Hu, Zhong-Wen, Jia, Lei, Jiang, Fang-Hua, Jiang, Xiang, Jiang, Zi-Bo, Jin, Ge, Li, Ai-Hua, Li, Yan, Li, Ye-Ping, Liu, Guan-Qun, Liu, Zhi-Gang, Lu,

- Wen-Zhi, Mao, Yin-Dun, Men, Li, Qi, Yong-Jun, Qi, Zhao-Xiang, Shi, Huo-Ming, Tang, Zheng-Hong, Tao, Qing-Sheng, Wang, Da-Qi, Wang, Dan, Wang, Guo-Min, Wang, Hai, Wang, Jia-Ning, Wang, Jian, Wang, Jian-Ling, Wang, Jian-Ping, Wang, Lei, Wang, Shu-Qing, Wang, You, Wang, Yue-Fei, Xu, Ling-Zhe, Xu, Yan, Yang, Shi-Hai, Yu, Yong, Yuan, Hui, Yuan, Xiang-Yan, Zhai, Chao, Zhang, Jing, Zhang, Yan-Xia, Zhang, Yong, Zhao, Ming, Zhou, Fang, Zhou, Guo-Hua, Zhu, Jie and Zou, Si-Cheng, 2012, “The Large Sky Area Multi-Object Fiber Spectroscopic Telescope (LAMOST)”, *Research in Astronomy and Astrophysics*, **12**(9), 1197–1242. [DOI], [ADS]
- Delgado Mena, E., Israelian, G., González Hernández, J. I., Bond, J. C., Santos, N. C., Udry, S. and Mayor, M., 2010, “Chemical Clues on the Formation of Planetary Systems: C/O Versus Mg/Si for HARPS GTO Sample”, *Astrophys. J.*, **725**(2), 2349–2358. [DOI], [ADS], [arXiv:1009.5224 [astro-ph.SR]]
- Delgado Mena, E., Israelian, G., González Hernández, J. I., Sousa, S. G., Mortier, A., Santos, N. C., Adibekyan, V. Zh., Fernandes, J., Rebolo, R., Udry, S. and Mayor, M., 2014, “Li depletion in solar analogues with exoplanets. Extending the sample”, *Astron. Astrophys.*, **562**, A92. [DOI], [ADS], [arXiv:1311.6414 [astro-ph.EP]]
- Delgado Mena, E., Bertrán de Lis, S., Adibekyan, V. Zh., Sousa, S. G., Figueira, P., Mortier, A., González Hernández, J. I., Tsantaki, M., Israelian, G. and Santos, N. C., 2015, “Li abundances in F stars: planets, rotation, and Galactic evolution”, *Astron. Astrophys.*, **576**, A69. [DOI], [ADS], [arXiv:1412.4618 [astro-ph.SR]]
- Dumusque, Xavier, Glenday, Alex, Phillips, David F., Buchschacher, Nicolas, Collier Cameron, Andrew, Ceconi, Massimo, Charbonneau, David, Cosentino, Rosario, Ghedina, Adriano, Latham, David W., Li, Chih-Hao, Lodi, Marcello,

- Lovis, Christophe, Molinari, Emilio, Pepe, Francesco, Udry, Stéphane, Sasselov, Dimitar, Szentgyorgyi, Andrew and Walsworth, Ronald, 2015, “HARPS-N Observes the Sun as a Star”, *Astrophys. J. Lett.*, **814**(2), L21. [DOI], [ADS], [arXiv:1511.02267 [astro-ph.EP]]
- Ecuivillon, A., Israelian, G., Santos, N. C., Mayor, M., Villar, V. and Bihain, G., 2004, “C, S, Zn and Cu abundances in planet-harboring stars”, *Astron. Astrophys.*, **426**, 619–630. [DOI], [ADS], [arXiv:astro-ph/0406584 [astro-ph]]
- Espinoza, Néstor, Rackham, Benjamin V., Jordán, Andrés, Apai, Dániel, López-Morales, Mercedes, Osip, David J., Grimm, Simon L., Hoeijmakers, Jens, Wilson, Paul A., Bixel, Alex, McGruder, Chima, Rodler, Florian, Weaver, Ian, Lewis, Nikole K., Fortney, Jonathan J. and Fraine, Jonathan, 2019, “ACCESS: a featureless optical transmission spectrum for WASP-19b from Magellan/IMACS”, *Mon. Not. Roy. Astron. Soc.*, **482**(2), 2065–2087. [DOI], [ADS], [arXiv:1807.10652 [astro-ph.EP]]
- Figueira, P., Faria, J. P., Delgado-Mena, E., Adibekyan, V. Zh., Sousa, S. G., Santos, N. C. and Israelian, G., 2014, “Exoplanet hosts reveal lithium depletion. Results from a homogeneous statistical analysis”, *Astron. Astrophys.*, **570**, A21. [DOI], [ADS], [arXiv:1409.0890 [astro-ph.EP]]
- Fischer, Debra A. and Valenti, Jeff, 2005a, “The Planet-Metallicity Correlation”, *Astrophys. J.*, **622**(2), 1102–1117. [DOI], [ADS]
- Fischer, Debra A. and Valenti, Jeff, 2005b, “The Planet-Metallicity Correlation”, *Astrophys. J.*, **622**(2), 1102–1117. [DOI], [ADS]
- Fulton, Benjamin J., Petigura, Erik A., Howard, Andrew W., Isaacson, Howard, Marcy, Geoffrey W., Cargile, Phillip A., Hebb, Leslie, Weiss, Lauren M., Johnson, John Asher, Morton, Timothy D., Sinukoff, Evan, Crossfield, Ian J. M. and Hirsch, Lea A., 2017a, “The California-Kepler Survey. III. A Gap in the Radius Distribution of Small Planets”, *Astron. J.*, **154**(3), 109. [DOI], [ADS], [arXiv:1703.10375 [astro-ph.EP]]

- Fulton, Benjamin J., Petigura, Erik A., Howard, Andrew W., Isaacson, Howard, Marcy, Geoffrey W., Cargile, Phillip A., Hebb, Leslie, Weiss, Lauren M., Johnson, John Asher, Morton, Timothy D., Sinukoff, Evan, Crossfield, Ian J. M. and Hirsch, Lea A., 2017b, “The California-Kepler Survey. III. A Gap in the Radius Distribution of Small Planets”, *Astron. J.*, **154**(3), 109. [DOI], [ADS], [arXiv:1703.10375 [astro-ph.EP]]
- Gaudi, B. Scott, Meyer, Michael and Christiansen, Jessie, 2021, “The Demographics of Exoplanets”, in *ExoFrontiers; Big Questions in Exoplanetary Science*, (Ed.) Madhusudhan, Nikku, pp. 2–1. [DOI], [ADS]
- Gebek, Andrea and Oza, Apurva V., 2020, “Alkaline exospheres of exoplanet systems: evaporative transmission spectra”, *Mon. Not. Roy. Astron. Soc.*, **497**(4), 5271–5291. [DOI], [ADS], [arXiv:2005.02536 [astro-ph.EP]]
- Gibson, N. P., Aigrain, S., Barstow, J. K., Evans, T. M., Fletcher, L. N. and Irwin, P. G. J., 2013, “The optical transmission spectrum of the hot Jupiter HAT-P-32b: clouds explain the absence of broad spectral features?”, *Mon. Not. Roy. Astron. Soc.*, **436**(4), 2974–2988. [DOI], [ADS], [arXiv:1309.6998 [astro-ph.EP]]
- Gomes da Silva, J., Santos, N. C., Bonfils, X., Delfosse, X., Forveille, T. and Udry, S., 2011, “Long-term magnetic activity of a sample of M-dwarf stars from the HARPS program. I. Comparison of activity indices”, *Astron. Astrophys.*, **534**, A30. [DOI], [ADS], [arXiv:1109.0321 [astro-ph.SR]]
- Gonzalez, G., 2014, “Parent stars of extrasolar planets – XIV. Strong evidence of Li abundance deficit”, *MNRAS*, **446**(1), 1020–1025. [DOI], [https://academic.oup.com/mnras/article-pdf/446/1/1020/13767221/stu2156.pdf]URL: <https://doi.org/10.1093/mnras/stu2156>
- Gonzalez, G., Carlson, M. K. and Tobin, R. W., 2010, “Parent stars of extrasolar planets - XI. Trends with condensation temperature revisited”, *Mon. Not. Roy. Astron. Soc.*, **407**(1), 314–320. [DOI], [ADS], [arXiv:1004.3313 [astro-ph.SR]]

- Gonzalez, Guillermo, 1997a, “The stellar metallicity-giant planet connection”, *Mon. Not. Roy. Astron. Soc.*, **285**(2), 403–412. [DOI], [ADS]
- Gonzalez, Guillermo, 1997b, “The stellar metallicity-giant planet connection”, *Mon. Not. Roy. Astron. Soc.*, **285**(2), 403–412. [DOI], [ADS]
- Gonzalez, Guillermo, 1998, “Spectroscopic analyses of the parent stars of extrasolar planetary system candidates”, *Astron. Astrophys.*, **334**, 221–238. [ADS]
- González Hernández, J. I., Israelian, G., Santos, N. C., Sousa, S., Delgado-Mena, E., Neves, V. and Udry, S., 2010, “Searching for the Signatures of Terrestrial Planets in Solar Analogs”, *Astrophys. J.*, **720**(2), 1592–1602. [DOI], [ADS], [arXiv:1007.0580 [astro-ph.SR]]
- González Hernández, J. I., Delgado-Mena, E., Sousa, S. G., Israelian, G., Santos, N. C., Adibekyan, V. Zh. and Udry, S., 2013, “Searching for the signatures of terrestrial planets in F-, G-type main-sequence stars”, *A&A*, **552**, A6. [DOI]URL: <https://doi.org/10.1051/0004-6361/201220165>
- Grevesse, N., Asplund, M. and Sauval, A. J., 2007, “The Solar Chemical Composition”, *Space Sci. Rev.*, **130**(1-4), 105–114. [DOI], [ADS]
- Gustafsson, B., Karlsson, T., Olsson, E., Edvardsson, B. and Ryde, N., 1999, “The origin of carbon, investigated by spectral analysis of solar-type stars in the Galactic Disk”, *Astron. Astrophys.*, **342**, 426–439. [ADS], [arXiv:astro-ph/9811303 [astro-ph]]
- Hamer, Jacob H. and Schlaufman, Kevin C., 2019, “Hot Jupiters Are Destroyed by Tides While Their Host Stars Are on the Main Sequence”, *Astron. J.*, **158**(5), 190. [DOI], [ADS], [arXiv:1908.06998 [astro-ph.EP]]
- Haywood, Raphaëlle Dawn, Collier Cameron, A, Unruh, YC, Lovis, C, Lanza, Antonino Francesco, Llama, Joe, Deleuil, M, Fares, Rim, Gillon, Michaël, Moutou, C *et al.*, 2016, “The Sun as a planet-host star: proxies from SDO images for

HARPS radial-velocity variations”, *Monthly Notices of the Royal Astronomical Society*, **457**(4), 3637–3651

Haywood, RD, Milbourne, TW, Saar, SH, Mortier, A, Phillips, D, Charbonneau, D, Cameron, A Collier, Cegla, HM, Meunier, N and Palumbo III, ML, 2020, “Unsigned magnetic flux as a proxy for radial-velocity variations in Sun-like stars”, *arXiv preprint arXiv:2005.13386*

Heng, Kevin, Wytttenbach, Aurélien, Lavie, Baptiste, Sing, David K., Ehrenreich, David and Lovis, Christophe, 2015, “A Non-isothermal Theory for Interpreting Sodium Lines in Transmission Spectra of Exoplanets”, *Astrophys. J. Lett.*, **803**(1), L9. [DOI], [ADS], [arXiv:1503.05582 [astro-ph.EP]]

Hoeijmakers, H. J., Seidel, J. V., Pino, L., Kitzmann, D., Sindel, J. P., Ehrenreich, D., Oza, A. V., Bourrier, V., Allart, R., Gebek, A., Lovis, C., Yurchenko, S. N., Astudillo-Defru, N., Bayliss, D., Cegla, H., Lavie, B., Lendl, M., Melo, C., Murgas, F., Nascimbeni, V., Pepe, F., Ségransan, D., Udry, S., Wytttenbach, A. and Heng, K., 2020, “Hot Exoplanet Atmospheres Resolved with Transit Spectroscopy (HEARTS). IV. A spectral inventory of atoms and molecules in the high-resolution transmission spectrum of WASP-121 b”, *Astron. Astrophys.*, **641**, A123. [DOI], [ADS], [arXiv:2006.11308 [astro-ph.EP]]

Howard, Andrew W., Marcy, Geoffrey W., Bryson, Stephen T., Jenkins, Jon M., Rowe, Jason F., Batalha, Natalie M., Borucki, William J., Koch, David G., Dunham, Edward W., Gautier, Thomas N., III, Van Cleve, Jeffrey, Cochran, William D., Latham, David W., Lissauer, Jack J., Torres, Guillermo, Brown, Timothy M., Gilliland, Ronald L., Buchhave, Lars A., Caldwell, Douglas A., Christensen-Dalsgaard, Jørgen, Ciardi, David, Fressin, Francois, Haas, Michael R., Howell, Steve B., Kjeldsen, Hans, Seager, Sara, Rogers, Leslie, Sasselov, Dimitar D., Steffen, Jason H., Basri, Gibor S., Charbonneau, David, Christiansen, Jessie, Clarke, Bruce, Dupree, Andrea, Fabrycky, Daniel C., Fischer, Debra A., Ford, Eric B., Fortney, Jonathan J., Tarter, Jill, Girouard, Forrest R., Holman, Matthew J., Johnson, John Asher, Klaus, Todd C., Machalek,

- Pavel, Moorhead, Althea V., Morehead, Robert C., Ragozzine, Darin, Tenenbaum, Peter, Twicken, Joseph D., Quinn, Samuel N., Isaacson, Howard, Shporer, Avi, Lucas, Philip W., Walkowicz, Lucianne M., Welsh, William F., Boss, Alan, Devore, Edna, Gould, Alan, Smith, Jeffrey C., Morris, Robert L., Prsa, Andrej, Morton, Timothy D., Still, Martin, Thompson, Susan E., Mulally, Fergal, Endl, Michael and MacQueen, Phillip J., 2012, “Planet Occurrence within 0.25 AU of Solar-type Stars from Kepler”, *Astrophys. J. Suppl.*, **201**(2), 15. [DOI], [ADS], [arXiv:1103.2541 [astro-ph.EP]]
- III, Claude E. Mack, Schuler, Simon C., Stassun, Keivan G. and Norris, John, 2014, “Detailed abundances of planet-hosting wide binaries. I. Did planet formation imprint chemical signatures in the atmospheres of HD 20782/81?*”, *The Astrophysical Journal*, **787**(2), 98. [DOI]URL: <https://dx.doi.org/10.1088/0004-637X/787/2/98>
- Israelian, Garik, Mena, Elisa Delgado, Santos, Nuno C., Sousa, Sergio G., Mayor, Michel, Udry, Stephane, Cerdeña, Carolina Domínguez, Rebolo, Rafael and Randich, Sofia, 2009, “Enhanced lithium depletion in Sun-like stars with orbiting planets”, *Nature*, **462**(7270), 189–191. [DOI]URL: <https://doi.org/10.1038/nature08483>
- Jensen, Adam G., Cauley, P. Wilson, Redfield, Seth, Cochran, William D. and Endl, Michael, 2018, “Hydrogen and Sodium Absorption in the Optical Transmission Spectrum of WASP-12b”, *The Astronomical Journal*, **156**(4), 154. [DOI]URL: <https://doi.org/10.3847/1538-3881/aadca7>
- Johnson, Dean R. H. and Soderblom, David R., 1987, “Calculating Galactic Space Velocities and Their Uncertainties, with an Application to the Ursa Major Group”, *Astron. J.*, **93**, 864. [DOI], [ADS]
- Johnson, John Asher, Aller, Kimberly M., Howard, Andrew W. and Crepp, Justin R., 2010a, “Giant Planet Occurrence in the Stellar Mass-Metallicity

- Plane”, *Pub. Astron. Soc. Pac.*, **122**(894), 905. [DOI], [ADS], [arXiv:1005.3084 [astro-ph.EP]]
- Johnson, John Asher, Aller, Kimberly M., Howard, Andrew W. and Crepp, Justin R., 2010b, “Giant Planet Occurrence in the Stellar Mass-Metallicity Plane”, *Pub. Astron. Soc. Pac.*, **122**(894), 905. [DOI], [ADS], [arXiv:1005.3084 [astro-ph.EP]]
- Kausch, W., Noll, S., Smette, A., Kimeswenger, S., Barden, M., Szyszka, C., Jones, A. M., Sana, H., Horst, H. and Kerber, F., 2015, “Molecfit: A general tool for telluric absorption correction. II. Quantitative evaluation on ESO-VLT/X-Shooterspectra”, *Astron. Astrophys.*, **576**, A78. [DOI], [ADS], [arXiv:1501.07265 [astro-ph.IM]]
- Kawauchi, Kiyoe, Narita, Norio, Sato, Bun’ei and Kawashima, Yui, 2021, “Investigation of the upper atmosphere in ultra-hot Jupiter WASP-76 b with high-resolution spectroscopy”, *arXiv e-prints*, arXiv:2112.02546. [ADS], [arXiv:2112.02546 [astro-ph.EP]]
- Kempton, Eliza M. R., Lupu, Roxana, Owusu-Asare, Albert, Slough, Patrick and Cale, Bryson, 2017, “Exo-Transmit: An Open-Source Code for Calculating Transmission Spectra for Exoplanet Atmospheres of Varied Composition”, *Pub. Astron. Soc. Pac.*, **129**(974), 044 402. [DOI], [ADS], [arXiv:1611.03871 [astro-ph.EP]]
- Khalafinejad, S., von Essen, C., Hoeijmakers, H. J., Zhou, G., Klocová, T., Schmitt, J. H. M. M., Dreizler, S., Lopez-Morales, M., Husser, T. O., Schmidt, T. O. B. and Collet, R., 2017, “Exoplanetary atmospheric sodium revealed by orbital motion. Narrow-band transmission spectroscopy of HD 189733b with UVES”, *Astron. Astrophys.*, **598**, A131. [DOI], [ADS], [arXiv:1610.01610 [astro-ph.EP]]
- Knutson, Heather A., Charbonneau, David, Noyes, Robert W., Brown, Timothy M. and Gilliland, Ronald L., 2007, “Using Stellar Limb-Darkening to Refine

- the Properties of HD 209458b”, *The Astrophysical Journal*, **655**(1), 564–575.
[DOI]URL:
<https://doi.org/10.1086%2F510111>
- Kobayashi, Chiaki, Karakas, Amanda I. and Lugaro, Maria, 2020, “The Origin of Elements from Carbon to Uranium”, *The Astrophysical Journal*, **900**(2), 179.
[DOI]URL:
<https://doi.org/10.3847/1538-4357/abae65>
- Koch, David G., Borucki, William, Dunham, Edward, Geary, John, Gilliland, Ronald, Jenkins, Jon, Latham, David, Bachtell, Eric, Berry, Dan, Deining, William, Duren, Riley, Gautier, Thomas N., Gillis, Ladd, Mayer, David, Miller, Chris D., Shafer, Dan, Sobek, Charles K., Stewart, Chris and Weiss, Michael, 2004, “Overview and status of the Kepler Mission”, in *Optical, Infrared, and Millimeter Space Telescopes*, (Ed.) Mather, John C., Society of Photo-Optical Instrumentation Engineers (SPIE) Conference Series, 5487, [DOI], [ADS]
- Kratter, K. M., 2011, “The Formation of Close Binaries”, in *Evolution of Compact Binaries*, (Eds.) Schmidtbreick, L., Schreiber, M. R., Tappert, C., Astronomical Society of the Pacific Conference Series, 447, [ADS], [arXiv:1109.3740 astro-ph.SR]
- Lam, K. W. F., Faedi, F., Brown, D. J. A., Anderson, D. R., Delrez, L., Gillon, M., Hébrard, G., Lendl, M., Mancini, L., Southworth, J., Smalley, B., Triaud, A. H. M., Turner, O. D., Hay, K. L., Armstrong, D. J., Barros, S. C. C., Bonomo, A. S., Bouchy, F., Boumis, P., Collier Cameron, A., Doyle, A. P., Hellier, C., Henning, T., Jehin, E., King, G., Kirk, J., Louden, T., Maxted, P. F. L., McCormac, J. J., Osborn, H. P., Palle, E., Pepe, F., Pollacco, D., Prieto-Arranz, J., Queloz, D., Rey, J., Ségransan, D., Udry, S., Walker, S., West, R. G. and Wheatley, P. J., 2017, “From dense hot Jupiter to low-density Neptune: The discovery of WASP-127b, WASP-136b, and WASP-138b”, *Astron. Astrophys.*, **599**, A3. [DOI], [ADS], [arXiv:1607.07859 astro-ph.EP]

- Lecavelier Des Etangs, A., Vidal-Madjar, A., Désert, J. M. and Sing, D., 2008, “Rayleigh scattering by H₂ in the extrasolar planet HD 209458b”, *Astron. Astrophys.*, **485**(3), 865–869. [DOI], [ADS], [arXiv:0805.0595 [astro-ph]]
- Lee, Young Sun, Beers, Timothy C., Sivarani, Thirupathi, Allende Prieto, Carlos, Koesterke, Lars, Wilhelm, Ronald, Re Fiorentin, Paola, Bailer-Jones, Coryn A. L., Norris, John E., Rockosi, Constance M., Yanny, Brian, Newberg, Heidi J., Covey, Kevin R., Zhang, Hao-Tong and Luo, A. Li, 2008, “The SEGUE Stellar Parameter Pipeline. I. Description and Comparison of Individual Methods”, *Astron. J.*, **136**(5), 2022–2049. [DOI], [ADS], [arXiv:0710.5645 [astro-ph]]
- Lendl, M., Anderson, D. R., Collier-Cameron, A., Doyle, A. P., Gillon, M., Hellier, C., Jehin, E., Lister, T. A., Maxted, P. F. L., Pepe, F., Pollacco, D., Queloz, D., Smalley, B., Ségransan, D., Smith, A. M. S., Triaud, A. H. M. J., Udry, S., West, R. G. and Wheatley, P. J., 2012, “WASP-42 b and WASP-49 b: two new transiting sub-Jupiters”, *Astron. Astrophys.*, **544**, A72. [DOI], [ADS], [arXiv:1205.2757 [astro-ph.EP]]
- Liu, F., Asplund, M., Ramirez, I., Yong, D. and Melendez, J., 2014, “A high-precision chemical abundance analysis of the HAT-P-1 stellar binary: constraints on planet formation.”, *Mon. Not. Roy. Astron. Soc.*, **442**, L51–L55. [DOI], [ADS], [arXiv:1404.2112 [astro-ph.SR]]
- Liu, F., Asplund, M., Yong, D., Meléndez, J., Ramírez, I., Karakas, A. I., Carlos, M. and Marino, A. F., 2016, “The chemical compositions of solar twins in the open cluster M67”, *Monthly Notices of the Royal Astronomical Society*, **463**(1), 696–704. [DOI], [https://academic.oup.com/mnras/article-pdf/463/1/696/18756852/stw2045.pdf]URL: <https://doi.org/10.1093/mnras/stw2045>
- Liu, F., Yong, D., Asplund, M., Feltzing, S., Mustill, A. J., Meléndez, J., Ramírez, I. and Lin, J., 2018, “Detailed chemical compositions of the wide binary HD

- 80606/80607: revised stellar properties and constraints on planet formation”, *Astron. Astrophys.*, **614**, A138. [DOI], [ADS], [arXiv:1802.09306 [astro-ph.SR]]
- Liu, Y, Hoeksema, JT, Scherrer, PH, Schou, J, Couvidat, S, Bush, RI, Duvall, TL, Hayashi, K, Sun, X and Zhao, X, 2012, “Comparison of line-of-sight magnetograms taken by the solar dynamics observatory/helioseismic and magnetic imager and solar and heliospheric observatory/Michelson Doppler imager”, *Solar Physics*, **279**(1), 295–316
- Liu (), Fan, Bitsch, Bertram, Asplund, Martin, Liu (), Bei-Bei, Murphy, Michael T, Yong, David, Ting (), Yuan-Sen and Feltzing, Sofia, 2021, “Detailed elemental abundances of binary stars: searching for signatures of planet formation and atomic diffusion”, *Monthly Notices of the Royal Astronomical Society*, **508**(1), 1227–1240. [DOI], [https://academic.oup.com/mnras/article-pdf/508/1/1227/40503211/stab2471.pdf]URL: <https://doi.org/10.1093/mnras/stab2471>
- Lodders, Katharina, 2003, “Solar System Abundances and Condensation Temperatures of the Elements”, *Astrophys. J.*, **591**(2), 1220–1247. [DOI], [ADS]
- Louden, Tom and Wheatley, Peter J., 2015, “Spatially Resolved Eastward Winds and Rotation of HD 189733b”, *Astrophys. J. Lett.*, **814**(2), L24. [DOI], [ADS], [arXiv:1511.03689 [astro-ph.EP]]
- Luo, Ali, Zhang, Jiannan, Chen, Jianjun, Song, Yihan, Wu, Yue, Bai, Zhongrui, Wang, Fengfei, Du, Bing and Zhang, Haotong, 2014, “Data reduction and calibration for LAMOST survey”, in *Setting the scene for Gaia and LAMOST*, (Eds.) Feltzing, Sofia, Zhao, Gang, Walton, Nicholas A., Whitelock, Patricia, 298, [DOI], [ADS]
- Mack, Claude E., III, Stassun, Keivan G., Schuler, Simon C., Hebb, Leslie and Pepper, Joshua A., 2016, “Detailed Abundances of Planet-hosting Wide Binaries. II. HD80606+HD80607”, *Astrophys. J.*, **818**(1), 54. [DOI], [ADS], [arXiv:1601.00018 [astro-ph.SR]]

- Madhusudhan, Nikku, 2012, “C/O RATIO AS A DIMENSION FOR CHARACTERIZING EXOPLANETARY ATMOSPHERES”, *The Astrophysical Journal*, **758**(1), 36. [DOI]URL:
<https://doi.org/10.1088/0004-637x/758/1/36>
- Madhusudhan, Nikku, 2019, “Exoplanetary Atmospheres: Key Insights, Challenges, and Prospects”, *Ann. Rev. Astron. Astrophys.*, **57**, 617–663. [DOI], [ADS], [arXiv:1904.03190 [astro-ph.EP]]
- Mandell, Avi, 2011, “Protoplanetary Disk, Instability”, in *Encyclopedia of Astrobiology*, (Eds.) Gargaud, Muriel, Amils, Ricardo, Quintanilla, José Cernicharo, Cleaves, Henderson James (Jim), Irvine, William M., Pinti, Daniele L., Viso, Michel, Springer Berlin Heidelberg, Berlin, Heidelberg. pp. 1376–1377. [DOI]URL:
https://doi.org/10.1007/978-3-642-11274-4_443
- Manoj, P. and Bhatt, H. C., 2005, “Kinematics of Vega-like stars: Lifetimes and temporal evolution of circumstellar dust disks”, *Astron. Astrophys.*, **429**, 525–530. [DOI], [ADS], [arXiv:astro-ph/0409317 [astro-ph]]
- Mathur, Savita, Huber, Daniel, Batalha, Natalie M., Ciardi, David R., Bastien, Fabienne A., Bieryla, Allyson, Buchhave, Lars A., Cochran, William D., Endl, Michael, Esquerdo, Gilbert A., Furlan, Elise, Howard, Andrew, Howell, Steve B., Isaacson, Howard, Latham, David W., MacQueen, Phillip J. and Silva, David R., 2017, “Revised Stellar Properties of iKepler/i Targets for the Q1-17 (DR25) Transit Detection Run”, *The Astrophysical Journal Supplement Series*, **229**(2), 30. [DOI]URL:
<https://doi.org/10.3847/1538-4365/229/2/30>
- Mayor, M., Pepe, F., Queloz, D., Bouchy, F., Rupprecht, G., Lo Curto, G., Avila, G., Benz, W., Bertaux, J. L., Bonfils, X., Dall, Th., Dekker, H., Delabre, B., Eckert, W., Fleury, M., Gilliotte, A., Gojak, D., Guzman, J. C., Kohler, D., Lizon, J. L., Longinotti, A., Lovis, C., Megevand, D., Pasquini, L., Reyes, J.,

- Sivan, J. P., Sosnowska, D., Soto, R., Udry, S., van Kesteren, A., Weber, L. and Weilenmann, U., 2003, “Setting New Standards with HARPS”, *The Messenger*, **114**, 20–24. [[ADS](#)]
- Mayor, Michel and Queloz, Didier, 1995, “A Jupiter-mass companion to a solar-type star”, *Nature*, **378**(6555), 355–359. [[DOI](#)], [[ADS](#)]
- McLeod, Kim K., Rodriguez, Joseph E., Oelkers, Ryan J., Collins, Karen A., Bieryla, Allyson, Fulton, Benjamin J., Stassun, Keivan G., Gaudi, B. Scott, Penev, Kaloyan, Stevens, Daniel J., Colón, Knicole D., Pepper, Joshua, Narita, Norio, Tsuguru, Ryu, Fukui, Akihiko, Reed, Phillip A., Tirrell, Bethany, Visgaitis, Tiffany, Kielkopf, John F., Cohen, David H., Jensen, Eric L. N., Gregorio, Joao, Baştürk, Özgür, Oberst, Thomas E., Melton, Casey, Kempton, Eliza M. R., Baldrige, Andrew, Zhao, Y. Sunny, Zambelli, Roberto, Latham, David W., Esquerdo, Gilbert A., Berlind, Perry, Calkins, Michael L., Howard, Andrew W., Isaacson, Howard, Weiss, Lauren M., Benni, Paul, Beatty, Thomas G., Eastman, Jason D., Penny, Matthew T., Siverd, Robert J., Lund, Michael B., Labadie-Bartz, Jonathan, Zhou, G., Curtis, Ivan A., Joner, Michael D., Manner, Mark, Relles, Howard, Scarpetta, Gaetano, Stephens, Denise C., Stockdale, Chris, Tan, T. G., DePoy, D. L., Marshall, Jennifer L., Pogge, Richard W., Trueblood, Mark and Trueblood, Patricia, 2017, “KELT-18b: Puffy Planet, Hot Host, Probably Perturbed”, *Astron. J.*, **153**(6), 263. [[DOI](#)], [[ADS](#)], [[arXiv:1702.01657 \[astro-ph.EP\]](#)]
- Meléndez, J., Asplund, M., Gustafsson, B. and Yong, D., 2009a, “The Peculiar Solar Composition and Its Possible Relation to Planet Formation”, *Astrophys. J. Lett.*, **704**(1), L66–L70. [[DOI](#)], [[ADS](#)], [[arXiv:0909.2299 \[astro-ph.SR\]](#)]
- Meléndez, J., Asplund, M., Gustafsson, B. and Yong, D., 2009b, “The Peculiar Solar Composition and Its Possible Relation to Planet Formation”, *Astrophys. J. Lett.*, **704**(1), L66–L70. [[DOI](#)], [[ADS](#)], [[arXiv:0909.2299 \[astro-ph.SR\]](#)]

- Meléndez, J., Bergemann, M., Cohen, J. G., Endl, M., Karakas, A. I., Ramírez, I., Cochran, W. D., Yong, D., MacQueen, P. J., Kobayashi, C. and Asplund, M., 2012, “The remarkable solar twin HIP 56948: a prime target in the quest for other Earths”, *Astron. Astrophys.*, **543**, A29. [DOI], [ADS], [arXiv:1204.2766 [astro-ph.SR]]
- Milbourne, TW, Haywood, RD, Phillips, DF, Saar, SH, Cegla, HM, Cameron, AC, Costes, J, Dumusque, X, Langellier, N, Latham, DW *et al.*, 2019, “HARPS-n solar RVs are dominated by large, bright magnetic regions”, *The Astrophysical Journal*, **874**(1), 107
- Milbourne, TW, Phillips, DF, Langellier, N, Mortier, A, Haywood, RD, Saar, SH, Cegla, HM, Cameron, A Collier, Dumusque, X, Latham, DW *et al.*, 2021, “Estimating Magnetic Filling Factors from Simultaneous Spectroscopy and Photometry: Disentangling Spots, Plage, and Network”, *The Astrophysical Journal*, **920**(1), 21
- Mishenina, T., Kovtyukh, V., Soubiran, C. and Adibekyan, V. Zh., 2016a, “Behaviour of elements from lithium to europium in stars with and without planets”, *Mon. Not. Roy. Astron. Soc.*, **462**(2), 1563–1576. [DOI], [ADS], [arXiv:1609.01851 [astro-ph.SR]]
- Mishenina, T., Kovtyukh, V., Soubiran, C. and Adibekyan, V. Zh., 2016b, “Behaviour of elements from lithium to europium in stars with and without planets”, *Mon. Not. Roy. Astron. Soc.*, **462**(2), 1563–1576. [DOI], [ADS], [arXiv:1609.01851 [astro-ph.SR]]
- Moses, J. I., Madhusudhan, N., Visscher, C. and Freedman, R. S., 2013, “Chemical Consequences of the C/O Ratio on Hot Jupiters: Examples from WASP-12b, CoRoT-2b, XO-1b, and HD 189733b”, *Astrophys. J.*, **763**(1), 25. [DOI], [ADS], [arXiv:1211.2996 [astro-ph.EP]]

- Mulders, Gijs D., 2018, “Planet Populations as a Function of Stellar Properties”, in *Handbook of Exoplanets*, (Eds.) Deeg, Hans J., Belmonte, Juan Antonio, [DOI], [ADS]
- Mulders, Gijs D., Pascucci, Ilaria, Apai, Dániel, Frasca, Antonio and Molenda-Żakowicz, Joanna, 2016, “A Super-solar Metallicity for Stars with Hot Rocky Exoplanets”, *Astron. J.*, **152**(6), 187. [DOI], [ADS], [arXiv:1609.05898 [astro-ph.EP]]
- Murgas, F., Pallé, E., Zapatero Osorio, M. R., Nortmann, L., Hoyer, S. and Cabrera-Lavers, A., 2014, “The GTC exoplanet transit spectroscopy survey . I. OSIRIS transmission spectroscopy of the short period planet WASP-43b”, *Astron. Astrophys.*, **563**, A41. [DOI], [ADS], [arXiv:1401.3692 [astro-ph.EP]]
- Murgas, F., Chen, G., Pallé, E., Nortmann, L. and Nowak, G., 2019, “The GTC exoplanet transit spectroscopy survey. X. Stellar spots versus Rayleigh scattering: the case of HAT-P-11b”, *Astron. Astrophys.*, **622**, A172. [DOI], [ADS], [arXiv:1812.10154 [astro-ph.EP]]
- Naef, D., Latham, D. W., Mayor, M., Mazeh, T., Beuzit, J. L., Drukier, G. A., Perrier-Bellet, C., Queloz, D., Sivan, J. P., Torres, G., Udry, S. and Zucker, S., 2001, “HD 80606 b, a planet on an extremely elongated orbit”, *Astron. Astrophys.*, **375**, L27–L30. [DOI], [ADS], [arXiv:astro-ph/0106256 [astro-ph]]
- Narang, Mayank, Manoj, P., Furlan, E., Mordasini, C., Henning, Thomas, Mathew, Blesson, Banyal, Ravinder K. and Sivarani, T., 2018, “Properties and Occurrence Rates for Kepler Exoplanet Candidates as a Function of Host Star Metallicity from the DR25 Catalog”, *Astron. J.*, **156**(5), 221. [DOI], [ADS], [arXiv:1809.08385 [astro-ph.EP]]
- Nascimbeni, V., Cunial, A., Murabito, S., Sada, P. V., Aparicio, A., Piotto, G., Bedin, L. R., Milone, A. P., Rosenberg, A., Zurlo, A., Borsato, L., Damasso, M., Granata, V. and Malavolta, L., 2013, “TASTE. III. A homogeneous study

- of transit time variations in WASP-3b”, *Astron. Astrophys.*, **549**, A30. [DOI], [ADS], [arXiv:1210.3045 [astro-ph.EP]]
- Neves, V., Santos, N. C., Sousa, S. G., Correia, A. C. M. and Israelian, G., 2009, “Chemical abundances of 451 stars from the HARPS GTO planet search program. Thin disc, thick disc, and planets”, *Astron. Astrophys.*, **497**(2), 563–581. [DOI], [ADS], [arXiv:0902.3374 [astro-ph.GA]]
- Nikolov, N., Sing, D. K., Pont, F., Burrows, A. S., Fortney, J. J., Ballester, G. E., Evans, T. M., Huitson, C. M., Wakeford, H. R., Wilson, P. A., Aigrain, S., Deming, D., Gibson, N. P., Henry, G. W., Knutson, H., Lecavelier des Etangs, A., Showman, A. P., Vidal-Madjar, A. and Zahnle, K., 2014, “Hubble Space Telescope hot Jupiter transmission spectral survey: a detection of Na and strong optical absorption in HAT-P-1b”, *Mon. Not. Roy. Astron. Soc.*, **437**(1), 46–66. [DOI], [ADS], [arXiv:1310.0083 [astro-ph.SR]]
- Nikolov, Nikolay, Sing, David K., Gibson, Neale P., Fortney, Jonathan J., Evans, Thomas M., Barstow, Joanna K., Kataria, Tiffany and Wilson, Paul A., 2016, “VLT FORS2 COMPARATIVE TRANSMISSION SPECTROSCOPY: DETECTION OF Na IN THE ATMOSPHERE OF WASP-39b FROM THE GROUND”, *The Astrophysical Journal*, **832**(2), 191. [DOI]URL: <https://doi.org/10.3847/0004-637x/832/2/191>
- Nissen, P. E., 2015, “High-precision abundances of elements in solar twin stars. Trends with stellar age and elemental condensation temperature”, *Astron. Astrophys.*, **579**, A52. [DOI], [ADS], [arXiv:1504.07598 [astro-ph.SR]]
- Nortmann, L., Pallé, E., Murgas, F., Dreizler, S., Iro, N. and Cabrera-Lavers, A., 2016, “The GTC exoplanet transit spectroscopy survey. IV. Confirmation of the flat transmission spectrum of HAT-P-32b”, *Astron. Astrophys.*, **594**, A65. [DOI], [ADS], [arXiv:1604.06041 [astro-ph.EP]]
- Oh, Semyeong, Price-Whelan, Adrian M., Brewer, John M., Hogg, David W., Spergel, David N. and Myles, Justin, 2018, “Kronos and Krios: Evidence for

- Accretion of a Massive, Rocky Planetary System in a Comoving Pair of Solar-type Stars”, *Astrophys. J.*, **854**(2), 138. [DOI], [ADS], [arXiv:1709.05344 [astro-ph.SR]]
- Önehag, Anna, Gustafsson, Bengt and Korn, Andreas, 2014, “Abundances and possible diffusion of elements in M 67 stars”, *Astron. Astrophys.*, **562**, A102. [DOI], [ADS], [arXiv:1310.6297 [astro-ph.SR]]
- Owen, James E., 2019, “Atmospheric Escape and the Evolution of Close-In Exoplanets”, *Annual Review of Earth and Planetary Sciences*, **47**, 67–90. [DOI], [ADS], [arXiv:1807.07609 [astro-ph.EP]]
- Oza, Apurva V., Johnson, Robert E., Lellouch, Emmanuel, Schmidt, Carl, Schneider, Nick, Huang, Chenliang, Gamborino, Diana, Gebek, Andrea, Wyttenbach, Aurelien, Demory, Brice-Olivier, Mordasini, Christoph, Saxena, Prabal, Dubois, David, Moullet, Arielle and Thomas, Nicolas, 2019, “Sodium and Potassium Signatures of Volcanic Satellites Orbiting Close-in Gas Giant Exoplanets”, *Astrophys. J.*, **885**(2), 168. [DOI], [ADS], [arXiv:1908.10732 [astro-ph.EP]]
- Palle, E., Chen, G., Prieto-Arranz, J., Nowak, G., Murgas, F., Nortmann, L., Pollacco, D., Lam, K., Montanes-Rodriguez, P., Parviainen, H. and Casasayas-Barris, N., 2017, “Feature-rich transmission spectrum for WASP-127b. Cloud-free skies for the puffiest known super-Neptune?”, *Astron. Astrophys.*, **602**, L15. [DOI], [ADS], [arXiv:1705.09230 [astro-ph.EP]]
- Panwar, Vatsal, Désert, Jean-Michel, Todorov, Kamen O., Bean, Jacob L., Stevenson, Kevin B., Huitson, C. M., Fortney, Jonathan J. and Bergmann, Marcel, 2022, “A new method to measure the spectra of transiting exoplanet atmospheres using multi-object spectroscopy”, *Mon. Not. Roy. Astron. Soc.*, **510**(3), 3236–3265. [DOI], [ADS], [arXiv:2112.06678 [astro-ph.EP]]
- Pepe, F., Cristiani, S., Rebolo, R., Santos, N. C., Dekker, H., Cabral, A., Di Marcantonio, P., Figueira, P., Lo Curto, G., Lovis, C., Mayor, M., Mégevand, D., Molaro, P., Riva, M., Zapatero Osorio, M. R., Amate, M., Manescau, A.,

- Pasquini, L., Zerbi, F. M., Adibekyan, V., Abreu, M., Affolter, M., Alibert, Y., Aliverti, M., Allart, R., Allende Prieto, C., Álvarez, D., Alves, D., Avila, G., Baldini, V., Bandy, T., Barros, S. C. C., Benz, W., Bianco, A., Borsa, F., Bourrier, V., Bouchy, F., Broeg, C., Calderone, G., Cirami, R., Coelho, J., Conconi, P., Coretti, I., Cumani, C., Cupani, G., D’Odorico, V., Damasso, M., Deiries, S., Delabre, B., Demangeon, O. D. S., Dumusque, X., Ehrenreich, D., Faria, J. P., Fragoso, A., Genolet, L., Genoni, M., Génova Santos, R., González Hernández, J. I., Hughes, I., Iwert, O., Kerber, F., Knudstrup, J., Landoni, M., Lavie, B., Lillo-Box, J., Lizon, J. L., Maire, C., Martins, C. J. A. P., Mehner, A., Micela, G., Modigliani, A., Monteiro, M. A., Monteiro, M. J. P. F. G., Moschetti, M., Murphy, M. T., Nunes, N., Oggioni, L., Oliveira, A., Oshagh, M., Pallé, E., Pariani, G., Poretti, E., Rasilla, J. L., Rebordão, J., Redaelli, E. M., Santana Tschudi, S., Santin, P., Santos, P., Ségransan, D., Schmidt, T. M., Segovia, A., Sosnowska, D., Sozzetti, A., Sousa, S. G., Spanò, P., Suárez Mascareño, A., Taberner, H., Tenegi, F., Udry, S. and Zanutta, A., 2021, “ESPRESSO at VLT. On-sky performance and first results”, *Astron. Astrophys.*, **645**, A96. [[DOI](#)], [[ADS](#)], [[arXiv:2010.00316 \[astro-ph.IM\]](#)]
- Petigura, Erik A., Marcy, Geoffrey W., Winn, Joshua N., Weiss, Lauren M., Fulton, Benjamin J., Howard, Andrew W., Sinukoff, Evan, Isaacson, Howard, Morton, Timothy D. and Johnson, John Asher, 2018a, “The California-Kepler Survey. IV. Metal-rich Stars Host a Greater Diversity of Planets”, *Astron. J.*, **155**(2), 89. [[DOI](#)], [[ADS](#)], [[arXiv:1712.04042 \[astro-ph.EP\]](#)]
- Petigura, Erik A., Marcy, Geoffrey W., Winn, Joshua N., Weiss, Lauren M., Fulton, Benjamin J., Howard, Andrew W., Sinukoff, Evan, Isaacson, Howard, Morton, Timothy D. and Johnson, John Asher, 2018b, “The California-Kepler Survey. IV. Metal-rich Stars Host a Greater Diversity of Planets”, *Astron. J.*, **155**(2), 89. [[DOI](#)], [[ADS](#)], [[arXiv:1712.04042 \[astro-ph.EP\]](#)]
- Plez, B., 2012, “Turbospectrum: Code for spectral synthesis”, [[ADS](#)]

- Pollack, James B., Hubickyj, Olenka, Bodenheimer, Peter, Lissauer, Jack J., Podolak, Morris and Greenzweig, Yuval, 1996a, “Formation of the Giant Planets by Concurrent Accretion of Solids and Gas”, , **124**(1), 62–85. [DOI], [ADS]
- Pollack, James B., Hubickyj, Olenka, Bodenheimer, Peter, Lissauer, Jack J., Podolak, Morris and Greenzweig, Yuval, 1996b, “Formation of the Giant Planets by Concurrent Accretion of Solids and Gas”, , **124**(1), 62–85. [DOI], [ADS]
- Quirrenbach, A., Amado, P. J., Caballero, J. A., Mundt, R., Reiners, A., Ribas, I., Seifert, W., Abril, M., Aceituno, J., Alonso-Floriano, F. J., Ammler-von Eiff, M., Antona Jiménez, R., Anwand-Heerwart, H., Azzaro, M., Bauer, F., Barrado, D., Becerril, S., Béjar, V. J. S., Benítez, D., Berdiñas, Z. M., Cárdenas, M. C., Casal, E., Claret, A., Colomé, J., Cortés-Contreras, M., Czesla, S., Doellinger, M., Dreizler, S., Feiz, C., Fernández, M., Galadí, D., Gálvez-Ortiz, M. C., García-Piquer, A., García-Vargas, M. L., Garrido, R., Gesa, L., Gómez Galera, V., González Álvarez, E., González Hernández, J. I., Grözinger, U., Guàrdia, J., Guenther, E. W., de Guindos, E., Gutiérrez-Soto, J., Hagen, H. J., Hatzes, A. P., Hauschildt, P. H., Helmling, J., Henning, T., Hermann, D., Hernández Castaño, L., Herrero, E., Hidalgo, D., Holgado, G., Huber, A., Huber, K. F., Jeffers, S., Joergens, V., de Juan, E., Kehr, M., Klein, R., Kürster, M., Lamert, A., Lalitha, S., Laun, W., Lemke, U., Lenzen, R., López del Fresno, Mauro, López Martí, B., López-Santiago, J., Mall, U., Mandel, H., Martín, E. L., Martín-Ruiz, S., Martínez-Rodríguez, H., Marvin, C. J., Mathar, R. J., Mirabet, E., Montes, D., Morales Muñoz, R., Moya, A., Naranjo, V., Ofir, A., Oreiro, R., Pallé, E., Panduro, J., Passegger, V. M., Pérez-Calpena, A., Pérez Medialdea, D., Perger, M., Pluto, M., Ramón, A., Rebolo, R., Redondo, P., Reffert, S., Reinhardt, S., Rhode, P., Rix, H. W., Rodler, F., Rodríguez, E., Rodríguez-López, C., Rodríguez-Pérez, E., Rohloff, R. R., Rosich, A., Sánchez-Blanco, E., Sánchez Carrasco, M. A., Sanz-Forcada, J., Sarmiento, L. F., Schäfer, S., Schiller, J., Schmidt, C., Schmitt, J. H. M. M., Solano, E., Stahl, O., Storz, C., Stürmer, J., Suárez, J. C., Ulbrich, R. G., Veredas, G., Wagner, K., Winkler, J., Zapatero

- Osorio, M. R., Zechmeister, M., Abellán de Paco, F. J., Anglada-Escudé, G., del Burgo, C., Klutsch, A., Lizon, J. L., López-Morales, M., Morales, J. C., Perryman, M. A. C., Tulloch, S. M. and Xu, W., 2014, “CARMENES instrument overview”, in *Ground-based and Airborne Instrumentation for Astronomy V*, (Eds.) Ramsay, Suzanne K., McLean, Ian S., Takami, Hideki, Society of Photo-Optical Instrumentation Engineers (SPIE) Conference Series, 9147, [DOI], [ADS]
- Rackham, Benjamin, Espinoza, Néstor, Apai, Dániel, López-Morales, Mercedes, Jordán, Andrés, Osip, David J., Lewis, Nikole K., Rodler, Florian, Fraine, Jonathan D., Morley, Caroline V. and Fortney, Jonathan J., 2017, “ACCESS I. AN OPTICAL TRANSMISSION SPECTRUM OF GJ 1214b REVEALS A HETEROGENEOUS STELLAR PHOTOSPHERE”, *The Astrophysical Journal*, **834**(2), 151. [DOI]URL: <https://doi.org/10.3847/1538-4357/aa4f6c>
- Rackham, Benjamin V., Apai, Dániel and Giampapa, Mark S., 2018, “The Transit Light Source Effect: False Spectral Features and Incorrect Densities for M-dwarf Transiting Planets”, *Astrophys. J.*, **853**(2), 122. [DOI], [ADS], [arXiv:1711.05691 [astro-ph.EP]]
- Ramírez, I., Meléndez, J. and Asplund, M., 2009, “Accurate abundance patterns of solar twins and analogs. Does the anomalous solar chemical composition come from planet formation?”, *Astron. Astrophys.*, **508**(1), L17–L20. [DOI], [ADS]
- Raymond, S. N., Izidoro, A. and Morbidelli, A., 2020, “Solar System Formation in the Context of Extrasolar Planets”, in *Planetary Astrobiology*, (Eds.) Meadows, Victoria S., Arney, Giada N., Schmidt, Britney E., Des Marais, David J., p. 287. [DOI], [ADS]
- Redfield, Seth, Endl, Michael, Cochran, William D. and Koesterke, Lars, 2008, “Sodium Absorption from the Exoplanetary Atmosphere of HD 189733b Detected in the Optical Transmission Spectrum”, *Astrophys. J. Lett.*, **673**(1), L87. [DOI], [ADS], [arXiv:0712.0761 [astro-ph]]

- Ren, Anbing, Fu, Jianning, De Cat, Peter, Wu, Yue, Yang, Xiaohu, Shi, Jianrong, Luo, Ali, Zhang, Haotong, Dong, Subo, Zhang, Ruyuan, Zhang, Yong, Hou, Yonghui, Wang, Yuefei, Cao, Zihuang and Du, Bing, 2016, “LAMOST Observations in the Kepler Field. Analysis of the Stellar Parameters Measured with LASP Based on Low-resolution Spectra”, *Astrophys. J. Suppl.*, **225**(2), 28. [DOI], [ADS], [arXiv:1607.01453 [astro-ph.SR]]
- Saffe, C., Flores, M. and Buccino, A., 2015, “HD 80606: searching for the chemical signature of planet formation”, *Astron. Astrophys.*, **582**, A17. [DOI], [ADS], [arXiv:1507.08125 [astro-ph.SR]]
- Saffe, C., Flores, M., Jaque Arancibia, M., Buccino, A. and Jofré, E., 2016, “Temperature condensation trend in the debris-disk binary system ζ^2 Reticuli”, *Astron. Astrophys.*, **588**, A81. [DOI], [ADS], [arXiv:1602.01320 [astro-ph.SR]]
- Saffe, C., Jofré, E., Martioli, E., Flores, M., Petrucci, R. and Jaque Arancibia, M., 2017, “Signatures of rocky planet engulfment in HAT-P-4. Implications for chemical tagging studies”, *Astron. Astrophys.*, **604**, L4. [DOI], [ADS], [arXiv:1707.02180 [astro-ph.SR]]
- Sánchez-Janssen, R., Mieske, S., Selman, F., Bristow, P., Hammersley, P., Hilker, M., Rejkuba, M. and Wolff, B., 2014, “Revisiting the impact of atmospheric dispersion and differential refraction on widefield multiobject spectroscopic observations. From VLT/VIMOS to next generation instruments”, *Astron. Astrophys.*, **566**, A2. [DOI], [ADS], [arXiv:1402.5970 [astro-ph.IM]]
- Sánchez-López, A., Alonso-Floriano, F. J., López-Puertas, M., Snellen, I. A. G., Funke, B., Nagel, E., Bauer, F. F., Amado, P. J., Caballero, J. A., Czesla, S., Nortmann, L., Pallé, E., Salz, M., Reiners, A., Ribas, I., Quirrenbach, A., Anglada-Escudé, G., Béjar, V. J. S., Casasayas-Barris, N., Galadí-Enríquez, D., Guenther, E. W., Henning, Th., Kaminski, A., Kürster, M., Lampón, M., Lara, L. M., Montes, D., Morales, J. C., Stangret, M., Tal-Or, L., Sanz-Forcada, J., Schmitt, J. H. M. M., Zapatero Osorio, M. R. and Zechmeister, M.,

- 2019, “Water vapor detection in the transmission spectra of HD 209458 b with the CARMENES NIR channel”, *Astron. Astrophys.*, **630**, A53. [DOI], [ADS], [arXiv:1908.08754 [astro-ph.EP]]
- Santos, N. C., Israelian, G. and Mayor, M., 2001, “The metal-rich nature of stars with planets*”, *A&A*, **373**(3), 1019–1031. [DOI]URL: <https://doi.org/10.1051/0004-6361:20010648>
- Santos, N. C., Israelian, G. and Mayor, M., 2004a, “Spectroscopic [Fe/H] for 98 extra-solar planet-host stars. Exploring the probability of planet formation”, *Astron. Astrophys.*, **415**, 1153–1166. [DOI], [ADS], [arXiv:astro-ph/0311541 [astro-ph]]
- Santos, N. C., Israelian, G. and Mayor, M., 2004b, “Spectroscopic [Fe/H] for 98 extra-solar planet-host stars. Exploring the probability of planet formation”, *Astron. Astrophys.*, **415**, 1153–1166. [DOI], [ADS], [arXiv:astro-ph/0311541 [astro-ph]]
- Scherrer, Philip Hanby, Schou, Jesper, Bush, RI, Kosovichev, AG, Bogart, RS, Hoeksema, JT, Liu, Y, Duvall, TL, Zhao, J, Schrijver, CJ *et al.*, 2012, “The helioseismic and magnetic imager (HMI) investigation for the solar dynamics observatory (SDO)”, *Solar Physics*, **275**(1), 207–227
- Schlaufman, Kevin C. and Laughlin, Gregory, 2011, “Kepler Exoplanet Candidate Host Stars Are Preferentially Metal Rich”, *Astrophys. J.*, **738**(2), 177. [DOI], [ADS], [arXiv:1106.6043 [astro-ph.EP]]
- Schou, Jørgen, Scherrer, Philip H, Bush, Rock Irvin, Wachter, Richard, Couvidat, S’ebastien, Rabello-Soares, Maria Cristina, Bogart, Richard S, Hoeksema, JT, Liu, Y, Duvall, TL *et al.*, 2012, “Design and ground calibration of the Helioseismic and Magnetic Imager (HMI) instrument on the Solar Dynamics Observatory (SDO)”, *Solar Physics*, **275**(1), 229–259
- Seager, S. and Sasselov, D. D., 2000, “Theoretical Transmission Spectra during Extrasolar Giant Planet Transits”, *The Astrophysical Journal*, **537**(2), 916–921.

[DOI]URL:

<https://doi.org/10.1086%2F309088>

Seidel, J. V., Ehrenreich, D., Wyttenbach, A., Allart, R., Lendl, M., Pino, L., Bourrier, V., Cegla, H. M., Lovis, C., Barrado, D., Bayliss, D., Astudillo-Defru, N., Deline, A., Fisher, C., Heng, K., Joseph, R., Lavie, B., Melo, C., Pepe, F., Ségransan, D. and Udry, S., 2019, “Hot Exoplanet Atmospheres Resolved with Transit Spectroscopy (HEARTS). II. A broadened sodium feature on the ultra-hot giant WASP-76b”, *Astron. Astrophys.*, **623**, A166. [DOI], [ADS], [arXiv:1902.00001 [astro-ph.EP]]

Seidel, J. V., Ehrenreich, D., Bourrier, V., Allart, R., Attia, O., Hoeijmakers, H. J., Lendl, M., Linder, E., Wyttenbach, A., Astudillo-Defru, N., Bayliss, D., Cegla, H. M., Heng, K., Lavie, B., Lovis, C., Melo, C., Pepe, F., dos Santos, L. A., Ségransan, D. and Udry, S., 2020a, “Hot Exoplanet Atmospheres Resolved with Transit Spectroscopy (HEARTS). V. Detection of sodium on the bloated super-Neptune WASP-166b”, *Astron. Astrophys.*, **641**, L7. [DOI], [ADS], [arXiv:2007.01783 [astro-ph.EP]]

Seidel, J. V., Lendl, M., Bourrier, V., Ehrenreich, D., Allart, R., Sousa, S. G., Cegla, H. M., Bonfils, X., Conod, U., Grandjean, A., Wyttenbach, A., Astudillo-Defru, N., Bayliss, D., Heng, K., Lavie, B., Lovis, C., Melo, C., Pepe, F., Ségransan, D. and Udry, S., 2020b, “Hot Exoplanet Atmospheres Resolved with Transit Spectroscopy (HEARTS). VI. Non-detection of sodium with HARPS on the bloated super-Neptune WASP-127b”, *Astron. Astrophys.*, **643**, A45. [DOI], [ADS], [arXiv:2009.13386 [astro-ph.EP]]

Seidel, J. V., Lendl, M., Bourrier, V., Ehrenreich, D., Allart, R., Sousa, S. G., Cegla, H. M., Bonfils, X., Conod, U., Grandjean, A., Wyttenbach, A., Astudillo-Defru, N., Bayliss, D., Heng, K., Lavie, B., Lovis, C., Melo, C., Pepe, F., Ségransan, D. and Udry, S., 2020c, “Hot Exoplanet Atmospheres Resolved with Transit Spectroscopy (HEARTS). VI. Non-detection of sodium with HARPS on

- the bloated super-Neptune WASP-127b”, *Astron. Astrophys.*, **643**, A45. [DOI], [ADS], [arXiv:2009.13386 [astro-ph.EP]]
- Sing, D. K., Désert, J. M., Fortney, J. J., Lecavelier Des Etangs, A., Ballester, G. E., Cepa, J., Ehrenreich, D., López-Morales, M., Pont, F., Shabram, M. and Vidal-Madjar, A., 2011, “Gran Telescopio Canarias OSIRIS transiting exoplanet atmospheric survey: detection of potassium in XO-2b from narrowband spectrophotometry”, *Astron. Astrophys.*, **527**, A73. [DOI], [ADS], [arXiv:1008.4795 [astro-ph.EP]]
- Sing, D. K., Huitson, C. M., Lopez-Morales, M., Pont, F., Désert, J.-M., Ehrenreich, D., Wilson, P. A., Ballester, G. E., Fortney, J. J., Lecavelier des Etangs, A. and Vidal-Madjar, A., 2012, “GTC OSIRIS transiting exoplanet atmospheric survey: detection of sodium in XO-2b from differential long-slit spectroscopy”, *Monthly Notices of the Royal Astronomical Society*, **426**(2), 1663–1670. [DOI], [https://academic.oup.com/mnras/article-pdf/426/2/1663/2979957/426-2-1663.pdf]URL: <https://doi.org/10.1111/j.1365-2966.2012.21938.x>
- Sing, David K., Fortney, Jonathan J., Nikolov, Nikolay, Wakeford, Hannah R., Kataria, Tiffany, Evans, Thomas M., Aigrain, Suzanne, Ballester, Gilda E., Burrows, Adam S., Deming, Drake, Désert, Jean-Michel, Gibson, Neale P., Henry, Gregory W., Huitson, Catherine M., Knutson, Heather A., Etangs, Alain Lecavelier des, Pont, Frederic, Showman, Adam P., Vidal-Madjar, Alfred, Williamson, Michael H. and Wilson, Paul A., 2016, “A continuum from clear to cloudy hot-Jupiter exoplanets without primordial water depletion”, *Nature*, **529**(7584), 59–62. [DOI]URL: <https://doi.org/10.1038/nature16068>
- Smette, A., Sana, H., Noll, S., Horst, H., Kausch, W., Kimeswenger, S., Barden, M., Szyszka, C., Jones, A., Gallenne, A., Vinther, J., Ballester, P. and Taylor, J., 2015, “Molecfit: A general tool for telluric absorption correction - I. Method and application to ESO instruments”, *Astronomy and Astrophysics*, **576**

- Snellen, I. A. G., Albrecht, S., de Mooij, E. J. W. and Le Poole, R. S., 2008, “Ground-based detection of sodium in the transmission spectrum of exoplanet HD 209458b”, *Astron. Astrophys.*, **487**(1), 357–362. [DOI], [ADS], [arXiv:0805.0789 [astro-ph]]
- Snellen, Ignas A. G., de Kok, Remco J., de Mooij, Ernst J. W. and Albrecht, Simon, 2010, “The orbital motion, absolute mass and high-altitude winds of exoplanet HD 209458b”, *Nature*, **465**(7301), 1049–1051. [DOI]URL: <https://doi.org/10.1038/nature09111>
- Snellen, Ignas A. G., de Kok, Remco J., de Mooij, Ernst J. W. and Albrecht, Simon, 2010, “The orbital motion, absolute mass and high-altitude winds of exoplanet HD209458b”, *Nature*, **465**(7301), 1049–1051. [DOI], [ADS], [arXiv:1006.4364 [astro-ph.EP]]
- Sousa, S. G., Santos, N. C., Mayor, M., Udry, S., Casagrande, L., Israelian, G., Pepe, F., Queloz, D. and Monteiro, M. J. P. F. G., 2008, “Spectroscopic parameters for 451 stars in the HARPS GTO planet search program. Stellar [Fe/H] and the frequency of exo-Neptunes”, *Astron. Astrophys.*, **487**(1), 373–381. [DOI], [ADS], [arXiv:0805.4826 [astro-ph]]
- Sriram, S., Kumar, Amit, Surya, Arun, Sivarani, T., Giridhar, Sunetra, Kathiravan, S., Anand, M. N., Jones, Damien, Grobler, Deon, Jakobsson, Robert, Chanumolu, Anantha, Unni, Athira, Dorje, Angchuk, Dorje, Tsewang and Gyalson, Tsewang, 2018, “Hanle echelle spectrograph: design and performance”, in *Ground-based and Airborne Instrumentation for Astronomy VII*, (Eds.) Evans, Christopher J., Simard, Luc, Takami, Hideki, Society of Photo-Optical Instrumentation Engineers (SPIE) Conference Series, 10702, [DOI], [ADS]
- Stangret, M., Casasayas-Barris, N., Pallé, E., Orell-Miquel, J., Morello, G., Luque, R., Nowak, G. and Yan, F., 2021, “High-resolution transmission spectroscopy study of ultra-hot Jupiters HAT-P-57b, KELT-17b, KELT-21b, KELT-7b, MASCARA-1b, and WASP-189b”, *arXiv e-prints*, arXiv:2111.13064. [ADS],

[[arXiv:2111.13064](https://arxiv.org/abs/2111.13064) [[astro-ph.EP](#)]]

Stevenson, Kevin B., Bean, Jacob L., Seifahrt, Andreas, Désert, Jean-Michel, Madhusudhan, Nikku, Bergmann, Marcel, Kreidberg, Laura and Homeier, Derek, 2014, “TRANSMISSION SPECTROSCOPY OF THE HOT JUPITER WASP-12b FROM 0.7 TO 5 μm ”, *The Astronomical Journal*, **147**(6), 161. [[DOI](#)]URL: <https://doi.org/10.1088/0004-6256/147/6/161>

Suárez-Andrés, L., Israelian, G., González Hernández, J. I., Adibekyan, V. Zh., Delgado Mena, E., Santos, N. C. and Sousa, S. G., 2017, “CNO behaviour in planet-harboring stars. II. Carbon abundances in stars with and without planets using the CH band”, *Astron. Astrophys.*, **599**, A96. [[DOI](#)], [[ADS](#)], [[arXiv:1611.10092](https://arxiv.org/abs/1611.10092) [[astro-ph.SR](#)]]

Swastik, C., Banyal, Ravinder K., Narang, Mayank, Manoj, P., Sivarani, T., Rajaguru, S. P., Unni, Athira and Banerjee, Bihan, 2022, “Galactic chemical evolution of exoplanet host stars: Are high-mass planetary systems young?”, *arXiv e-prints*, arXiv:2205.15793. [[ADS](#)], [[arXiv:2205.15793](https://arxiv.org/abs/2205.15793) [[astro-ph.EP](#)]]

Tennyson, Jonathan and Yurchenko, Sergei N., 2012, “ExoMol: molecular line lists for exoplanet and other atmospheres”, *Monthly Notices of the Royal Astronomical Society*, **425**(1), 21–33. [[DOI](#)], [<http://oup.prod.sis.lan/mnras/article-pdf/425/1/21/3182616/425-1-21.pdf>]URL: <https://doi.org/10.1111/j.1365-2966.2012.21440.x>

Teske, Johanna K., Ghezzi, Luan, Cunha, Katia, Smith, Verne V., Schuler, Simon C. and Bergemann, Maria, 2015, “Abundance Differences between Exoplanet Binary Host Stars XO-2N and XO-2S—Dependence on Stellar Parameters”, *Astrophys. J. Lett.*, **801**(1), L10. [[DOI](#)], [[ADS](#)], [[arXiv:1501.02167](https://arxiv.org/abs/1501.02167) [[astro-ph.EP](#)]]

Teske, Johanna K., Khanal, Sandhya and Ramírez, Ivan, 2016a, “The curious case of elemental abundances in the dual hot Jupiter hosts WASP-94A AND B*”,

- The Astrophysical Journal*, **819**(1), 19. [DOI]URL:
<https://dx.doi.org/10.3847/0004-637X/819/1/19>
- Teske, Johanna K., Shectman, Stephen A., Vogt, Steve S., Díaz, Matías, Butler, R. Paul, Crane, Jeffrey D., Thompson, Ian B. and Arriagada, Pamela, 2016b, “The MAGELLAN PFS planet search program: radial velocity and stellar abundance analysis of the 360 au, metal-poor binary ”twins” HD 133131A and B*”, *The Astronomical Journal*, **152**(6), 167. [DOI]URL:
<https://dx.doi.org/10.3847/0004-6256/152/6/167>
- Thompson, WT, 2006, “Coordinate systems for solar image data”, *Astronomy & Astrophysics*, **449**(2), 791–803
- Todorov, Kamen O., Désert, Jean-Michel, Huitson, Catherine M., Bean, Jacob L., Panwar, Vatsal, de Matos, Filipe, Stevenson, Kevin B., Fortney, Jonathan J. and Bergmann, Marcel, 2019, “Ground-based optical transmission spectrum of the hot Jupiter HAT-P-1b”, *Astron. Astrophys.*, **631**, A169. [DOI], [ADS], [arXiv:1903.05563 [astro-ph.EP]]
- Tsiaras, A., Waldmann, I. P., Rocchetto, M., Varley, R., Morello, G., Damiano, M. and Tinetti, G., 2016, “A New Approach to Analyzing HST Spatial Scans: The Transmission Spectrum of HD 209458 b”, *Astrophys. J.*, **832**(2), 202. [DOI], [ADS], [arXiv:1511.07796 [astro-ph.EP]]
- Tucci Maia, Marcelo, Meléndez, Jorge and Ramírez, Iván, 2014, “High Precision Abundances in the 16 Cyg Binary System: A Signature of the Rocky Core in the Giant Planet”, *Astrophys. J. Lett.*, **790**(2), L25. [DOI], [ADS], [arXiv:1407.4132 [astro-ph.SR]]
- Ujjwal, K., Kartha, Sreeja S., Mathew, Blesson, Manoj, P. and Narang, Mayank, 2020, “Analysis of Membership Probability in Nearby Young Moving Groups with Gaia DR2”, *Astron. J.*, **159**(4), 166. [DOI], [ADS], [arXiv:2002.04801 [astro-ph.SR]]

- Vidal-Madjar, A., Huitson, C. M., Lecavelier Des Etangs, A., Sing, D. K., Ferlet, R., Désert, J. M., Hébrard, G., Boisse, I., Ehrenreich, D. and Moutou, C., 2011a, “The upper atmosphere of the exoplanet HD209458b revealed by the sodium D lines: temperature-pressure profile, ionization layer and thermosphere (Corrigendum)”, [[ADS](#)]
- Vidal-Madjar, A., Sing, D. K., Lecavelier Des Etangs, A., Ferlet, R., Désert, J. M., Hébrard, G., Boisse, I., Ehrenreich, D. and Moutou, C., 2011b, “The upper atmosphere of the exoplanet HD 209458 b revealed by the sodium D lines. Temperature-pressure profile, ionization layer, and thermosphere”, *Astron. Astrophys.*, **527**, A110. [[DOI](#)], [[ADS](#)], [[arXiv:1012.5938 \[astro-ph.EP\]](#)]
- Vogt, N., Schmidt, T. O. B., Neuhäuser, R., Bedalov, A., Roell, T., Seifahrt, A. and Mugrauer, M., 2012, “Astrometric confirmation of young low-mass binaries and multiple systems in the Chamaeleon star-forming regions”, *Astron. Astrophys.*, **546**, A63. [[DOI](#)], [[ADS](#)], [[arXiv:1204.3332 \[astro-ph.SR\]](#)]
- Vogt, S. S., Allen, S. L., Bigelow, B. C., Bresee, L., Brown, B., Cantrall, T., Conrad, A., Couture, M., Delaney, C., Epps, H. W., Hilyard, D., Hilyard, D. F., Horn, E., Jern, N., Kanto, D., Keane, M. J., Kibrick, R. I., Lewis, J. W., Osborne, J., Pardeilhan, G. H., Pfister, T., Ricketts, T., Robinson, L. B., Stover, R. J., Tucker, D., Ward, J. and Wei, M. Z., 1994a, “HIRES: the high-resolution echelle spectrometer on the Keck 10-m Telescope”, in *Instrumentation in Astronomy VIII*, (Eds.) Crawford, David L., Craine, Eric R., Society of Photo-Optical Instrumentation Engineers (SPIE) Conference Series, 2198, [[DOI](#)], [[ADS](#)]
- Vogt, S. S., Allen, S. L., Bigelow, B. C., Bresee, L., Brown, B., Cantrall, T., Conrad, A., Couture, M., Delaney, C., Epps, H. W., Hilyard, D., Hilyard, D. F., Horn, E., Jern, N., Kanto, D., Keane, M. J., Kibrick, R. I., Lewis, J. W., Osborne, J., Pardeilhan, G. H., Pfister, T., Ricketts, T., Robinson, L. B., Stover, R. J., Tucker, D., Ward, J. and Wei, M. Z., 1994b, “HIRES: the high-resolution

- echelle spectrometer on the Keck 10-m Telescope”, in *Instrumentation in Astronomy VIII*, (Eds.) Crawford, David L., Craine, Eric R., Society of Photo-Optical Instrumentation Engineers (SPIE) Conference Series, 2198, [DOI], [ADS]
- Wachter, R, Schou, Jesper, Rabello-Soares, MC, Miles, JW, Duvall, TL and Bush, RI, 2011, “Image quality of the helioseismic and magnetic imager (HMI) onboard the solar dynamics observatory (SDO)”, in *The Solar Dynamics Observatory*, pp. 261–284, Springer
- Wang, Songhu, Jones, Matias, Shporer, Avi, Fulton, Benjamin J., Paredes, Leonardo A., Trifonov, Trifon, Kossakowski, Diana, Eastman, Jason, Redfield, Seth, Günther, Maximilian N., Kreidberg, Laura, Huang, Chelsea X., Millholland, Sarah, Seligman, Darryl, Fischer, Debra, Brahm, Rafael, Wang, Xian-Yu, Cruz, Bryndis, Henry, Todd, James, Hodari-Sadiki, Addison, Brett, Liang, En-Si, Davis, Allen B., Tronsgaard, René, Worku, Keduse, Brewer, John M., Kürster, Martin, Zhang, Hui, Beichman, Charles A., Bieryla, Allyson, Brown, Timothy M., Christiansen, Jessie L., Ciardi, David R., Collins, Karen A., Esquerdo, Gilbert A., Howard, Andrew W., Isaacson, Howard, Latham, David W., Mazeh, Tsevi, Petigura, Erik A., Quinn, Samuel N., Shahaf, Sahar, Siverd, Robert J., Rodler, Florian, Reffert, Sabine, Zakhzhay, Olga, Ricker, George R., Vanderspek, Roland, Seager, Sara, Winn, Joshua N., Jenkins, Jon M., Boyd, Patricia T., Fűrész, Gábor, Henze, Christopher, Levine, Alen M., Morris, Robert, Paegert, Martin, Stassun, Keivan G., Ting, Eric B., Vezie, Michael and Laughlin, Gregory, 2019, “HD 202772A b: A Transiting Hot Jupiter around a Bright, Mildly Evolved Star in a Visual Binary Discovered by TESS”, *Astron. J.*, **157**(2), 51. [DOI], [ADS], [arXiv:1810.02341 [astro-ph.EP]]
- Wilson, Jamie, Gibson, Neale P., Nikolov, Nikolay, Constantinou, Savvas, Madhusudhan, Nikku, Goyal, Jayesh, Barstow, Joanna K., Carter, Aarynn L., de Mooij, Ernst J. W., Drummond, Benjamin, Mikal-Evans, Thomas, Helling, Christiane, Mayne, Nathan J. and Sing, David K., 2020, “Ground-based transmission spectroscopy with FORS2: A featureless optical transmission spectrum

and detection of H₂O for the ultra-hot Jupiter WASP-103b”, *Mon. Not. Roy. Astron. Soc.*, **497**(4), 5155–5170. [DOI], [ADS], [arXiv:2007.13510 [astro-ph.EP]]

Winn, Joshua N., 2010, “Transits and Occultations”

Wood, P. L., Maxted, P. F. L., Smalley, B. and Iro, N., 2011, “Transmission spectroscopy of the sodium ‘D’ doublet in WASP-17b with the VLT*”, *Monthly Notices of the Royal Astronomical Society*, **412**(4), 2376–2382. [DOI], [https://academic.oup.com/mnras/article-pdf/412/4/2376/3342240/mnras0412-2376.pdf]URL:

<https://doi.org/10.1111/j.1365-2966.2010.18061.x>

Wytttenbach, A., Ehrenreich, D., Lovis, C., Udry, S. and Pepe, F., 2015a, “Spectrally resolved detection of sodium in the atmosphere of HD 189733b with the HARPS spectrograph”, *Astron. Astrophys.*, **577**, A62. [DOI], [ADS], [arXiv:1503.05581 [astro-ph.EP]]

Wytttenbach, A., Ehrenreich, D., Lovis, C., Udry, S. and Pepe, F., 2015b, “Spectrally resolved detection of sodium in the atmosphere of HD 189733b with the HARPS spectrograph”, *Astron. Astrophys.*, **577**, A62. [DOI], [ADS], [arXiv:1503.05581 [astro-ph.EP]]

Wytttenbach, A., Lovis, C., Ehrenreich, D., Bourrier, V., Pino, L., Allart, R., Astudillo-Defru, N., Cegla, H. M., Heng, K., Lavie, B., Melo, C., Murgas, F., Santerne, A., Ségransan, D., Udry, S. and Pepe, F., 2017a, “Hot Exoplanet Atmospheres Resolved with Transit Spectroscopy (HEARTS). I. Detection of hot neutral sodium at high altitudes on WASP-49b”, *Astron. Astrophys.*, **602**, A36. [DOI], [ADS], [arXiv:1702.00448 [astro-ph.EP]]

Wytttenbach, A., Lovis, C., Ehrenreich, D., Bourrier, V., Pino, L., Allart, R., Astudillo-Defru, N., Cegla, H. M., Heng, K., Lavie, B., Melo, C., Murgas, F., Santerne, A., Ségransan, D., Udry, S. and Pepe, F., 2017b, “Hot Exoplanet Atmospheres Resolved with Transit Spectroscopy (HEARTS). I. Detection of

- hot neutral sodium at high altitudes on WASP-49b”, *Astron. Astrophys.*, **602**, A36. [DOI], [ADS], [arXiv:1702.00448 [astro-ph.EP]]
- Yan, Hongliang, Li, Haining, Wang, Song, Zong, Weikai, Yuan, Haibo, Xiang, Maosheng, Huang, Yang, Xie, Jiwei, Dong, Subo, Yuan, Hailong, Bi, Shaolan, Chu, Yaoquan, Cui, Xiangqun, Deng, Licai, Fu, Jianning, Han, Zhanwen, Hou, Jinliang, Li, Guoping, Liu, Chao, Liu, Jifeng, Liu, Xiaowei, Luo, Ali, Shi, Jianrong, Wu, Xuebing, Zhang, Haotong, Zhao, Gang and Zhao, Yongheng, 2022, “Overview of the LAMOST survey in the first decade”, *The Innovation*, **3**(2), 100 224. [DOI]URL:
<https://www.sciencedirect.com/science/article/pii/S2666675822000200>
- Yeo, KL, Solanki, SK and Krivova, NA, 2013, “Intensity contrast of solar network and faculae”, *Astronomy & Astrophysics*, **550**, A95
- Youdin, Andrew N., 2011, “The Exoplanet Census: A General Method Applied to Kepler”, *Astrophys. J.*, **742**(1), 38. [DOI], [ADS], [arXiv:1105.1782 [astro-ph.EP]]
- Zhao, Gang, Zhao, Yong-Heng, Chu, Yao-Quan, Jing, Yi-Peng and Deng, Li-Cai, 2012, “LAMOST spectral survey — An overview”, *Research in Astronomy and Astrophysics*, **12**(7), 723–734. [DOI]URL:
<https://doi.org/10.1088/1674-4527/12/7/002>
- Zhao, Gang, Zhao, Yong-Heng, Chu, Yao-Quan, Jing, Yi-Peng and Deng, Li-Cai, 2012a, “LAMOST spectral survey — An overview”, *Research in Astronomy and Astrophysics*, **12**(7), 723–734. [DOI], [ADS]
- Zhao, Gang, Zhao, Yongheng, Chu, Yaoquan, Jing, Yipeng and Deng, Licai, 2012b, “LAMOST Spectral Survey”, *arXiv e-prints*, arXiv:1206.3569. [ADS], [arXiv:1206.3569 [astro-ph.IM]]
- Zhou, G. and Bayliss, D. D. R., 2012, “Detection of sodium absorption in WASP-17b with Magellan”, *Mon. Not. Roy. Astron. Soc.*, **426**(3), 2483–2488. [DOI], [ADS], [arXiv:1207.6895 [astro-ph.EP]]

Zong, Weikai, Fu, Jian-Ning, Cat, Peter De, Shi, Jianrong, Luo, Ali, Zhang, Hao-tong, Frasca, A., Corbally, C. J., Molenda-Żakowicz, J., Catanzaro, G., Gray, R. O., Wang, Jiangtao, Pan, Yang, Ren, Anbing, Zhang, Ruyuan, Jin, Mengqi, Wu, Yue, Dong, Subo, Xie, Ji-Wei, Zhang, Wei and and, Yonghui Hou, 2018, “LAMOST Observations in the Kepler Field. II. Database of the Low-resolution Spectra from the Five-year Regular Survey”, *The Astrophysical Journal Supplement Series*, **238**(2), 30. [DOI]URL:

<https://doi.org/10.3847/1538-4365/aadf81>